RESPONSE OF A CRACKED ROTATING SHAFT WITH A DISK DURING PASSAGE THROUGH A CRITICAL SPEED

by

Surjani Suherman

Thesis submitted to the Faculty of the
Virginia Polytechnic Institute and State University
in partial fulfillment of the requirements for the degree of
MASTER OF SCIENCE
in
Civil Engineering

APPROVED

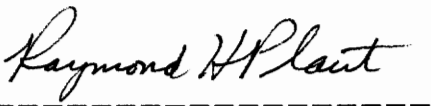

Raymond H. Plaut, Chairman

R. Gordon Kirk

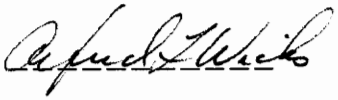

Alfred L. Wicks

December, 1992

Blacksburg, Virginia

C.2

RESPONSE OF A CRACKED ROTATING SHAFT WITH A DISK DURING PASSAGE THROUGH A CRITICAL SPEED

by

Surjani Suherman

Raymond H. Plaut, Chairman

Civil Engineering

(ABSTRACT)

Non-stationary motion of a cracked rotating shaft with accelerating or decelerating angular velocity Ω through a critical speed is studied. The shaft has a breathing transverse crack and a disk. There are two parts, which are the investigation of flexural response, neglecting the torsional vibrations, and the investigation of flexural-torsional response. In both studies the longitudinal vibration and the influence of shear deformation are neglected. The boundary conditions of the supports are simply supported for the transverse displacements and fixed-free in relation to torsion (for the flexural-torsional response only).

The transverse surface crack, which causes a geometric discontinuity, is replaced by generalized moments at the crack location. The equations of motion follow the formulation of Wauer. Galerkin's method and numerical integration are used to obtain approximate solutions. The maximum responses are determined.

The effects of the acceleration and deceleration rate and the different parameters of the breathing cracked rotating shaft, such as crack depth, crack

location, disk location, disk eccentricity, disk eccentricity angle, and disk mass, are studied. The influence of internal damping, external damping, and torsional external damping, are investigated. Comparisons with an open cracked rotating shaft and an uncracked rotating shaft are also presented. The influence of torsional deformation is analyzed. The results are presented in tables and figures.

ACKNOWLEDGMENTS

I would like to express my appreciation to Dr. Raymond H. Plaut for his guidance, patience, understanding, and support throughout my work on this research. I would also like to thank Dr. R. Gordon Kirk and Dr. Alfred L. Wicks for their support and time in serving on my committee.

I am grateful to the National Science Foundation for supporting this research under Grant No. MSS-9114529.

I would like to dedicate this thesis to my husband and my parents.

TABLE OF CONTENTS

LIST OF FIGURES

LIST OF TABLES

NOMENCLATURE

a : crack height

b : crack location

$\tilde{b}$: nondimensional crack location

c : disk location

$\tilde{c}$: nondimensional disk location

c_{44}, c_{55}, c_{66} : reciprocals of stiffness coefficients k_{44}, k_{55}, k_{66}

$\tilde{c}_{44}$, $\tilde{c}_{55}$, $\tilde{c}_{66}$: nondimensional reciprocals of stiffness coefficients k_{44}, k_{55}, k_{66}

d_c : crack damping coefficient

$\tilde{d}_c$: nondimensional crack damping coefficient

d_e : external damping coefficient

$\tilde{d}_e$: nondimensional external damping coefficient

d_i : internal damping coefficient

$\tilde{d}_i$: nondimensional internal damping coefficient

d_T : torsional external damping coefficient

$\tilde{d}_T$: nondimensional torsional external damping coefficient

D : shaft diameter

e_m : disk eccentricity

$\tilde{e}_m$: nondimensional disk eccentricity

E : Young's modulus

g : gravity

G : shear modulus of shaft

I_1 : moment of inertia of shaft with respect to the 1 - principal axis

I_2 : moment of inertia of shaft with respect to the 2 - principal axis

I_p : polar mass moment of inertia of disk

J : torsional constant of shaft

L : length of shaft

m : mass of disk

$\tilde{m}$: nondimensional disk mass

r_1, r_2 : radii of gyration of shaft

r_s : radius of shaft

R_d : radius of disk

t : time

v : transverse displacement in η-direction

$\tilde{v}$: nondimensional transverse displacement in η-direction

w : transverse displacement in the ζ-direction

$\tilde{w}$: nondimensional transverse displacement in ζ-direction

x : location of measurement

$\tilde{x}$: nondimensional location of measurement

z : nondimensional transverse displacement in vertical direction

$z_{max,w}$: nondimensional maximum z-transverse displacement over the whole length

$z_{max,x}$: nondimensional maximum z-transverse displacement at $\tilde{x} = 0.7$

Γ : ratio between I_2 and I_1

δ_m : disk eccentricity angle

ϵ : crack width parameter

θ : rotational angle (in radians)

λ : nondimensional rotational acceleration/deceleration

Λ : crack condition parameter; $\Lambda = 1$ for open crack, $\Lambda = 0$ for closed crack

μ : mass of shaft per unit length

$\tilde{\mu}$: nondimensional shaft mass

ν : Poisson's ratio

ρ : density of shaft

τ : nondimensional time

τ_{crit} : nondimensional time when the angular velocity passes the critical speed

τ_{max} : nondimensional time when the maximum response occurs

ϕ : torsional deformation

$\phi_{\text{max,f}}$: maximum ϕ-torsional deformation after transient response

$\phi_{\text{min,f}}$: minimum ϕ-torsional deformation after transient response

$\phi_{\text{ampl,f}}$: maximum amplitude of ϕ-torsional deformation after transient response

$\phi_{\text{mean,f}}$: mean amplitude of ϕ-torsional deformation after transient response

ω : natural frequency

Ω : nondimensional angular velocity

Ω_{crit} : first critical speed

Note: in the figures of time history, all parameters are nondimensional (tilde is left off).

Chapter 1
Introduction

1.1. Scope

Cracks in rotating shafts can cause problems. It is important to understand the behavior of cracked rotating shafts, so that cracks can be detected as early as possible. Transverse surface cracks cause geometric discontinuities on the rotating shaft. Therefore, there are non-linearities in the stiffness and damping of the system.

In this present study, the behavior of a cracked rotating shaft with a disk is investigated analytically. The shaft is accelerated or decelerated and the angular velocity Ω, a function of time, passes through a critical speed. When the shaft is rotating, the crack is assumed to be either completely open or completely closed at any one time, called a breathing condition, depending on the curvature of the shaft at the cracked cross section.

The mathematical formulation of this system is derived following the previous work of Wauer. Galerkin's method is used to obtain approximate solutions of the equations. The parameters in the equations are non-dimensionalized. Then, the approximate solutions of the non-dimensionalized responses are calculated numerically, using the Adams-Moulton method.

In the first part of this study, the flexural response neglecting torsional

vibration is considered. In the second part, the interaction between flexural and torsional responses is studied. In both studies, the longitudinal vibration and the shear deformation are neglected. The boundary conditions of the shaft are simply supported on transverse displacements and fixed-free in relation to torsion (for the second part of the study). The influence of torsional deformation is analyzed.

There are four types of damping, i.e., internal damping, external damping, torsional external damping, and crack damping. The influence of the dampings is studied. Also, the relation between the internal damping and the external damping for instability under constant angular velocity is determined.

The relationships of various parameters, i.e., crack depth, crack location, disk location, disk eccentricity, disk eccentricity angle, and disk mass under certain acceleration and deceleration rates are investigated. The influence of the acceleration and deceleration rate is analyzed. The responses under various crack conditions, i.e., breathing crack, open crack, and no crack, are also evaluated. The maximum responses are determined.

The results are illustrated in graphs and tables. Based on those results, the conclusions are drawn. Finally, suggestions for future research are presented.

1.2. Literature Review

Many investigations on rotating shafts with a transverse crack have been published. In a paper by Muszynska[23], asymmetrical shafts with a heavy unbalanced disk in the center, and with gaping or breathing cracks, were analyzed and the results were compared with experimental results. The crack was modelled by local changes in stiffness. Ying[41] also studied the transient whirling of a rotating shaft with an unbalanced disk. He showed for low damping cases of

rotating shafts with low acceleration that the maximum responses decrease as the acceleration increases. Using the finite element method, Bachschmid, Diana, and Pizzigoni[3] investigated the effects of unbalance on a cracked rotor. The unbalance reduced the vibration of the cracked rotor when passing through a critical speed. They also determined the vibrations in the case of different crack depths.

There are many models for replacing the crack in an analytical method to obtain the equations of motion. Gasch[11], who analyzed the dynamic behavior of a simple rotor with a disk and a cross-sectional crack, replaced the crack by a simple mechanism that described the breathing action. In another paper, Gasch, Person, and Weitz[12] made a comparison of crack models with regard to the behavior of a Laval rotor with a cracked hollow shaft.

Mayes and Davies[22] described analytical and experimental work on the coupled behavior of a rotating shaft with a transverse crack. They used finite element computer programs to calculate the vibrations of the shaft, and they developed a method of successive approximations. Likewise, Nelson and Nataraj[25] analyzed the dynamics of a rotor system with a cracked shaft by using a finite element methodology and a time-varying crack together with a series expansion of the solution. The presence of a crack was taken into account by a rotating stiffness variation represented by a Fourier series expansion. Schmied and Krämer[34] calculated the vibrational behavior of a rotor with a crack, including unbalance response, transient vibration, and the control of stability for a rotor with an arbitrary number of degrees of freedom. They described the opening and closing of the crack by a certain function.

The effect of cracks on cylindrical shells was studied by Petroski and Glazik[32]. The presence of cracks in cylindrical shells increases the bending deformations. Moreover, Petroski[31] considered simple beams with cracks and

modeled the effect of a crack by a pair of concentrated moments acting at the location of the crack.

Gudmundson[13] discussed a dynamic model for beams with cross-sectional cracks that remain open. The crack was represented by a consistent, static flexibility matrix. Papadopoulos and Dimarogonas[27,29,30] investigated coupled longitudinal and bending vibration of a cracked shaft. The crack was described by a local flexibility matrix, whose dimension depended on the number of degrees of freedom considered. Jun, Lee, and co-workers[17,18,20] developed the equation of motion for a simple rotor with a breathing crack based on fracture mechanics. They simplified the breathing crack model to a switching crack model having two different stiffnesses.

The effects of acceleration and deceleration through a critical speed on the vibration of a shaft is one of the interesting subjects to be discussed. Lewis[21] gave an exact solution for a single degree of freedom system with linear damping during acceleration through a critical speed. Baker[4] investigated the vibration of an unbalanced rotor under different rates of constant angular acceleration and deceleration. He also discussed the effect of the spring constant, damping, and mass.

An energy approach was used by Bodger[5] to solve the problem of a single-degree-of-freedom rotor decelerating slowly through a critical speed; the approach gave a closed solution. Aiba[1] considered a rotating shaft under angular acceleration passing through the critical speed and included the gyroscopic effect in the problem. He solved the equations of motion by using Runge-Kutta-Gill's numerical method. Naveh and Brach[24] studied the behavior of an eccentric rotating shaft and disk with an exponential transition of the angular velocity through a critical speed. The results gave higher amplitudes than the results

under a linear transition of the angular velocity.

Gasch, Markert, and Pfützner[10] investigated the bending vibrational behavior of a flexible rotor passing its critical speed under a driving torque. They showed that the effect of the torsional flexibility of the shaft on the bending vibrational behavior was negligible. Tsuchiya[36] worked on the oscillations of a rotor passing through a critical speed. His analysis was based on the method of multiple scales and the method of matched asymptotic expansions. Zobnin, Kelzon, and Neigebauer [42] analyzed the influence of gyroscopic effects on resonance avoidance during acceleration of unbalanced flexible rotors. Ishida, Ikeda, Yamamoto and Murakami[15] dealt with the vibration of a flexible rotating shaft with nonlinear spring characteristics during constant acceleration and deceleration through a critical speed. They examined the influence of the angular acceleration and the angular position of the unbalance at the start of the acceleration. They compared the theoretical results to experiments. Wang, Duan , Huang, and Wen[37] discussed the responses of a simple rotor with a transverse surface crack. They also showed the transitional response of the rotor passing through a subcritical speed.

Collins, Plaut, and Wauer[8] discussed detection of cracks of a rotating Timoshenko shaft by using axial impulses at a constant angular speed. Generalized forces and moments represented the open and closed conditions. They also investigated free and forced longitudinal vibrations of a cantilever bar with a transverse crack[9]. Andruet[2] studied the behavior of a rotating Euler-Bernoulli shaft with a breathing crack under acceleration and deceleration through a critical speed. He neglected torsional and longitudinal vibrations.

The effect of torsional vibration of a cracked shaft has been investigated by several researchers. Christides and Barr[7] derived the equation of motion and

associated boundary conditions for a cracked beam subjected to torsional vibration. The beam was uniform with non-circular cross section, and contained one or more pairs of symmetric cracks. They used the Hu-Washizu variational principle. Papadopoulos and Dimarogonas [28] analyzed a non-rotating cracked Timoshenko shaft with coupling of bending and torsional vibrations. They showed the influence of the bending vibration on the torsional vibration spectrum, and vice-versa. They derived the equations of motion of the shaft with three degrees of freedom and the relation of the eigenvalues of the system to the crack depth and the slenderness ratio of the shaft. Iwatsubo, Yamamoto, and Kawai[16] investigated the torsional vibration of a rotating machine due to the interaction between electrical and mechanical systems.

Wauer[39] presented a literature survey on the dynamics of cracked rotors, including descriptions of crack models and detection procedures. Then Wauer[40] derived the equation of motion for a cracked, rotating, Timoshenko shaft including extension and torsion. He formulated the open-close condition and replaced the crack with a load discontinuity at the crack location. Furthermore, to simulate an open crack, he reduced the stiffness and the damping. In another paper, Wauer[38] showed the secondary effects in transient vibrations of rotating shafts during passage through a critical speeds. He also considered non-symmetry, torsional motion of the shaft, and gyroscopic effects.

A recent paper dealing with torsional vibration is by Ostachowicz and Krawczuk[26]. They considered the influence of transverse cracks, considered to be open, on the coupled torsional and bending vibrations of a rotor. They also calculated the stiffness matrix for a beam finite element containing a single-sided open crack.

Chapter 2
Flexural Response of Cracked Rotating Shaft with a Disk

2.1. Physical Model

The physical model of a cracked shaft with a disk is shown in Fig. 2.1. The idealized model consists of a uniform non-circular shaft of length L with mass per unit length μ, flexural rigidities EI_1 and EI_2 (E: Young's modulus; I_1 and I_2: moments of inertia with respect to the principal directions 1,2), and mass of disk m, rotating at an angular velocity Ω, a function of time. The shaft is assumed to be homogeneous and linearly elastic. Both ends of the shaft are simply supported. The crack is located at a distance b from the left support, and the disk is at a distance c from the same reference point.

Two coordinate systems are used to define the model (Fig. 2.2), i.e., fixed coordinates (x,y,z) and shaft coordinates (ξ,η,ζ). The x-axis coincides with the axial direction of the shaft (ξ-axis). The slope between the x-axis and a horizontal plane is the angle γ; therefore, if γ is zero the shaft lies in a horizontal position and the z-axis is in the gravitational direction. The η-axis is parallel to the 2-principal axis and the ζ-axis is parallel to the 1-principal axis. The 1- and 2-principal axes divide the cross section of the shaft symmetrically. The x,y,z coordinate system is stationary, but the ξ,η,ζ coordinate system rotates with the

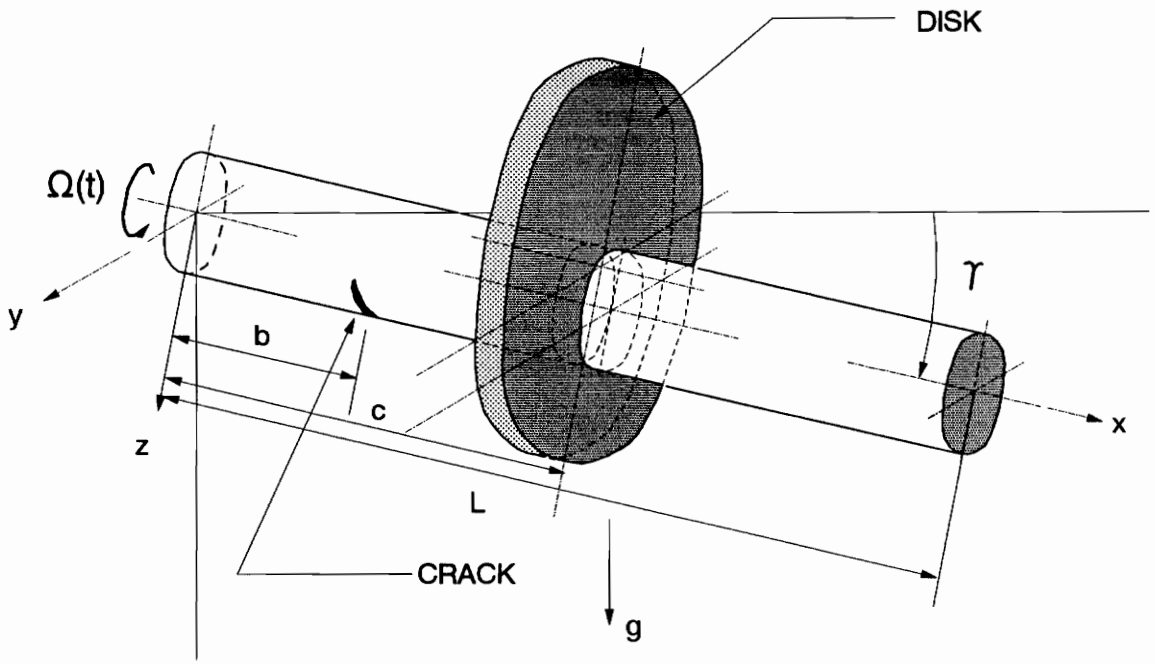

Fig. 2.1 Model of Cracked Shaft
(Non-Specified Boundary Conditions)

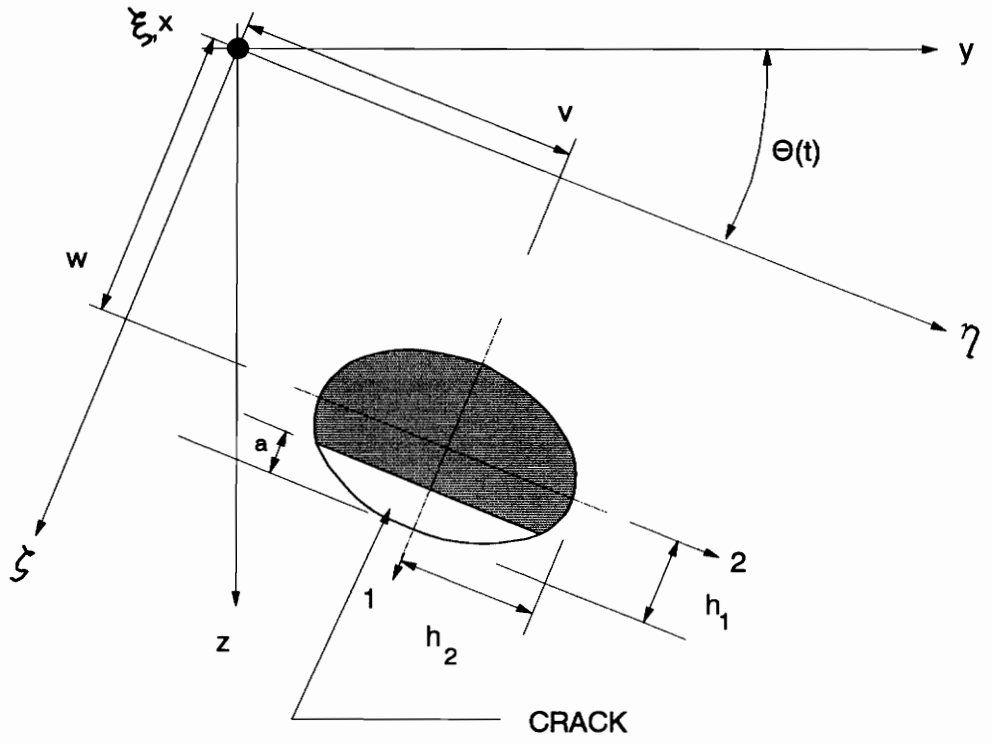

Fig. 2.2 Coordinate Systems and Cracked Cross-Sectional Area

same angular velocity as the shaft.

The coordinates of motion (u,v,w) are the space- and time- dependent displacements and are measured in the shaft coordinates (ξ,η,ζ), with u(x,t) in the axial direction (ξ-axis), and v(x,t), w(x,t) in the transverse direction (η-, ζ- axes, respectively). In this study, the longitudinal displacement is neglected; only transverse displacements (v and w) are taken into account. Additionally, the shear deformation is also neglected; therefore, the model is based on the Euler-Bernoulli theory. The transverse displacements (v and w) are continuous along the shaft, including at the crack location.

Other parameters of the shaft are also shown in Fig. 2.2. The crack depth of the shaft is ' a ' , measured parallel to the 2- principal axis. The distance from the center of geometry of the uncracked cross section to the perimeter of the shaft parallel to the 2- principal axis is called h_1; similarly, the distance parallel to the 1- principal axis is called h_2. I_1 and I_2 are the moments of inertia related to the 1- and 2- principal axes, and r_1 and r_2 are the radii of gyration, respectively. It is assumed that I_2 is less than or equal to I_1, so h_2 is less than or equal to h_1.

The geometrical center of the cross section is the same as the center of mass. As a result, there is no eccentricity for the shaft. However, there is unbalance in the disk. As is shown in Fig. 2.3, the distance e_m is the eccentricity of the disk and δ_m is the angle of the center of mass of the disk from the 2- principal axis.

In this chapter, it is assumed that there are three types of damping in the shaft, i.e., external damping with coefficient d_e, internal damping with coefficient d_i, and damping at the crack when the crack is closed with coefficient d_c. It is assumed that the external and crack damping act only on the shaft, not on the disk.

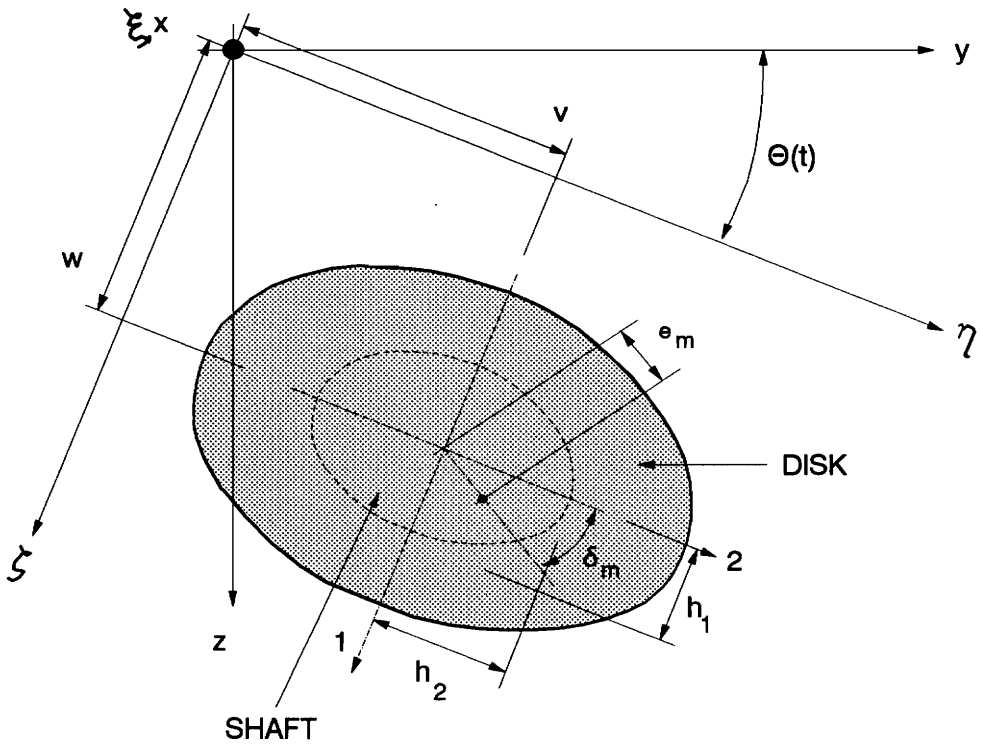

Fig. 2.3 Disk Cross-Sectional Area

The transverse surface crack causes a geometric discontinuity on the shaft. To avoid the complexity of this discontinuity, the crack is replaced by two generalized moments (M and m) at the crack location, i.e., $x=b_-$ and $x=b_+$ (Fig. 2.4). The quantity ϵ is the crack width parameter, where $\epsilon=b_+-b_-$ and $\epsilon \rightarrow 0$. There is a local reduction of the shaft stiffness and damping when the crack is open. The replacement of the concentrated geometric discontinuity at the transverse surface crack by loads at the crack location was previously used by Kirmser[19], Thomson[35], Petroski and Glazik[32], Petroski[31], and Chang and Petroski[6].

2.2. Mathematical Model

The governing equations of motion were derived by Wauer[40]. They include gyroscopic effects and neglect the influence of shear, longitudinal vibrations, and torsional vibrations in this first part of the study. Euler-Bernoulli theory is applied. The equations of motion for a cracked rotating shaft with a disk, as Wauer formulated in his paper[40], are as follows:

$$\begin{aligned} &EI_1 v_{xxxx} + \left[\mu + m\delta(x-c)\right]\left[v_{tt} - 2\dot{\theta}w_t - \dot{\theta}^2 v - \ddot{\theta}w\right] + d_e \mu (v_t - \dot{\theta}w) + EI_1 d_i v_{txxxx} \\ &+ (1-\Lambda)\, d_c \mu (v_t - \dot{\theta}w)\, \delta(x-b) + \Lambda\left[\delta'(x-b_+) - \delta'(x-b_-)\right](M_\zeta + m_\zeta) \\ &= \left[\mu + m\delta(x-c)\right] g \sin\theta + m e_m \delta(x-c)\left[\dot{\theta}^2 \cos\delta_m + \ddot{\theta} \sin\delta_m\right] \end{aligned} \tag{2.1}$$

$$\begin{aligned} &\Gamma EI_1 w_{xxxx} + \left[\mu + m\delta(x-c)\right]\left[w_{tt} + 2\dot{\theta}v_t - \dot{\theta}^2 w + \ddot{\theta}v\right] + d_e \mu (w_t + \dot{\theta}v) \\ &+ \Gamma EI_1 d_i w_{txxxx} + (1-\Lambda)\, d_c \mu (w_t + \dot{\theta}v)\, \delta(x-b) - \Lambda\left[\delta'(x-b_+) - \delta'(x-b_-)\right](M\eta + m_\eta) \\ &= \left[\mu + m\,\delta(x-c)\right] g \cos\theta + m e_m \delta(x-c)\left[\dot{\theta}^2 \sin\delta_m - \ddot{\theta} \cos\delta_m\right] \end{aligned} \tag{2.2}$$

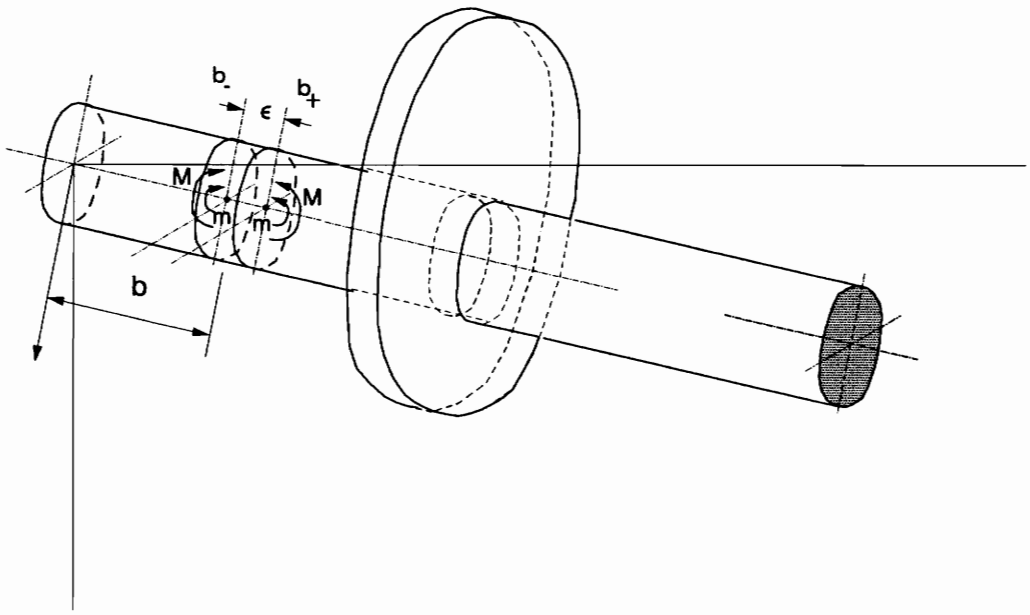

Fig. 2.4 Generalized Forces M and m
(Non-Specified Boundary Conditions)

In these equations, the crack has to be either completely open or completely closed; this condition is called *breathing.* Λ is the parameter defining the breathing condition, where $\Lambda = 1$ if the crack is open, $\Lambda = 0$ if the crack is closed. The subscripts x and t on displacements v and w represent partial derivatives with respect to x and t, respectively. δ(x-c) and δ(x-b) denote the Dirac delta function. The parameter Γ is the ratio of the 2- principal axis moment of inertia (I_2) to the 1- principal axis moment of inertia (I_1). θ is the rotational angle.

To establish the load discontinuity, as shown in the equations, generalized loads are defined:

$$\underline{F} = (M_\zeta, M\eta)^T$$
$$\underline{f} = (m_\zeta, m_\eta)^T \tag{2.3}$$

At the edges of the crack, $x = b_- = b - \frac{\epsilon}{2}$ and $x = b_+ = b + \frac{\epsilon}{2}$.
Based on the static calculation, the deformation at the crack location can be defined as

$$\Delta\underline{u}(b) = \epsilon\, S\, \underline{F}$$

$$v_x\,(b_+,t) - v_x\,(b_-,t) = \epsilon\, \frac{M_\zeta}{EI_1}$$

and

$$w_x\,(b_+,t) - w_x\,(b_-,t) = -\epsilon\, \frac{M\eta}{EI_2} \tag{2.4}$$

and its time derivative

$$\Delta\underline{u}_t(b) = \epsilon\, \frac{S}{d_i}\, \underline{f}$$

$$v_{tx}\,(b_+,t) - v_{tx}\,(b_-,t) = \epsilon\, \frac{m_\zeta}{d_i EI_1}$$

and

$$w_{tx}\,(b_+,t) - w_{tx}\,(b_-,t) = -\epsilon\,\frac{m_\eta}{d_i EI_2} \tag{2.5}$$

Combining equations 2.4 and 2.5 gives

$$\Delta\underline{u}(b) + d_i\,\Delta\underline{u}_t(b) = \epsilon\,S\,(\underline{F} + \underline{f}) \tag{2.6}$$

The transition conditions at the crack location for an open crack at time t are

$$\underline{P}\,(b_-) = \underline{P}\,(b_+)$$

$$\underline{P}\,(b_+) = K\left[\,\Delta\underline{u}(b) + d_i\,\Delta\underline{u}_t(b)\,\right] \tag{2.7}$$

where

$$\underline{P} = \begin{bmatrix} EI_1(v_{xx} + d_i\,v_{txx}) \\ EI_2(w_{xx} + d_i\,w_{txx}) \end{bmatrix},\quad K = \begin{bmatrix} k_{44} & 0 \\ 0 & k_{55} \end{bmatrix} \tag{2.8}$$

The relation of the deformation and the transition condition follows:

$$\epsilon\,S\,(\underline{F} + \underline{f}) = K^{-1}\,\underline{P}\,(b_+)$$

K^{-1} is the inverse stiffness matrix or compliance matrix. Therefore, the relations become

$$(M_\zeta + m_\zeta) = c_{44}\,\frac{(EI_1)^2}{\epsilon}\,(v_{xx} + d_i\,v_{txx})\,\Big/_{x=b}$$

$$(M\eta + m_\eta) = -c_{55}\,\frac{(EI_2)^2}{\epsilon}\,(w_{xx} + d_i\,w_{txx})\,\Big/_{x=b} \tag{2.9}$$

The compliances c_{44} and c_{55} are the reciprocals of the stiffness coefficients k_{44} and k_{55}, respectively. They can be obtained from the work of Papadopoulos and Dimarogonas[27], and are functions of the relative crack depth, i.e., the ratio of the crack depth and the shaft diameter.

Finally, the equations of motion can be written as follows:

$$EI_1 v_{xxxx} + [\mu + m\delta(x\text{-}c)]\left[v_{tt} - 2\dot{\theta}w_t - \dot{\theta}^2 v - \ddot{\theta}w\right]$$

$$+ d_e \mu (v_t - \dot{\theta}w) + EI_1 d_i v_{txxxx} + (1-\Lambda) d_c \mu (v_t - \dot{\theta}w) \delta(x\text{-}b)$$

$$+ \Lambda\left[\delta'(x\text{-}b_+) - \delta'(x\text{-}b_-)\right] c_{44} \frac{(EI_1)^2}{\epsilon} (v_{xx} + d_i v_{txx}) \Big/_{x=b}$$

$$= [\mu + m\delta(x\text{-}c)] g \sin\theta + m e_m \delta(x\text{-}c)\left[\dot{\theta}^2 \cos\delta_m + \ddot{\theta} \sin\delta_m\right] \quad (2.10)$$

$$\Gamma EI_1 w_{xxxx} + [\mu + m\delta(x\text{-}c)]\left[w_{tt} + 2\dot{\theta}v_t - \dot{\theta}^2 w + \ddot{\theta}v\right]$$

$$+ d_e \mu (w_t + \dot{\theta}v) + \Gamma EI_1 d_i w_{txxxx} + (1-\Lambda) d_c \mu (w_t + \dot{\theta}v) \delta(x\text{-}b)$$

$$+ \Lambda\left[\delta'(x\text{-}b_+) - \delta'(x\text{-}b_-)\right] c_{55} \frac{(EI_2)^2}{\epsilon} (w_{xx} + d_i w_{txx}) \Big/_{x=b}$$

$$= [\mu + m\delta(x\text{-}c)] g \cos\theta + m e_m \delta(x\text{-}c)\left[\dot{\theta}^2 \sin\delta_m - \ddot{\theta} \cos\delta_m\right] \quad (2.11)$$

The crack condition, either completely open or completely closed at any given time t, depends on the curvature of the shaft, where

$$w_{xx}(b,t) \leq 0 \text{ for an open crack, } w_{xx}(b,t) > 0 \text{ for a closed crack} \quad (2.12)$$

2.3. Solution

Galerkin's approximation method is used to solve the equations. Both ends of the shaft are simply supported. The boundary conditions are

$$v(0,t) = w(0,t) = v(L,t) = w(L,t) = 0$$
$$EI_1\, v_{xx}(0,t) = EI_2\, w_{xx}(0,t) = 0,\ EI_1\, v_{xx}(L,t) = EI_2\, w_{xx}(L,t) = 0 \qquad (2.13)$$

The approximate solutions, satisfying the boundary conditions, are

$$v(x,t) = \sum_{k=1}^{N} v_k(t) \sin \frac{k\pi x}{L}$$

$$w(x,t) = \sum_{k=1}^{N} w_k(t) \sin \frac{k\pi x}{L} \qquad (2.14)$$

The quantities v_k and w_k are functions of time, and the sines are the assumed spatial functions. Using the approximate solutions, the governing equation (2.10) becomes

$$EI_1 \sum_{k=1}^{N} v_k \left(\frac{k\pi}{L}\right)^4 \sin \frac{k\pi x}{L} + \left[\mu + m\delta(x-c)\right] \cdot$$

$$\left[\sum_{k=1}^{N} \ddot{v}_k \sin \frac{k\pi x}{L} - 2\dot{\theta} \sum_{k=1}^{N} \dot{w}_k \sin \frac{k\pi x}{L} - \dot{\theta}^2 \sum_{k=1}^{N} v_k \sin \frac{k\pi x}{L} - \ddot{\theta} \sum_{k=1}^{N} w_k \sin \frac{k\pi x}{L} \right]$$

$$+ d_e\, \mu \left[\sum_{k=1}^{N} \dot{v}_k \sin \frac{k\pi x}{L} - \dot{\theta} \sum_{k=1}^{N} w_k \sin \frac{k\pi x}{L} \right] + EI_1\, d_i \sum_{k=1}^{N} \dot{v}_k \left(\frac{k\pi}{L}\right)^4 \sin \frac{k\pi x}{L}$$

$$+ (1-\Lambda)\, d_c\, \mu \left[\sum_{k=1}^{N} \dot{v}_k \sin \frac{k\pi x}{L} - \dot{\theta} \sum_{k=1}^{N} w_k \sin \frac{k\pi x}{L} \right] \delta(x-b)$$

$$- \Lambda \left[\delta'(x\text{-}b_+) - \delta'(x\text{-}b_-)\right] c_{44} \frac{(EI_1)^2}{\epsilon} .$$

$$\left[\sum_{k=1}^{N} v_k \left(\frac{k\pi}{L}\right)^2 \sin \frac{k\pi b}{L} + d_i \sum_{k=1}^{N} \dot{v}_k \left(\frac{k\pi}{L}\right)^2 \sin \frac{k\pi b}{L}) \right]$$

$$= \left[\mu + m\delta(x\text{-}c)\right] g \sin \theta + m\, e_m\, \delta(x\text{-}c) \left[\dot{\theta}^2 \cos \delta_m + \ddot{\theta} \sin \delta_m\right] \qquad (2.15)$$

By multiplying equation (2.15) with $\sin \frac{n\pi x}{L}$ and integrating over the length of the shaft, the equation becomes dependent only on time:

$$\int_0^L \Big\{ EI_1 \sum_{k=1}^{N} v_k \left(\frac{k\pi}{L}\right)^4 \sin \frac{k\pi x}{L} + \left[\mu + m\delta(x\text{-}c)\right] .$$

$$\left[\sum_{k=1}^{N} \ddot{v}_k \sin \frac{k\pi x}{L} - 2\dot{\theta} \sum_{k=1}^{N} \dot{w}_k \sin \frac{k\pi x}{L} - \dot{\theta}^2 \sum_{k=1}^{N} v_k \sin \frac{k\pi x}{L} - \ddot{\theta} \sum_{k=1}^{N} w_k \sin \frac{k\pi x}{L} \right]$$

$$+ d_e\, \mu \left[\sum_{k=1}^{N} \dot{v}_k \sin \frac{k\pi x}{L} - \dot{\theta} \sum_{k=1}^{N} w_k \sin \frac{k\pi x}{L} \right] + EI_1\, d_i \sum_{k=1}^{N} \dot{v}_k \left(\frac{k\pi}{L}\right)^4 \sin \frac{k\pi x}{L}$$

$$+ (1\text{-}\Lambda)\, d_c\, \mu \left[\sum_{k=1}^{N} \dot{v}_k \sin \frac{k\pi x}{L} - \dot{\theta} \sum_{k=1}^{N} w_k \sin \frac{k\pi x}{L} \right] \delta(x\text{-}b)$$

$$- \Lambda \left[\delta'(x\text{-}b_+) - \delta'(x\text{-}b_-)\right] c_{44} \frac{(EI_1)^2}{\epsilon} .$$

$$\left[\sum_{k=1}^{N} v_k \left(\frac{k\pi}{L}\right)^2 \sin \frac{k\pi b}{L} + d_i \sum_{k=1}^{N} \dot{v}_k \left(\frac{k\pi}{L}\right)^2 \sin \frac{k\pi b}{L}) \right] \Big\} \sin \frac{n\pi x}{L}\, dx$$

$$= \int_0^L \Big\{ \left[\mu + m\delta(x\text{-}c)\right] g \sin \theta$$

$$+ m\, e_m\, \delta(x\text{-}c) \left[\dot{\theta}^2 \cos \delta_m + \ddot{\theta} \sin \delta_m\right] \Big\} \sin \frac{n\pi x}{L}\, dx \qquad (2.16)$$

Based on the formulas

$$\int_a^b f(x)\,\delta(x-\xi)\,dx = f(\xi) \qquad (a<\xi<b)$$

$$\int_0^L \sin\frac{k\pi x}{L}\,\sin\frac{n\pi x}{L}\,dx = \begin{cases} 0 & \text{if } k \neq n \\ \frac{L}{2} & \text{if } k = n \end{cases}$$

$$\int_0^L \sin\frac{n\pi x}{L}\,dx = \begin{cases} 0 & \text{if n is even} \\ \frac{2L}{n\pi} & \text{if n is odd} \end{cases}$$

$$\int_0^L \delta'(x-b_+)\,\sin\frac{n\pi x}{L}\,dx - \int_0^L \delta'(x-b_-)\,\sin\frac{n\pi x}{L}\,dx =$$

$$= \left[\delta(x-b_+)\,\sin\frac{n\pi x}{L}\right]_0^L - \int_0^L \delta(x-b_+)\,\frac{n\pi}{L}\cos\frac{n\pi x}{L}\,dx$$

$$- \left[\delta(x-b_-)\,\sin\frac{n\pi x}{L}\right]_0^L + \int_0^L \delta(x-b_-)\,\frac{n\pi}{L}\cos\frac{n\pi x}{L}\,dx$$

$$= -\frac{n\pi}{L}\left[\cos\frac{n\pi b_+}{L} - \cos\frac{n\pi b_-}{L}\right]$$

$$= -\frac{n\pi}{L}\left[-2\,\sin\frac{n\pi b}{L}\,\sin\frac{n\pi\epsilon}{2L}\right]$$

$$= -\frac{n\pi}{L}\left[-2\,\sin\frac{n\pi b}{L}\cdot\frac{n\pi\epsilon}{2L}\right]$$

$$= \left(\frac{n\pi}{L}\right)^2 \epsilon\,\sin\frac{n\pi b}{L} \qquad (2.17)$$

equation 2.16 becomes

$$EI_1 v_n \frac{L}{2} \left(\frac{n\pi}{L}\right)^4 + \mu \ddot{v}_n \frac{L}{2} - 2\dot{\theta}\mu \dot{w}_n \frac{L}{2} - \mu \dot{\theta}^2 v_n \frac{L}{2} - \mu \ddot{\theta} w_n \frac{L}{2}$$

$$+ m \sin\frac{n\pi c}{L} \sum_{k=1}^{N} \ddot{v}_k \sin\frac{k\pi c}{L} - 2\dot{\theta} m \sin\frac{n\pi c}{L} \sum_{k=1}^{N} \dot{w}_k \sin\frac{k\pi c}{L}$$

$$- \dot{\theta}^2 m \sin\frac{n\pi c}{L} \sum_{k=1}^{N} v_k \sin\frac{k\pi c}{L} - m \ddot{\theta} \sin\frac{n\pi c}{L} \sum_{k=1}^{N} w_k \sin\frac{k\pi c}{L}$$

$$+ d_e \mu \dot{v}_n \frac{L}{2} - d_e \mu \dot{\theta} w_n \frac{L}{2} + EI_1 d_i \dot{v}_n \left(\frac{n\pi}{L}\right)^4 \frac{L}{2}$$

$$+ (1-\Lambda) d_c \mu \sin\frac{n\pi b}{L} \left[\sum_{k=1}^{N} \dot{v}_k \sin\frac{k\pi b}{L} - \dot{\theta} \sum_{k=1}^{N} w_k \sin\frac{k\pi b}{L} \right]$$

$$- \Lambda c_{44} (EI_1)^2 \left(\frac{n\pi}{L}\right)^2 \sin\frac{n\pi b}{L} \sum_{k=1}^{N} (v_k + d_i \dot{v}_k) \left(\frac{k\pi}{L}\right)^2 \sin\frac{k\pi b}{L}$$

$$= \mu g \sin\theta \frac{L}{n\pi} (1-(-1)^n) + mg \sin\theta \sin\frac{n\pi c}{L}$$

$$+ m e_m \left[\dot{\theta}^2 \cos\delta_m + \ddot{\theta} \sin\delta_m\right] \sin\frac{n\pi c}{L} \qquad (2.18)$$

Similarly, equation (2.11) becomes

$$EI_2 w_n \frac{L}{2} \left(\frac{n\pi}{L}\right)^4 + \mu \ddot{w}_n \frac{L}{2} + 2\dot{\theta}\mu \dot{v}_n \frac{L}{2} - \mu \dot{\theta}^2 w_n \frac{L}{2} + \mu \ddot{\theta} v_n \frac{L}{2}$$

$$+ m \sin\frac{n\pi c}{L} \sum_{k=1}^{N} \ddot{w}_k \sin\frac{k\pi c}{L} + 2\dot{\theta} m \sin\frac{n\pi c}{L} \sum_{k=1}^{N} \dot{v}_k \sin\frac{k\pi c}{L}$$

$$- \dot{\theta}^2 m \sin\frac{n\pi c}{L} \sum_{k=1}^{N} w_k \sin\frac{k\pi c}{L} + m \ddot{\theta} \sin\frac{n\pi c}{L} \sum_{k=1}^{N} v_k \sin\frac{k\pi c}{L}$$

$$+ d_e \mu \dot{w}_n \frac{L}{2} + d_e \mu \dot{\theta} v_n \frac{L}{2} + EI_2 d_i \dot{w}_n \left(\frac{n\pi}{L}\right)^4 \frac{L}{2}$$

$$+ (1-\Lambda) d_c \mu \sin \frac{n\pi b}{L} \left[\sum_{k=1}^{N} \dot{w}_k \sin \frac{k\pi b}{L} + \dot{\theta} \sum_{k=1}^{N} v_k \sin \frac{k\pi b}{L} \right]$$

$$- \Lambda c_{55} (EI_2)^2 \left(\frac{n\pi}{L}\right)^2 \sin \frac{n\pi b}{L} \sum_{k=1}^{N} (w_k + d_i \dot{w}_k) \left(\frac{k\pi}{L}\right)^2 \sin \frac{k\pi b}{L}$$

$$= \mu g \cos \theta \frac{L}{n\pi} (1-(-1)^n) + mg \cos \theta \sin \frac{n\pi c}{L}$$

$$+ m e_m \left[\dot{\theta}^2 \sin \delta_m - \ddot{\theta} \cos \delta_m \right] \sin \frac{n\pi c}{L} \qquad (2.19)$$

Calculations are carried out in non-dimensionalized form. The non-dimensionalized form for each parameter is defined as follows:

$$\tilde{v}_n = \frac{v_n}{L}, \quad \tilde{w}_n = \frac{w_n}{L}$$

$$\tilde{b} = \frac{b}{L}, \quad \tilde{c} = \frac{c}{L}, \quad \tilde{x} = \frac{x}{L}$$

$$\tau = \frac{\pi^2}{L^2} \sqrt{\frac{EI_1}{\mu}}\, t, \quad \Gamma = \frac{I_2}{I_1}$$

$$\tilde{e}_m = \frac{e_m}{L}$$

$$\tilde{m} = \frac{2m}{\mu L}, \quad \tilde{\mu} = \frac{2L^3 \mu g}{\pi^5 EI_1}$$

$$\tilde{d}_i = \frac{\pi^2}{L^2} \sqrt{\frac{EI_1}{\mu}}\, d_i, \quad \tilde{d}_e = \frac{L^2}{\pi^2} \sqrt{\frac{\mu}{EI_1}}\, d_e, \quad \tilde{d}_c = \frac{2L}{\pi^2} \sqrt{\frac{\mu}{EI_1}}\, d_c$$

$$\tilde{c}_{44} = \frac{EI_1}{L} c_{44}, \quad \tilde{c}_{55} = \frac{EI_1}{L} c_{55}$$

$$\gamma_k = \frac{k\pi b}{L} = k\pi\tilde{b}\ ,\quad \alpha_k = \frac{k\pi c}{L} = k\pi\tilde{c}$$

$$\Omega = \frac{d\theta}{d\tau}\ ,\quad \lambda = \frac{d\Omega}{d\tau} = \frac{d^2\theta}{d\tau^2} \tag{2.20}$$

Then equation (2.18) becomes

$$n^4\,\tilde{v}_n + \ddot{\tilde{v}}_n - 2\Omega\dot{\tilde{w}}_n - \Omega^2\tilde{v}_n - \lambda\tilde{w}_n$$

$$+ \tilde{m}\sin\alpha_n \sum_{k=1}^{N}(\ddot{\tilde{v}}_k - 2\Omega\dot{\tilde{w}}_k - \Omega^2\tilde{v}_k - \lambda\tilde{w}_k)\sin\alpha_k$$

$$+ \tilde{d}_e\,(\dot{\tilde{v}}_n - \Omega\tilde{w}_n) + \tilde{d}_i\,\dot{\tilde{v}}_n\,n^4$$

$$+ (1-\Lambda)\,\tilde{d}_c \sin\gamma_n \sum_{k=1}^{N}(\dot{\tilde{v}}_k - \Omega\tilde{w}_k)\sin\gamma_k$$

$$- 2\Lambda\tilde{c}_{44}\,n^2 \sin\gamma_n \sum_{k=1}^{N} k^2\,(\tilde{v}_k + \tilde{d}_i\dot{\tilde{v}}_k)\sin\gamma_k$$

$$= \left[\frac{(1-(-1)^n)}{n} + \tilde{m}\,\frac{\pi}{2}\sin\alpha_n\right]\tilde{\mu}\sin\theta$$

$$+ \tilde{m}\,\tilde{e}_m \sin\alpha_n\left[\Omega^2\cos\delta_m + \lambda\sin\delta_m\right] \tag{2.21}$$

where overdots denote differentiation with respect to τ. Similarly, equation (2.19) becomes

$$\Gamma n^4\tilde{w}_n + \ddot{\tilde{w}}_n + 2\Omega\dot{\tilde{v}}_n - \Omega^2\tilde{w}_n + \lambda\tilde{v}_n$$

$$+ \tilde{m} \sin \alpha_n \sum_{k=1}^{N} (\ddot{\tilde{w}}_k + 2\Omega\dot{\tilde{v}}_k - \Omega^2\tilde{w}_k + \lambda\tilde{v}_k) \sin \alpha_k$$

$$+ \tilde{d}_e (\dot{\tilde{w}}_n + \Omega\tilde{v}_n) + \Gamma \tilde{d}_i \dot{\tilde{w}}_n n^4$$

$$+ (1-\Lambda) \tilde{d}_c \sin \gamma_n \sum_{k=1}^{N} (\dot{\tilde{w}}_k + \Omega\tilde{v}_k) \sin \gamma_k$$

$$- 2\Gamma^2\Lambda\tilde{c}_{55} n^2 \sin \gamma_n \sum_{k=1}^{N} k^2 (\tilde{w}_k + \tilde{d}_i\dot{\tilde{w}}_k) \sin \gamma_k$$

$$= \left[\frac{(1-(-1)^n)}{n} + \tilde{m} \frac{\pi}{2} \sin \alpha_n\right] \tilde{\mu} \cos \theta$$

$$+ \tilde{m} \tilde{e}_m \sin \alpha_n \left[\Omega^2 \sin \delta_m - \lambda \cos \delta_m\right] \qquad (2.22)$$

The solutions of these two equations are obtained by numerical integration that calculates the approximate values of the time-dependent functions v_n and w_n. A Fortran program for IBM/PC was written to obtain the solution of the ordinary differential equations (ODE's). In this thesis, the DIVPAG subroutine from IMSL (International Mathematics and Statistics Library) is used. The DIVPAG subroutine offers two numerical integration method options, i.e., Adams-Moulton Method and Gear's Stiff Method. In this case, the Adams-Moulton Method is used.

The DIVPAG subroutine is applicable for first order differential equations, either explicit ODE ($\dot{y}$= f (x,y)) or implicit ODE (A$\dot{y}$= f (x,y)). Because of that, the second order differential equations in v_n and w_n have to be transformed to first order differential equations. The second order system can be transformed to the first order system by these definitions:

$$y_{2n-1} = \tilde{v}_n\,,\ \dot{y}_{2n-1} = \frac{d\tilde{v}_n}{d\tau}\,,\ y_{2n} = \tilde{w}_n\,,\ \dot{y}_{2n} = \frac{d\tilde{w}_n}{d\tau}\,,$$

$$y_{M+2n-1} = \frac{d\tilde{v}_n}{d\tau}\,,\ \dot{y}_{M+2n-1} = \frac{d^2\tilde{v}_n}{d\tau^2}\,,\ y_{M+2n} = \frac{d\tilde{w}_n}{d\tau}\,,\ \dot{y}_{M+2n} = \frac{d^2\tilde{w}_n}{d\tau^2}\,. \quad (2.23)$$

Hence,

$$\dot{y}_{2n-1} = y_{M+2n-1}$$

$$\dot{y}_{2n} = y_{M+2n}$$

where $M = 2N$

N = the highest mode considered

n = the number of the mode corresponding to the equations, ranging between 1 and N

Then equations (2.21) and (2.22) can be written in the form

$$A\,\dot{y} = F(t,y) \quad (2.24)$$

where A is a constant matrix of order 2M x 2M, y is a vector of order 2M, and F(t,y) is a vector of order 2M. Equation (2.24) is in a form suitable for solution by DIVPAG.

Chapter 3
Results of Flexural Response

3.1. Introduction

In order to make a comparison between the analytical study and a planned experimental study of a cracked rotating shaft, the shaft parameters are based on those that will be used in the experiments. In this study, the shaft and the disk are assumed to be circular. Therefore, the moments of inertia for both principal axes (I_1 and I_2) are the same.

The physical data of the shaft and the disk are:

- Length of the shaft: L = 15 in
- Radius of the shaft: $r_s = \frac{3}{16}$ in
- Radius of the disk: $R_d = 1\frac{7}{16}$ in
- Density of the shaft: $\rho g = 0.283$ lb/in^3
- Weight of the disk: mg = 1.788 lb
- Young's modulus: $E = 29 \times 10^6$ lb/in^2

For the standard case in this study, it is assumed that:

- Location of the crack: b = 0.4 L
- Location of the disk: c = 0.5 L
- Crack depth: a = 0.075 in
- Eccentricity of the disk: $e_m = 0.015$ in (about $\frac{1}{100}$ of the disk radius)

- Angle of the mass center of the disk: $\delta_m = 0.75\ \pi$
- Poisson's ratio: $\nu = 0.3$

Based on the above data, the non-dimensionalized shaft data for the standard case are as follows:

$$\tilde{b} = \frac{b}{L} = 0.4\ ;\ \tilde{c} = \frac{c}{L} = 0.5$$

$$\tilde{r}_s = \frac{r_s}{L} = 0.0125\ ;\ \tilde{R}_d = \frac{R_d}{L} = 0.0958$$

$$\tilde{e}_m = \frac{e_m}{L} = 0.001\ ;\ \delta_m = 0.75\ \pi$$

$$\tilde{\mu} = \frac{2L^3 \mu g}{\pi^5 E I_1} = 2.45\text{x}10^{-5}$$

$$\tilde{m} = \frac{2m}{\mu L} = 7.63$$

$$a/D = 0.2 \qquad (3.1)$$

The compliances $\tilde{c}_{44}$ and $\tilde{c}_{55}$ related to the relative crack depth (a/D) of the shaft are calculated based on the work of Papadopoulos and Dimarogonas[27]. From their work, the dimensional compliances c_{44} and c_{55} are determined from the following formulas:

$$c_{44} = \frac{(1-\nu^2)\,\overline{c}_{44}}{\pi\, E\, r_s^3}$$

$$c_{55} = \frac{(1-\nu^2)\,\overline{c}_{55}}{\pi\, E\, r_s^3} \qquad (3.2)$$

The non-dimensionalized compliances $\tilde{c}_{44}$ and $\tilde{c}_{55}$ can be obtained as follows :

$$\tilde{c}_{44} = \frac{EI_1}{L} c_{44} = \frac{1}{4} \frac{r_s}{L} (1-\nu^2) \bar{c}_{44}$$

$$\tilde{c}_{55} = \frac{EI_1}{L} c_{55} = \frac{1}{4} \frac{r_s}{L} (1-\nu^2) \bar{c}_{55} \tag{3.3}$$

For the standard case, the relative crack depth (a/D) of the shaft is 0.2 and the ratio of the shaft radius to the shaft length (r_s/L) is $\frac{1}{80}$, so the compliance $\tilde{c}_{44}$ is 0.00059 and the compliance $\tilde{c}_{55}$ is 0.0080. The other parameters, i.e., internal damping d_i, external damping d_e, and crack damping d_c, are assumed as follows:

$$\tilde{d}_e = 0.1$$
$$\tilde{d}_i = 0.1$$
$$\tilde{d}_c = 0 \tag{3.4}$$

The shaft rotates under the rotational acceleration $\lambda = 0.001$ until it reaches the maximum angular velocity $\Omega = 0.7$, in this standard case.

Based on equation (2.21) and equation (2.22) and all of the shaft parameters, the behavior of the cracked rotating shaft for the standard case can be determined. From those results, the transverse displacements (v and w) in the shaft coordinates can be calculated for any time and any location. The z-displacement in the fixed coordinates, which in this case is the displacement in the gravitational direction, is calculated by the following formula:

$$z = \tilde{v}(\tilde{x},\tau) \sin \theta(\tau) + \tilde{w}(\tilde{x},\tau) \cos \theta(\tau) \tag{3.5}$$

(see Fig. 2.2).

It is interesting to know the behavior of the breathing cracked rotating shaft around the critical speed. Therefore the time histories of the z-displacement under acceleration and deceleration are given. Also, the influence of different parameters

is also presented. The breathing crack in the time histories is shown by different types of lines, a solid line for a closed crack and a dashed line for an open crack.

3.2. Natural Frequencies

To find the natural frequencies of the uncracked rotating shaft with a disk, equation (2.21) and equation (2.22) are used with no damping, no eccentricity, and no acceleration. In that case, the following parameters are set to be zero:

$\tilde{d}_i = 0 \qquad \tilde{d}_e = 0 \qquad \tilde{d}_c = 0$

$\tilde{c}_{44} = 0 \qquad \tilde{c}_{55} = 0 \qquad \tilde{e}_m = 0$

$\lambda = 0 \qquad \tilde{\mu} = 0$

Also, $\Gamma = 1$. Therefore, the equations of motion become

$$n^4 \tilde{v}_n + \ddot{\tilde{v}}_n - 2\Omega\dot{\tilde{w}}_n - \Omega^2\tilde{v}_n + \tilde{m} \sin \alpha_n \sum_{k=1}^{N} (\ddot{\tilde{v}}_k - 2\Omega\dot{\tilde{w}}_k - \Omega^2\tilde{v}_k) \sin \alpha_k = 0 \qquad (3.6)$$

$$n^4\tilde{w}_n + \ddot{\tilde{w}}_n + 2\Omega\dot{\tilde{v}}_n - \Omega^2\tilde{w}_n + \tilde{m} \sin \alpha_n \sum_{k=1}^{N} (\ddot{\tilde{w}}_k + 2\Omega\dot{\tilde{v}}_k - \Omega^2\tilde{w}_k) \sin \alpha_k = 0 \qquad (3.7)$$

By assuming $\tilde{v}_n = v_n e^{i\omega t}$ and $\tilde{w}_n = w_n e^{i\omega t}$, the first natural frequency can be obtained. With n=1 and $\alpha_1 = \pi\ \tilde{c} = \frac{\pi}{2}$, equation (3.6) becomes

$$v_1 e^{i\omega t} - \omega^2 v_1 e^{i\omega t} - 2\ \Omega\ i\omega\ w_1 e^{i\omega t} - \Omega^2\ v_1 e^{i\omega t}$$
$$+ \tilde{m} \sin \frac{\pi}{2} (- \omega^2 v_1 e^{i\omega t} - 2\ \Omega\ i\omega\ w_1 e^{i\omega t} - \Omega^2\ v_1 e^{i\omega t}) \sin \frac{\pi}{2} = 0 \qquad (3.8)$$

which leads to

$$(1 - \Omega^2 - \omega^2)\ v_1 - 2\ \Omega\ i\omega\ w_1 + \tilde{m}\ (- \omega^2\ v_1 - 2\ \Omega\ i\omega\ w_1\ - \Omega^2\ v_1) = 0 \qquad (3.9)$$

If the angular velocity (Ω) is zero, the first natural frequency can be determined

as follows: $\Omega = 0$

$$(1 - 8.63\ \omega^2)\ v_1 = 0$$

$$\omega_1 = 0.3404 \tag{3.10}$$

The corresponding dimensional value for ω_1 is 278.6 rad/sec. In the opposite way, if the first natural frequency becomes zero, the first critical speed (Ω_{crit}) can also be determined, as follows:

$$\omega = 0$$

$$(1 - 8.63\ \Omega^2)\ v_1 = 0$$

$$\Omega_{crit} = 0.3404 \tag{3.11}$$

The corresponding dimensional value for Ω_{crit} is 278.6 rad/sec. The same value can also be found from equation (3.7) in the same way. Because the compliances c_{44} and c_{55} only give a small effect, the critical speed of the breathing crack shaft is assumed to be the same as the uncracked shaft.

To get the other natural frequencies, the angular velocity is set to be zero and the equations of motions are

$$n^4\ \tilde{v}_n + \ddot{\tilde{v}}_n + \tilde{m} \sin \alpha_n \sum_{k=1}^{N} \ddot{\tilde{v}}_k \sin \alpha_k = 0 \tag{3.12}$$

$$n^4 \tilde{w}_n + \ddot{\tilde{w}}_n + \tilde{m} \sin \alpha_n \sum_{k=1}^{N} \ddot{\tilde{w}}_k \sin \alpha_k = 0 \tag{3.13}$$

If n = 5, $\tilde{m}$ = 7.63, and $\sin \alpha_n = \sin \frac{n\pi}{2}$, five natural frequencies can be calculated, i.e.:

$$\omega_1 = 0.3385,\ \omega_2 = 4,\ \omega_3 = 6.4908,\ \omega_4 = 16, \text{ and } \omega_5 = 20.9523 \tag{3.14}$$

The corresponding dimensional values are 277.0 rad/sec, 3273.2 rad/sec, 5311.5 rad/sec, 13092.9 rad/sec, and 17145.4 rad/sec.

3.3. Convergency

In order to get accurate results using the approximate solutions, at first it is necessary to know the influence of each term (mode). After that, the number of modes to include in the approximate solutions can be determined.

In Fig. 3.1, the time history of the z-displacement for the standard case at the location $\tilde{x} = 0.7$ is shown. As stated earlier, the dashed part of the curve indicates when the crack is open. The contribution of each of the five terms is shown with solid curves in Fig. 3.2.a-e. From those graphs, it is clear that the first mode gives the most dominant contribution to the final result. The other modes only give a small portion to the final result, because their amplitudes are less than $\frac{1}{100}$ of that of the first mode. The odd modes have similar characteristics, as do the even modes. Higher modes give smaller contributions.

The time when the angular velocity passes the critical speed is defined as τ_{crit}. Right after the system passes τ_{crit}, the z-displacement becomes larger and reaches its maximum. The maximum z-displacement, in this case, is called z_{max} and the time corresponding to z_{max} is called τ_{max}.

Table 3.1 and Fig. 3.3 give values of the maximum z-displacement at the location $\tilde{x} = 0.7$ based on different numbers of modes. From Table 3.1, it can be calculated that the difference between that for one mode and seven modes is only 0.42% and the difference between that for 5 modes and 7 modes is only 0.02%. Therefore, based on these facts, five modes are sufficient to get accurate results. In this chapter, five modes are used to calculate the approximate solutions.

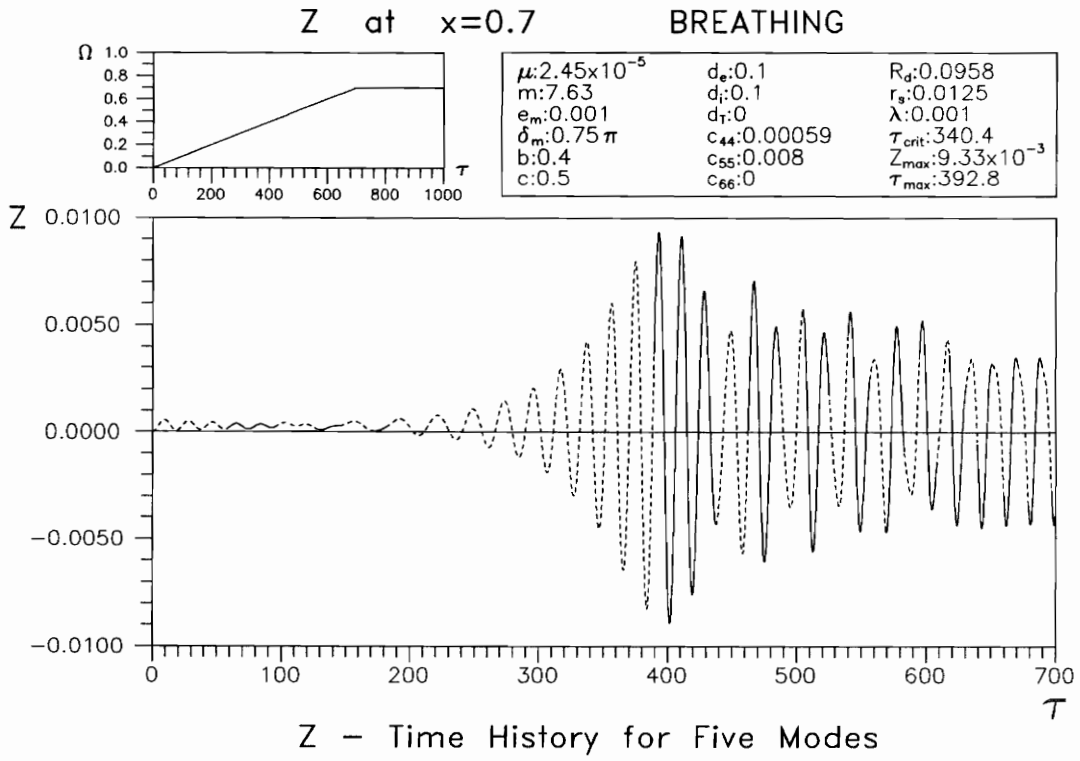

Fig. 3.1 Time History for Five Modes

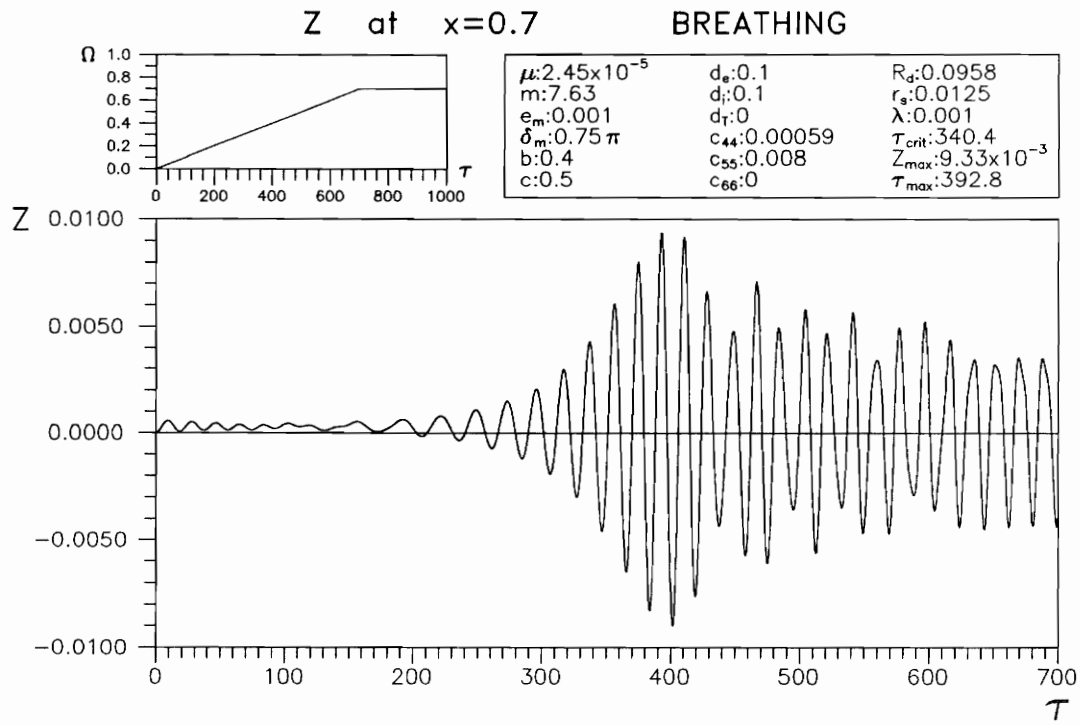

a. Z – Time History for Mode 1

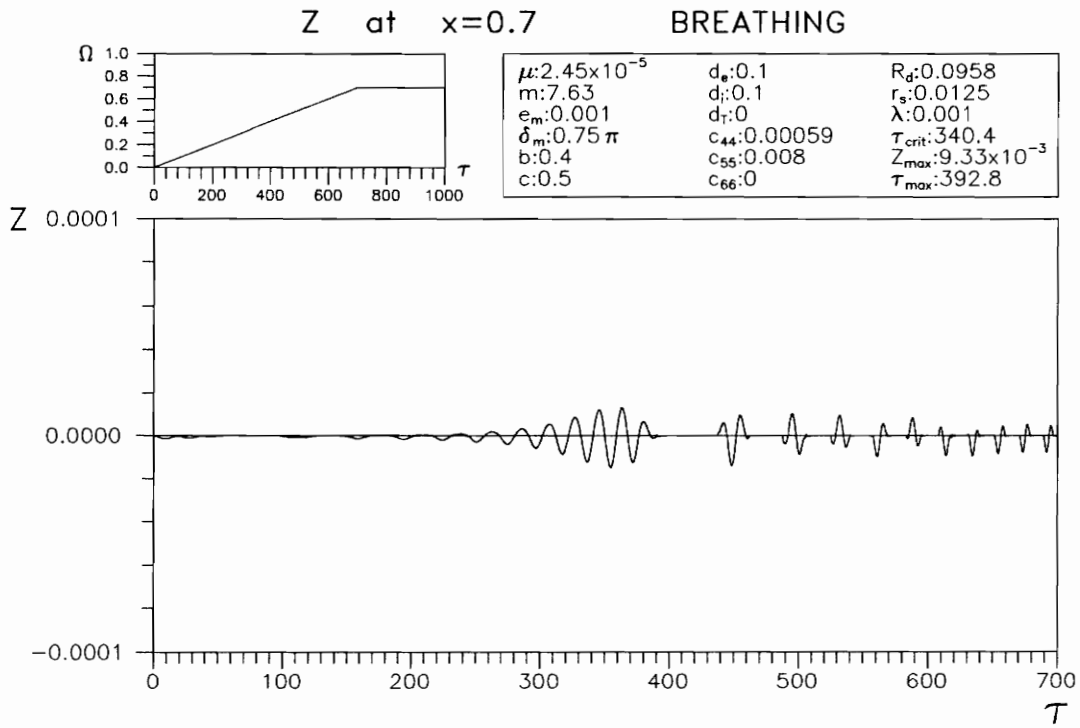

b. Z – Time History for Mode 2

Fig. 3.2 Time History for Each Mode

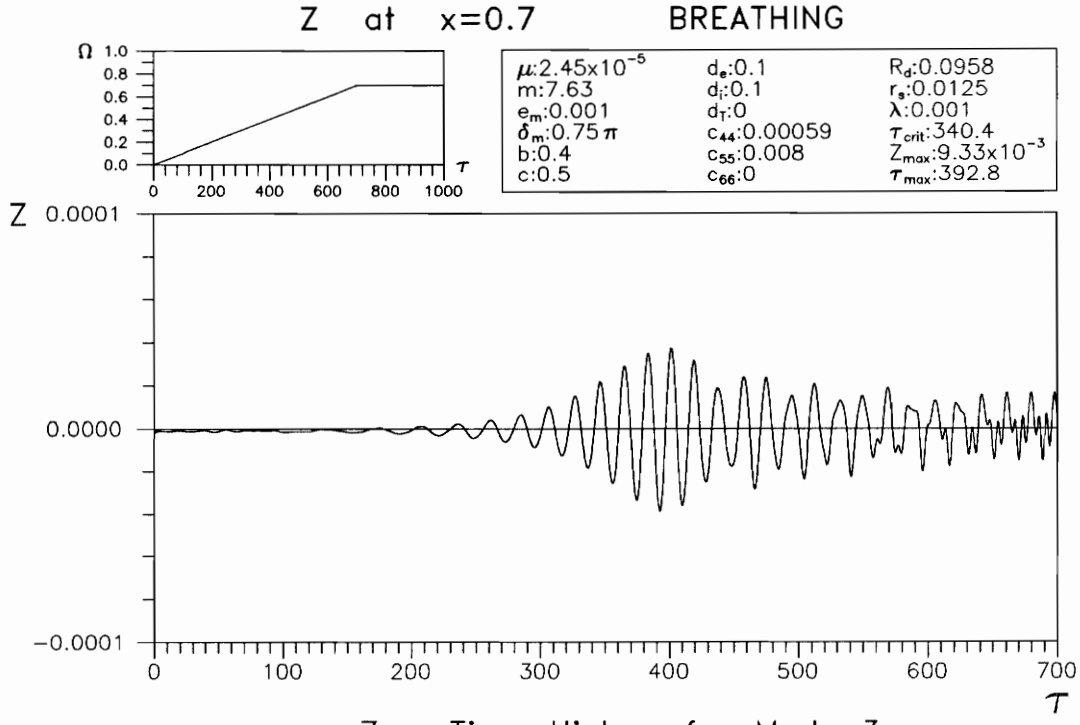

c. Z – Time History for Mode 3

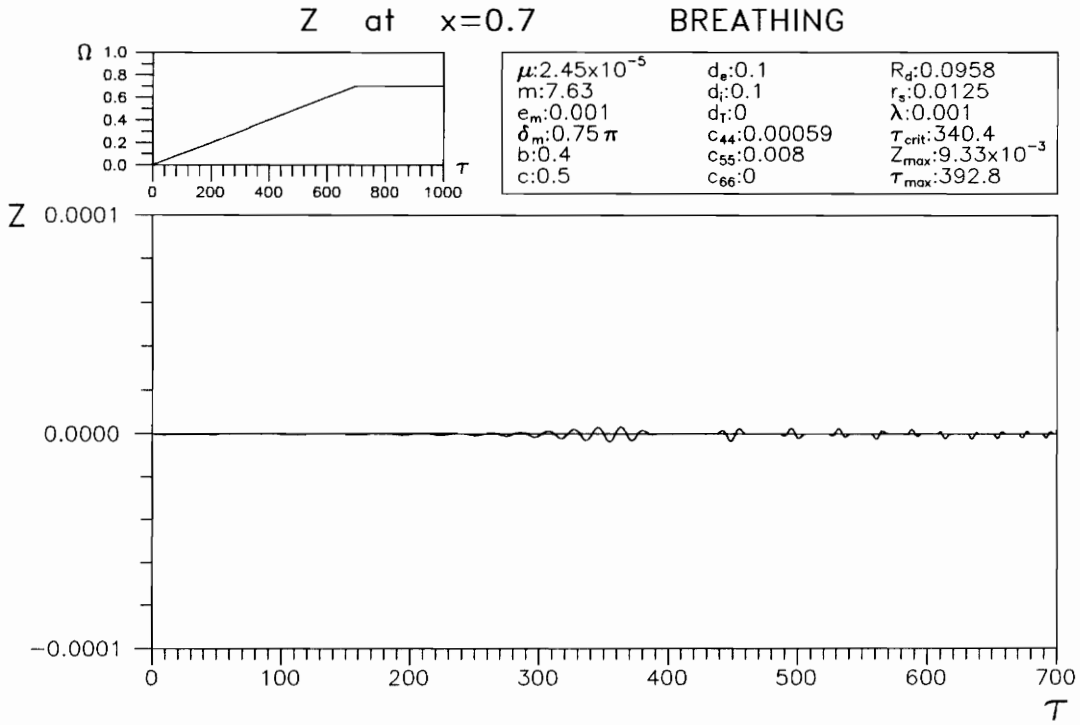

d. Z – Time History for Mode 4

Fig. 3.2 Time History for Each Mode

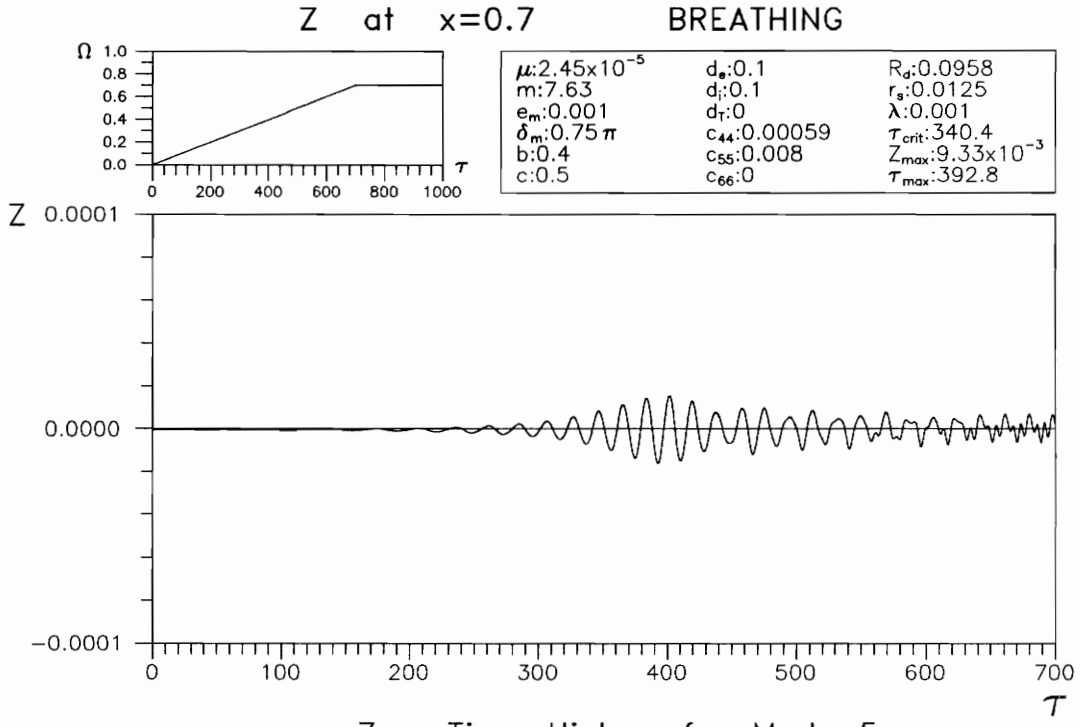

e. Z – Time History for Mode 5

Fig. 3.2 Time History for Each Mode

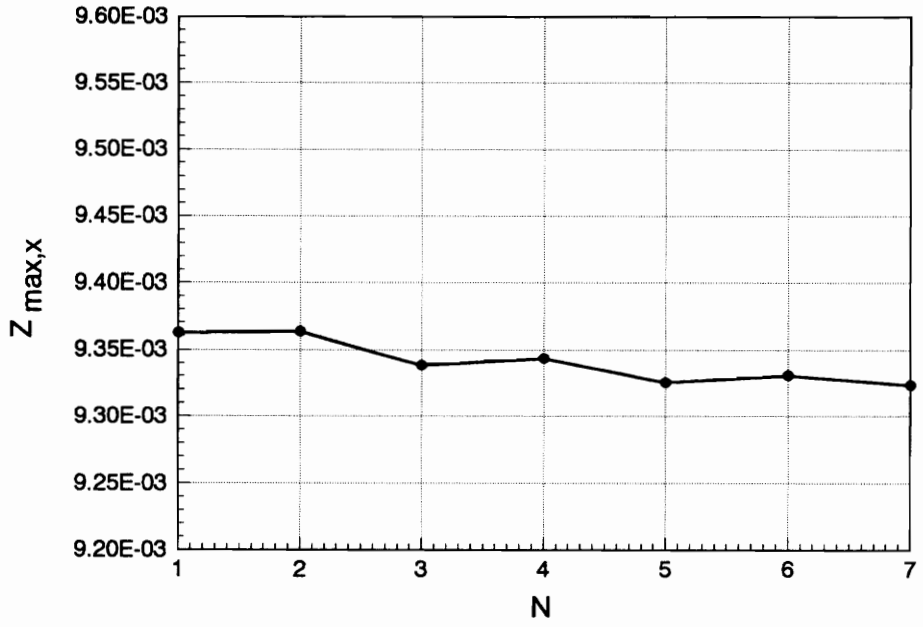

Fig. 3.3 Influence of Number of Modes

Table 3.1 Relation between number of modes and $z_{max,x}$

Number of modes	$z_{max,x}$
1	9.363×10^{-3}
2	9.364×10^{-3}
3	9.338×10^{-3}
4	9.343×10^{-3}
5	9.325×10^{-3}
6	9.331×10^{-3}
7	9.323×10^{-3}

3.4. Influence of Acceleration and Deceleration

The behavior of the cracked rotating shaft under acceleration and deceleration passing through the critical speed is investigated. For the acceleration, based on linear acceleration beginning from rest and ending when the angular velocity (Ω) reaches 0.7 (or about 2 times the first critical speed), one can write

$$0 \leq \tau \leq T_1 : \quad \Omega = \lambda \tau , \quad \theta = 0.5 \lambda \tau^2$$

$$\tau > T_1 : \quad \Omega = 0.7 , \quad \theta = 0.7 \tau - 0.35 T_1 \qquad (3.15)$$

where T_1 is the time when the angular velocity reaches 0.7 under constant acceleration (λ). For linear deceleration with the initial angular velocity $\Omega = 0.7$, it can be formulated as

$$0 \leq \tau \leq T_1 : \quad \Omega = 0.7 + \lambda \tau , \quad \theta = 0.7\tau + 0.5 \lambda \tau^2$$

$$\tau > T_1 ; \quad \Omega = 0 , \quad \theta = 0.35 T_1 \tag{3.16}$$

where T_1 is the time when the angular velocity reaches zero under constant deceleration (λ). The initial conditions for deceleration are taken as $v_1 = 0.001$ and $w_1 = 0.001$. The corresponding dimensional values for Ω, λ, and τ are given by 818.31 Ω rad/sec, 6.70×10^5 λ rad/sec^2, and 1.22×10^{-3} τ sec.

Table 3.2 Relation between acceleration/deceleration and τ_{crit}

λ	T_1	τ_{crit} Acceleration	τ_{crit} Deceleration
± 0.0001	7000	3404	3596
± 0.0005	1400	680.8	719.2
± 0.0010	700	340.4	359.6
± 0.0020	350	170.2	179.8
± 0.0030	233.33	113.47	119.86

Figures 3.4 and 3.5 show graphically the different rates of acceleration and deceleration, respectively, that are used in this study. There are 5 different rates of acceleration, i.e., λ = 0.0001, 0.0005, 0.001, 0.002, and 0.003. Also, there are 5 different rates of deceleration, i.e., λ = -0.0001, -0.0005, -0.001, -0.002, and -0.003. The quantities T_1 and τ_{crit} are given in Table 3.2. Figures 3.6.a-e and 3.7.a-e show the time histories of the z displacement at the location $\tilde{x}$ = 0.7 under different acceleration and deceleration rates based on the standard parameters. From the results, the maximum z-displacement is always reached after $\tau = \tau_{crit}$, that is, after the angular velocity passes the critical speed. Note that the abscissa

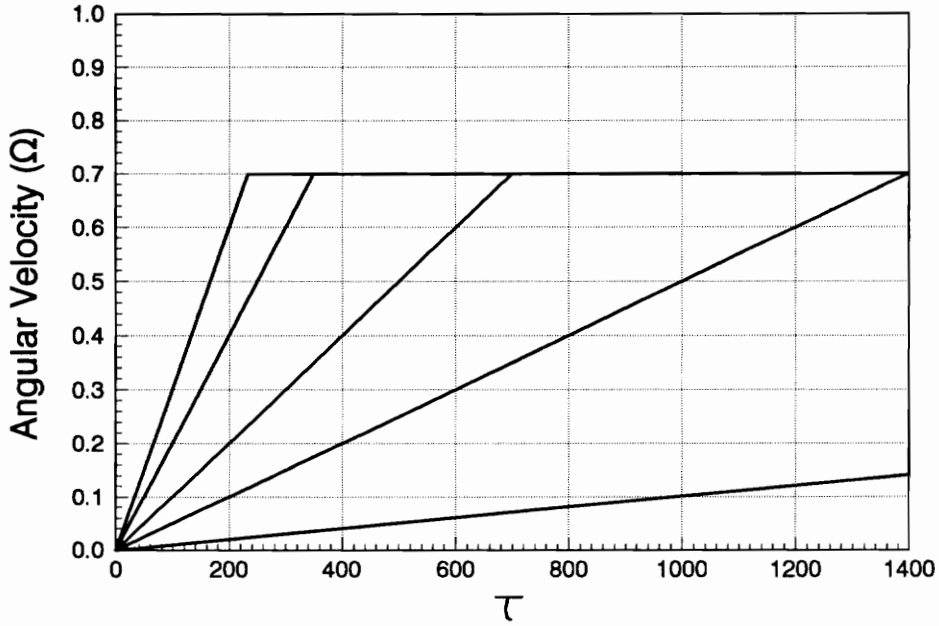

Fig. 3.4 Rates of Linear Acceleration

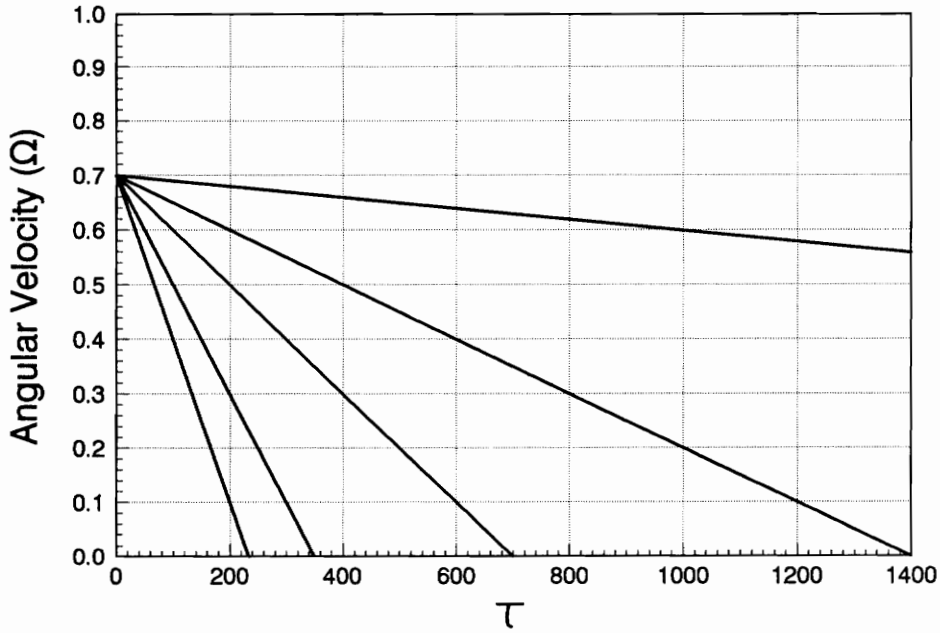

Fig. 3.5 Rates of Linear Deceleration

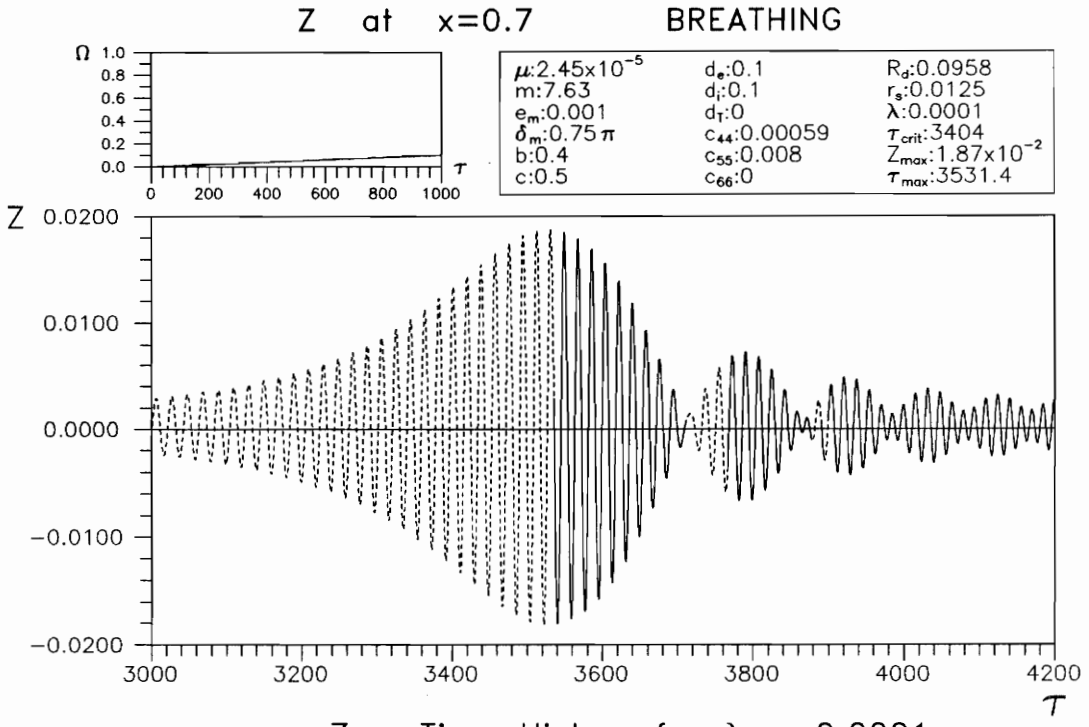

a. Z – Time History for λ = 0.0001

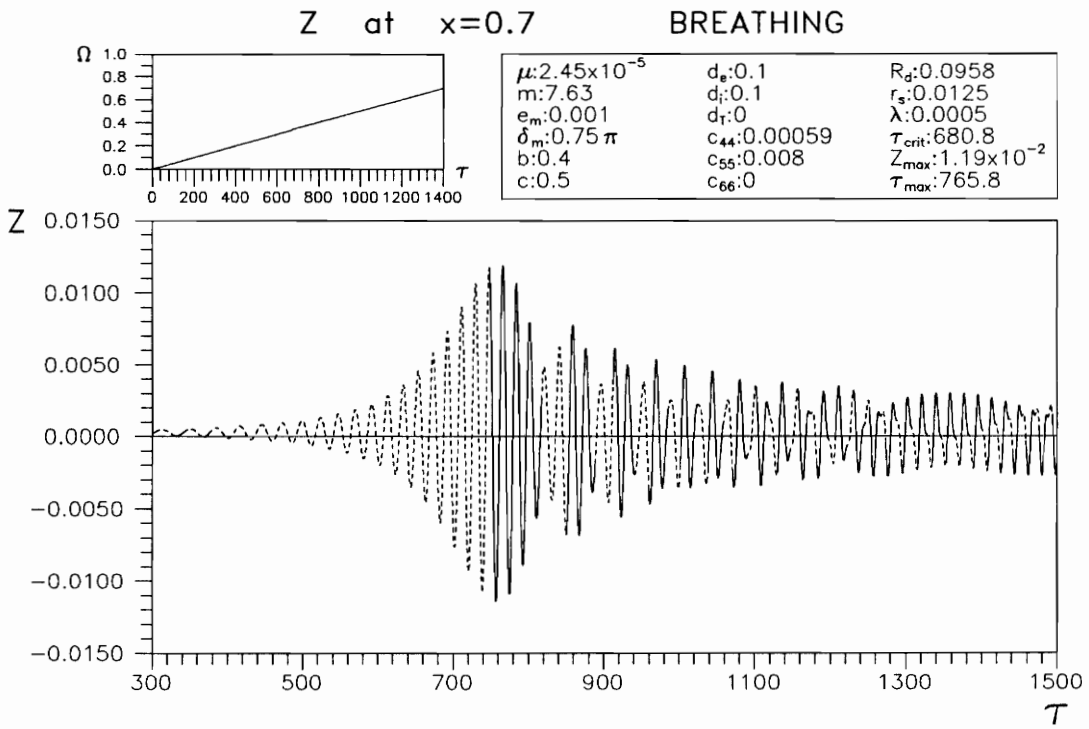

b. Z – Time History for λ = 0.0005

Fig. 3.6 Time History for Linear Acceleration

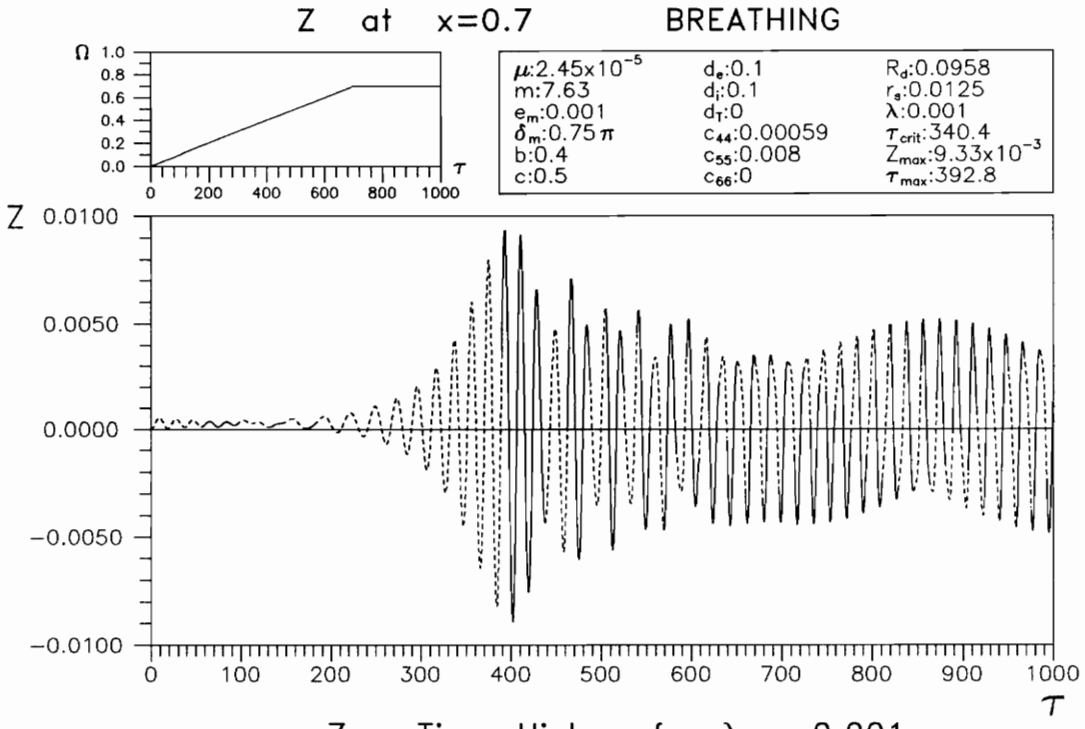

c. Z – Time History for λ = 0.001

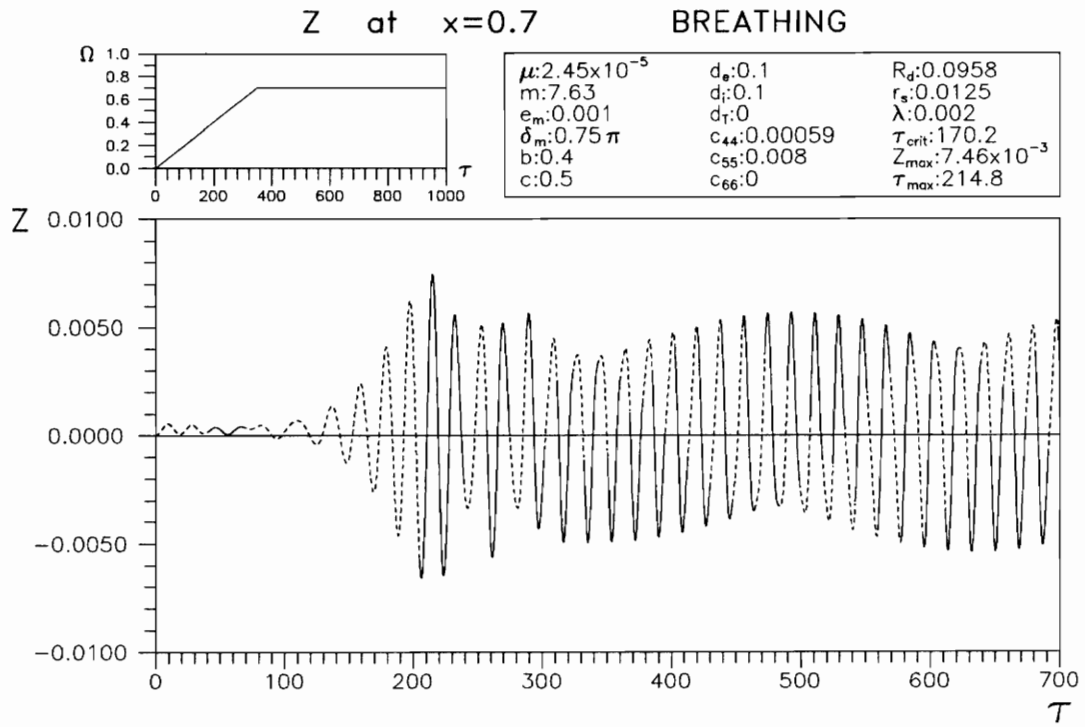

d. Z – Time History for λ = 0.002

Fig. 3.6 Time History for Linear Acceleration

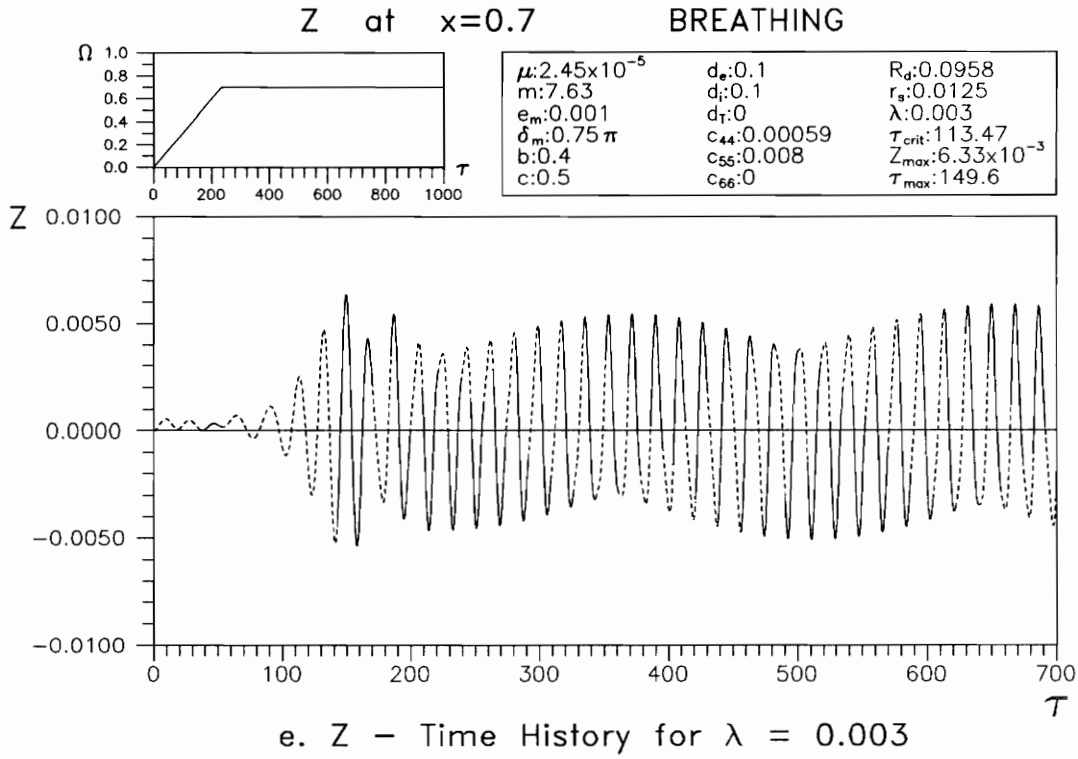

e. Z – Time History for λ = 0.003

Fig. 3.6 Time History for Linear Acceleration

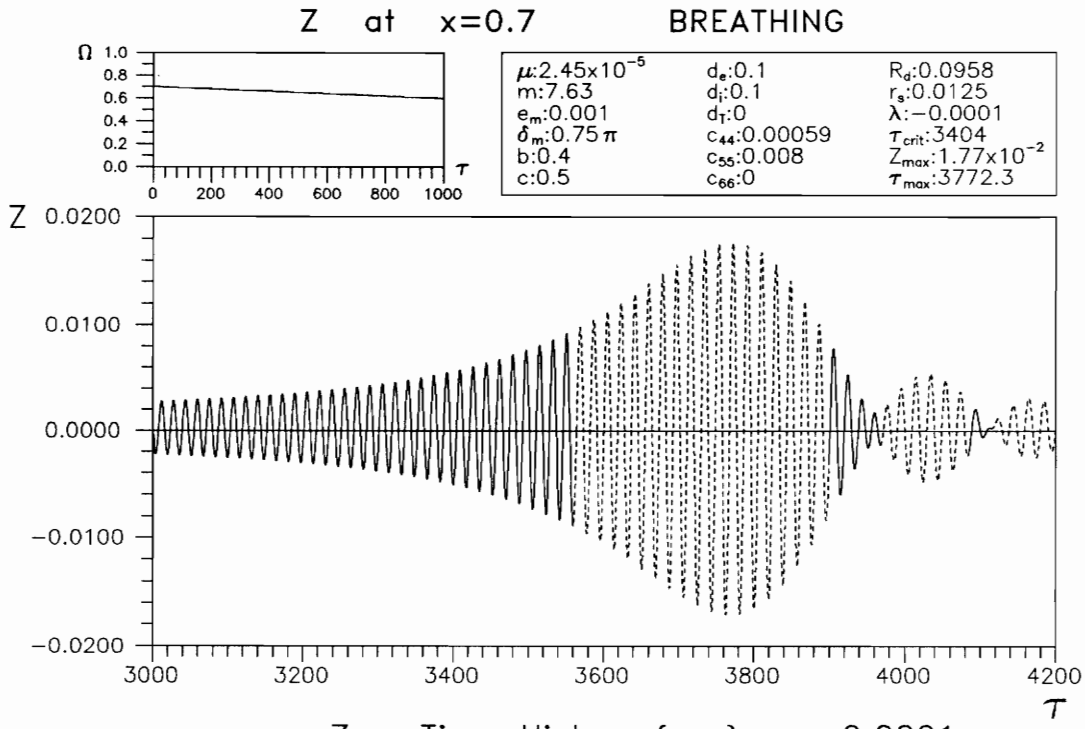

a. Z – Time History for λ = −0.0001

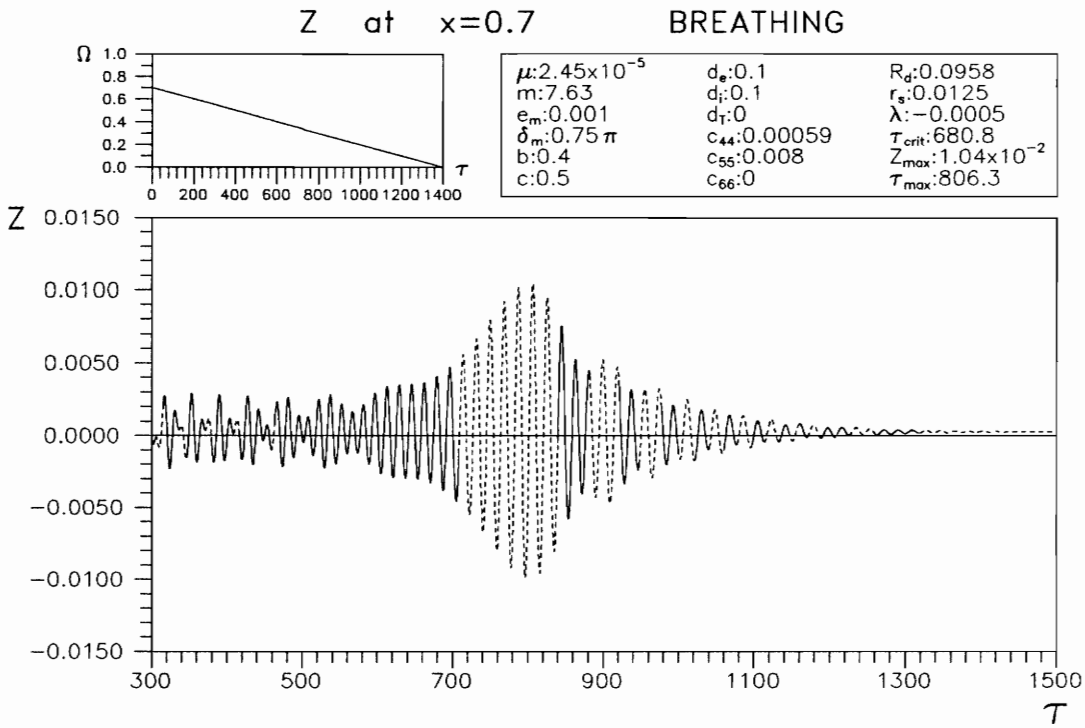

b. Z – Time History for λ = −0.0005

Fig. 3.7 Time History for Linear Deceleration

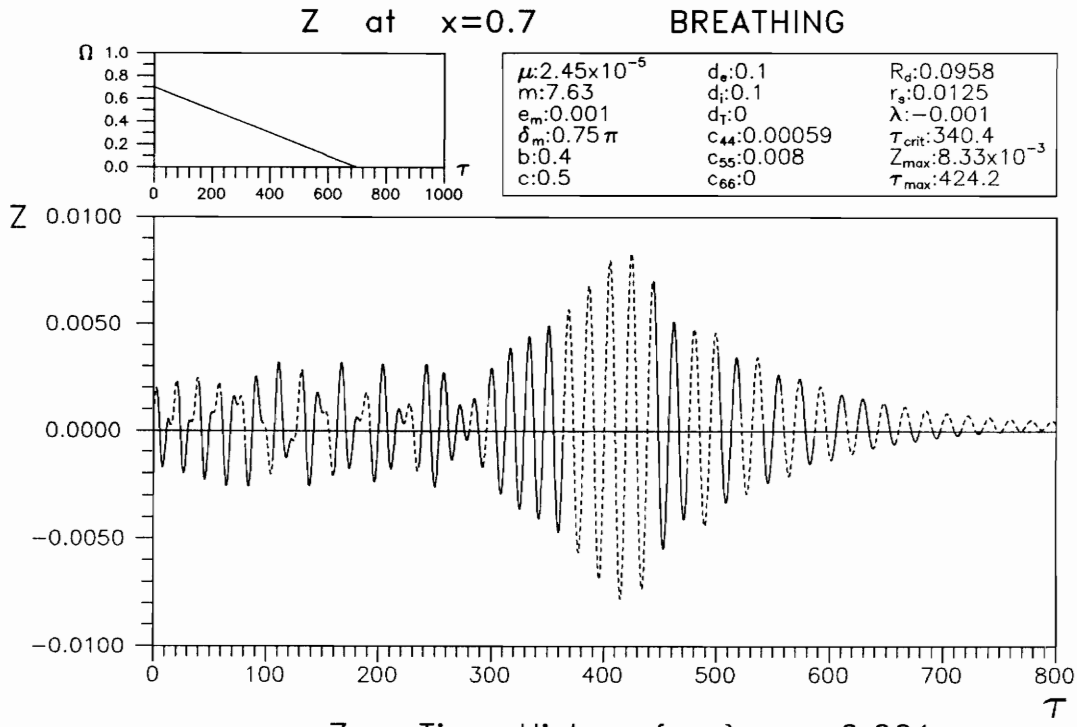

c. Z – Time History for $\lambda = -0.001$

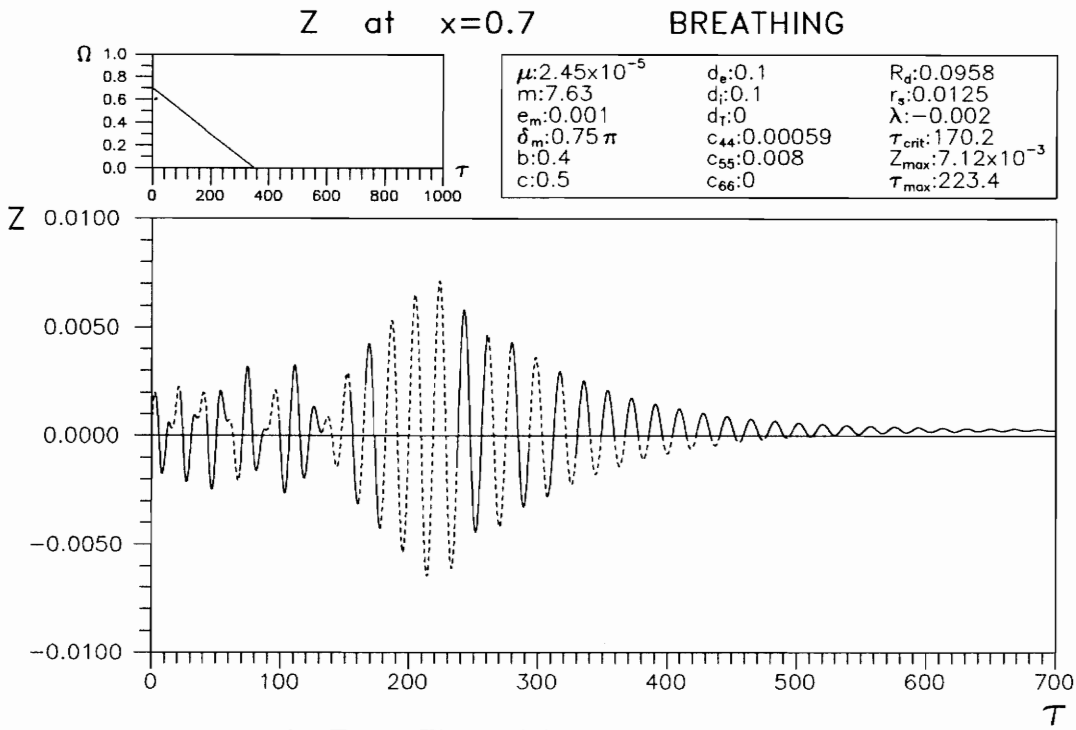

d. Z – Time History for $\lambda = -0.002$

Fig. 3.7 Time History for Linear Deceleration

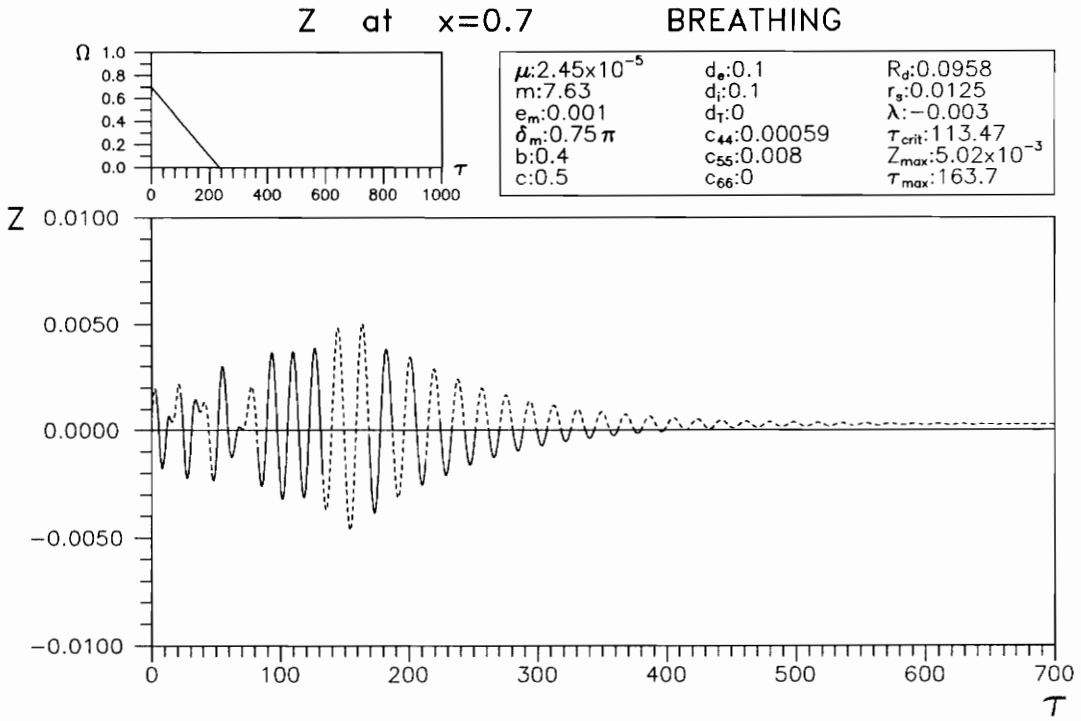

e. Z − Time History for λ = −0.003

Fig. 3.7 Time History for Linear Deceleration

in part a and part b does not begin at τ=0.

The z-displacement for $\tau < 3800$ in Fig. 3.6.a increases very slowly from zero initial conditions until it reaches its maximum and, as in most cases, the shaft is open during this time. In Fig. 3.6.b, the z-displacement for $\tau < 300$ is very small, almost zero. After $\tau \approx 350$ the z-displacement increases and reaches its maximum at $\tau = 765.8$.

Under linear acceleration with zero initial conditions, the shaft is open all or most of the time before the z-displacement reaches its maximum value. In all the cases under linear acceleration, after the shaft passes the velocity $\Omega = 0.7$ the z-displacement is not constant but it fluctuates up and down as shown in Fig. 3.6.d. For the low acceleration $\lambda = 0.0001$ in Fig. 3.6.a, after the maximum z-displacement is reached, there is a beat phenomenon, the condition when the modal amplitudes tend to reinforce each other at one time and tend to cancel each other at another time. The peak-to-peak amplitude at $\tau \approx 3800$ during the first beat after z_{max} is reached is approximately 38% of the maximum amplitude. After that, the amplitude become smaller and smaller. In other figures, Fig. 3.6.b-e, there is no beat phenomenon, but there is still a decay condition after the amplitude reaches the maximum. The decay condition is stronger for lower acceleration. It can be seen in Fig. 3.6.b ($\lambda = 0.0005$) that the peak-to-peak amplitude at $\tau \approx 1500$ is only 22% of the maximum amplitude. However, in Fig. 3.6.e (λ=0.003) the peak-to-peak amplitude at $\tau \approx 250$ is about 80% of the maximum amplitude. For the standard condition (Fig. 3.6.c), the difference between the amplitude at $\tau \approx 800$ and the maximum amplitude is about 47%.

Figure 3.8 presents the relation between the rate of acceleration and both the maximum z-displacement at location $\tilde{x} = 0.7$ ($z_{max,x}$) and the maximum z-displacement over the whole length of the cracked shaft ($z_{max,w}$). The shaft

rotating under a lower acceleration has a larger z-displacement. The reason is that the shaft motion has more time to build itself up from the beginning until the shaft reaches the critical speed.

Under deceleration, when the shaft reaches the maximum z-displacement in Fig. 3.7.a-e, the crack is open. It is clear under deceleration in Fig. 3.7.a-e that the z-displacement still increases as τ passes τ_{crit} until it reaches a maximum. After the z-displacement reaches the maximum, it decreases quickly. The beat phenomenon for low deceleration λ=-0.0001 (Fig. 3.7.a) still occurs. The amplitude at $\tau \approx 4030$ during the first beat is about 30% of the maximum amplitude. Compared to the low acceleration λ=0.0001, the difference of the amplitudes in this case is larger. For other deceleration cases (Fig. 3.7.b-e), the amplitude after z_{max} becomes smaller and smaller. The relation between the rate of deceleration and the maximum z-displacement is shown in Fig. 3.9. The characteristic of that relation is similar to the previous one under acceleration. In Fig. 3.9, the maximum z-displacement under deceleration is always less than that under acceleration with the same rate, because deceleration tends to reduce the amplitude.

In Fig. 3.10.a-b and Fig. 3.11.a-b, the time histories of the z-displacement at location $\tilde{x} = 0.7$ for the open crack shaft and the uncracked shaft under acceleration and deceleration, respectively, are presented with the standard parameters. The forms of the time histories of the z-displacement for the breathing crack, open crack, and uncracked conditions are the same. Table 3.3 shows the maximum z-displacement for the breathing crack, open crack, and uncracked shaft. For these cases, the breathing crack gives the biggest z_{max}.

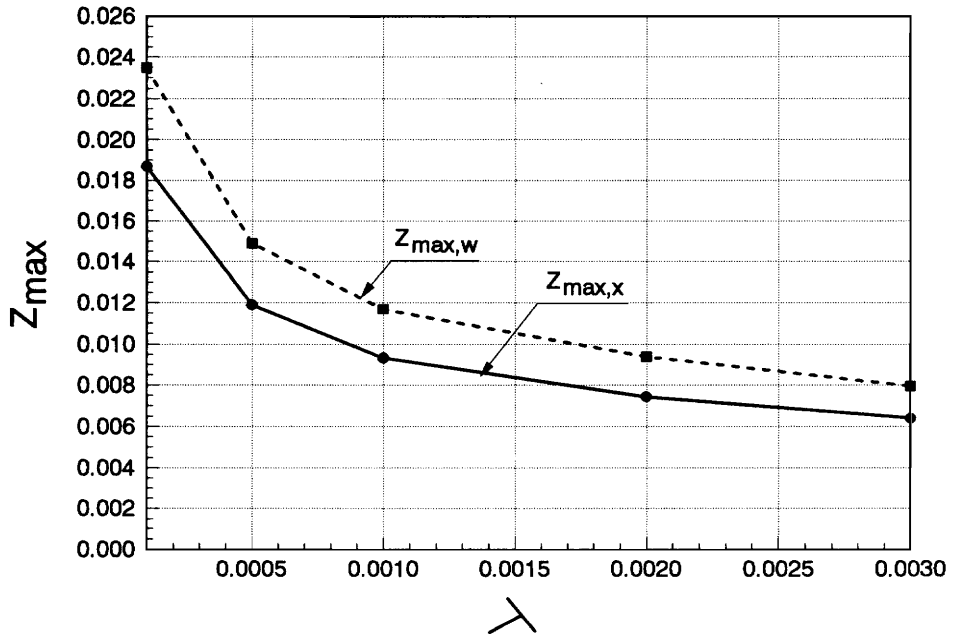

Fig. 3.8 Influence of Linear Acceleration Rate

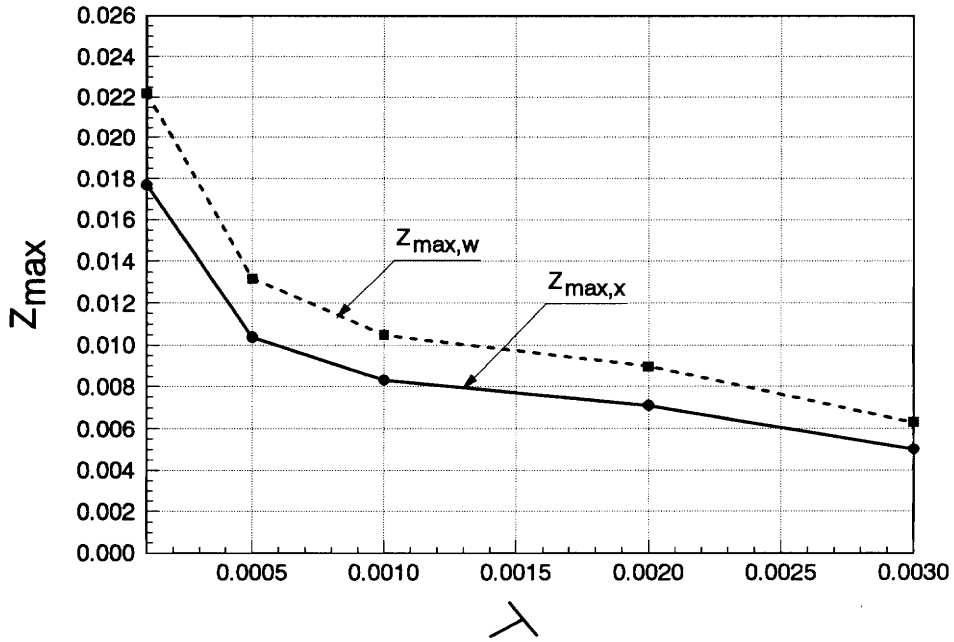

Fig. 3.9 Influence of Linear Deceleration Rate

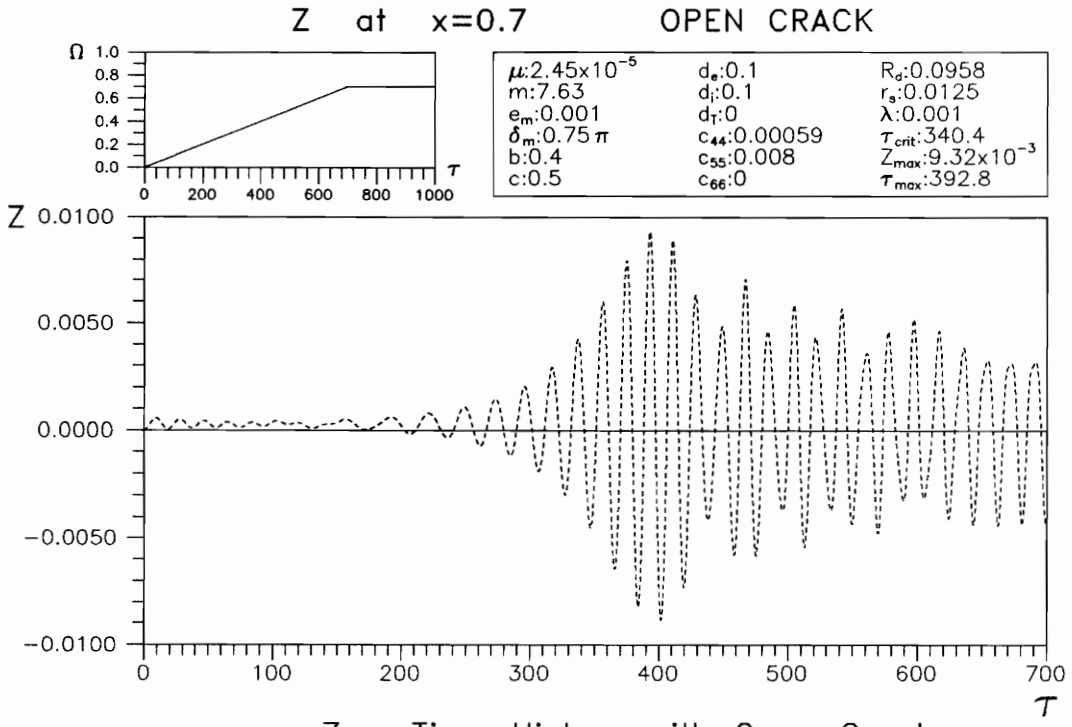

a. Z – Time History with Open Crack

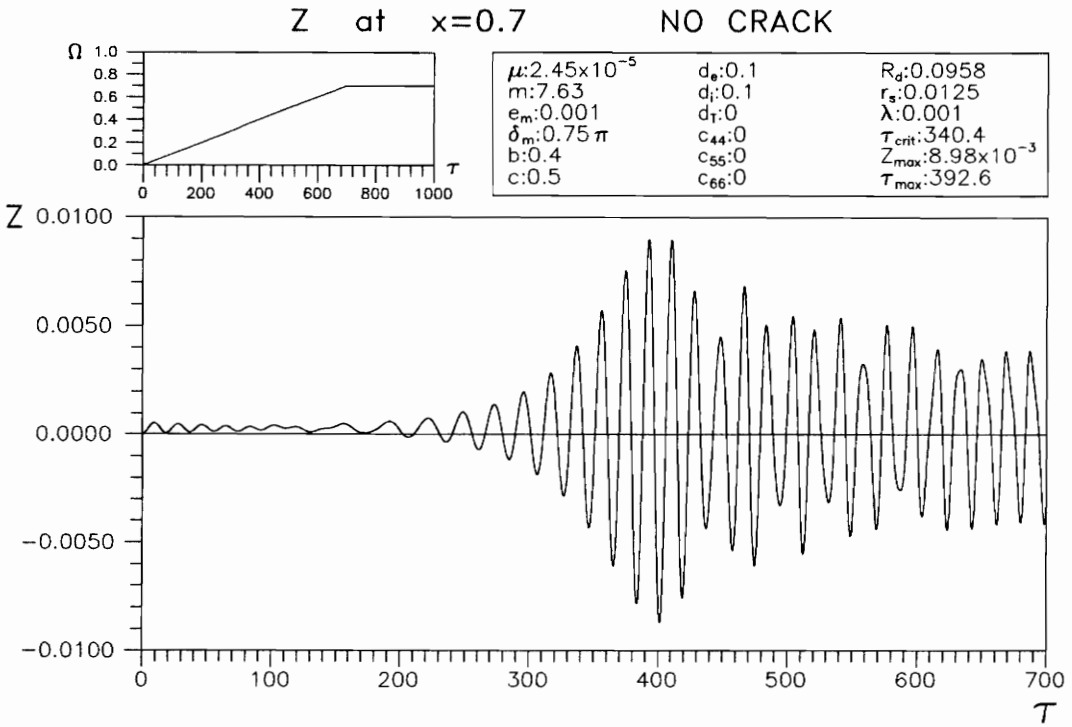

b. Z – Time History without Crack

Fig. 3.10 Time History for Standard Case with λ = 0.001

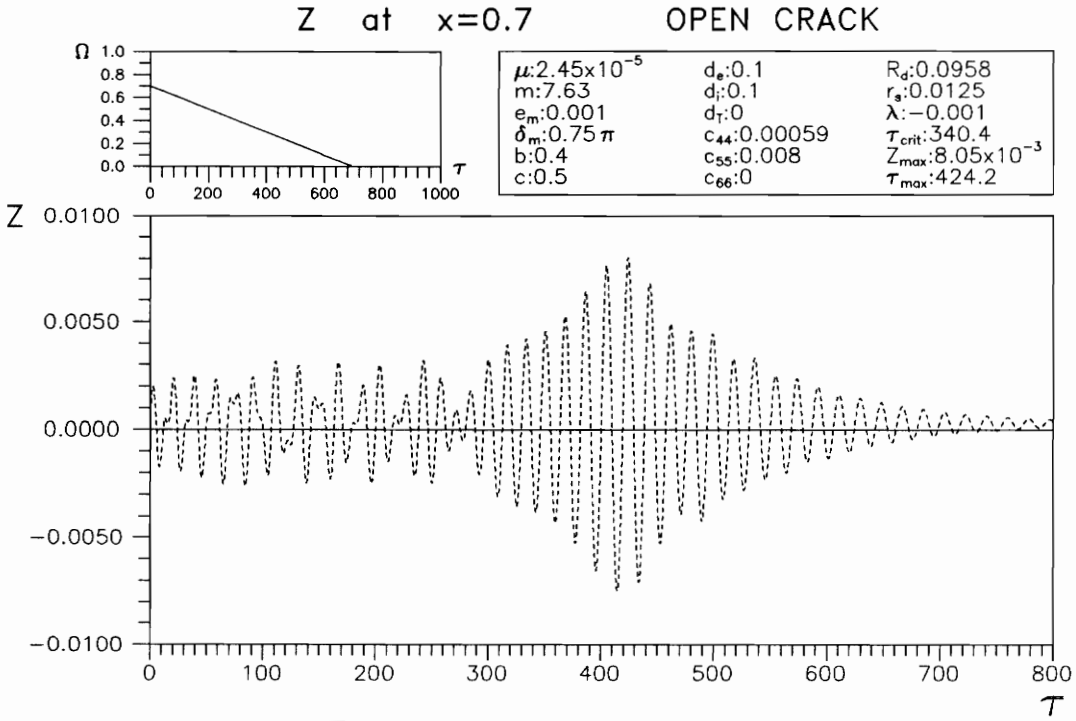

a. Z – Time History with Open Crack

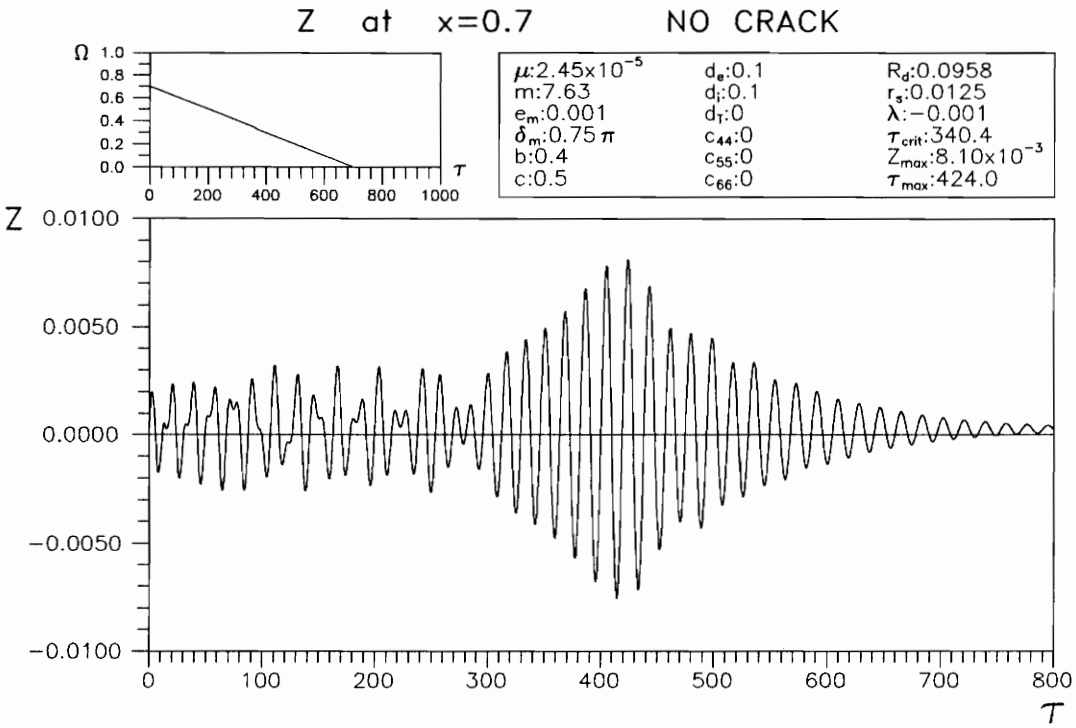

b. Z – Time History without Crack

Fig. 3.11 Time History for Standard Case with $\lambda = -0.001$

Table 3.3 Maximum z-displacement for acceleration and deceleration

	Acceleration		Deceleration	
z_{max}	$\tilde{x} = 0.7$	over the whole length	$\tilde{x} = 0.7$	over the whole length
Breathing Crack	9.33×10^{-3}	1.17×10^{-3}	8.33×10^{-3}	1.05×10^{-3}
Open Crack	9.32×10^{-3}	1.17×10^{-3}	8.05×10^{-3}	1.02×10^{-3}
No Crack	8.98×10^{-3}	1.13×10^{-3}	8.10×10^{-3}	1.02×10^{-3}

3.5. Influence of Crack Location

Based on the standard parameters and $\lambda = 0.001$ for acceleration, various locations of the crack ($\tilde{b}$) on the shaft were considered. The relation between the crack location and the maximum z-displacement ($z_{max,x}$ for $\tilde{x} = 0.7$ and $z_{max,w}$ over the whole length) is presented in Fig. 3.12. The boundary conditions for both ends are the same and the disk is located at the middle of the shaft. Therefore the curve for $z_{max,w}$ must be symmetric, and the curve for $z_{max,x}$ is almost symmetric. The maximum z-displacement over the whole length occurs when the crack is at the middle of the shaft. If the crack is located near the ends, the maximum z-displacement for the cracked shaft is almost the same as that for the uncracked shaft.

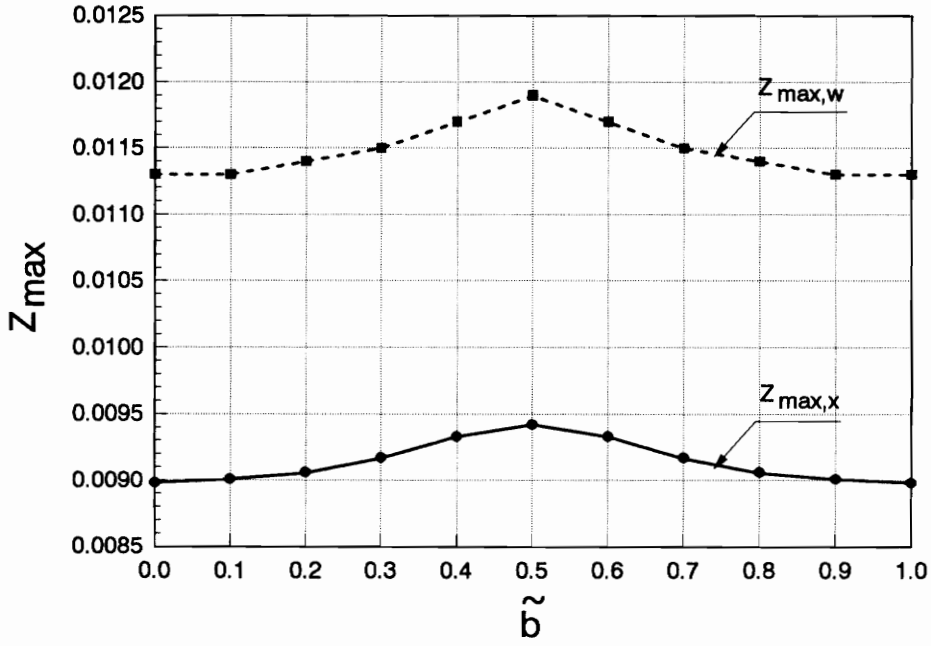

Fig. 3.12 Influence of Crack Location

3.6. Influence of Disk Location

In order to know the effect of the location of a disk on the shaft, several cases have been examined with different disk locations ($\tilde{c}$) between 0.1 and 0.9, and the other parameters are based on the standard parameters. A comparison between the breathing crack shaft and uncracked shaft also has been made.

Figure 3.13 shows the time history of the z-displacement at location $\tilde{x} = 0.7$ when the disk is located at $\tilde{c} = 0.1$. The time history for $\tilde{c} = 0.9$ is similar to the time history for $\tilde{c} = 0.1$. Also, the time histories for $\tilde{c}$ between 0.2 and 0.8 are similar to the time history for $\tilde{c} = 0.5$, which is presented in Fig. 3.6.c. The time histories of the z-displacement for $\tilde{c} = 0.1$ and $\tilde{c} = 0.9$ are totally different from those for $\tilde{c}$ between 0.2 and 0.8; the amplitude of the z-displacement does not decrease significantly after reaching its maximum value, which occurs much later in Fig. 3.13 than in Fig. 3.6.c. After the shaft velocity is constant, the z-displacement amplitude becomes constant.

The relation between the disk location and the maximum z-displacement is shown in Fig. 3.14. There are two curves, i.e., $z_{max,x}$ for z_{max} at $\tilde{x} = 0.7$ and $z_{max,w}$ for z_{max} over the whole length of the shaft. The graph of $z_{max,x}$ is not symmetric, because of the crack location $\tilde{b} = 0.4$ and the distance between the disk location and the location of the measurement of z_{max}. The largest value occurs when $\tilde{c} = 0.8$. However, the curve of the maximum z-displacement over the whole length of the shaft, $z_{max,w}$, is almost symmetric. For both curves, the z-displacement if the disk is located at $\tilde{c} = 0.2$ or $\tilde{c} = 0.8$ is larger than that if the disk is located at the middle of the shaft.

The comparison of $z_{max,w}$ between the breathing crack shaft and uncracked shaft is presented in Fig. 3.15. The symmetry condition is satisfied exactly if there

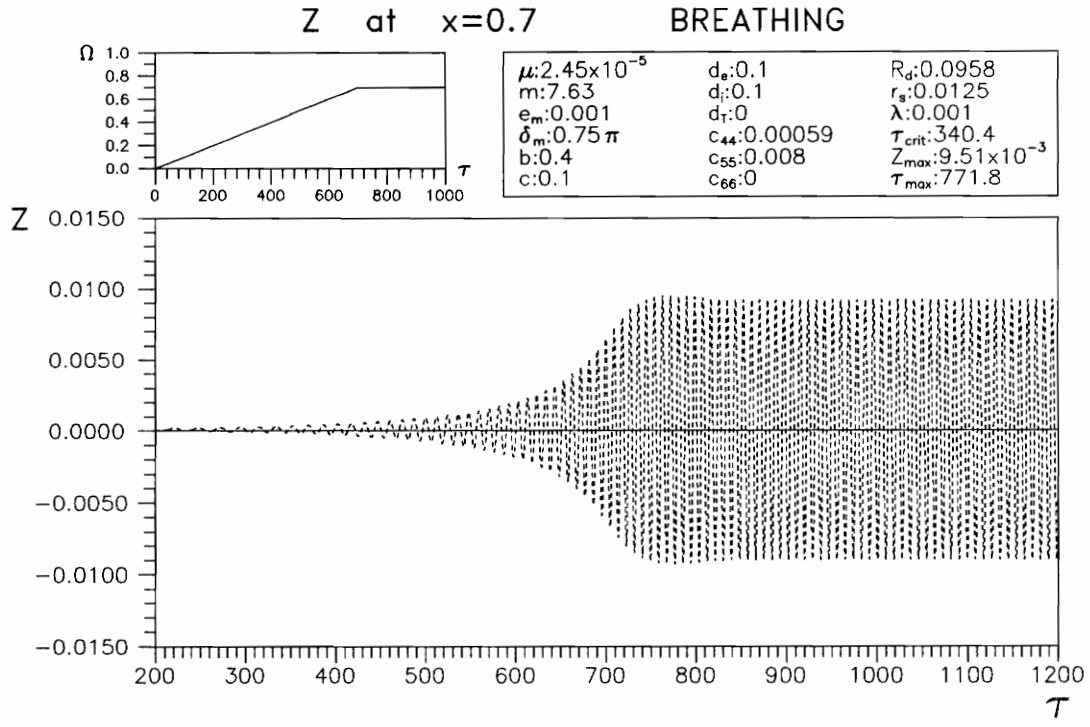

Fig. 3.13 Z – Time History for Disk Location $\tilde{c}$=0.1

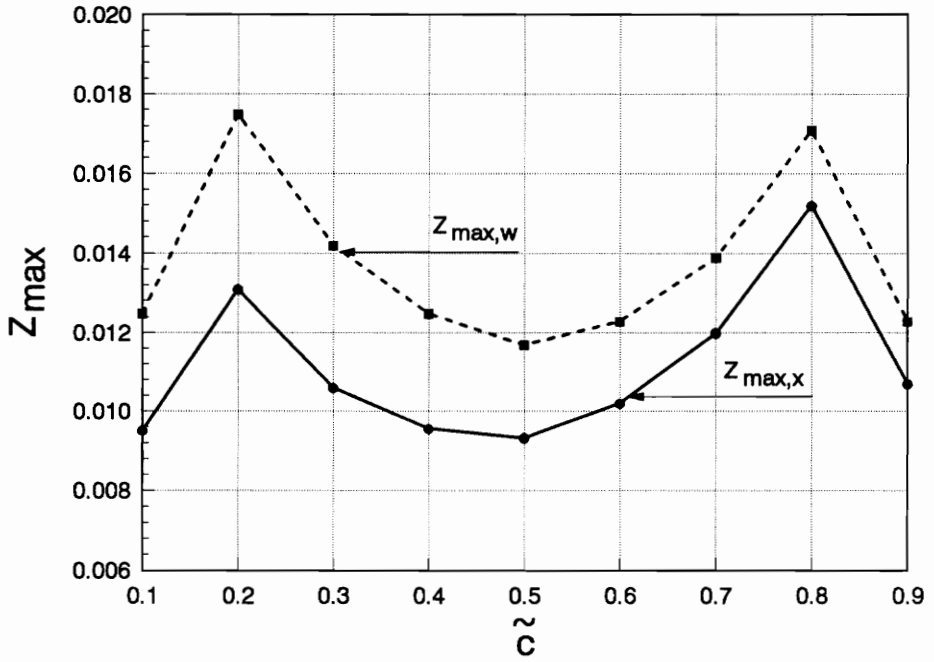

Fig. 3.14 Influence of Disk Location

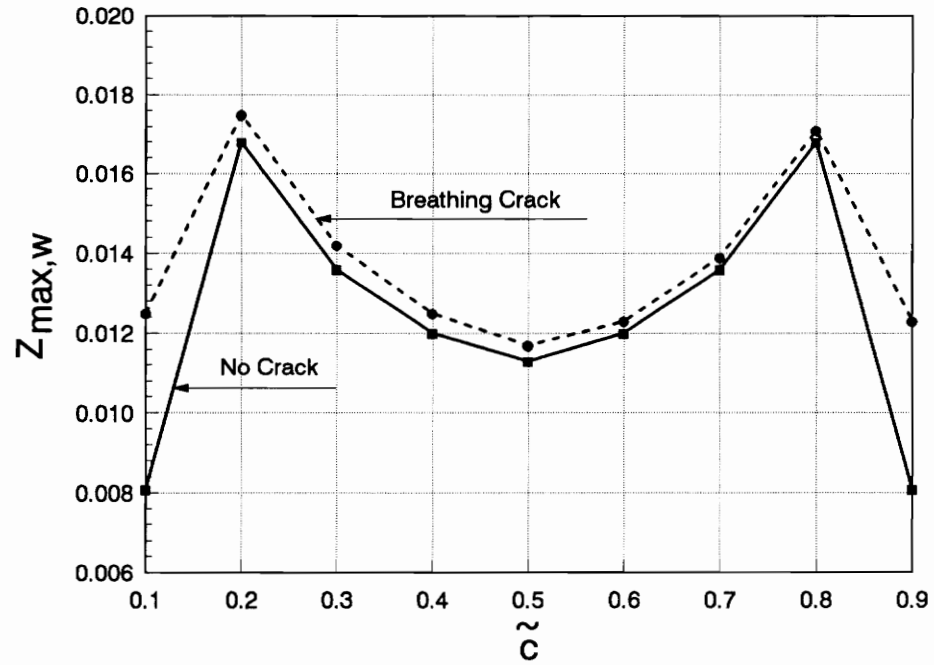

Fig. 3.15 Influence of Disk Location
for Breathing Crack and Uncracked Shaft

is no crack in the shaft. For all cases of different disk locations computed for Fig. 3.15, z_{max} for the shaft with a breathing crack is greater than z_{max} for the shaft without a crack.

3.7. Influence of Crack Depth

The crack depth (a) affects the transverse displacements of the cracked rotating shaft. To determine the magnitude of this effect, cases of different relative crack depths (a/D) have been investigated.

The compliances $\tilde{c}_{44}$ and $\tilde{c}_{55}$ are functions of the crack depth. Table 3.4 contains the data of the compliances $\tilde{c}_{44}$ and $\tilde{c}_{55}$ based on the work of Papadopoulos and Dimarogonas[27].

Table 3.4 Nondimensional compliances $\tilde{c}_{44}$ and $\tilde{c}_{55}$

a/D	$\tilde{c}_{44}$	$\tilde{c}_{55}$
0	0	0
0.10	0.00004	0.0012
0.20	0.00059	0.0080
0.25	0.0012	0.01292
0.30	0.00215	0.02153

Figure 3.16 displays the relation between the crack depth (a/D) and the maximum z-displacement at location $\tilde{x} = 0.7$. If the crack depth (a/D) is 0.1, the shaft almost gives the same z_{max} as the shaft without a crack; the difference is less than 0.5 %. If the crack depth becomes larger, z_{max} becomes much larger. The difference of z_{max} between a/D = 0.2 and a/D=0.3 is about twice as much as the difference of z_{max} between a/D=0.1 and a/D=0.2.

3.8. Influence of Disk Eccentricity

The effect of disk eccentricity ($\tilde{e}_m$) is shown in Fig. 3.17. Six cases were computed, i.e., $\tilde{e}_m$ = 0, 0.001, 0.005, 0.01, 0.05, 0.10. The cases with $\tilde{e}_m$ = 0.05 and $\tilde{e}_m$= 0.10 are extreme conditions. From this graph, the maximum z-displacement at location $\tilde{x} = 0.7$ is approximately proportional to the disk eccentricity. The complete results of z_{max} with different disk eccentricities are written in Table 3.5.

Table 3.5 Influence of disk eccentricity

$\tilde{e}_m$	z_{max} at $\tilde{x} = 0.7$	z_{max} over the whole length
0.000	5.34×10^{-4}	6.69×10^{-4}
0.001	9.33×10^{-3}	1.17×10^{-2}
0.005	4.58×10^{-2}	5.76×10^{-2}
0.010	9.18×10^{-2}	1.16×10^{-1}
0.050	4.60×10^{-1}	5.79×10^{-1}
0.100	9.20×10^{-1}	1.16

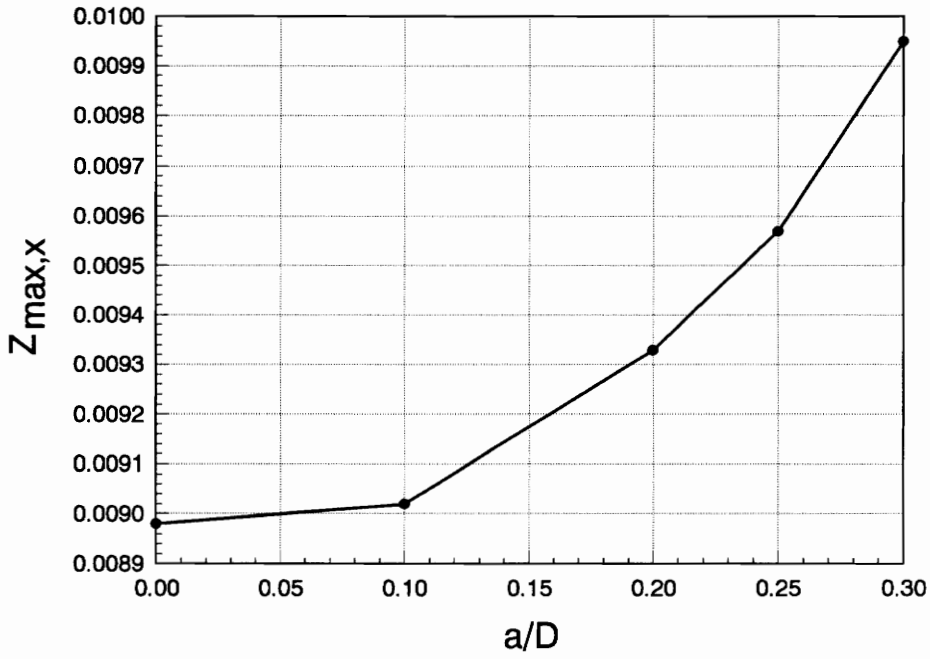

Fig. 3.16 Influence of Crack Depth

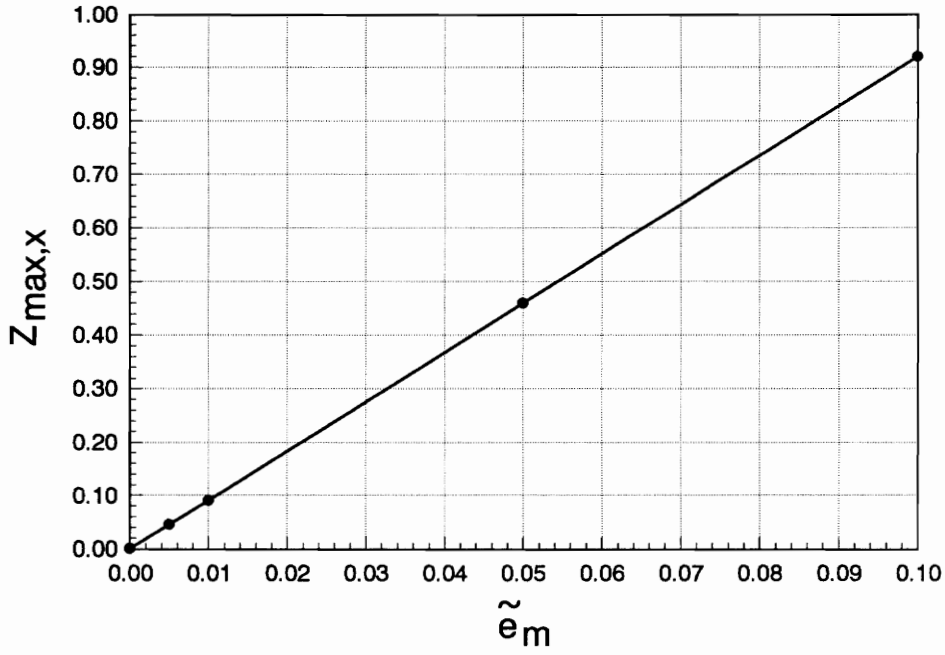

Fig. 3.17 Influence of Disk Eccentricity

3.9. Influence of Disk Eccentricity Angle

Figure 3.18 shows the relation between the disk eccentricity angle δ_m (see Fig. 2.3) and the maximum z-displacement at location $\tilde{x} = 0.7$ for three cases of crack conditions, i.e., breathing crack, open crack, and no crack. The results are interesting, because the effect of the crack conditions is not always the same. Sometime the breathing crack gives the largest z_{max}, and other times the uncracked shaft gives the largest z_{max}.

There are three basic ranges of δ_m with respect to the largest z_{max}. First, if δ_m is between 0 and 0.9π, the breathing crack shaft gives the largest z_{max}. Second, if δ_m is between 0.9π and 1.6π, the uncracked shaft gives the largest z_{max}. Last, if δ_m is between 1.6π and 2π, the open crack shaft gives the largest z_{max}.

The values of z_{max} for the breathing crack shaft and open crack shaft are the same if δ_m is between 0.75π and $9\pi/8$. If δ_m is close to zero, the breathing crack shaft gives the same result as the uncracked shaft. In other words, the effect of the breathing crack on z_{max} does not exist in this case. Another interesting result is that if δ_m is between $9\pi/8$ and 2π, the uncracked shaft gives a larger z_{max} than the breathing crack shaft.

In Fig. 3.19, the effects of the disk eccentricity angle together with the mass of the shaft ($\tilde{\mu} = 2.45\text{x}10^{-5}$ and $\tilde{\mu} = 0$) are presented for the uncracked shaft. The mass of the shaft causes δ_m to have a larger influence on the z-displacement. In the case of no gravitation (or no mass of the shaft), the z-displacement is always the same at every π radians. This condition does not occur for the other case.

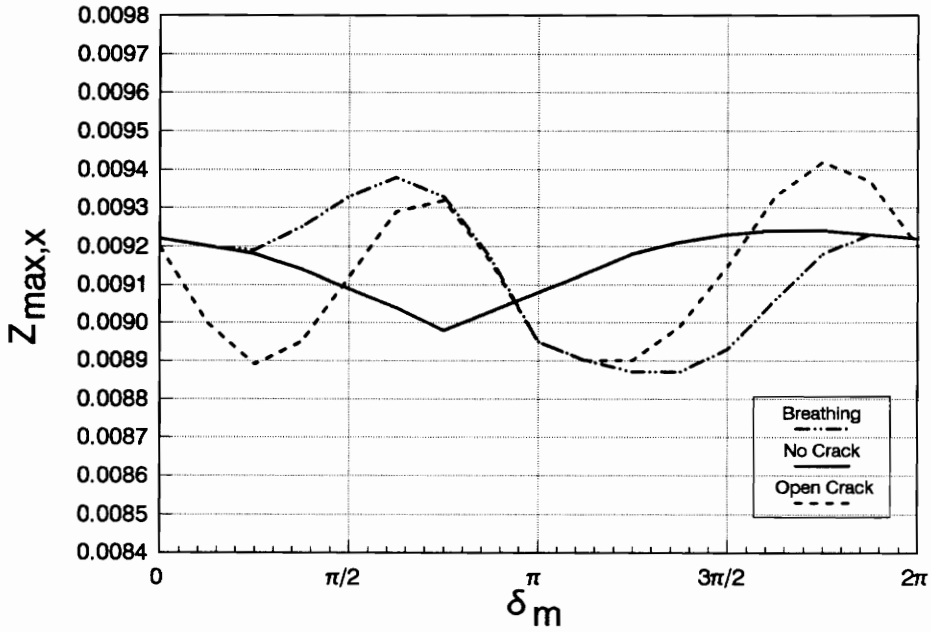

Fig. 3.18 Influence of Disk Eccentricity Angle and Crack Condition

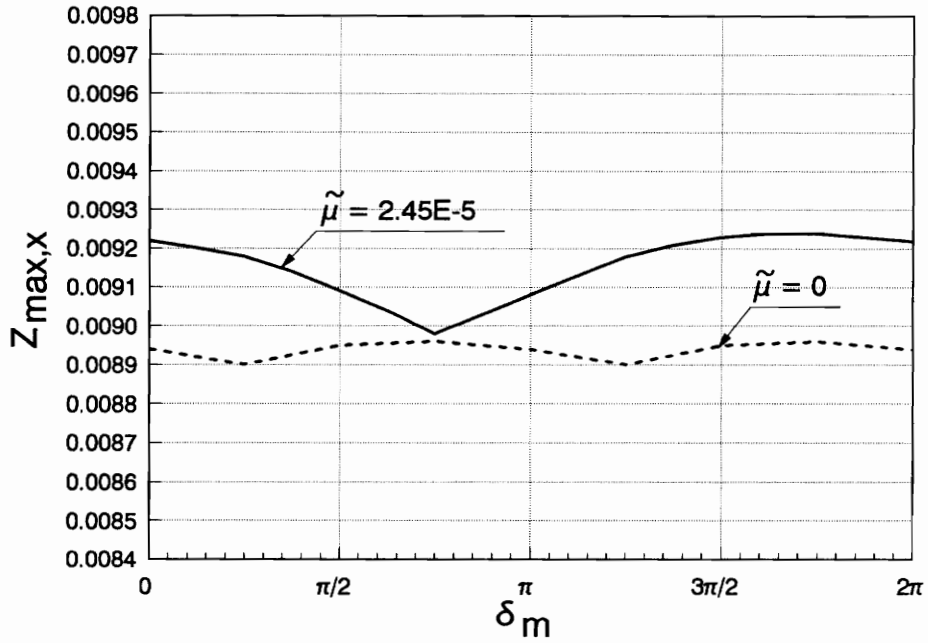

Fig. 3.19 Influence of Disk Eccentricity Angle and Shaft Mass for Uncracked Shaft

3.10. Influence of Disk Mass

The relation between disk mass and the maximum z-displacement is presented in Fig. 3.20. The non-dimensionalized mass of the disk varies from 1 to 10 and the other parameters are based on the standard case. The difference of $z_{max,x}$ between $\tilde{m} = 1$ and $\tilde{m}$=2 is almost 20%. The difference becomes smaller when the disk mass becomes larger. After $\tilde{m} = 5$ the influence of the disk mass is small, less than 1%. After $\tilde{m} = 6$ there is a tendency for a smaller $z_{max,x}$ as $\tilde{m}$ increases.

3.11. Transverse Displacement at Certain Points

It is of interest to see the maximum z-displacement along the shaft. Therefore, based on the standard parameters, points along the shaft between 0.1 and 0.9 are considered. The result is shown in Fig. 3.21. From that figure, the maximum z-displacement over the whole length of the shaft occurs at the middle of the shaft. This is not surprising, since both ends are simply supported and the disk is located at the middle. The z-displacement is almost symmetric about the middle of the shaft; the difference between values of z_{max} on opposite sides of the center is less than 0.1%.

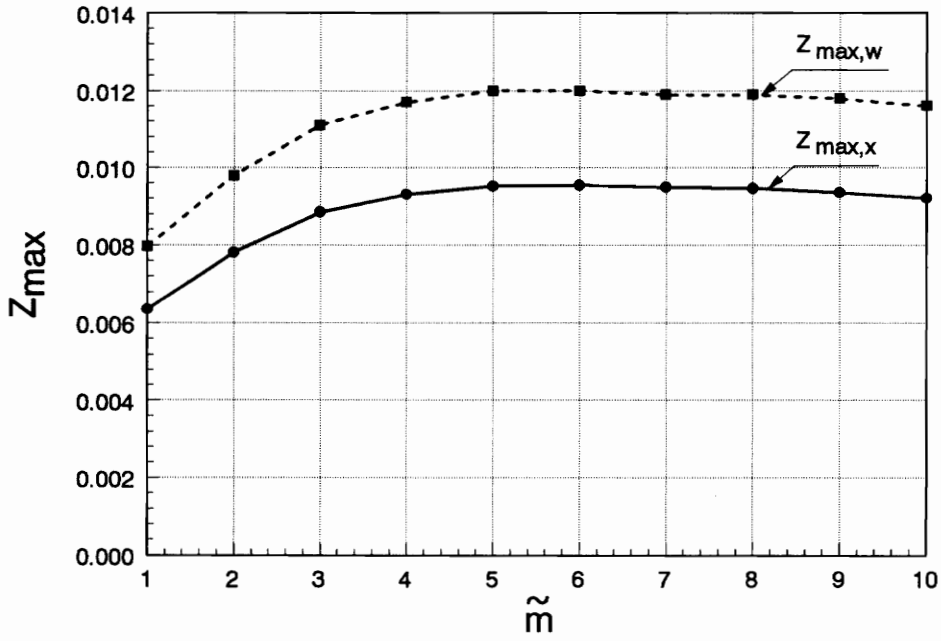

Fig. 3.20 Influence of Disk Mass

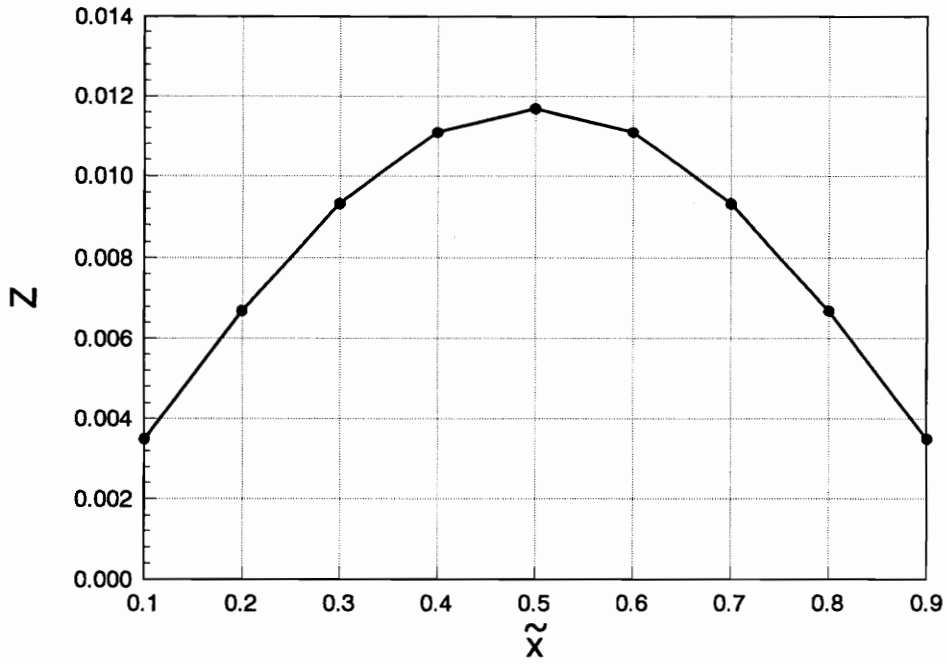

Fig. 3.21 Transverse Displacement Along Shaft

Chapter 4
Flexural - Torsional Response of Cracked Rotating Shaft with a Disk

4.1. Physical Model

Basically, the physical model of a cracked shaft with a disk under flexural - torsional conditions (Fig. 4.1) is the same as that under flexural condition only (see chapter 2) with some additions. Calculating the torsional vibrations, it is necessary to know the torsional stiffness GJ (G: shear modulus; J: torsional constant) and the polar mass moment of inertia I_p for the disk.

The simply supported case, neglecting longitudinal displacement and shear deformation, is investigated, so the results can be compared with the previous ones. The fixed coordinate system (x,y,z) and the shaft coordinate system (ξ,η,ζ) in Fig. 2.2 are still used in this second part of the study. Besides the displacements v(x,t), w(x,t) in the transverse direction, the torsional deformation ϕ(x,t) is also included (see Fig. 4.2).

The shaft has four types of damping, i.e., external damping d_e, internal damping d_i, crack damping d_c when the crack is closed, and torsional damping d_T. The external damping, crack damping, and torsional damping are assumed to act on the shaft only, not on the disk.

The geometric discontinuity caused by the transverse surface crack is

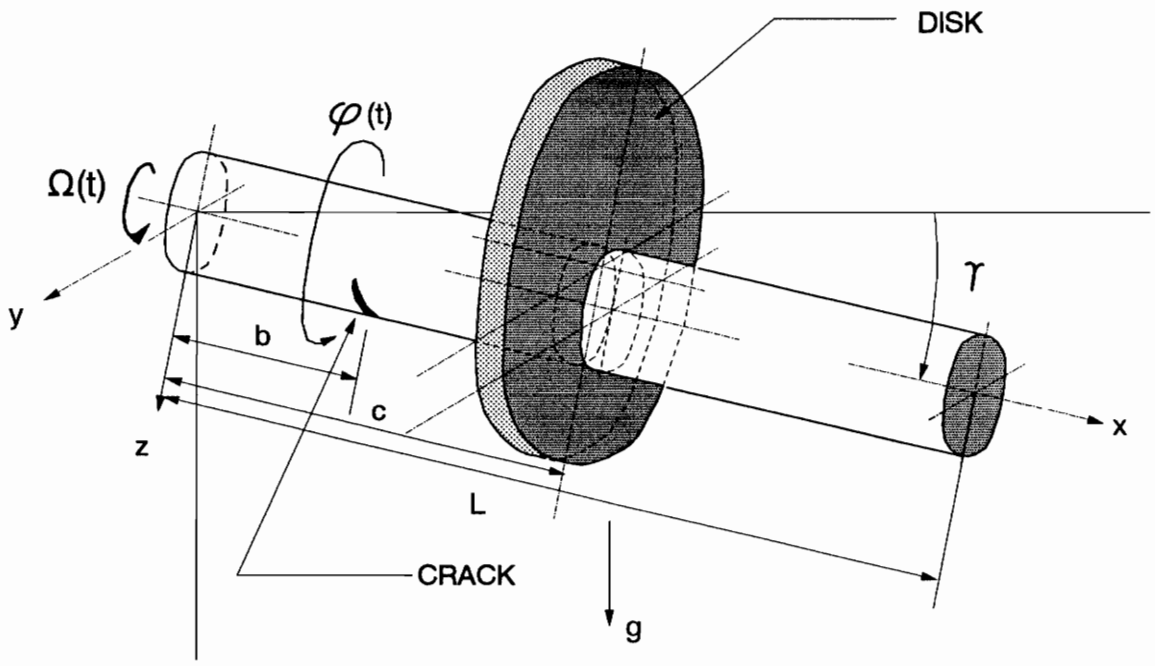

Fig. 4.1 Model of Cracked Shaft with Torsion
(Non-Specified Boundary Conditions)

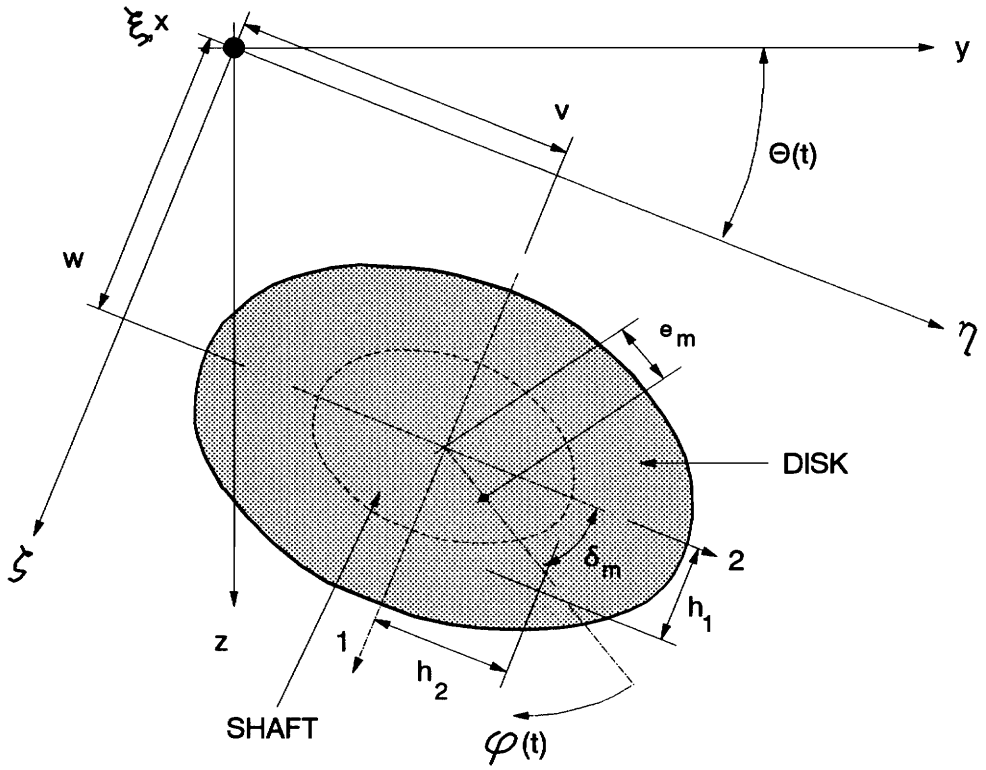

Fig. 4.2 Coordinate Systems and
Disk Cross-Sectional Area with Torsion

replaced by generalized moments (M and m) at the crack location, i.e., x=b$_-$ and x=b$_+$ (see Fig. 2.4). The external torque T is assumed to be located at a distance x=h from the left support.

4.2. Mathematical Model

Based on Wauer's formulation [40], the equations of motion for the flexural - torsional response of a cracked rotating shaft can be written as follows:

$$
\begin{aligned}
&EI_1 v_{xxxx} + [\mu + m\delta(x\text{-}c)]\left[v_{tt} - 2\dot{\theta}w_t - \dot{\theta}^2 v - \ddot{\theta}w\right] + d_e \mu (v_t - \dot{\theta}w) + EI_1 d_i v_{txxxx} \\
&+ (1\text{-}\Lambda)\, d_c \mu (v_t - \dot{\theta}w)\, \delta(x\text{-}b) + \Lambda\left[\delta'(x\text{-}b_+) - \delta'(x\text{-}b_-)\right](M_\zeta + m_\zeta) \\
&= [\mu + m\delta(x\text{-}c)]\, g \sin\theta + m e_m \delta(x\text{-}c)\,(\dot{\theta}^2 + 2\dot{\theta}\phi_t + \ddot{\theta}\phi)\cos\delta_m \\
&+ m e_m \delta(x\text{-}c)\,(\ddot{\theta} + \phi_{tt} - \dot{\theta}^2\phi)\sin\delta_m
\end{aligned}
\tag{4.1}
$$

$$
\begin{aligned}
&\Gamma EI_1 w_{xxxx} + [\mu + m\delta(x\text{-}c)]\left[w_{tt} + 2\dot{\theta}v_t - \dot{\theta}^2 w + \ddot{\theta}v\right] + d_e \mu (w_t + \dot{\theta}v) \\
&+ \Gamma EI_1 d_i w_{txxxx} + (1\text{-}\Lambda)\, d_c \mu (w_t + \dot{\theta}v)\, \delta(x\text{-}b) - \Lambda\left[\delta'(x\text{-}b_+) - \delta'(x\text{-}b_-)\right](M\eta + m_\eta) \\
&= [\mu + m\,\delta(x\text{-}c)]\, g \cos\theta + m e_m \delta(x\text{-}c)\,(\dot{\theta}^2 + 2\dot{\theta}\phi_t + \ddot{\theta}\phi)\sin\delta_m \\
&- m e_m \delta(x\text{-}c)\,(\ddot{\theta} + \phi_{tt} - \dot{\theta}^2\phi)\cos\delta_m
\end{aligned}
\tag{4.2}
$$

$$
\begin{aligned}
&I_p \delta(x\text{-}c)\,(\ddot{\theta} + \phi_{tt}) + \mu (r_1^2 + r_2^2)(\ddot{\theta} + \phi_{tt}) - GJ (\phi_{xx} + d_i \phi_{txx}) \\
&+ d_T \mu (r_1^2 + r_2^2)(\dot{\theta} + \phi_t) - \Lambda\left[\delta(x\text{-}b_+) - \delta(x\text{-}b_-)\right](M_x + m_x) \\
&= T\,\delta(x\text{-}h) + m e_m g\, \delta(x\text{-}c)\left[\cos\theta - \phi \sin\theta\right] \\
&+ m e_m \delta(x\text{-}c)\,(v_{tt} - 2\dot{\theta}w_t - \dot{\theta}^2 v - \ddot{\theta}w)\sin\delta_m \\
&- m e_m \delta(x\text{-}c)\,(w_{tt} + 2\dot{\theta}v_t - \dot{\theta}^2 w + \ddot{\theta}v)\cos\delta_m
\end{aligned}
\tag{4.3}
$$

The subscripts x and t on displacements v and w and on the torsional deformation ϕ represent partial derivatives with respect to x and t, respectively.

At the crack location, $x = b_- = b - \frac{\epsilon}{2}$ and $x = b_+ = b + \frac{\epsilon}{2}$, the generalized moments including torsional effect are

$$\underline{F} = (M_\zeta, M_\eta, M_X)^T$$
$$\underline{f} = (m_\zeta, m_\eta, m_X)^T \tag{4.4}$$

The transition conditions are derived by the same approach as for transverse deformation (see eqs. 2.3 - 2.9). Based on equation (2.4) and equation (2.5),

$$\Delta \underline{u}(b) = \epsilon \, S \, \underline{F}$$

$$\phi\,(b_+,t) - \phi\,(b_-,t) = \epsilon \, \frac{M_X}{GJ} \tag{4.5}$$

and the time derivatives satisfy

$$\Delta \underline{u}_t(b) = \epsilon \, \frac{S}{d_i} \, \underline{f}$$

$$\phi_t\,(b_+,t) - \phi_t\,(b_-,t) = \epsilon \, \frac{m_X}{d_i GJ} \tag{4.6}$$

The complete transition conditions at the crack location for an open crack at time t for this case are

$$\underline{P}\,(b_-) = \underline{P}\,(b_+)$$
$$\underline{P}\,(b_+) = K\left[\, \Delta \underline{u}(b) + d_i \, \Delta \underline{u}_t(b) \,\right] \tag{4.7}$$

where

$$\underline{P} = \begin{bmatrix} EI_1(v_{xx} + d_i\, v_{txx}) \\ EI_2(w_{xx} + d_i\, w_{txx}) \\ GJ(\phi_x + d_i\, \phi_{tx}) \end{bmatrix}, \quad K = \begin{bmatrix} k_{44} & 0 & 0 \\ 0 & k_{55} & 0 \\ 0 & 0 & k_{66} \end{bmatrix} \tag{4.8}$$

As a result, the final transition conditions become

$$M_\zeta + m_\zeta = c_{44} \frac{(EI_1)^2}{\epsilon} (v_{xx} + d_i\, v_{txx}) \Big/_{x=b}$$

$$M\eta + m_\eta = -c_{55} \frac{(EI_2)^2}{\epsilon} (w_{xx} + d_i\, w_{txx}) \Big/_{x=b}$$

$$M_X + m_X = c_{66} \frac{(GJ)^2}{\epsilon} (\phi_x + d_i\, \phi_{tx}) \Big/_{x=b} \tag{4.9}$$

The compliance c_{66}, like c_{44} and c_{55}, is the reciprocal of the stiffness coefficient k_{66}. The value of c_{66} can also be determined from the graph of Papadopoulos and Dimarogonas[27].

Now the equations of motion become

$$EI_1 v_{xxxx} + [\mu + m\delta(x-c)]\left[v_{tt} - 2\dot{\theta}w_t - \dot{\theta}^2 v - \ddot{\theta}w\right]$$

$$+ d_e\, \mu\, (v_t - \dot{\theta}w) + EI_1\, d_i\, v_{txxxx} + (1-\Lambda)\, d_c\, \mu\, (v_t - \dot{\theta}w)\, \delta(x-b)$$

$$+ \Lambda\left[\delta'(x-b_+) - \delta'(x-b_-)\right] c_{44} \frac{(EI_1)^2}{\epsilon} (v_{xx} + d_i\, v_{txx}) \Big/_{x=b}$$

$$= [\mu + m\delta(x-c)]\, g \sin\theta + m\, e_m\, \delta(x-c)\, (\dot{\theta}^2 + 2\dot{\theta}\phi_t + \ddot{\theta}\phi)\, \cos\delta_m$$

$$+ \quad m\, e_m\, \delta(x\text{-}c)\, (\ \ddot{\theta} + \phi_{tt} - \dot{\theta}^2 \phi\ )\, \sin \delta_m \tag{4.10}$$

$$\Gamma EI_1 w_{xxxx} \ + \ \left[\mu \ + \ m\delta(x\text{-}c)\right]\left[w_{tt} + 2\dot{\theta} v_t - \dot{\theta}^2 w + \ddot{\theta} v\right]$$

$$+ \ d_e\, \mu\, (w_t + \dot{\theta} v) \ + \ \Gamma EI_1\, d_i\, w_{txxxx} + (1\text{-}\Lambda)\, d_c\, \mu\, (w_t + \dot{\theta} v)\, \delta(x\text{-}b)$$

$$+ \ \Lambda\left[\delta'(x\text{-}b_+) - \delta'(x\text{-}b_-)\right] c_{55} \frac{(EI_2)^2}{\epsilon} (w_{xx} + d_i\, w_{txx}) \ \Big/_{x=b}$$

$$= \left[\mu \ + \ m\, \delta(x\text{-}c)\right] g \cos \theta \ + \ m\, e_m\, \delta(x\text{-}c)\, (\ \dot{\theta}^2 + 2\dot{\theta}\phi_t + \ddot{\theta}\phi\ )\, \sin \delta_m$$

$$- \ m\, e_m\, \delta(x\text{-}c)\, (\ \ddot{\theta} + \phi_{tt} - \dot{\theta}^2 \phi\ )\, \cos \delta_m \tag{4.11}$$

$$Ip\, \delta(x\text{-}c)\, (\ \ddot{\theta} + \phi_{tt}\ ) \ + \ \mu\, (\ r_1^2 \ + \ r_2^2\ )\, (\ \ddot{\theta} + \ \phi_{tt}\ )$$

$$- \ GJ\, (\ \phi_{xx} \ + \ d_i\, \phi_{txx}\ ) + \ d_T\, \mu\, (\ r_1^2 \ + \ r_2^2\ )\, (\ \dot{\theta} + \ \phi_t\ )$$

$$- \ \Lambda\ \left[\ \delta(x\text{-}b_+) - \delta(x\text{-}b_-)\ \right]\ c_{66} \frac{(GJ)^2}{\epsilon} (\phi_x + d_i\, \phi_{tx}) \ \Big/_{x=b}$$

$$= T\, \delta(x\text{-}h) \ + \ m\, e_m\, g\, \delta(x\text{-}c) \left[\ \cos \theta - \phi \sin \theta\ \right]$$

$$+ \ m\, e_m\, \delta(x\text{-}c)\, (\ v_{tt} \ - \ 2\dot{\theta} w_t - \dot{\theta}^2 v - \ddot{\theta} w\ )\, \sin \delta_m$$

$$- \; m\, e_m\, \delta(x-c)\, (\, w_{tt} \,+\, 2\dot{\theta} v_t - \dot{\theta}^2 w + \ddot{\theta} v \,)\, \cos \delta_m \tag{4.12}$$

2.3. Solution

In this second part of the study, the shaft and the disk are assumed to be circular with R_d the radius of the disk and r_s the radius of the shaft. So pure torsion (Saint-Venant's torsion) can be assumed, in which a cross-sectional plane remains plane during torsional motion. In other words, in pure torsion there is no warping.

It is assumed that the beam is fixed at one end (x=0) and free at the other end (x=L) with respect to torsion, so the torsional deformation at the fixed end can be defined as zero and the torsional moment at the free end is assumed to be zero. As a result, the boundary conditions become

$$\begin{aligned} &v(0,t) = w(0,t) = v(L,t) = w(L,t) = 0 \\ &EI_1\, v_{xx}(0,t) = EI_2\, w_{xx}(0,t) = 0,\; EI_1\, v_{xx}(L,t) = EI_2\, w_{xx}(L,t) = 0 \\ &\phi(0,t) = 0,\; \phi_x(L,t) = 0 \end{aligned} \tag{4.13}$$

In order to satisfy the boundary conditions, the approximation solutions can be chosen as follows:

$$v(x,t) = \sum_{k=1}^{N} v_k(t) \sin \frac{k\pi x}{L}$$

$$w(x,t) = \sum_{k=1}^{N} w_k(t) \sin \frac{k\pi x}{L}$$

$$\phi(x,t) = \sum_{k=1}^{N} \phi_k(t) \sin \frac{(2k-1)\pi x}{2L} \tag{4.14}$$

The quantities v_k, w_k, and ϕ_k are functions of time, and the sines are the assumed spatial functions.

Analogous with equation (2.18) and equation (2.19), by using the aproximate solutions, multiplying with $\sin \frac{n\pi x}{L}$ and integrating over the length of shaft, equation (4.10) and equation (4.11) become

$$EI_1 v_n \frac{L}{2} \left(\frac{n\pi}{L}\right)^4 + \mu \ddot{v}_n \frac{L}{2} - 2\dot{\theta} \mu \dot{w}_n \frac{L}{2} - \mu \dot{\theta}^2 v_n \frac{L}{2} - \mu \ddot{\theta} w_n \frac{L}{2}$$

$$+ m \sin \frac{n\pi c}{L} \sum_{k=1}^{N} \ddot{v}_k \sin \frac{k\pi c}{L} - 2\dot{\theta} m \sin \frac{n\pi c}{L} \sum_{k=1}^{N} \dot{w}_k \sin \frac{k\pi c}{L}$$

$$- \dot{\theta}^2 m \sin \frac{n\pi c}{L} \sum_{k=1}^{N} v_k \sin \frac{k\pi c}{L} - m \ddot{\theta} \sin \frac{n\pi c}{L} \sum_{k=1}^{N} w_k \sin \frac{k\pi c}{L}$$

$$+ d_e \mu \dot{v}_n \frac{L}{2} - d_e \mu \dot{\theta} w_n \frac{L}{2} + EI_1 d_i \dot{v}_n \left(\frac{n\pi}{L}\right)^4 \frac{L}{2}$$

$$+ (1-\Lambda) d_c \mu \sin \frac{n\pi b}{L} \left[\sum_{k=1}^{N} \dot{v}_k \sin \frac{k\pi b}{L} - \dot{\theta} \sum_{k=1}^{N} w_k \sin \frac{k\pi b}{L} \right]$$

$$- \Lambda c_{44} (EI_1)^2 \left(\frac{n\pi}{L}\right)^2 \sin \frac{n\pi b}{L} \sum_{k=1}^{N} (v_k + d_i \dot{v}_k) \left(\frac{k\pi}{L}\right)^2 \sin \frac{k\pi b}{L}$$

$$= \mu g \sin \theta \frac{L}{n\pi} (1-(-1)^n) + mg \sin \theta \sin \frac{n\pi c}{L}$$

$$+ m e_m \left[\dot{\theta}^2 \cos \delta_m + \ddot{\theta} \sin \delta_m\right] \sin \frac{n\pi c}{L}$$

$$+ m e_m \sin \frac{n\pi c}{L} \sum_{k=1}^{N} (2\dot{\theta}\dot{\phi}_k + \ddot{\theta}\phi_k) \cos \delta_m \sin \frac{(2k-1)\pi c}{2L}$$

$$+ \; m\, e_m \, \sin\frac{n\pi c}{L} \sum_{k=1}^{N} \left(\ddot{\phi}_k - \dot{\theta}^2 \phi_k \right) \sin \delta_m \, \sin\frac{(2k-1)\pi c}{2L} \qquad (4.15)$$

$$EI_2 \, w_n \frac{L}{2} \left(\frac{n\pi}{L}\right)^4 + \mu \, \ddot{w}_n \frac{L}{2} + 2\,\dot{\theta}\,\mu\,\dot{v}_n \frac{L}{2} - \mu\,\dot{\theta}^2 \, w_n \frac{L}{2} + \mu\,\ddot{\theta}\, v_n \frac{L}{2}$$

$$+ \; m \, \sin\frac{n\pi c}{L} \sum_{k=1}^{N} \ddot{w}_k \sin\frac{k\pi c}{L} + 2\,\dot{\theta}\, m \, \sin\frac{n\pi c}{L} \sum_{k=1}^{N} \dot{v}_k \sin\frac{k\pi c}{L}$$

$$- \dot{\theta}^2 \, m \, \sin\frac{n\pi c}{L} \sum_{k=1}^{N} w_k \sin\frac{k\pi c}{L} + m\,\ddot{\theta} \, \sin\frac{n\pi c}{L} \sum_{k=1}^{N} v_k \sin\frac{k\pi c}{L}$$

$$+ d_e \, \mu \, \dot{w}_n \frac{L}{2} + d_e \, \mu \, \dot{\theta} \, v_n \frac{L}{2} + EI_2 \, d_i \, \dot{w}_n \left(\frac{n\pi}{L}\right)^4 \frac{L}{2}$$

$$+ (1-\Lambda)\, d_c \, \mu \, \sin\frac{n\pi b}{L} \left[\sum_{k=1}^{N} \dot{w}_k \, \sin\frac{k\pi b}{L} + \dot{\theta} \sum_{k=1}^{N} v_k \, \sin\frac{k\pi b}{L} \right]$$

$$- \Lambda \, c_{55} \, (EI_2)^2 \left(\frac{n\pi}{L}\right)^2 \sin\frac{n\pi b}{L} \sum_{k=1}^{N} \left(w_k + d_i \, \dot{w}_k \right) \left(\frac{k\pi}{L}\right)^2 \sin\frac{k\pi b}{L}$$

$$= \mu \, g \cos\theta \, \frac{L}{n\pi} \left(1-(-1)^n\right) + mg \cos\theta \, \sin\frac{n\pi c}{L}$$

$$+ \; m \, e_m \left[\dot{\theta}^2 \sin\delta_m - \ddot{\theta} \cos\delta_m \right] \sin\frac{n\pi c}{L}$$

$$+ \; m \, e_m \, \sin\frac{n\pi c}{L} \sum_{k=1}^{N} \left(2\dot{\theta}\dot{\phi}_k + \ddot{\theta}\phi_k \right) \sin\delta_m \, \sin\frac{(2k-1)\pi c}{2L}$$

$$- \; m \, e_m \, \sin\frac{n\pi c}{L} \sum_{k=1}^{N} \left(\ddot{\phi}_k - \dot{\theta}^2 \phi_k \right) \cos\delta_m \, \sin\frac{(2k-1)\pi c}{2L} \qquad (4.16)$$

Using the approximate solutions, equation (4.12) becomes

$$
\begin{aligned}
&I_p\,\delta(x-c)\left(\ddot{\theta}+\sum_{k=1}^{N}\ddot{\phi}_k\,\sin\frac{(2k-1)\pi x}{2L}\right)\\
&+\mu\left(r_1^2+r_2^2\right)\left(\ddot{\theta}+\sum_{k=1}^{N}\ddot{\phi}_k\,\sin\frac{(2k-1)\pi x}{2L}\right)\\
&+GJ\sum_{k=1}^{N}\phi_k\,\frac{(2k-1)^2\pi^2}{4L^2}\,\sin\frac{(2k-1)\pi x}{2L}\\
&+GJ\,d_i\,\dot{\phi}_k\,\frac{(2k-1)^2\pi^2}{4L^2}\,\sin\frac{(2k-1)\pi x}{2L}\\
&+d_T\,\mu\left(r_1^2+r_2^2\right)\left(\dot{\theta}+\sum_{k=1}^{N}\dot{\phi}_k\,\sin\frac{(2k-1)\pi x}{2L}\right)\\
&-\Lambda\left[\delta(x-b_+)-\delta(x-b_-)\right]c_{66}\frac{(GJ)^2}{\epsilon}\\
&\sum_{k=1}^{N}\left[\phi_k\,\frac{(2k-1)\pi}{2L}\,\cos\frac{(2k-1)\pi b}{2L}+d_i\,\dot{\phi}_k\,\frac{(2k-1)\pi}{2L}\,\cos\frac{(2k-1)\pi b}{2L}\right]\\
&=T\,\delta(x-h)+m\,e_m\,g\,\delta(x-c)\,\cos(\theta+\delta_m)\\
&-m\,e_m\,g\,\delta(x-c)\sum_{k=1}^{N}\phi_k\,\sin\frac{(2k-1)\pi x}{2L}\sin(\theta+\delta_m)\\
&+m\,e_m\,\delta(x-c)\sin\delta_m\left(\sum_{k=1}^{N}\ddot{v}_k\,\sin\frac{k\pi x}{L}-2\dot{\theta}\sum_{k=1}^{N}\dot{w}_k\,\sin\frac{k\pi x}{L}\right.\\
&\left.-\dot{\theta}^2\sum_{k=1}^{N}v_k\,\sin\frac{k\pi x}{L}-\ddot{\theta}\sum_{k=1}^{N}w_k\,\sin\frac{k\pi x}{L}\right)\\
&-m\,e_m\,\delta(x-c)\cos\delta_m\left(\sum_{k=1}^{N}\ddot{w}_k\,\sin\frac{k\pi x}{L}+2\dot{\theta}\sum_{k=1}^{N}\dot{v}_k\,\sin\frac{k\pi x}{L}\right.\\
&\left.-\dot{\theta}^2\sum_{k=1}^{N}w_k\,\sin\frac{k\pi x}{L}+\ddot{\theta}\sum_{k=1}^{N}v_k\,\sin\frac{k\pi x}{L}\right)
\end{aligned}
\tag{4.17}
$$

Equation (4.17) is multiplied by $\sin \frac{(2n-1)\pi x}{2L}$ and integrated over the length of the shaft, and the following formulas are used:

$$\int_0^L \sin \frac{(2k-1)\pi x}{2L} \sin \frac{(2n-1)\pi x}{2L} \, dx = \begin{cases} 0 & \text{if } k \neq n \\ \frac{L}{2} & \text{if } k = n \end{cases}$$

$$\int_0^L \sin \frac{(2n-1)\pi x}{2L} \, dx = \frac{2L}{(2n-1)\pi}$$

$$\int_0^L \left[\delta(x-b_+) - \delta(x-b_-) \right] \sin \frac{(2n-1)\pi x}{2L} \, dx$$

$$= \sin \frac{(2n-1)\pi b_+}{2L} - \sin \frac{(2n-1)\pi b_-}{2L}$$

$$= 2 \cos \frac{(2n-1)\pi b}{2L} \sin \frac{1}{2} \frac{(2n-1)\pi \epsilon}{2L}$$

$$= 2 \cos \frac{(2n-1)\pi b}{2L} * \frac{1}{2} \frac{(2n-1)\pi \epsilon}{2L}$$

$$= \frac{(2n-1)\pi \epsilon}{2L} \cos \frac{(2n-1)\pi b}{2L} \qquad (4.18)$$

Then equation (4.17) becomes

$$I_p \sin \frac{(2n-1)\pi x}{2L} \left[\ddot{\theta} + \sum_{k=1}^{N} \ddot{\phi}_k \sin \frac{(2k-1)\pi x}{2L} \right]$$

$$+ \mu \left(r_1^2 + r_2^2 \right) \left[\ddot{\theta} \frac{2L}{(2n-1)\pi} + \frac{L}{2} \ddot{\phi}_n \right]$$

$$+ \; GJ \; \frac{(2n-1)^2\pi^2}{8L} \; (\; \phi_n + d_i \dot{\phi}_n \;)$$

$$+ \; d_T \; \mu \; (\; r_1^2 + r_2^2 \;) \; (\; \dot{\theta} \; \frac{2L}{(2n-1)\pi} + \frac{L}{2} \dot{\phi}_n \;)$$

$$- \; \Lambda \; c_{66} \, (GJ)^2 \; \frac{(2n-1)\pi}{2L} \sum_{k=1}^{N} \frac{(2k-1)\pi}{2L} \, (\phi_k + d_i \dot{\phi}_k) \cos \frac{(2k-1)\pi b}{2L} \cos \frac{(2n-1)\pi b}{2L}$$

$$= T \; \sin \frac{(2n-1)\pi h}{2L} \; + \; m \; e_m \; g \cos \theta \; \sin \frac{(2n-1)\pi c}{2L}$$

$$- \; m \; e_m \; g \sum_{k=1}^{N} \phi_k \; \sin \theta \sin \frac{(2k-1)\pi c}{2L} \; \sin \frac{(2n-1)\pi c}{2L}$$

$$+ \; m \; e_m \sin \delta_m \sin \frac{(2n-1)\pi c}{2L} \sum_{k=1}^{N} (\ddot{v}_k \; - 2\dot{\theta}\dot{w}_k - \dot{\theta}^2 \, v_k - \ddot{\theta} \; w_k \;) \sin \frac{k\pi c}{2L}$$

$$- \; m \; e_m \cos \delta_m \sin \frac{(2n-1)\pi c}{2L} \sum_{k=1}^{N} (\ddot{w}_k \; + 2\dot{\theta}\dot{v}_k - \dot{\theta}^2 \, w_k + \ddot{\theta} \; w_k) \sin \frac{k\pi c}{2L} \qquad (4.19)$$

In this study, some assumptions are used, i.e.:

1. The external torque (T) is zero.

2. The shaft and the disk are circular: $\Gamma = 1$.

3. Poisson's ratio (ν) of the shaft is 0.3.

Also, some formulas that are used are as follows:

- Shear modulus of the shaft : $G = \frac{E}{2(1+\nu)}$

- Torsional constant of the shaft : $J = \frac{\pi \; r_S^4}{2}$

- Moments of inertia of the shaft : $I_1 = I_2 = \frac{\pi \; r_S^4}{4}$

- Radii of gyration of the shaft : $r_1 = r_2 = \sqrt{\frac{I_1}{A}} = \frac{1}{2} r_s$

- Polar mass moment of inertia of the disk : $I_p = \frac{m R_d^2}{2}$

Based on the above formulas, equation (4.19) can be written as follows:

$$\frac{m R_d^2}{2} \sin\frac{(2n-1)\pi c}{2L} \left[\ddot{\theta} + \sum_{k=1}^{N} \ddot{\phi}_k \sin\frac{(2k-1)\pi c}{2L} \right]$$

$$+ \mu \frac{r_s^2}{2} \left[\ddot{\theta} \frac{2L}{(2n-1)\pi} + \frac{L}{2} \ddot{\phi}_n \right]$$

$$+ \frac{E}{2(1+\nu)} \frac{\pi r_s^4}{2} \frac{(2n-1)^2\pi^2}{8L} (\phi_n + d_i \dot{\phi}_n)$$

$$+ d_T \mu \frac{r_s^2}{2} \left[\dot{\theta} \frac{2L}{(2n-1)\pi} + \frac{L}{2} \dot{\phi}_n \right]$$

$$- \Lambda c_{66} \left[\frac{E}{2(1+\nu)} \frac{\pi r_s^4}{2} \right]^2 \frac{(2n-1)\pi}{2L} \cos\frac{(2n-1)\pi b}{2L}$$

$$\sum_{k=1}^{N} \frac{(2k-1)\pi}{2L} (\phi_k + d_i \dot{\phi}_k) \cos\frac{(2k-1)\pi b}{2L}$$

$$= m e_m g \cos\theta \sin\frac{(2n-1)\pi c}{2L}$$

$$- m e_m g \sin\theta \sum_{k=1}^{N} \phi_k \sin\frac{(2k-1)\pi c}{2L} \sin\frac{(2n-1)\pi c}{2L}$$

$$+ m e_m \sin\delta_m \sin\frac{(2n-1)\pi c}{2L} \sum_{k=1}^{N} (\ddot{v}_k - 2\dot{\theta}\dot{w}_k - \dot{\theta}^2 v_k - \ddot{\theta} w_k) \sin\frac{k\pi c}{2L}$$

$$- m e_m \cos\delta_m \sin\frac{(2n-1)\pi c}{2L} \sum_{k=1}^{N} (\ddot{w}_k + 2\dot{\theta}\dot{v}_k - \dot{\theta}^2 w_k + \ddot{\theta} w_k) \sin\frac{k\pi c}{2L} \quad (4.20)$$

To put the equations into non-dimensionalized form, equation (2.20) and the following non-dimensionalized quantities are used:

$$\tilde{R}_d = \frac{R_d}{L}\,,\quad \tilde{r}_s = \frac{r_s}{L}$$

$$\tilde{d}_T = \frac{L^2}{\pi^2}\sqrt{\frac{\mu}{EI_1}}\,d_T$$

$$\tilde{c}_{66} = \frac{E\,r_s^3}{4\pi\,(1+\nu)^2}\,c_{66}$$

$$\nu_k = \frac{(2k-1)\pi b}{2L} = \frac{(2k-1)\pi}{2}\,\tilde{b}\,,\quad \beta_k = \frac{(2k-1)\pi c}{2L} = \frac{(2k-1)\pi}{2}\,\tilde{c} \qquad (4.21)$$

Then equation (4.15), equation (4.16), and equation (4.20) become

$$\ddot{\tilde{v}}_n + \tilde{m}\sin\alpha_n \sum_{k=1}^{N} \ddot{\tilde{v}}_k \sin\alpha_k - \tilde{m}\,\tilde{e}_m \sin\alpha_n \sin\delta_m \sum_{k=1}^{N} \ddot{\phi}_k \sin\beta_k$$

$$= -\,n^4\,\tilde{v}_n + 2\Omega\dot{\tilde{w}}_n + \Omega^2\tilde{v}_n + \lambda\tilde{w}_n$$

$$+\ \tilde{m}\sin\alpha_n \sum_{k=1}^{N}\left(2\Omega\dot{\tilde{w}}_k + \Omega^2\tilde{v}_k + \lambda\tilde{w}_k\right)\sin\alpha_k$$

$$-\,\tilde{d}_e\,(\dot{\tilde{v}}_n - \Omega\tilde{w}_n) - \tilde{d}_i\,\dot{\tilde{v}}_n\,n^4$$

$$-\,(1-\Lambda)\,\tilde{d}_c \sin\gamma_n \sum_{k=1}^{N}(\dot{\tilde{v}}_k - \Omega\tilde{w}_k)\sin\gamma_k$$

$$+\ 2\Lambda\tilde{c}_{44}\,n^2 \sin\gamma_n \sum_{k=1}^{N} k^2\,(\tilde{v}_k + \tilde{d}_i\dot{\tilde{v}}_k)\sin\gamma_k$$

$$+\left[\frac{(1-(-1)^n)}{n} + \tilde{m}\frac{\pi}{2}\sin\alpha_n\right]\tilde{\mu}\sin\theta$$

$$+ \tilde{m}\,\tilde{e}_m \sin\alpha_n\left[\Omega^2\cos\delta_m + \lambda\sin\delta_m\right]$$

$$+ \tilde{m}\,\tilde{e}_m \sin\alpha_n \cos\delta_m \sum_{k=1}^{N}\left(2\Omega\dot{\phi}_k + \lambda\phi_k\right)\sin\beta_k$$

$$- \tilde{m}\,\tilde{e}_m\,\Omega^2 \sin\alpha_n \sin\delta_m \sum_{k=1}^{N}\phi_k \sin\beta_k \qquad (4.22)$$

$$\ddot{\tilde{w}}_n + \tilde{m}\sin\alpha_n \sum_{k=1}^{N}\ddot{\tilde{w}}_k \sin\alpha_k + \tilde{m}\,\tilde{e}_m \sin\alpha_n \cos\delta_m \sum_{k=1}^{N}\ddot{\phi}_k \sin\beta_k$$

$$= -\Gamma n^4\tilde{w}_n - 2\Omega\dot{\tilde{v}}_n + \Omega^2\tilde{w}_n - \lambda\tilde{v}_n$$

$$- \tilde{m}\sin\alpha_n \sum_{k=1}^{N}\left(2\Omega\dot{\tilde{v}}_k - \Omega^2\tilde{w}_k + \lambda\tilde{v}_k\right)\sin\alpha_k$$

$$- \tilde{d}_e\left(\dot{\tilde{w}}_n + \Omega\tilde{v}_n\right) - \Gamma\,\tilde{d}_i\,\dot{\tilde{w}}_n\,n^4$$

$$- (1-\Lambda)\,\tilde{d}_c \sin\gamma_n \sum_{k=1}^{N}\left(\dot{\tilde{w}}_k + \Omega\tilde{v}_k\right)\sin\gamma_k$$

$$+ 2\Gamma^2\Lambda\tilde{c}_{55}\,n^2 \sin\gamma_n \sum_{k=1}^{N} k^2\left(\tilde{w}_k + \tilde{d}_i\dot{\tilde{w}}_k\right)\sin\gamma_k$$

$$+ \left[\frac{(1-(-1)^n)}{n} + \tilde{m}\frac{\pi}{2}\sin\alpha_n\right]\tilde{\mu}\cos\theta$$

$$+ \tilde{m}\,\tilde{e}_m \sin\alpha_n\left[\Omega^2\sin\delta_m - \lambda\cos\delta_m\right]$$

$$+ \tilde{m}\,\tilde{e}_m \sin\alpha_n \sin\delta_m \sum_{k=1}^{N} (2\Omega\dot{\phi}_k + \lambda\phi_k) \sin\beta_k$$

$$+ \tilde{m}\,\tilde{e}_m\,\Omega^2 \sin\alpha_n \cos\delta_m \sum_{k=1}^{N} \phi_k \sin\beta_k \qquad (4.23)$$

$$\tilde{m}\,\tilde{R}_d^{\,2} \sin\beta_n \sum_{k=1}^{N} \ddot{\phi}_k \sin\beta_k + \tilde{r}_S^{\,2}\,\ddot{\phi}_n$$

$$- 2\,\tilde{m}\,\tilde{e}_m \sin\delta_m \sin\beta_n \sum_{k=1}^{N} \ddot{\tilde{v}}_k \sin\alpha_k$$

$$+ 2\,\tilde{m}\,\tilde{e}_m \cos\delta_m \sin\beta_n \sum_{k=1}^{N} \ddot{\tilde{w}}_k \sin\alpha_k$$

$$= - \tilde{m}\,\tilde{R}_d^{\,2}\,\lambda \sin\beta_n - \frac{4}{(2n-1)\pi}\,\tilde{r}_S^{\,2}\,\lambda$$

$$- \frac{(2n-1)^2}{2\pi^2\,(1+\nu)} (\phi_n + d_i\,\dot{\phi}_n)$$

$$- \frac{4}{(2n-1)\pi}\,\tilde{d}_T\,\tilde{r}_S^{\,2}\,\Omega - \tilde{d}_T\,\tilde{r}_S^{\,2}\,\dot{\phi}_n$$

$$+ \Lambda\,\tilde{c}_{66}\,\tilde{r}_S\,(2n-1)\cos\nu_n \sum_{k=1}^{N} (2k-1)\,(\phi_k + \tilde{d}_i\,\dot{\phi}_k)\cos\nu_k$$

$$+ \pi\,\tilde{m}\,\tilde{e}_m\,\tilde{\mu}\cos\theta \sin\beta_n$$

$$- \pi\,\tilde{m}\,\tilde{e}_m\,\tilde{\mu}\,\sin\theta \sin\beta_n \sum_{k=1}^{N} \phi_k \sin\beta_k$$

$$- 2\,\tilde{m}\,\tilde{e}_m \sin\delta_m \sin\beta_n \sum_{k=1}^{N} (2\Omega\dot{\tilde{w}}_k + \Omega^2\,\tilde{v}_k + \lambda\tilde{w}_k) \sin\alpha_k$$

$$- 2\,\tilde{m}\,\tilde{e}_m \cos\delta_m \sin\beta_n \sum_{k=1}^{N} (2\Omega\dot{\tilde{v}}_k - \Omega^2\,\tilde{w}_k + \lambda\tilde{v}_k\,) \sin\alpha_k \qquad (4.24)$$

To solve these equations, the same approach is used as in chapter 2. The relations to transform this second order system of equations to a first order system are

$$y_{3n-2} = \tilde{v}_n\,,\ \dot{y}_{3n-2} = \frac{d\tilde{v}_n}{d\tau}\,,\ y_{3n-1} = \tilde{w}_n\,,\ \dot{y}_{3n-1} = \frac{d\tilde{w}_n}{d\tau}\,,$$

$$y_{3n} = \tilde{\phi}_n\,,\ \dot{y}_{3n} = \frac{d\tilde{\phi}_n}{d\tau}\,,\ y_{M+3n-2} = \frac{d\tilde{v}_n}{d\tau}\,,\ \dot{y}_{M+3n-2} = \frac{d^2\tilde{v}_n}{d\tau^2}\,,$$

$$y_{M+3n-1} = \frac{d\tilde{w}_n}{d\tau}\,,\ \dot{y}_{M+3n-1} = \frac{d^2\tilde{w}_n}{d\tau^2}\,,\ y_{M+3n} = \frac{d\tilde{\phi}_n}{d\tau}\,,\ \dot{y}_{M+3n} = \frac{d^2\tilde{\phi}_n}{d\tau^2}\,. \qquad (4.25)$$

Therefore,

$$\dot{y}_{3n-2} = y_{M+3n-2}\,,\ \dot{y}_{3n-1} = y_{M+3n-1}\,,\ \dot{y}_{3n} = y_{M+3n}$$

where $M = 3N$

N = the highest mode considered

n = the number of the mode corresponding to the equations, ranging between 1 and N

Then equations (4.22), (4.23), and (4.24) can also be written in the form

$$A\,\dot{y} = F(t,y) \qquad (4.26)$$

where A is a constant matrix of order 3M x 3M, y is a vector of order 3M, and F(t,y) is a vector of order 3M. The DIVPAG subroutine for IBM/PC is used to

solve these equations.

Chapter 5
Results of Flexural - Torsional Response

5.1. Introduction

The parameters for the standard case of flexural-torsional response, basically, are the same as those for the standard case of flexural response (see section 3.1). However, there are some additional parameters for computing the flexural-torsional response, which are the torsional external damping $\tilde{d}_T$ and the compliance $\tilde{c}_{66}$. For the standard case, the torsional external damping $\tilde{d}_T$ is assumed to be zero. The compliance $\tilde{c}_{66}$, like the compliances $\tilde{c}_{44}$ and $\tilde{c}_{55}$, is also calculated based on the work of Papadopoulos and Dimarogonas[27]. The dimensional compliance c_{66} is determined as follows:

$$c_{66} = \frac{(1-\nu^2)\,\overline{c}_{66}}{\pi\, E\, r_S^3} \tag{5.1}$$

and the non-dimensionalized compliance $\tilde{c}_{66}$ becomes

$$\tilde{c}_{66} = \frac{E\, r_S^3\, c_{66}}{4\pi(1+\nu)^2} = \frac{(1-\nu)\,\overline{c}_{66}}{4\pi^2\,(1+\nu)} \tag{5.2}$$

Based on the relative crack depth for the standard case (a/D=0.2), the non-dimensionalized compliance $\tilde{c}_{66}$ is 0.00156.

In this chapter, the influence of acceleration, deceleration, and different parameters is investigated. Also, the cases of linear acceleration and linear deceleration are compared to the cases of exponential acceleration and exponential deceleration. The different types of lines are still used to show the breathing crack in the time histories, i.e., a solid line for a closed crack and a dashed line for an open crack.

5.2. Convergency

The time histories of the z-displacement and the ϕ-torsional deformation for the standard case at the location $\tilde{x}$=0.7 are shown in Fig. 5.1.a and Fig. 5.1.b, respectively. The time related to the maximum z-displacement in the z-time histories is called τ_{max} and the maximum z-displacement is called z_{max}. Also, for the ϕ-time histories, ϕ_{max} is the maximum ϕ-torsional deformation, including the transient response, in this case, and the time related to ϕ_{max} is called τ_{max}. τ_{crit} is the time when the angular velocity passes the critical speed.

The influence of each term (mode) in the approximate solutions is given in Fig. 5.2.a-j with solid lines. From those figures, it can be concluded that the first mode is the most dominant for the z-displacement as well as the ϕ-torsional deformation. The contribution of the other modes is very small, only less than $\frac{1}{100}$ of that of the first mode. The odd modes of the z-time history have similar characteristics and give more contribution than the even modes. All of the modes of the ϕ-time histories have similar characteristics except differences in sign. Higher modes give smaller contributions in both the z-time history and the ϕ-time history.

Table 5.1 gives a comparison of values using different total numbers of

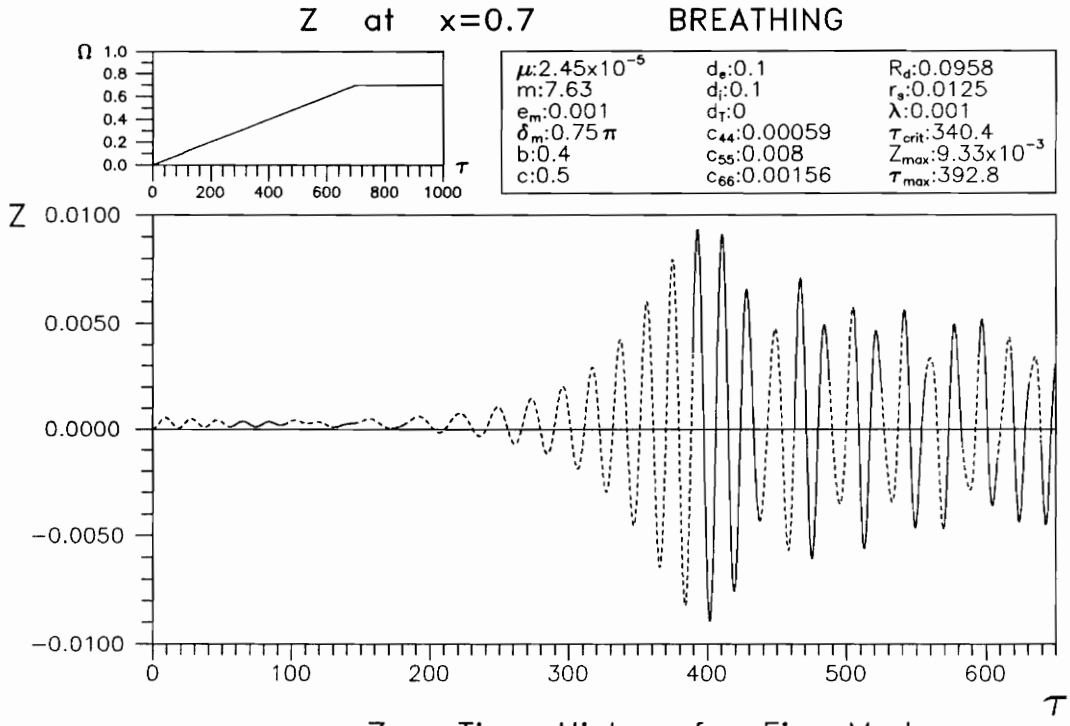

a. Z – Time History for Five Modes

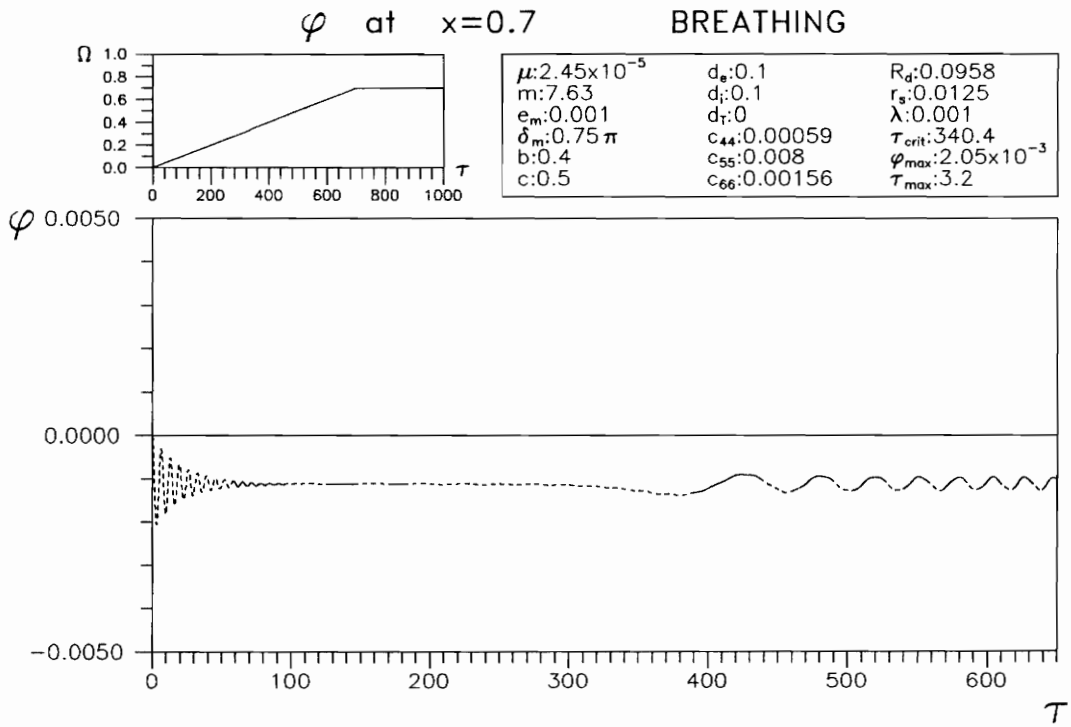

b. φ – Time History for Five Modes

Fig. 5.1 Time History for Five Modes

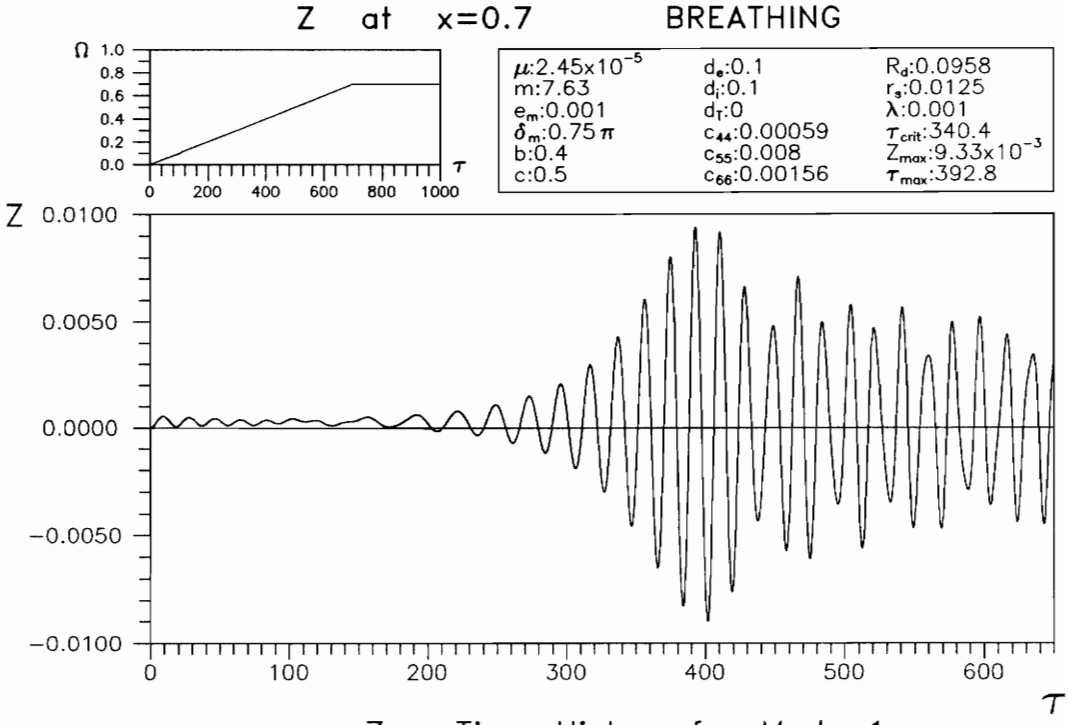

a. Z – Time History for Mode 1

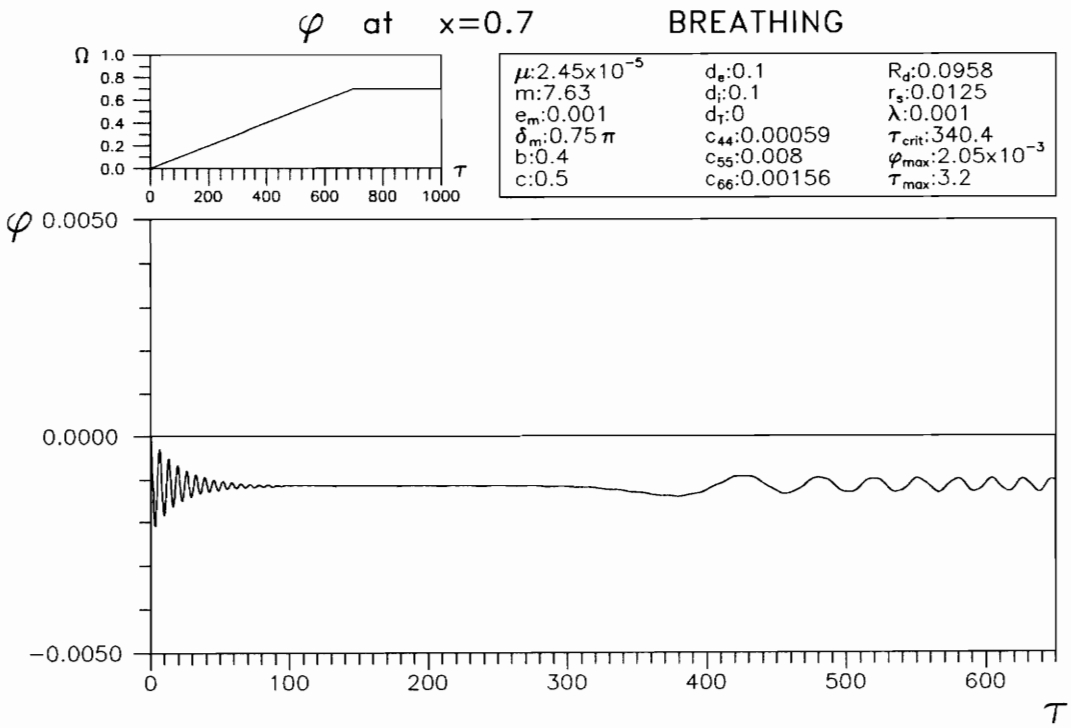

b. φ – Time History for Mode 1

Fig. 5.2 Time History for Each Mode

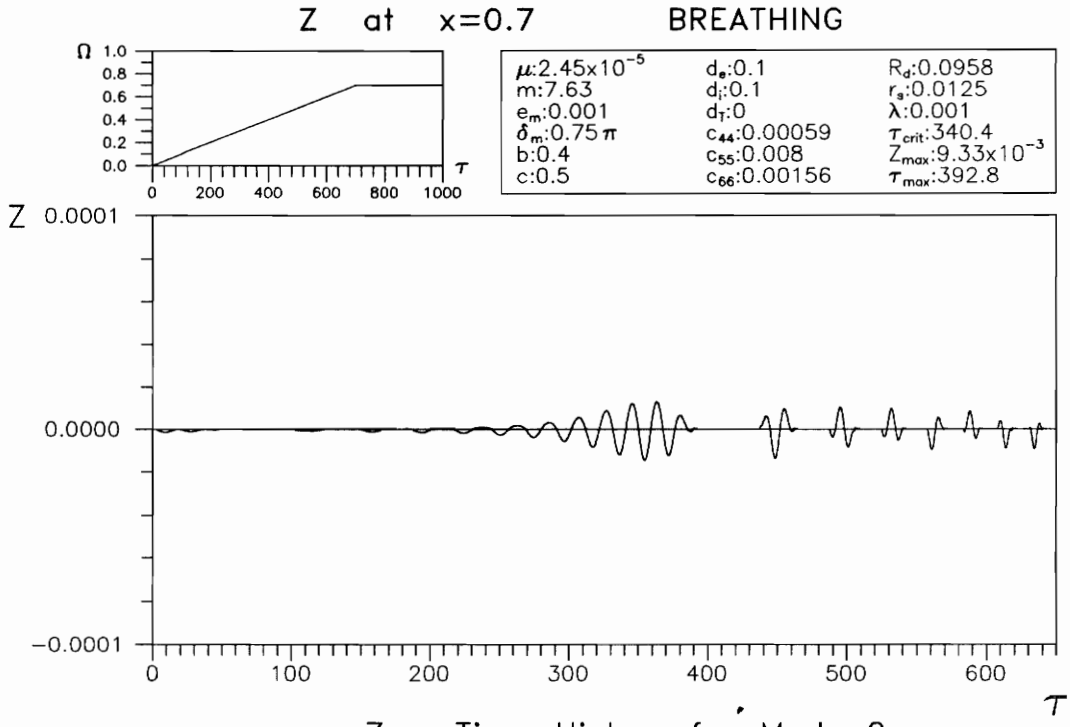

c. Z – Time History for Mode 2

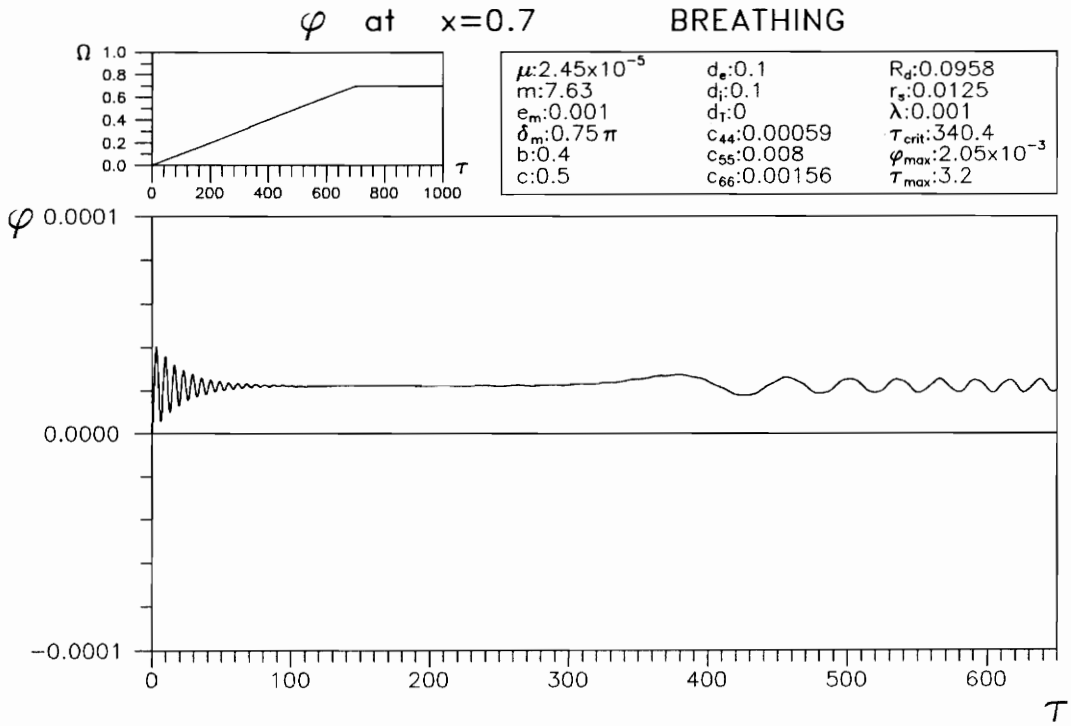

d. φ – Time History for Mode 2

Fig. 5.2 Time History for Each Mode

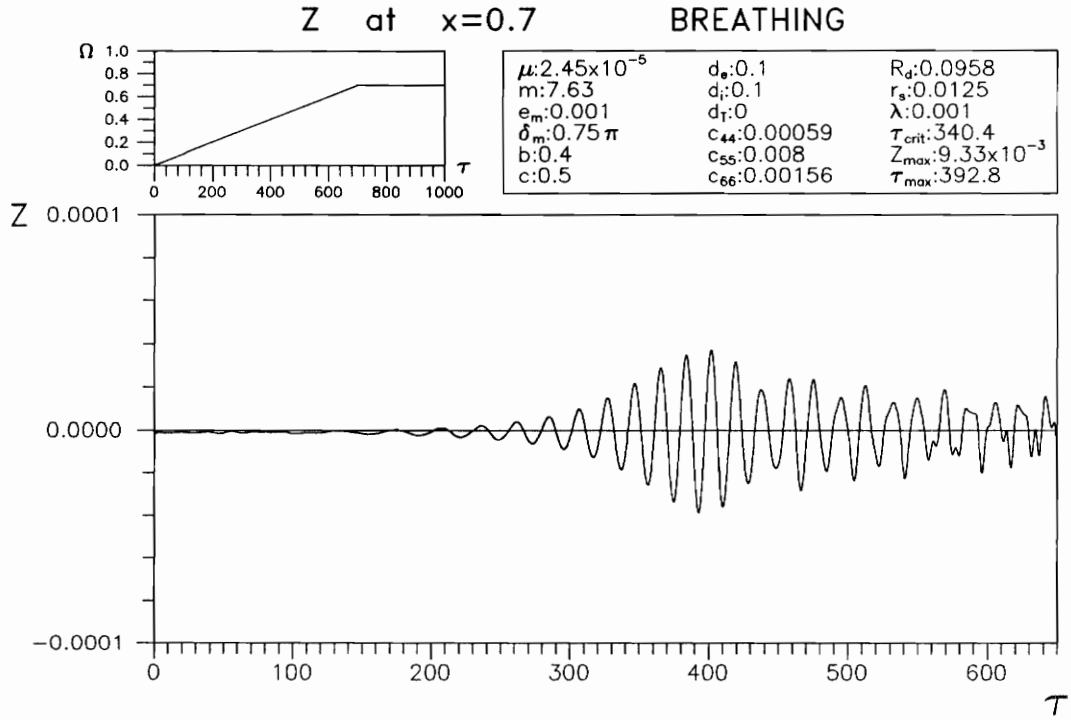

e. Z – Time History for Mode 3

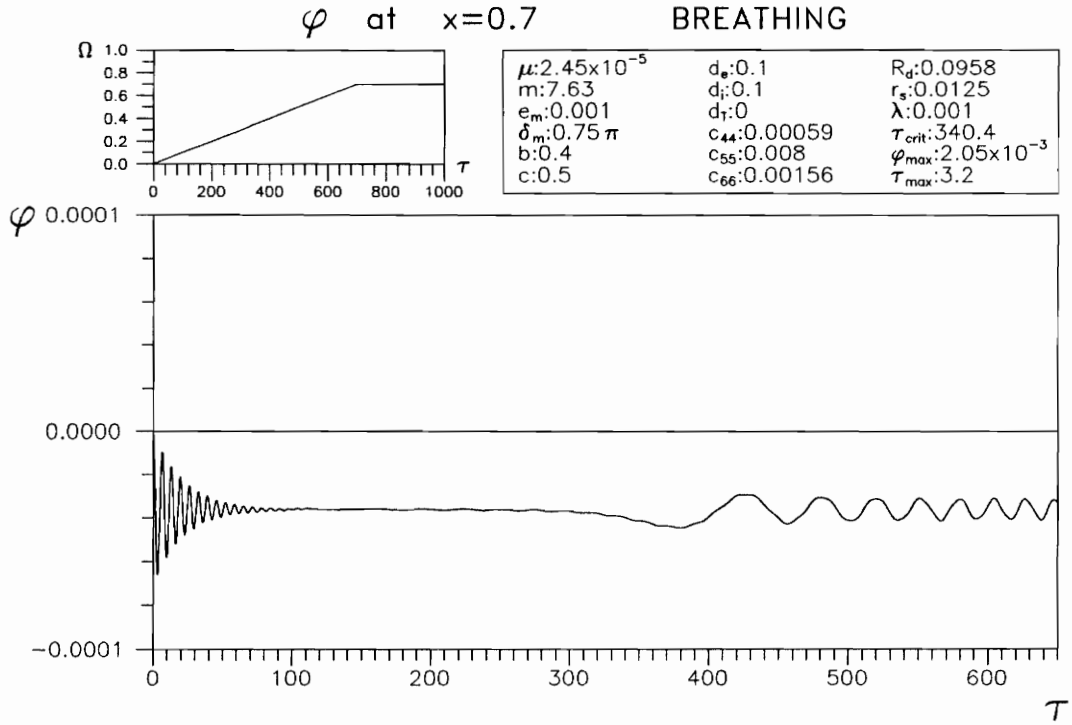

f. φ – Time History for Mode 3

Fig. 5.2 Time History for Each Mode

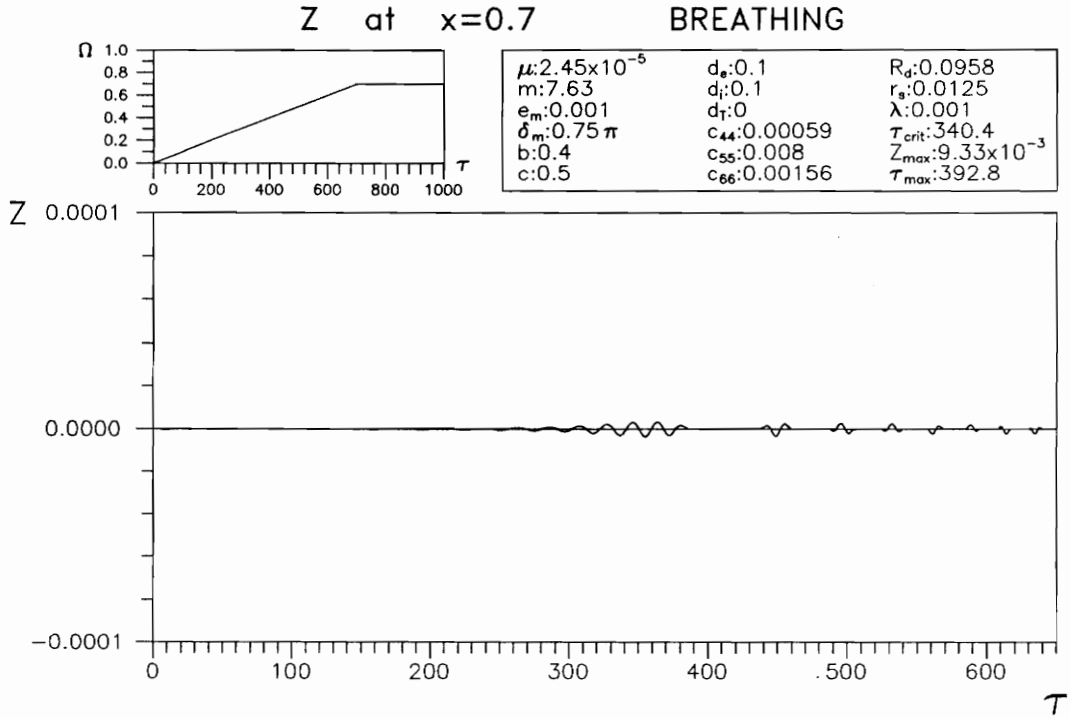

g. Z – Time History for Mode 4

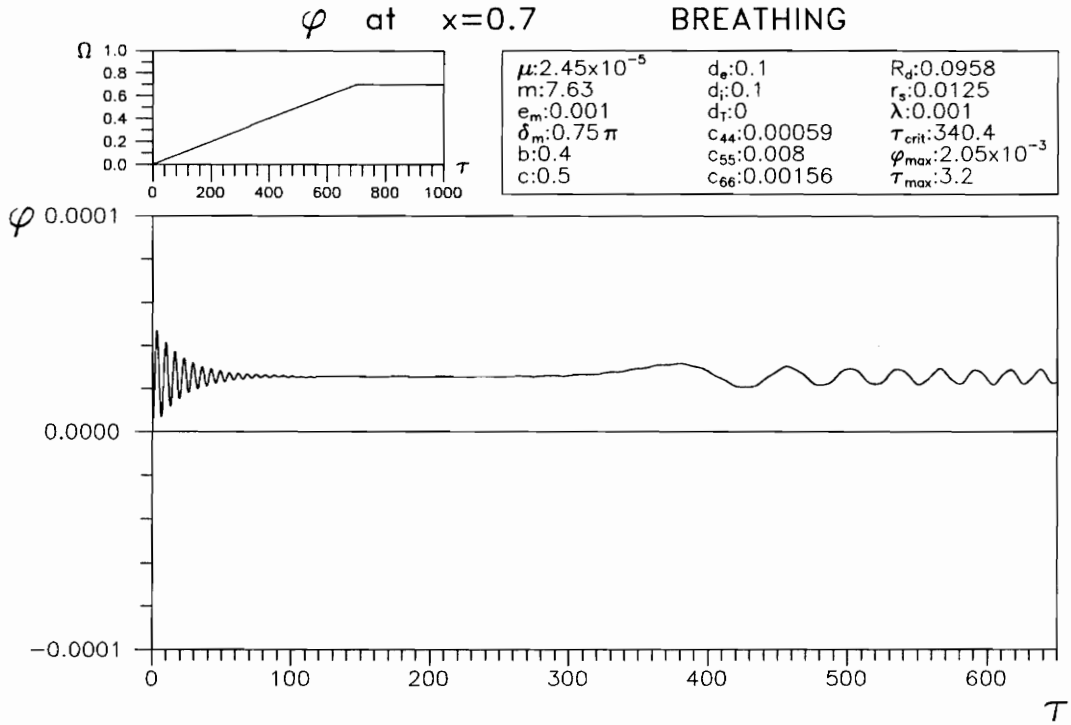

h. φ – Time History for Mode 4

Fig. 5.2 Time History for Each Mode

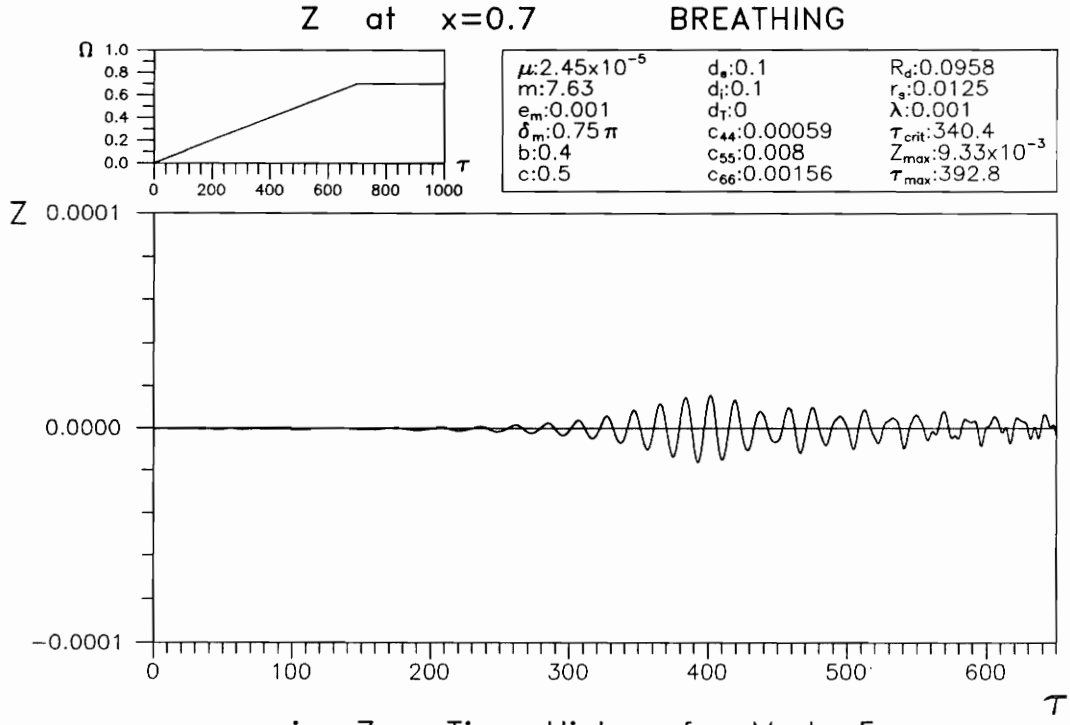

i. Z – Time History for Mode 5

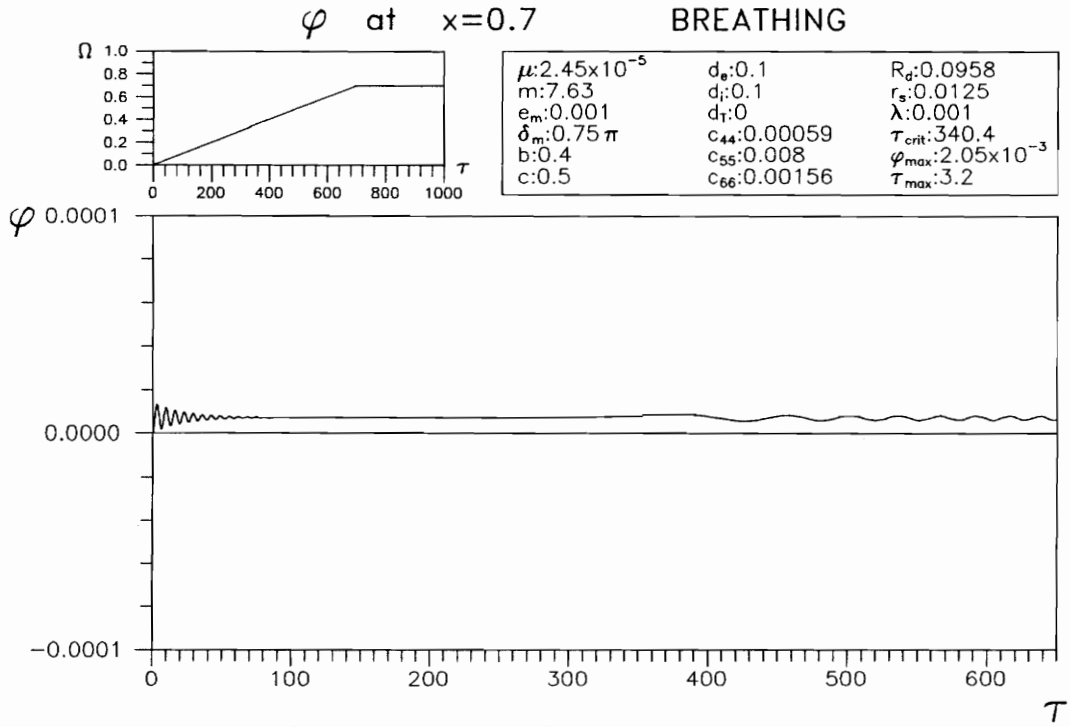

j. φ – Time History for Mode 5

Fig. 5.2 Time History for Each Mode

modes, related to the maximum z-displacement ($z_{max,x}$) and the torsional deformation (ϕ) at the location $\tilde{x}$=0.7.

Table 5.1 Convergency of different numbers of modes

Modes	$z_{max,x}$	ϕ_{max}	$\phi_{max,f}$	$\phi_{min,f}$	$\phi_{ampl,f}$	$\phi_{mean,f}$
1	9.362×10^{-3}	2.07×10^{-3}	-9.18×10^{-4}	-1.42×10^{-3}	2.49×10^{-4}	-1.17×10^{-3}
2	9.363×10^{-3}	2.04×10^{-3}	-9.00×10^{-4}	-1.39×10^{-3}	2.44×10^{-4}	-1.14×10^{-3}
3	9.338×10^{-3}	2.11×10^{-3}	-9.34×10^{-4}	-1.43×10^{-3}	2.48×10^{-4}	-1.18×10^{-3}
4	9.344×10^{-3}	2.06×10^{-3}	-9.14×10^{-4}	-1.40×10^{-3}	2.42×10^{-4}	-1.16×10^{-3}
5	9.325×10^{-3}	2.05×10^{-3}	-9.07×10^{-4}	-1.39×10^{-3}	2.41×10^{-4}	-1.15×10^{-3}

There are five different calculations of torsional deformation in Table 5.1, i.e.:

1. ϕ_{max} : the maximum ϕ-torsional deformation including transient response
2. $\phi_{max,f}$: the maximum ϕ-torsional deformation after transient response
3. $\phi_{min,f}$: the minimum ϕ-torsional deformation after transient response
4. $\phi_{ampl,f}$: the maximum amplitude of the ϕ-torsional deformation after transient response

   $$\phi_{ampl,f} = \frac{1}{2}(\phi_{max,f} - \phi_{min,f})$$

5. $\phi_{mean,f}$: the mean amplitude of the ϕ-torsional deformation after transient response

   $$\phi_{mean,f} = \frac{1}{2}(\phi_{max,f} + \phi_{min,f})$$

From Table 5.1, the difference of z_{max} between one mode and five modes is about 0.40% and the difference of z_{max} between three modes and five modes is only 0.14%. The difference of $\phi_{ampl,f}$ between one mode and five modes is about 3.1% and the difference of $\phi_{ampl,f}$ between three modes and five modes is about 2.8%. Figure 5.3.a shows the relation between the maximum z-displacement at location $\tilde{x}$=0.7 and the number of modes, and Fig. 5.3.b shows the relation between $\phi_{ampl,f}$ and the number of modes. The difference of the responses between three modes and five modes is not so significant and the computer time is almost three times longer using five modes. Therefore, in this chapter, the approximate solutions are calculated based on the first three modes.

5.3. Influence of Acceleration

The flexural-torsional response of the cracked rotating shaft under linear acceleration and exponential acceleration passing through the critical speed is studied in this chapter. For the linear acceleration, the formulas of the angular velocity and the rotational angle are the same as those in equation (3.15). For the exponential acceleration, the initial condition begins from the rest condition and the initial acceleration is the same as the linear acceleration λ. The angular velocity Ω in this study approaches 0.7 (or about 2 times the first critical speed) as $\tau \to \infty$. Therefore, the formula of the angular velocity, the rotational acceleration, and the rotational angle can be defined as follows:

$$\Omega = 0.7 \left(1 - e^{-a\tau} \right)$$

$$\lambda = 0.7\, a\, e^{-a\tau}$$

$$\theta = 0.7\, \tau + \frac{0.7}{a} e^{-a\tau} - \frac{0.7}{a} \tag{5.3}$$

where a is a constant that is determined by choosing the initial acceleration $\lambda_{initial}$

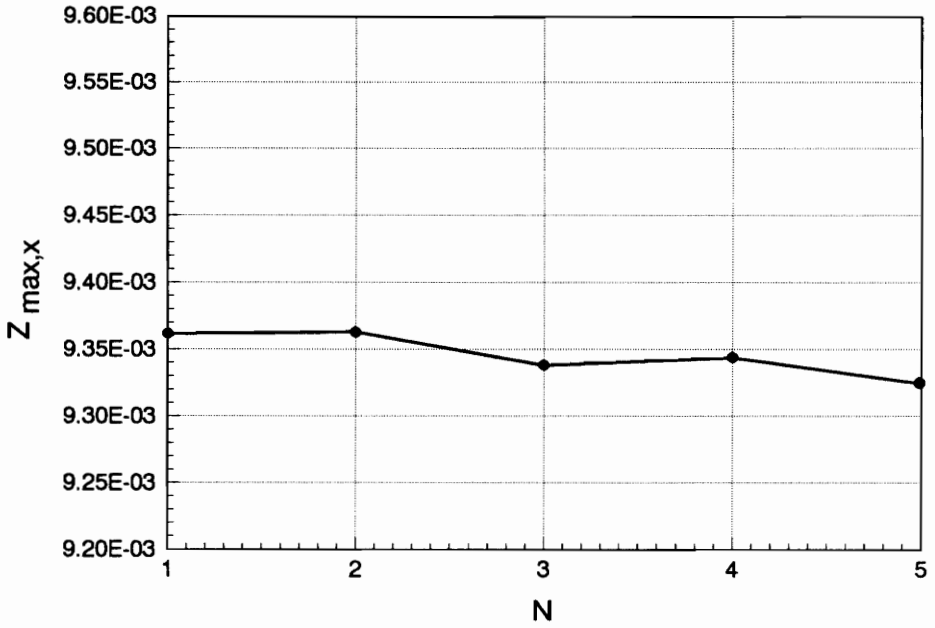

a. Number of Modes vs. $Z_{max,x}$

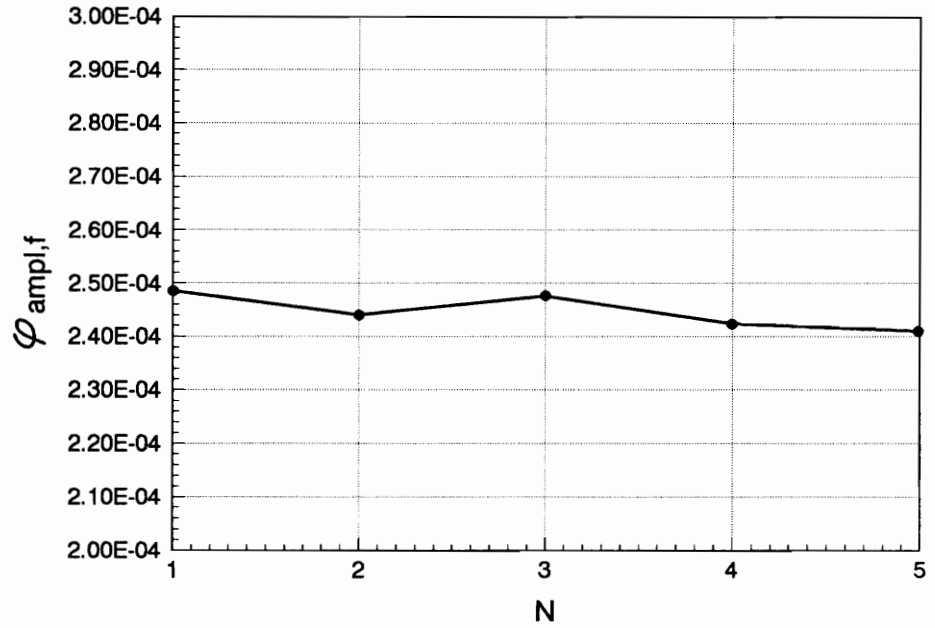

b. Number of Modes vs. $\varphi_{ampl,f}$

Fig. 5.3 Influence of Number of Modes

at τ=0, i.e., a = $\frac{\lambda_{initial}}{0.7}$.

Five different rates of linear acceleration from chapter 3.4, i.e., λ = 0.0001, 0.0005, 0.001, 0.002, and 0.003, are still used. For the exponential case, three different rates of initial acceleration $\lambda_{initial}$ are used, i.e., $\lambda_{initial}$ = 0.0005, 0.001, and 0.002. Table 5.2 gives the relation between the initial acceleration $\lambda_{initial}$ and τ_{crit} ; also, it gives the values of the constant a.

Table 5.2 τ_{crit} for exponential acceleration

$\lambda_{initial}$	a	τ_{crit}
0.0005	7.143×10^{-4}	932.50
0.0010	1.429×10^{-3}	466.12
0.0020	2.857×10^{-3}	233.14

Figures 5.4.a-j show the time histories of the z-displacement and the ϕ-torsional deformation, respectively, at location $\tilde{x}$=0.7 for the standard case and zero initial conditions under different rates of linear acceleration. From Fig. 5.4.a, c, e, g, and i, the characteristics of the time histories of the z-displacement in the case of flexural-torsional response are similar to those in the case of the flexural response (see Fig. 3.6.a-e). Therefore, in this case, inclusion of torsional motion does not have much effect on the transverse displacements. Figures 5.4.b, d, f, h, and j show the time histories of the ϕ-torsional deformation. From those figures, it is clear that a smaller linear acceleration gives larger ϕ-torsional deformation frequencies. The ϕ-torsional deformation begins vibrating around τ=τ_{crit},

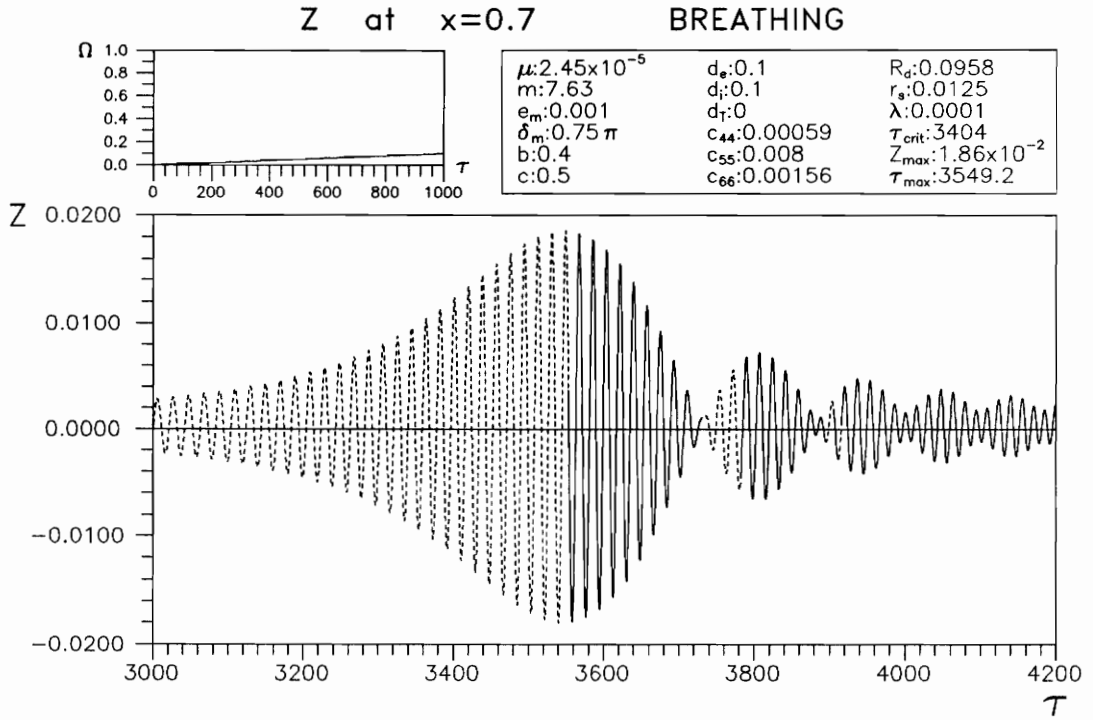

a. Z − Time History for λ = 0.0001

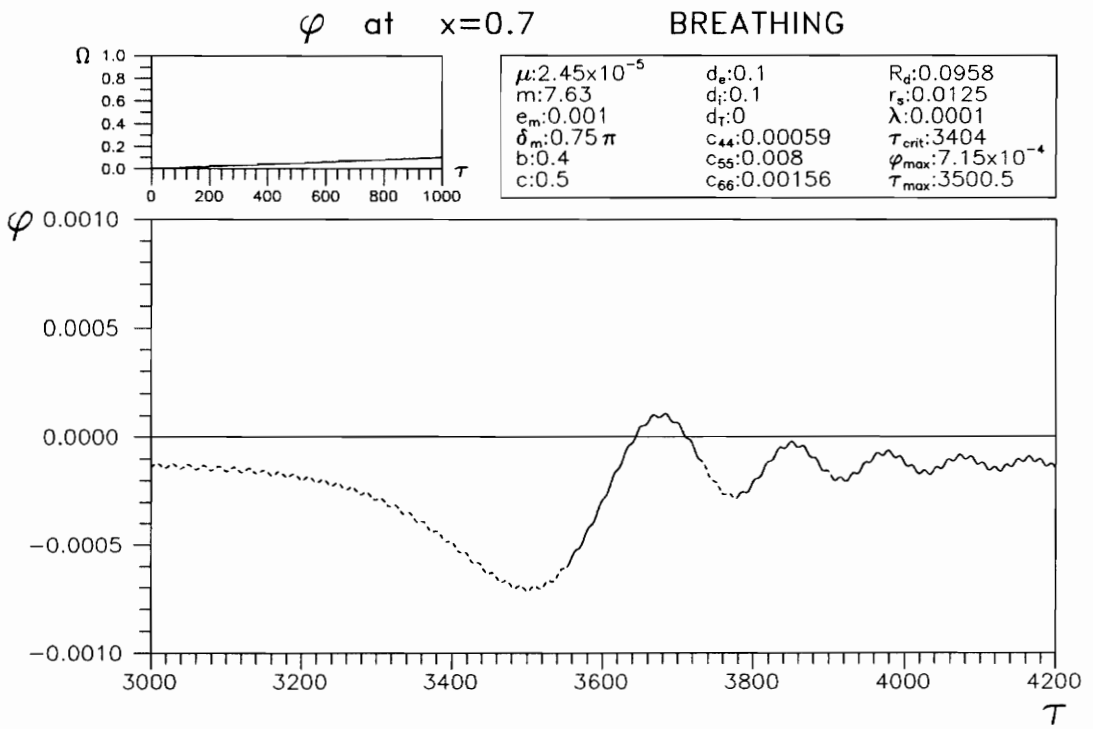

b. φ − Time History for λ = 0.0001

Fig. 5.4 Time History for Linear Acceleration

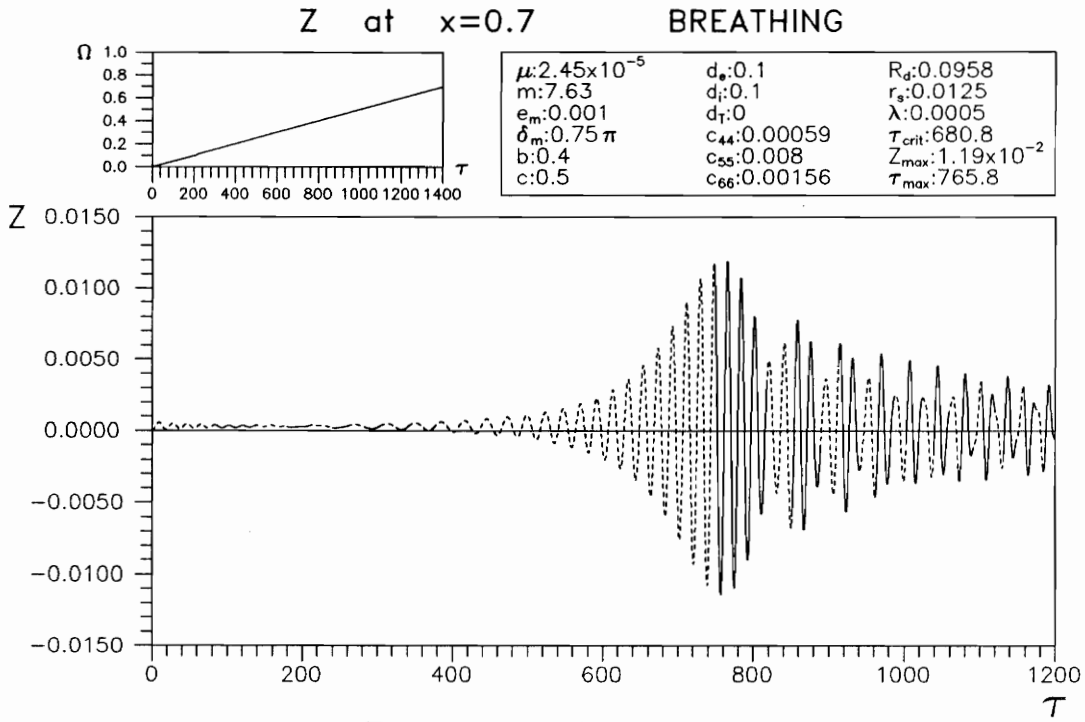

c. Z – Time History for λ = 0.0005

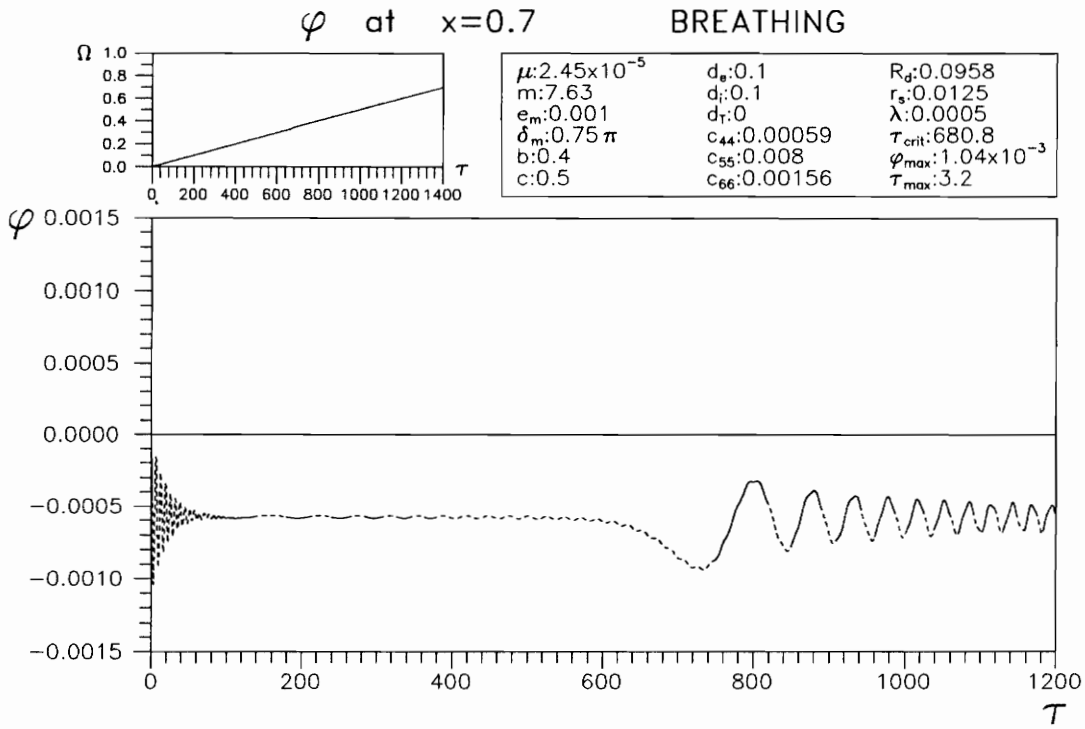

d. φ – Time History for λ = 0.0005

Fig. 5.4 Time History for Linear Acceleration

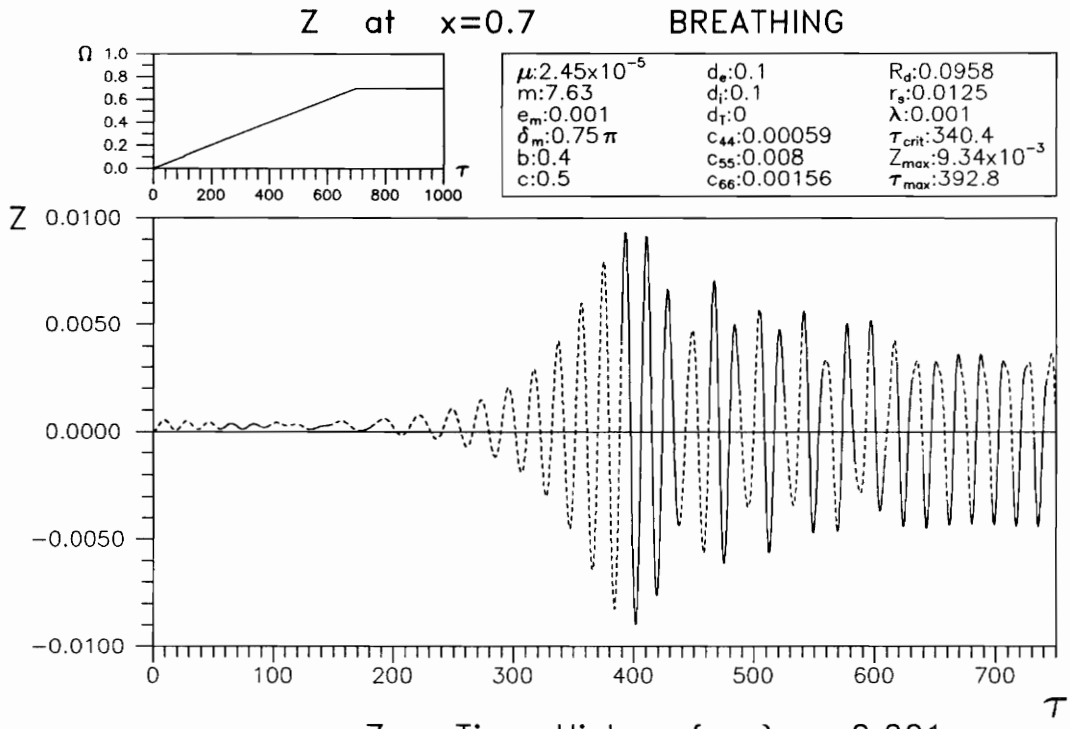

e. Z – Time History for λ = 0.001

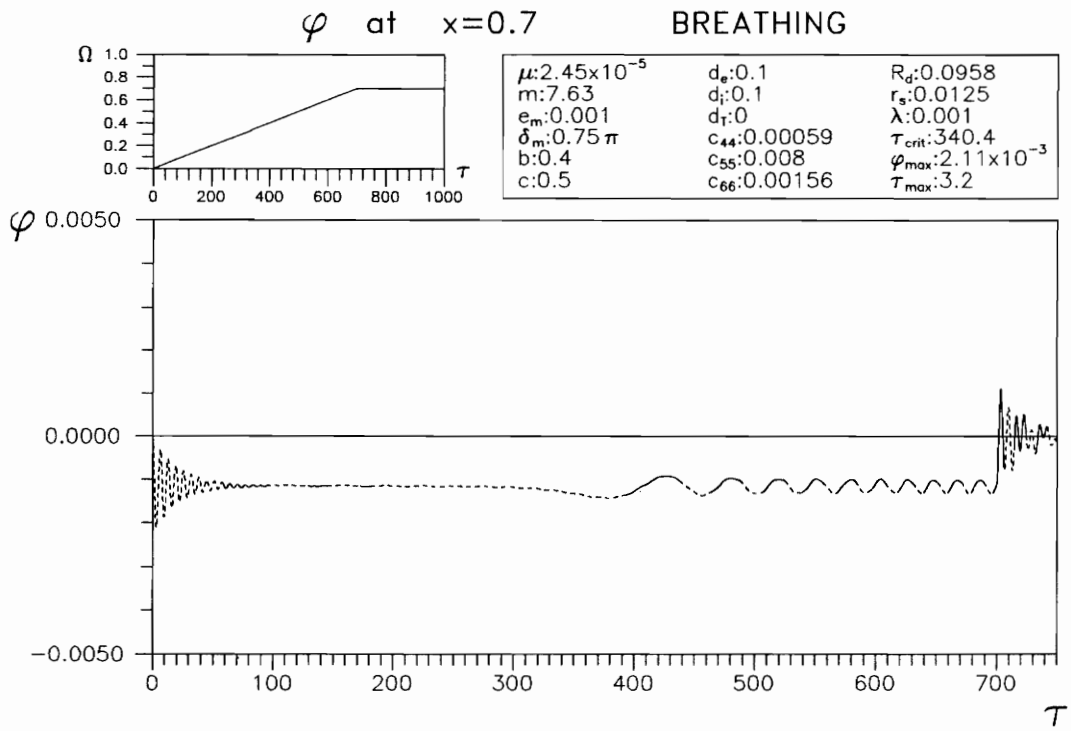

f. φ – Time History for λ = 0.001

Fig. 5.4 Time History for Linear Acceleration

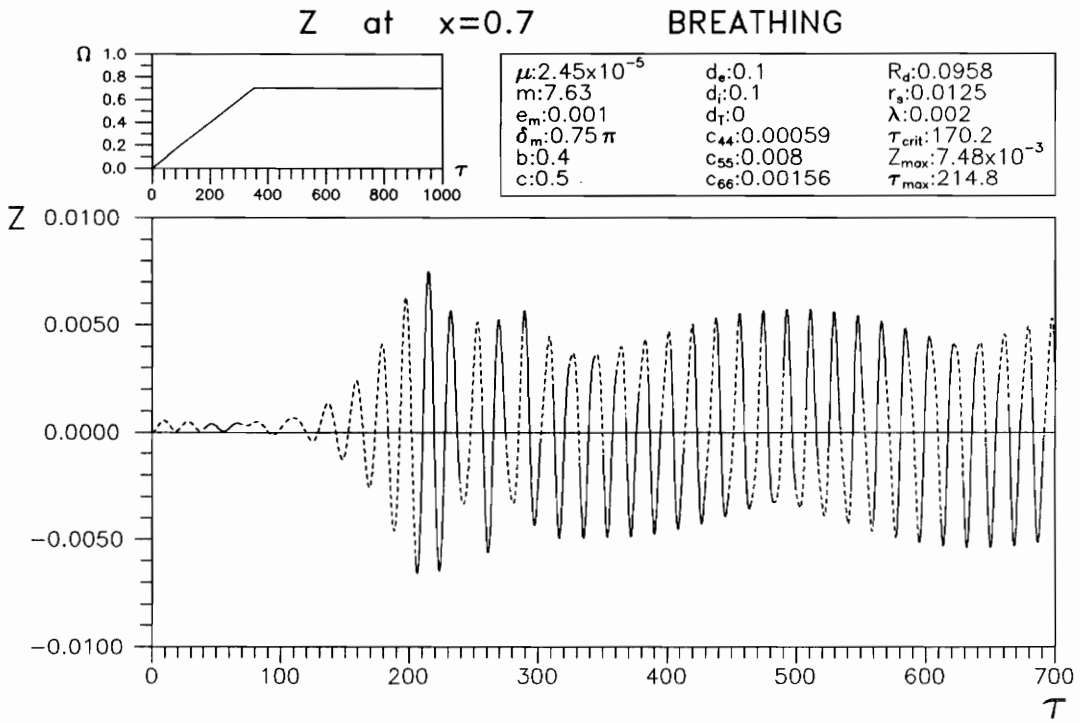

g. Z – Time History for λ = 0.002

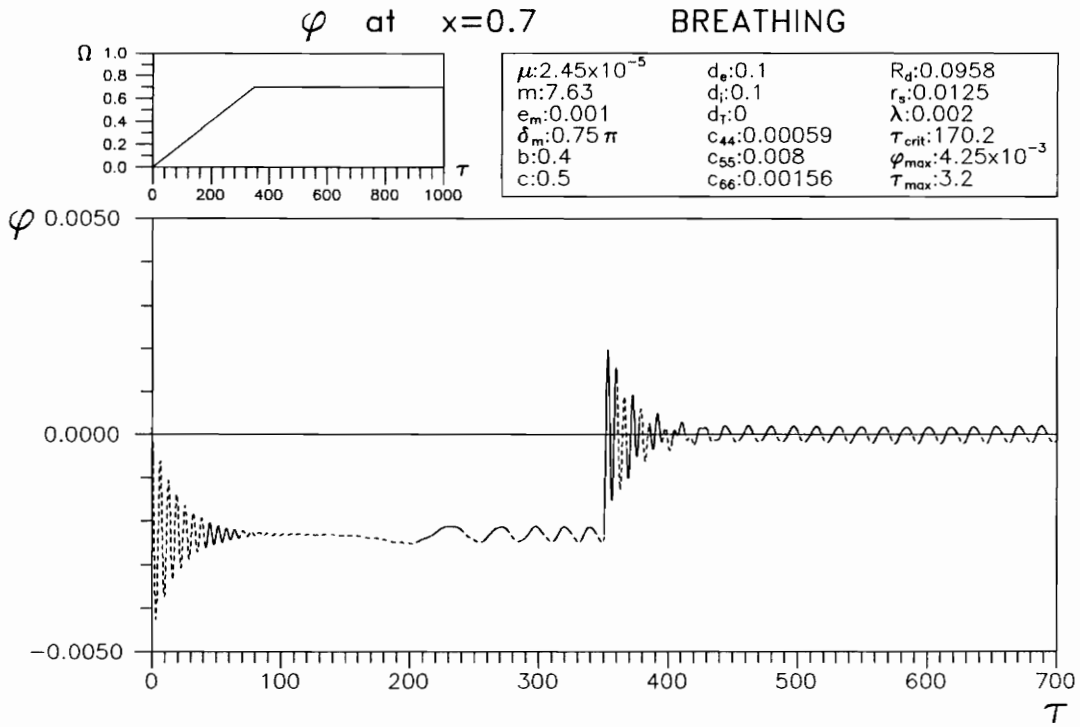

h. φ – Time History for λ = 0.002

Fig. 5.4 Time History for Linear Acceleration

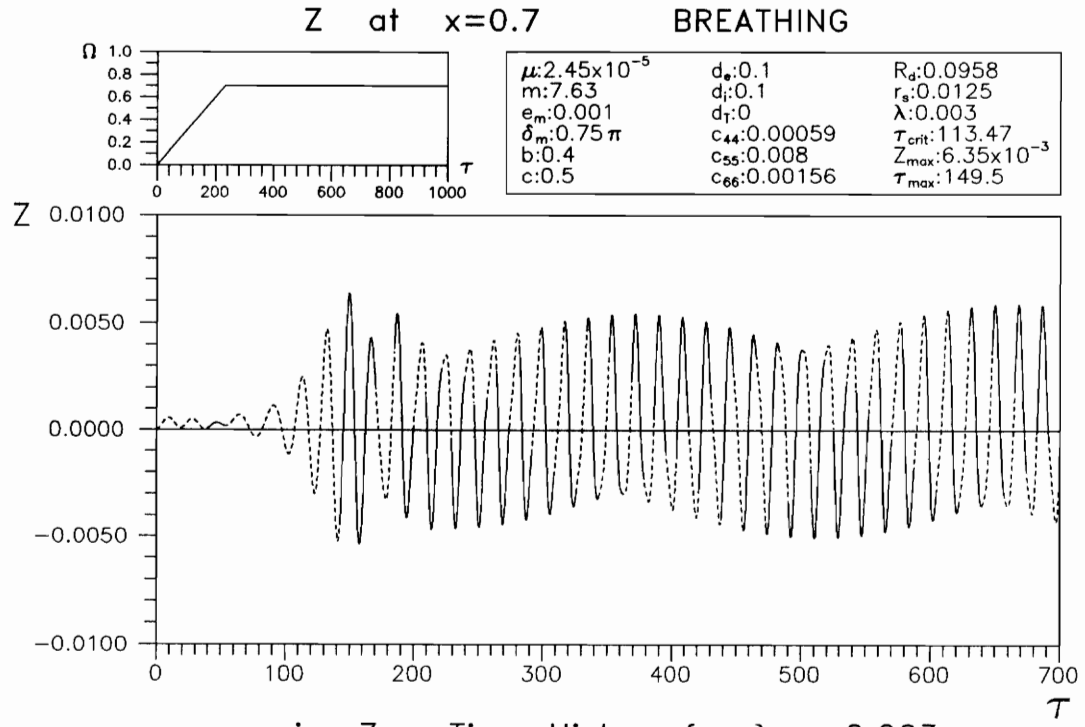

i. Z – Time History for λ = 0.003

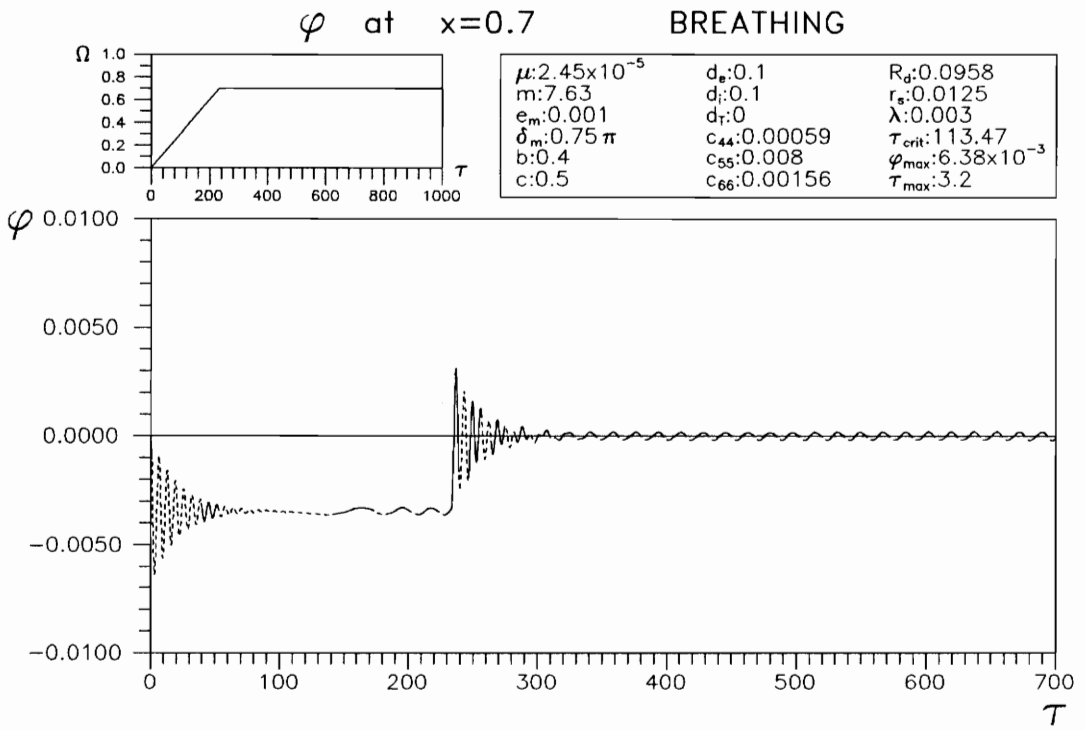

j. φ – Time History for λ = 0.003

Fig. 5.4 Time History for Linear Acceleration

neglecting the transient response. In Fig. 5.4.f, h, and j, there is a sudden change in the ϕ-torsional deformation when the angular velocity becomes constant. This occurs because from equation (4.24) there is a constant value in the equation when there is non-zero acceleration λ that suddenly becomes zero when λ suddenly becomes zero.

Figure 5.5.a shows the relation between the linear acceleration and the maximum z-displacement ($z_{max,x}$ at location $\tilde{x}$=0.7 and $z_{max,w}$ over the whole length) with the standard parameters. Lower acceleration gives a larger maximum z-displacement. Figure 5.5.b shows the relation between the linear acceleration and the maximum amplitude of the ϕ-torsional deformation after transient response at location $\tilde{x}$=0.7. Lower acceleration gives a larger $\phi_{ampl,f}$. The values of the linear acceleration, the maximum z-displacement and the ϕ-torsional deformation at location $\tilde{x}$=0.7 are given in Table 5.3.

Table 5.3 Influence of linear acceleration

λ	$z_{max,x}$	ϕ_{max}	$\phi_{max,f}$	$\phi_{min,f}$	$\phi_{ampl,f}$	$\phi_{mean,f}$
0.0001	1.86×10^{-2}	7.15×10^{-4}	1.08×10^{-4}	-7.15×10^{-4}	4.11×10^{-4}	-3.04×10^{-4}
0.0005	1.19×10^{-2}	1.04×10^{-3}	-3.20×10^{-4}	-9.37×10^{-4}	3.08×10^{-4}	-6.29×10^{-4}
0.0010	9.34×10^{-3}	2.11×10^{-3}	-9.34×10^{-4}	-1.43×10^{-3}	2.48×10^{-4}	-1.18×10^{-3}
0.0020	7.48×10^{-3}	4.25×10^{-3}	-2.12×10^{-3}	-2.51×10^{-3}	1.95×10^{-4}	-2.32×10^{-3}
0.0030	6.35×10^{-3}	6.38×10^{-3}	-3.28×10^{-3}	-3.64×10^{-3}	1.76×10^{-4}	-3.46×10^{-3}

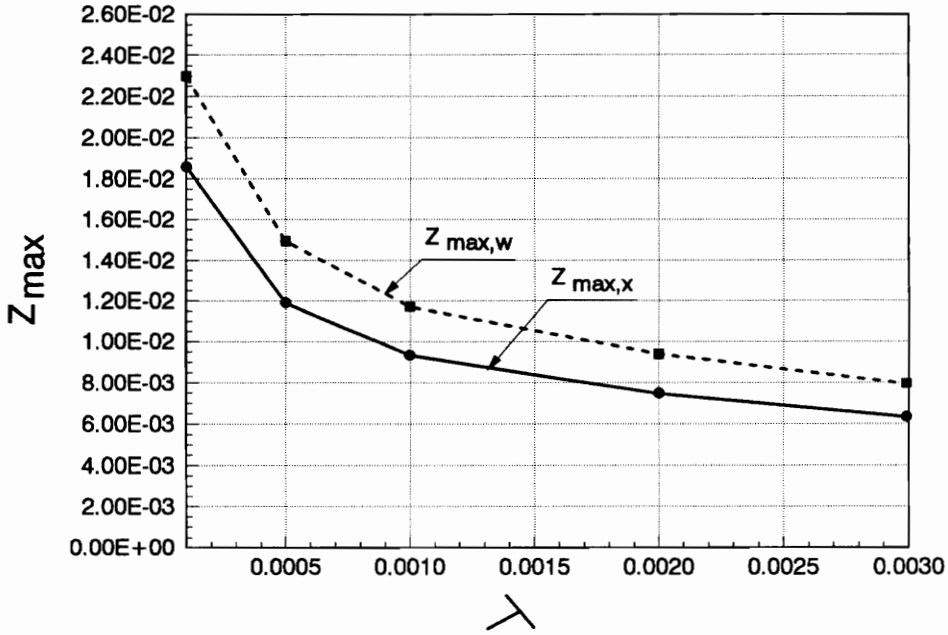

a. Linear Acceleration Rate vs. Z_{max}

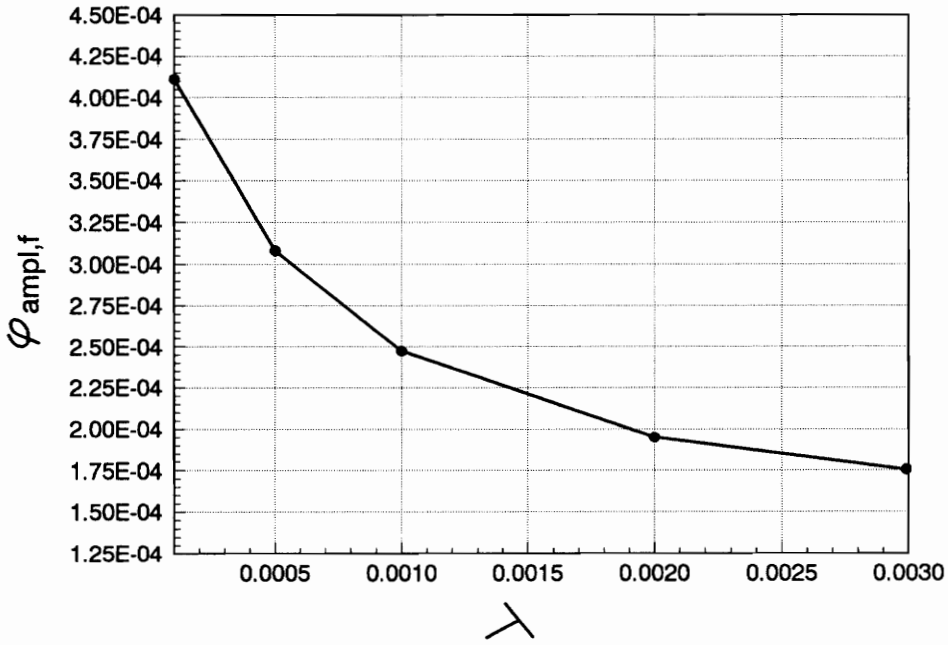

b. Linear Acceleration Rate vs. $\varphi_{ampl,f}$

Fig. 5.5 Influence of Linear Acceleration Rate

Figures 5.6.a-b present the time histories of the z-displacement and ϕ-torsional deformation for the standard case of the uncracked shaft. Figures 5.7.a-b give the time histories of the z-displacement and ϕ-torsional deformation for the standard case of the open-cracked shaft. The values of the z-displacement and ϕ-torsional deformation for the breathing crack, no crack, and open crack are given in Table 5.4. From this table, the breathing crack has the biggest influence on $\phi_{ampl,f}$. The difference of $z_{max,x}$ between the breathing crack and open crack is so small that it can be assumed the same. These properties are not necessarily true for other cases.

Table 5.4 Influence of crack condition

	$z_{max,x}$	ϕ_{max}	$\phi_{max,f}$	$\phi_{min,f}$	$\phi_{ampl,f}$	$\phi_{mean,f}$
Breathing Crack	$9.34x10^{-3}$	$2.11x10^{-3}$	$-9.34x10^{-4}$	$-1.43x10^{-3}$	$2.48x10^{-4}$	$-1.18x10^{-3}$
No Crack	$9.01x10^{-3}$	$2.11x10^{-3}$	$-9.39x10^{-4}$	$-1.42x10^{-3}$	$2.43x10^{-4}$	$-1.18x10^{-3}$
Open Crack	$9.34x10^{-3}$	$2.11x10^{-3}$	$-9.38x10^{-4}$	$-1.43x10^{-3}$	$2.46x10^{-4}$	$-1.18x10^{-3}$

The influence of the internal damping d_i on the ϕ-torsional deformation under different rates of linear acceleration can be seen in Fig. 5.8.a-e. These curves show the time histories of the ϕ-torsional deformation at location $\tilde{x}$=0.7 for $\tilde{d}_i$=0. From Fig. 5.4.b, d, f, h, j and 5.8.a-e, there are differences in the time histories of the ϕ-torsional deformation. In the case of zero internal damping, the torsional deformation vibrates more than in the case of internal damping $\tilde{d}_i$=0.1. Also, the vibration of the torsional deformation in the zero internal damping case starts

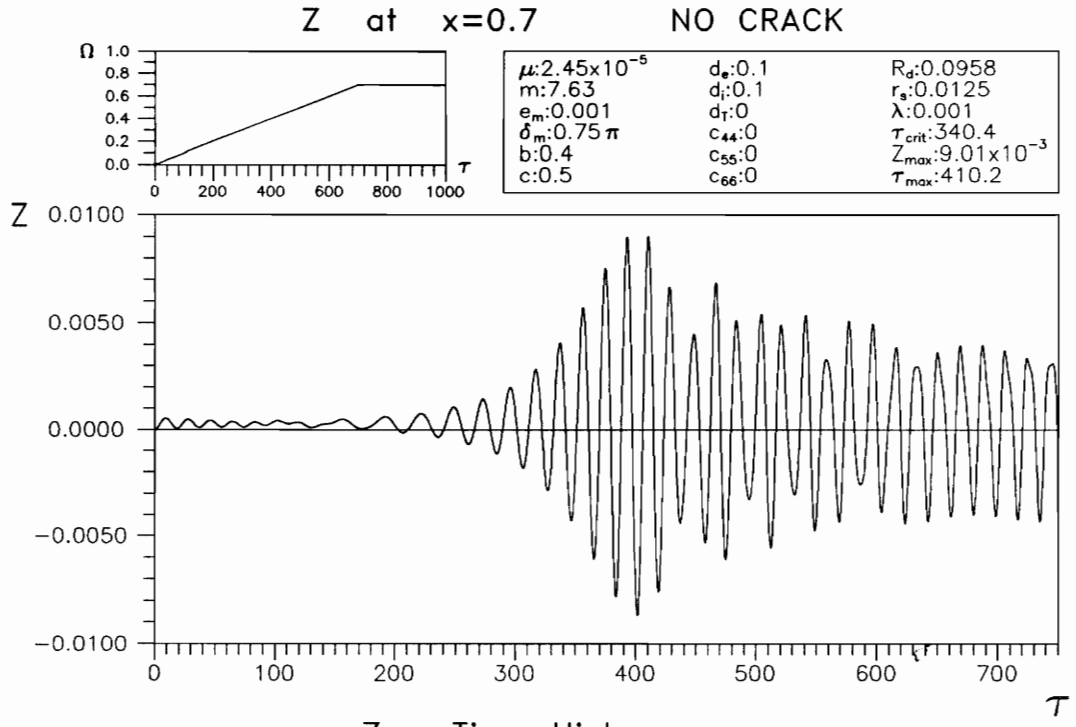

a. Z – Time History

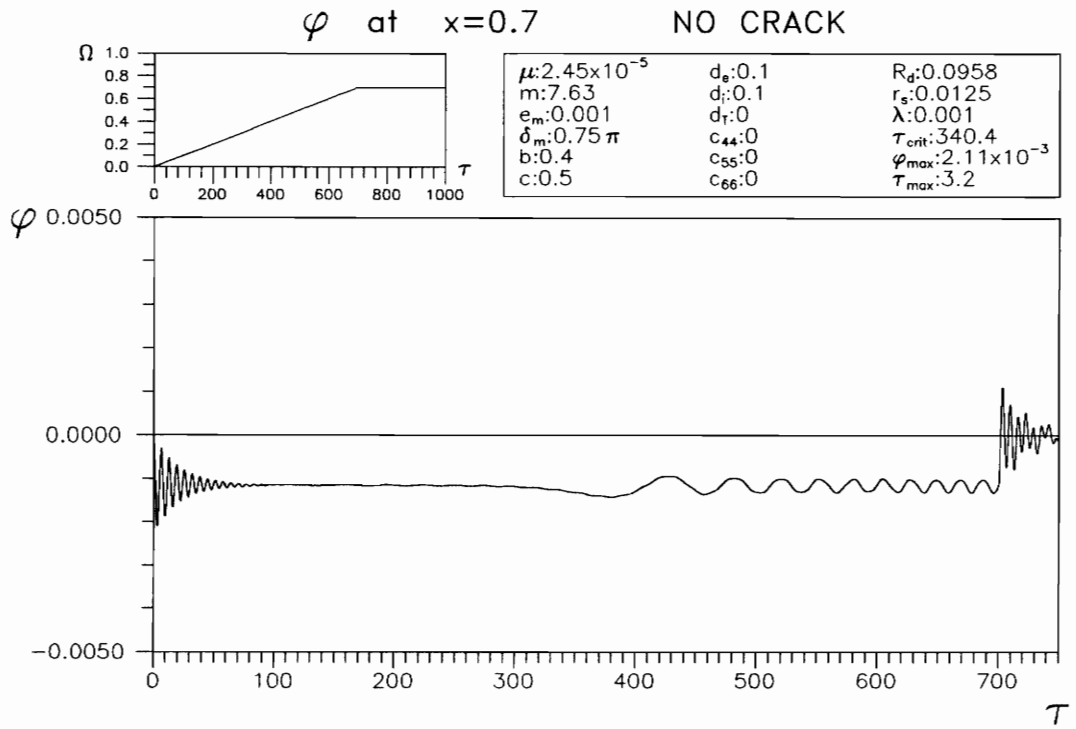

b. φ – Time History

Fig. 5.6 Time History for Standard Case without Crack

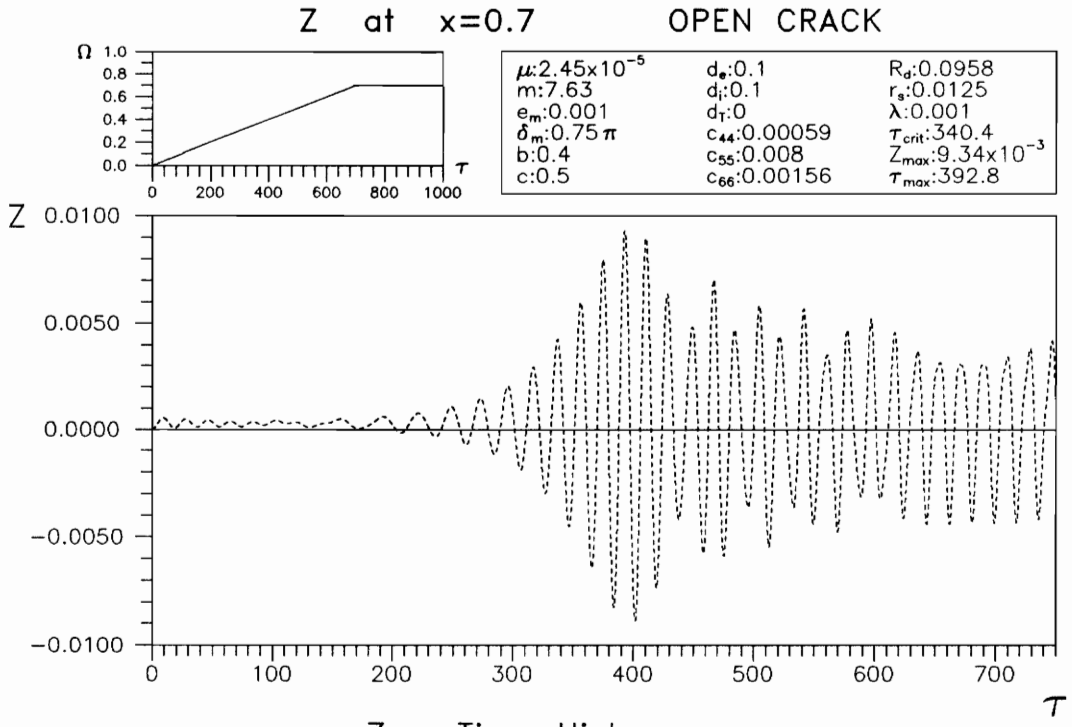

a. Z – Time History

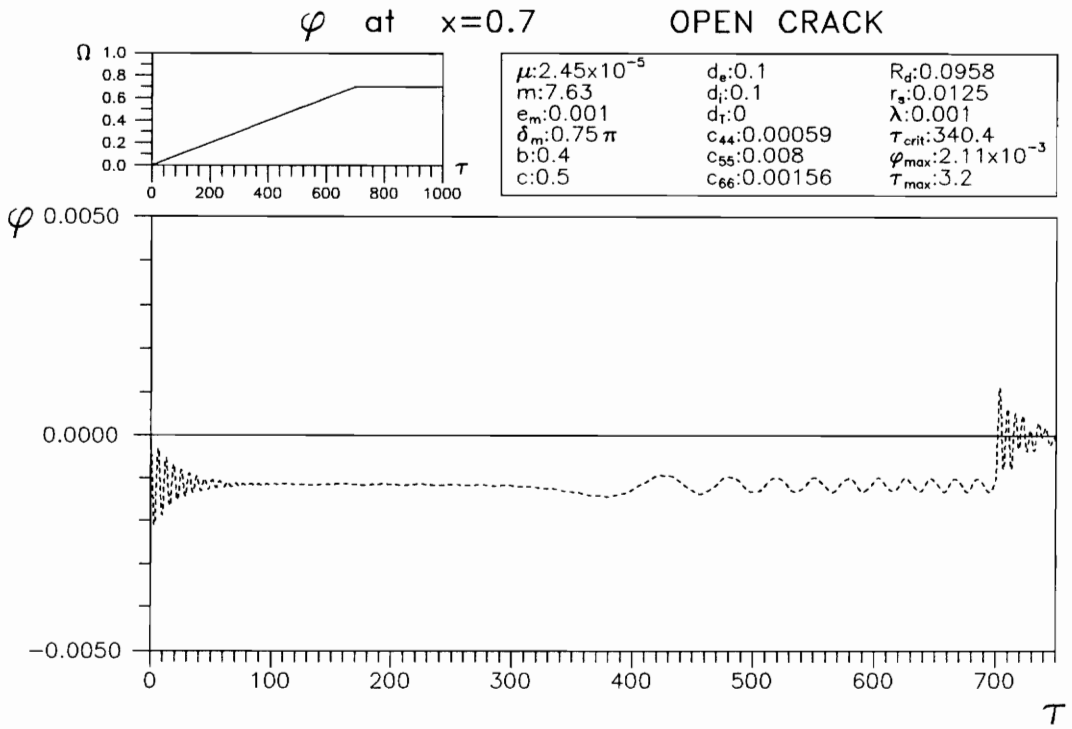

b. φ – Time History

Fig. 5.7 Time History for Standard Case with Open Crack

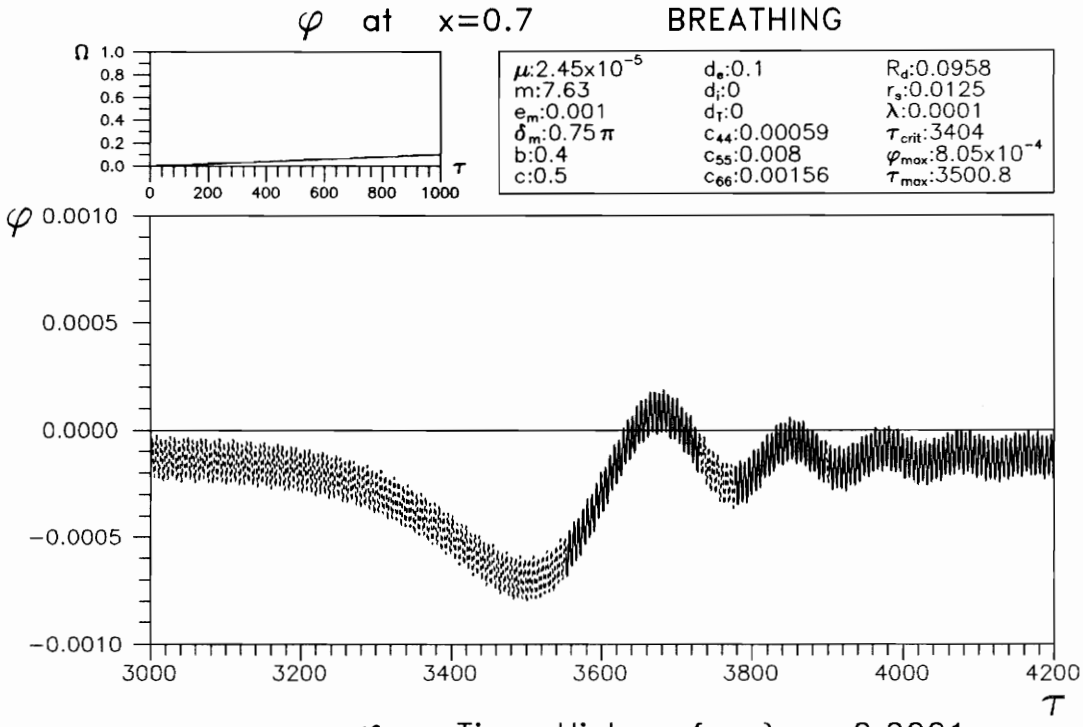

a. φ – Time History for $\lambda = 0.0001$

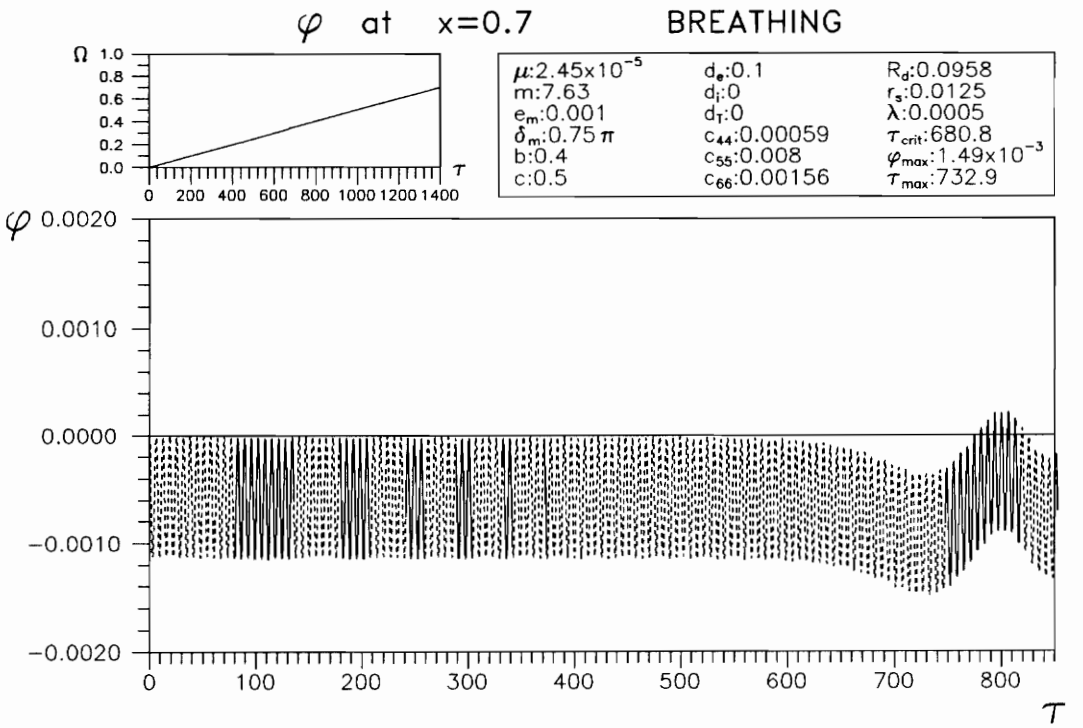

b. φ – Time History for $\lambda = 0.0005$

Fig. 5.8 φ – Time History for Linear Acceleration with $\tilde{d}_i=0$

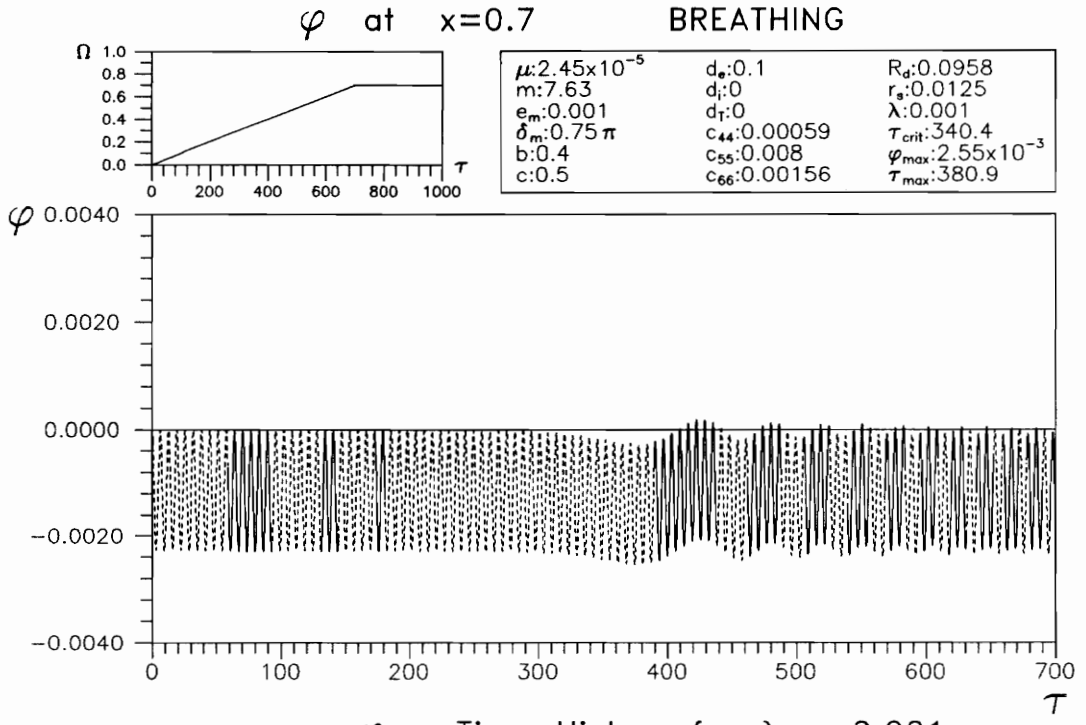

c. φ – Time History for $\lambda = 0.001$

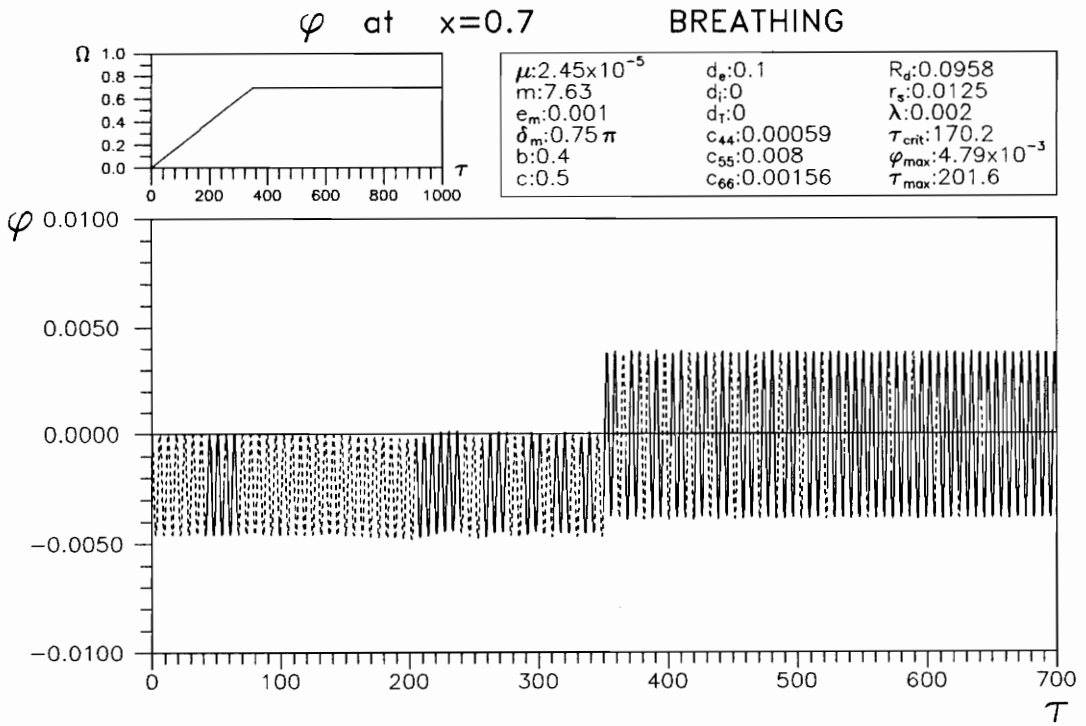

d. φ – Time History for $\lambda = 0.002$

Fig. 5.8 φ – Time History for Linear Acceleration with $\tilde{d}_i=0$

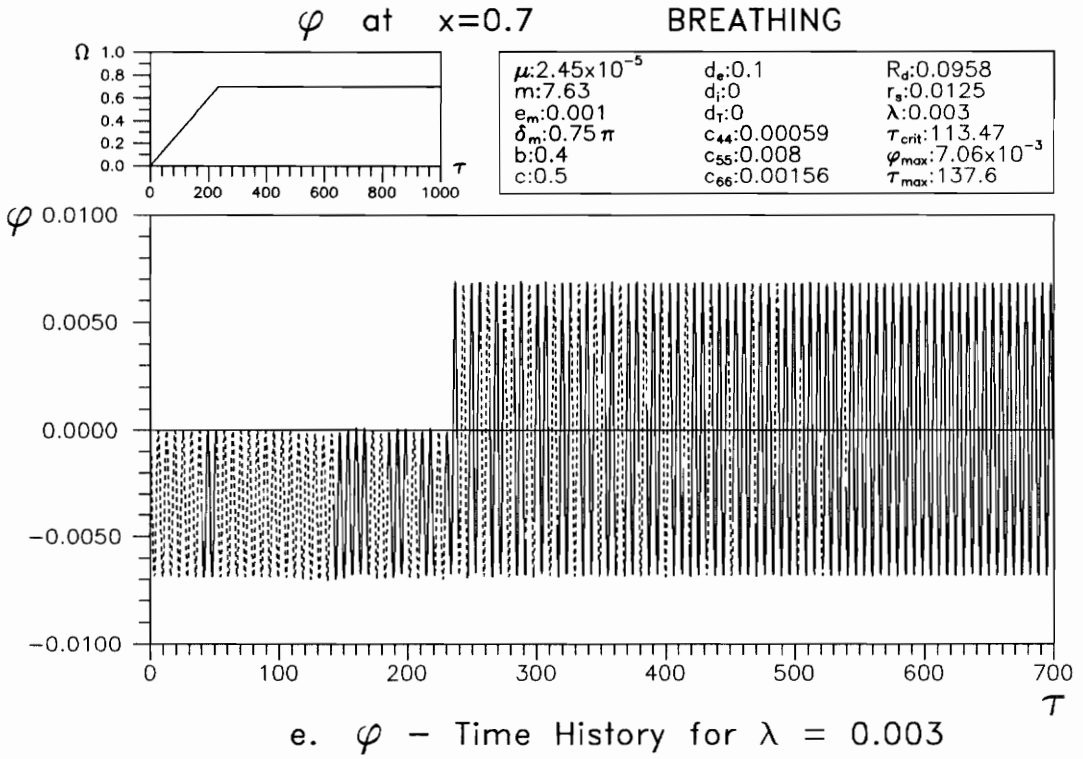

e. φ – Time History for $\lambda = 0.003$

Fig. 5.8 φ – Time History for Linear Acceleration with $\tilde{d}_i=0$

from the beginning of the ϕ-time history and keeps almost constant amplitude with varying mean until τ is near τ_{crit}. After a sudden change when the angular velocity Ω becomes constant, the ϕ-torsional deformation has another almost-constant amplitude. The time histories of the z-displacement in this zero internal damping case do not change very much. The difference of $z_{max,x}$ between the case of $\tilde{d}_i$ =0.1 and the case of $\tilde{d}_i$ = 0 is indicated in Table 5.5. The result is interesting, because the addition of internal damping gives a larger maximum z-displacement. Further discussion of the internal damping $\tilde{d}_i$ is presented in section 5.6.

Table 5.5 Influence of internal damping for linear acceleration

λ	$z_{max,x}$ - $\tilde{d}_i$=0.1	$z_{max,x}$ - $\tilde{d}_i$=0
0.0001	1.86×10^{-2}	1.83×10^{-2}
0.0005	1.19×10^{-2}	1.16×10^{-2}
0.0010	9.34×10^{-3}	9.16×10^{-3}
0.0020	7.48×10^{-3}	7.34×10^{-3}
0.0030	6.35×10^{-3}	6.14×10^{-3}

The time histories of the z-displacement and ϕ-torsional deformation under exponential acceleration at location $\tilde{x}$=0.7 with the standard parameters are shown in Fig. 5.9.a-f with different rates of initial acceleration. The time histories of the z-displacement in Fig. 5.9.a, c, and e have different characteristics from those in Fig. 5.4.c, e, and g. They have the same acceleration in the beginning

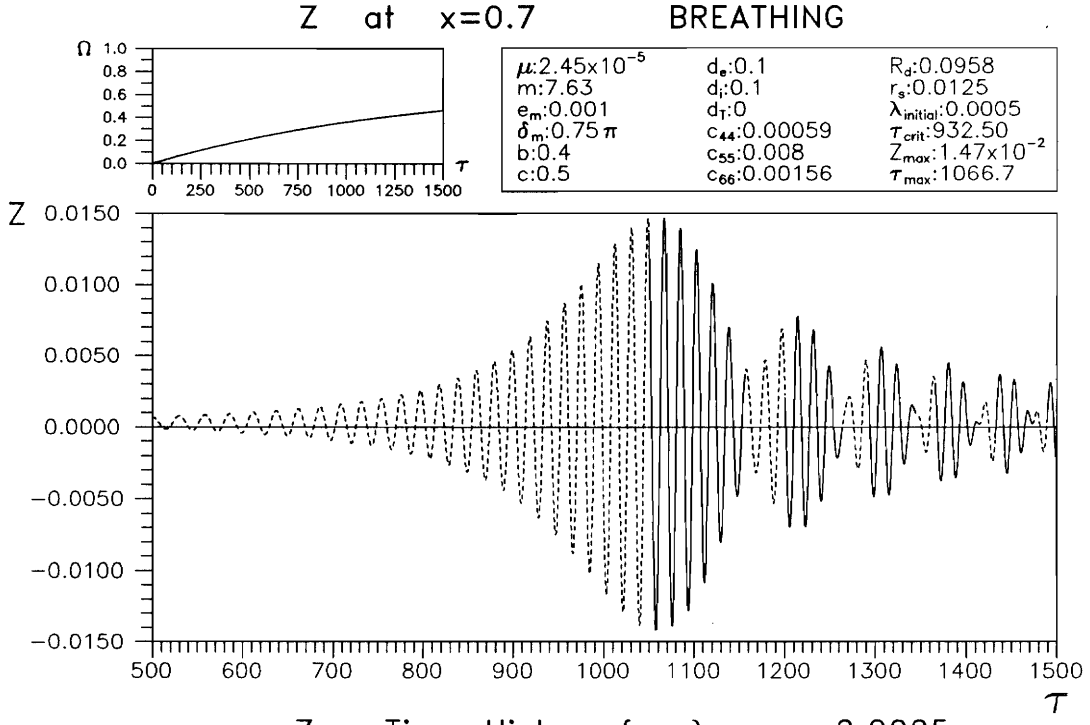

a. Z – Time History for $\lambda_{initial}$ = 0.0005

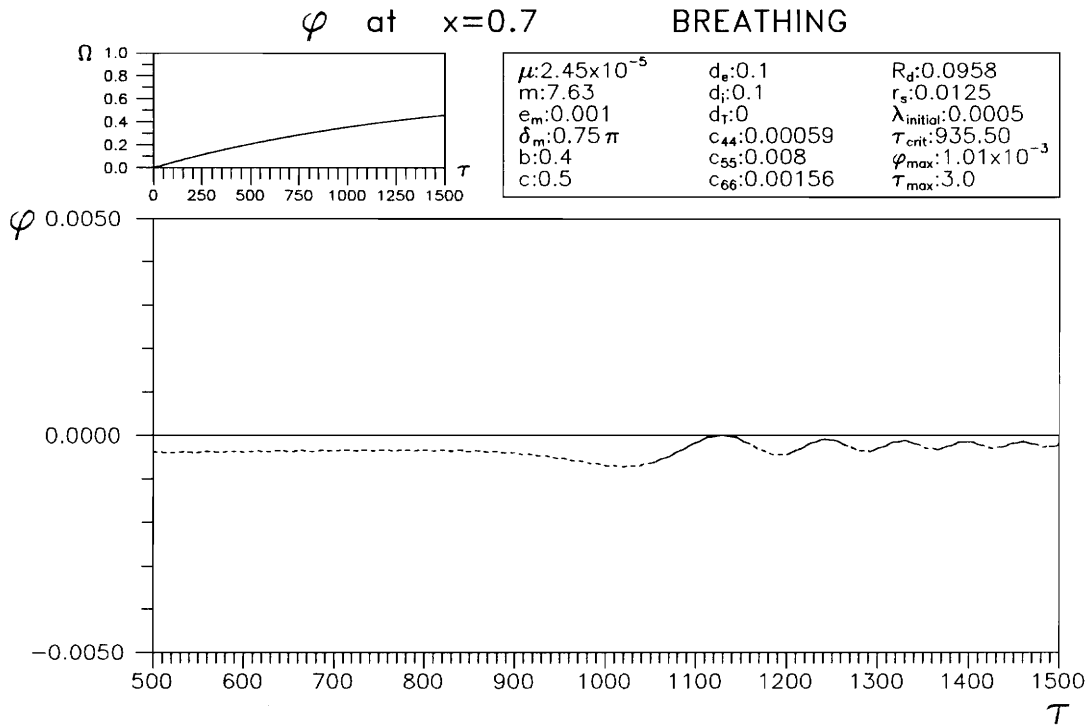

b. φ – Time History for $\lambda_{initial}$ = 0.0005

Fig. 5.9 Time History for Exponential Acceleration

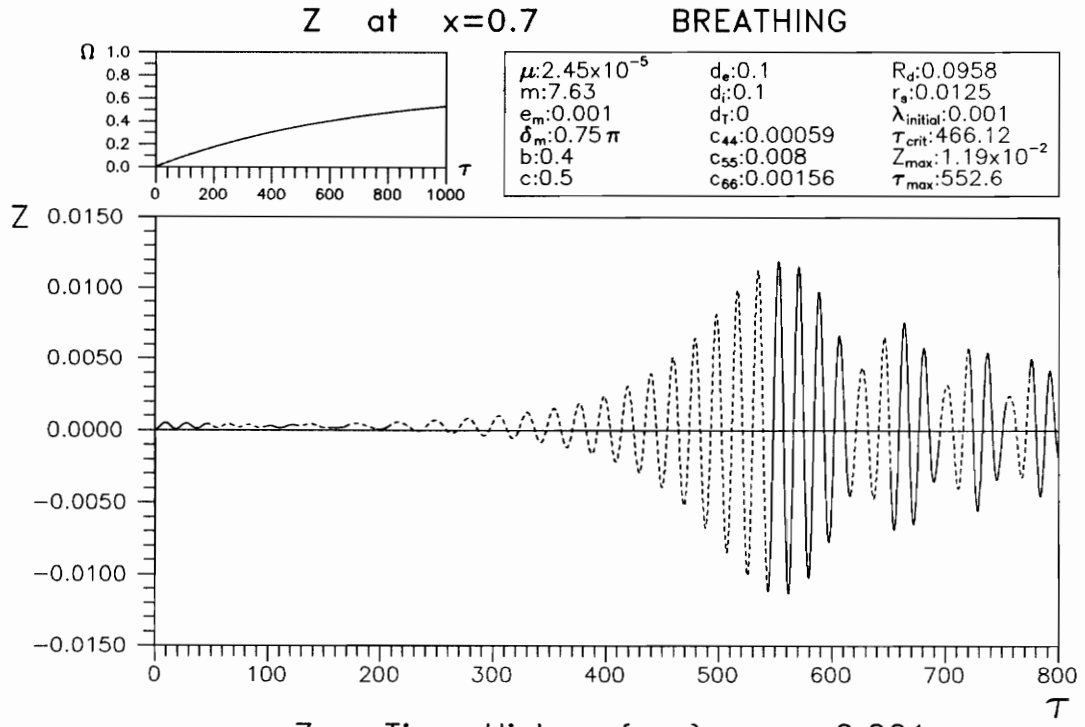

c. Z – Time History for $\lambda_{initial}$ = 0.001

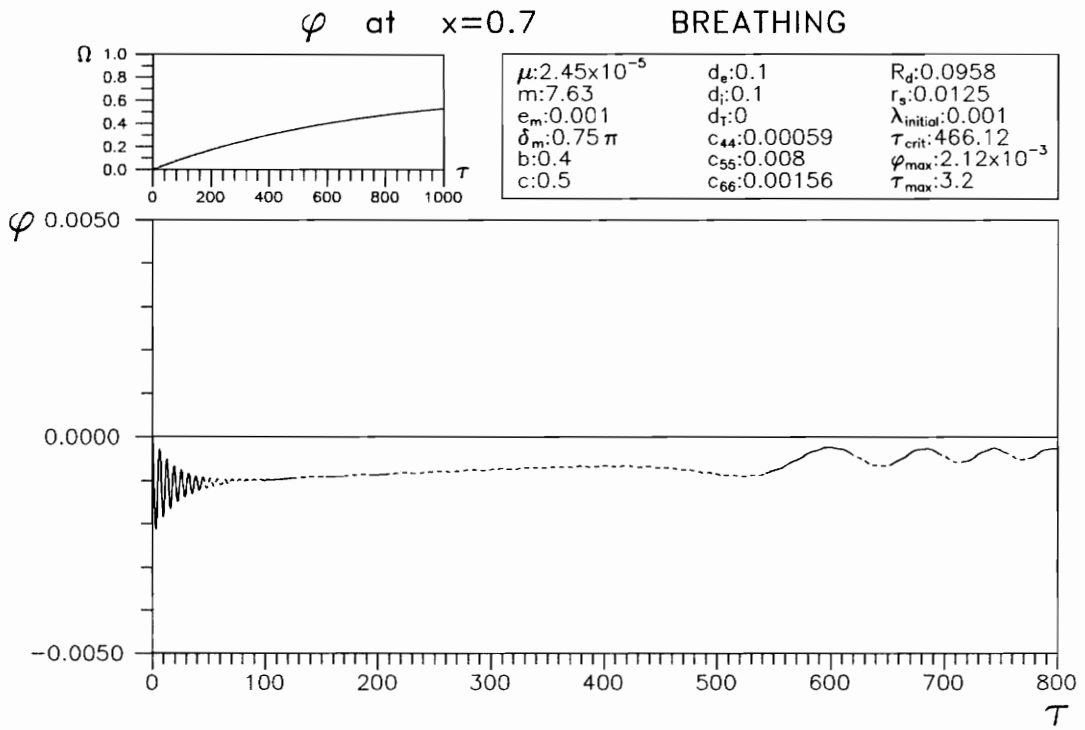

d. φ – Time History for $\lambda_{initial}$ = 0.001

Fig. 5.9 Time History for Exponential Acceleration

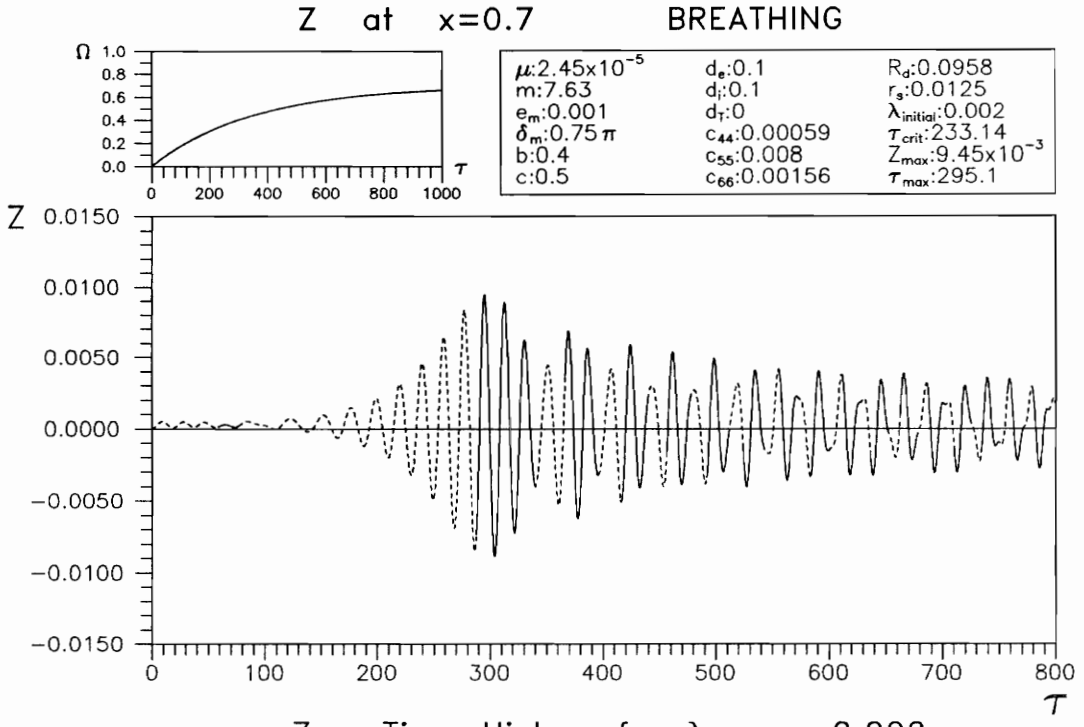

e. Z – Time History for $\lambda_{initial} = 0.002$

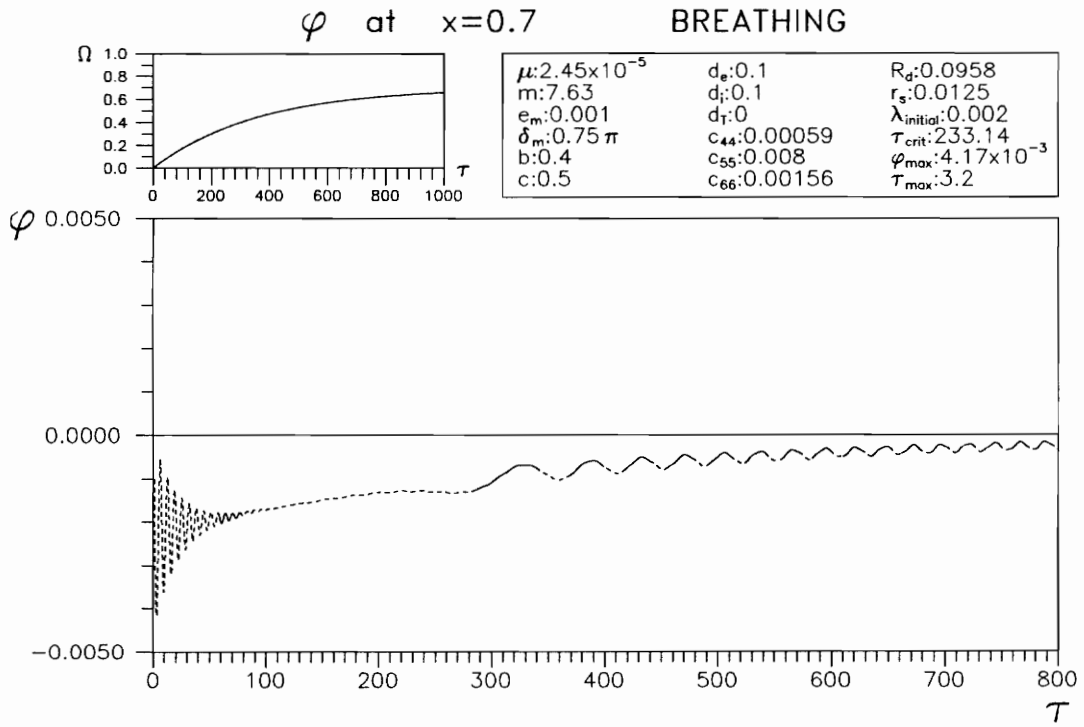

f. φ – Time History for $\lambda_{initial} = 0.002$

Fig. 5.9 Time History for Exponential Acceleration

only. In Fig. 5.9.b, d, and f there is no sudden change because the acceleration is continuous; Ω approaches the angular velocity Ω=0.7 but never becomes constant as in the linear acceleration case (see Fig. 5.4.d, f, and h). After the transient response, the value of the ϕ-torsional deformation tends to increase gradually toward zero.

5.4. Influence of Deceleration

As in the acceleration case, the linear deceleration and the exponential deceleration are investigated in this section. The formulas for the angular velocity and the rotational angle under linear deceleration are shown in equation (3.16). The initial angular velocity Ω under exponential deceleration is 0.7, the same as that under linear deceleration. The initial deceleration $\lambda_{initial}$ under exponential deceleration is taken the same as the linear deceleration λ. In this case, the angular velocity approaches zero as $\tau \to \infty$. The formulas to calculate the angular velocity, the rotational deceleration and the rotational angle for exponential deceleration are defined as follows:

$$\Omega = 0.7\ e^{-a\tau}$$

$$\lambda = -\ 0.7\ a\ e^{-a\tau}$$

$$\theta = -\ \frac{0.7}{a}\ e^{-a\tau} + \frac{0.7}{a} \qquad (5.4)$$

where a is a constant that is determined by $a = -\frac{\lambda_{initial}}{0.7}$. Table 5.6 gives the values of the initial exponential deceleration $\lambda_{initial}$, τ_{crit}, and the 'a' constant. The initial conditions for linear and exponential deceleration are v_1=0.001, w_1=0.001, and ϕ_1 is taken from the acceleration case just before the angular velocity becomes constant.

Table 5.6 τ_{crit} for exponential deceleration

$\lambda_{initial}$	a	τ_{crit}
-0.0005	7.143×10^{-4}	1009.3
-0.0010	1.429×10^{-3}	504.52
-0.0020	2.857×10^{-3}	252.35

The different rates of linear deceleration give different time histories of the z-displacement and the ϕ-torsional deformation as shown in Fig. 5.10.a-j at location $\tilde{x}$=0.7. The time histories of the z-displacement for the flexural-torsional response (Fig. 5.10.a, c, e, g, and i) have almost the same characteristics as those for flexural response only (Fig. 3.7.a-e). Following initial transient motion, the ϕ-torsional deformation under linear deceleration begins vibrating around τ=τ_{crit}; after that, the ϕ-torsional deformation reaches a maximum amplitude and then decreases gradually. When the linear deceleration λ reaches zero, there is a sudden change in the ϕ-time histories (see Fig. 5.10.h and 5.10.j). Then, the ϕ-torsional deformation vibrates as in the beginning for a while, decreasing and approaching zero.

The relation between the linear deceleration and the maximum z-displacement ($z_{max,x}$ at location $\tilde{x}$ = 0.7 and $z_{max,w}$ over the whole length) is shown in Fig. 5.11.a. Larger deceleration gives smaller maximum z-displacement. This relation is similar to the relation between the linear deceleration and the maximum amplitude of the ϕ-torsional deformation at location $\tilde{x}$ = 0.7 in Fig.

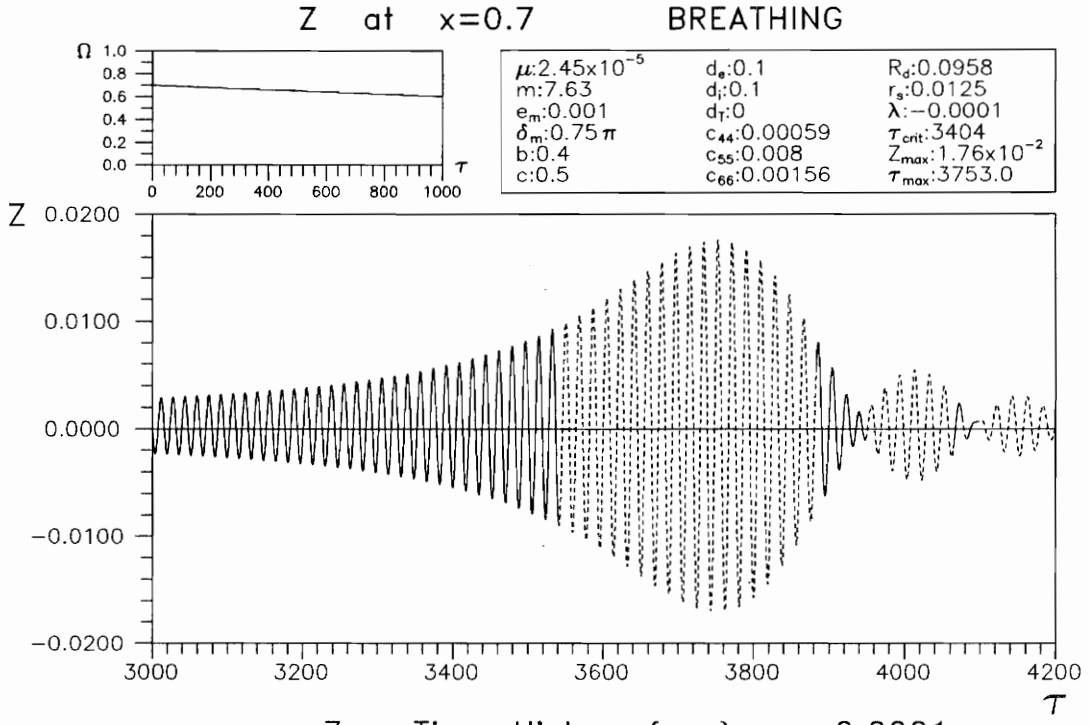

a. Z − Time History for λ = −0.0001

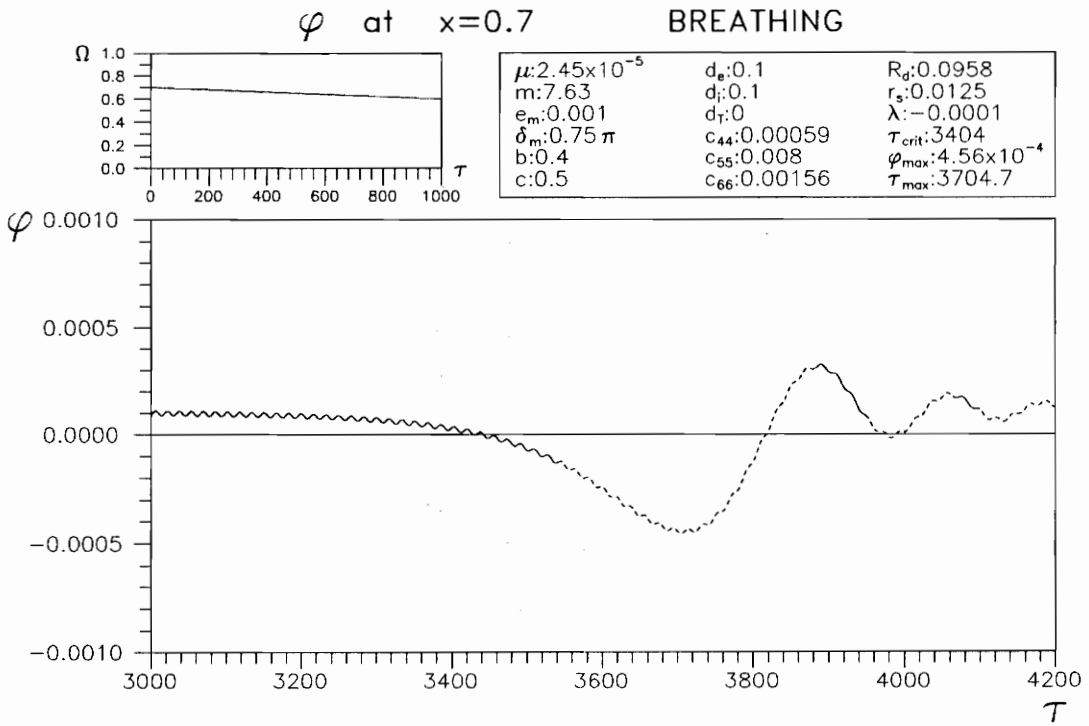

b. φ − Time History for λ = −0.0001

Fig. 5.10 Time History for Linear Deceleration

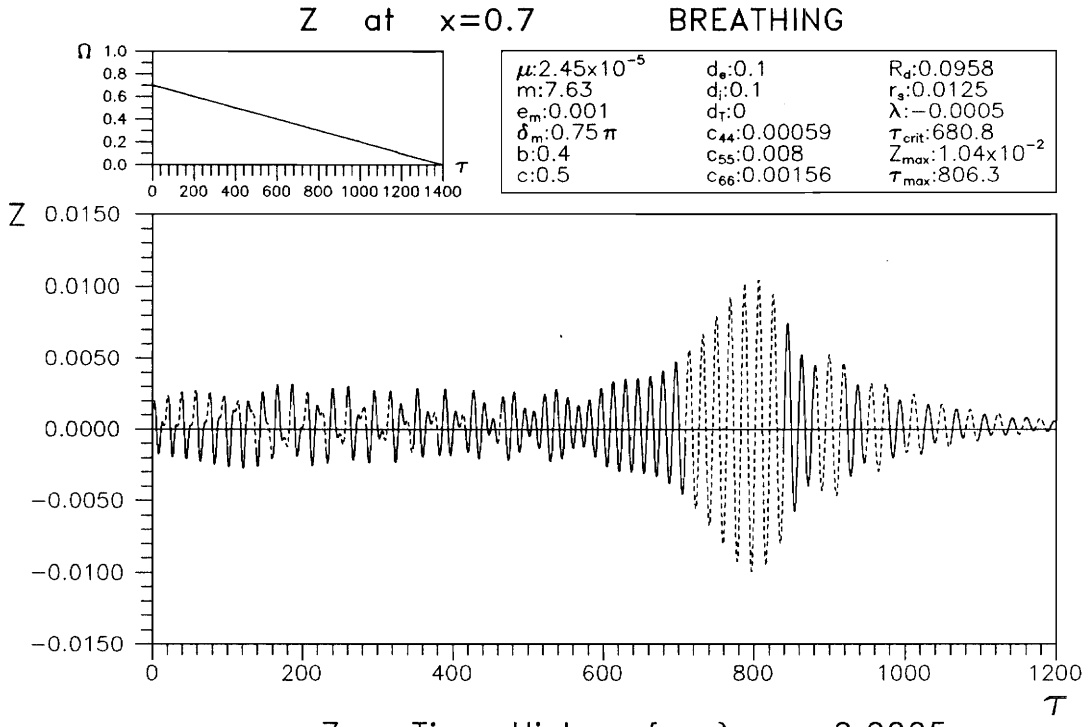

c. Z – Time History for λ = −0.0005

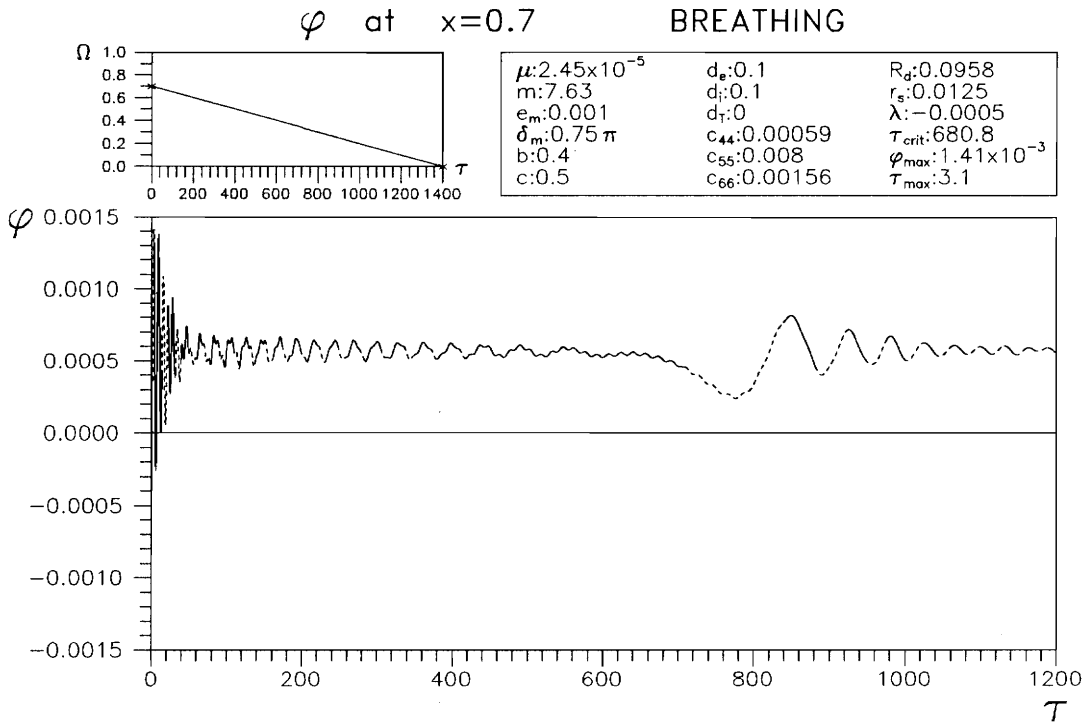

d. φ – Time History for λ = −0.0005

Fig. 5.10 Time History for Linear Deceleration

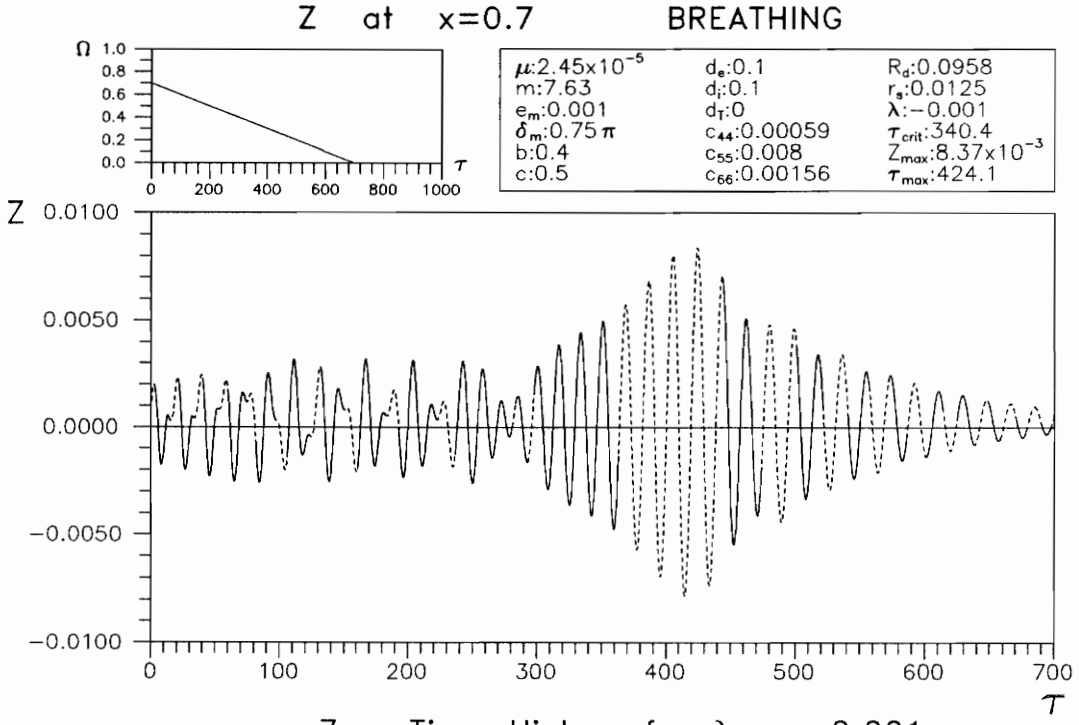

e. Z – Time History for λ = −0.001

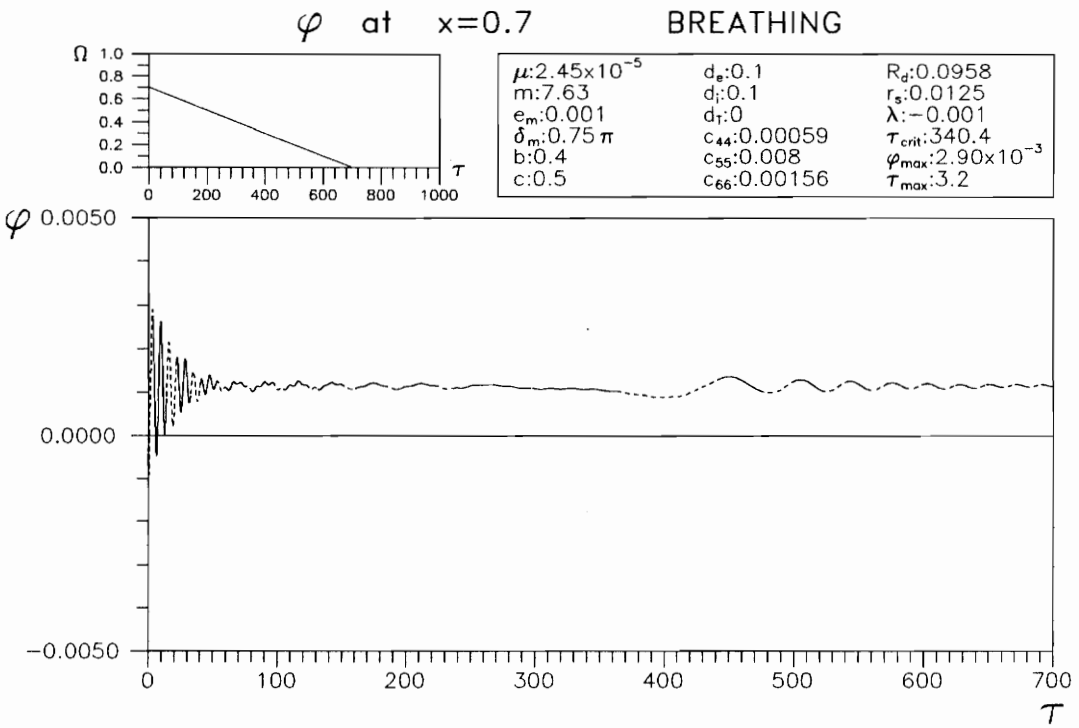

f. φ – Time History for λ = −0.001

Fig. 5.10 Time History for Linear Deceleration

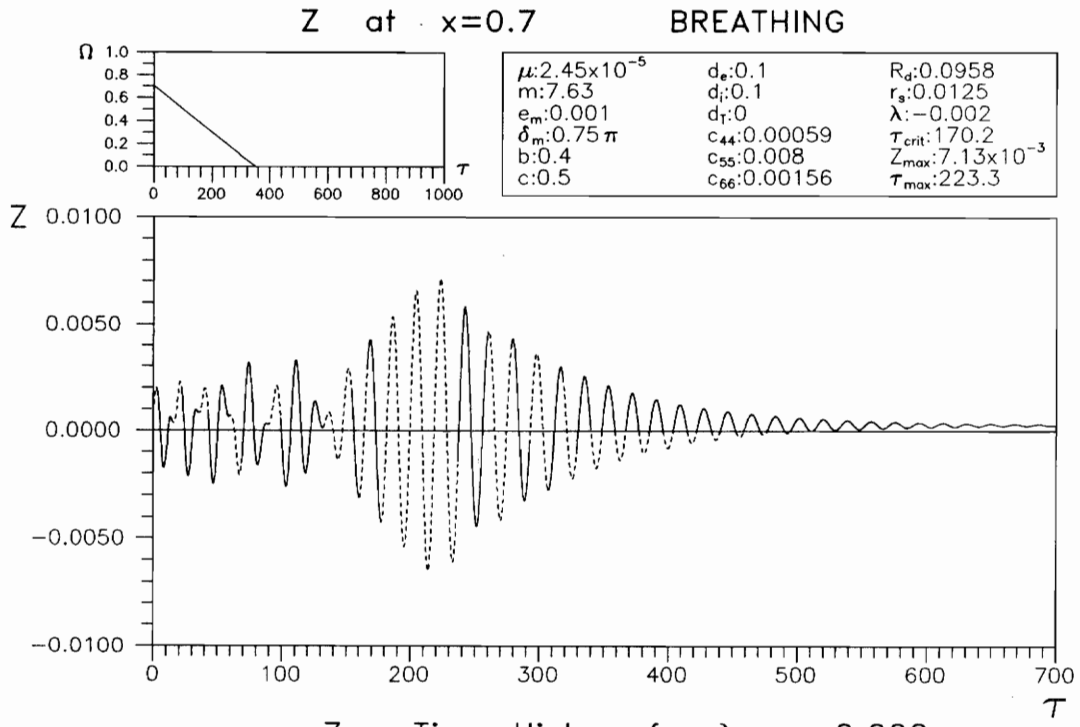

g. Z – Time History for λ = −0.002

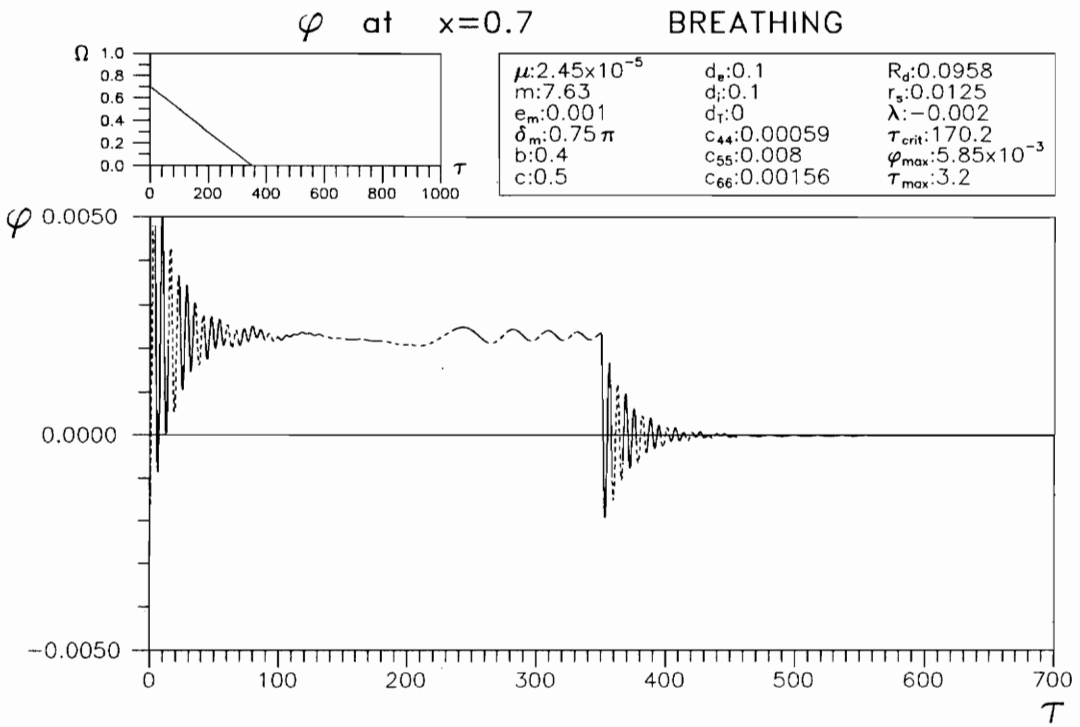

h. φ – Time History for λ = −0.002

Fig. 5.10 Time History for Linear Deceleration

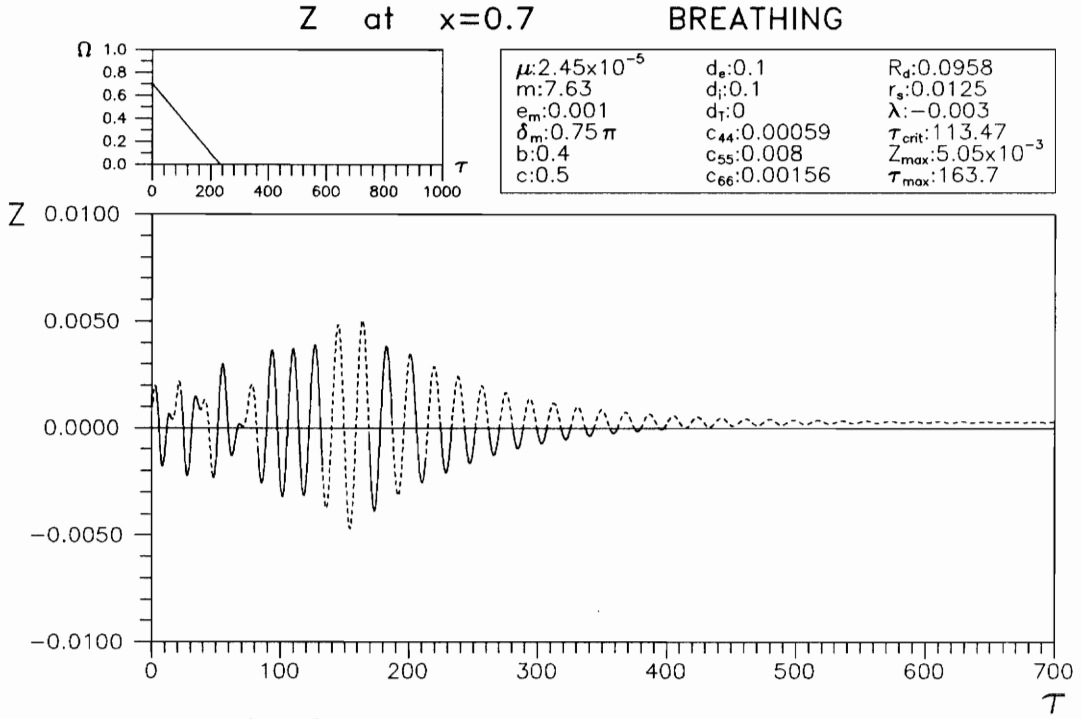

i. Z − Time History for $\lambda = -0.003$

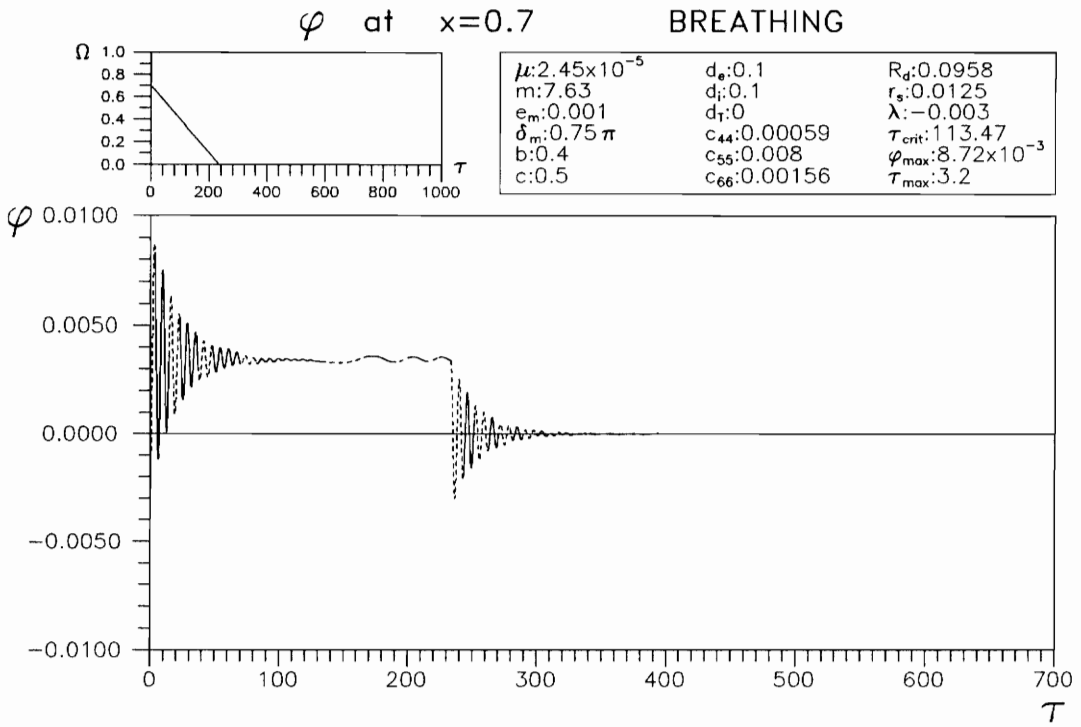

j. φ − Time History for $\lambda = -0.003$

Fig. 5.10 Time History for Linear Deceleration

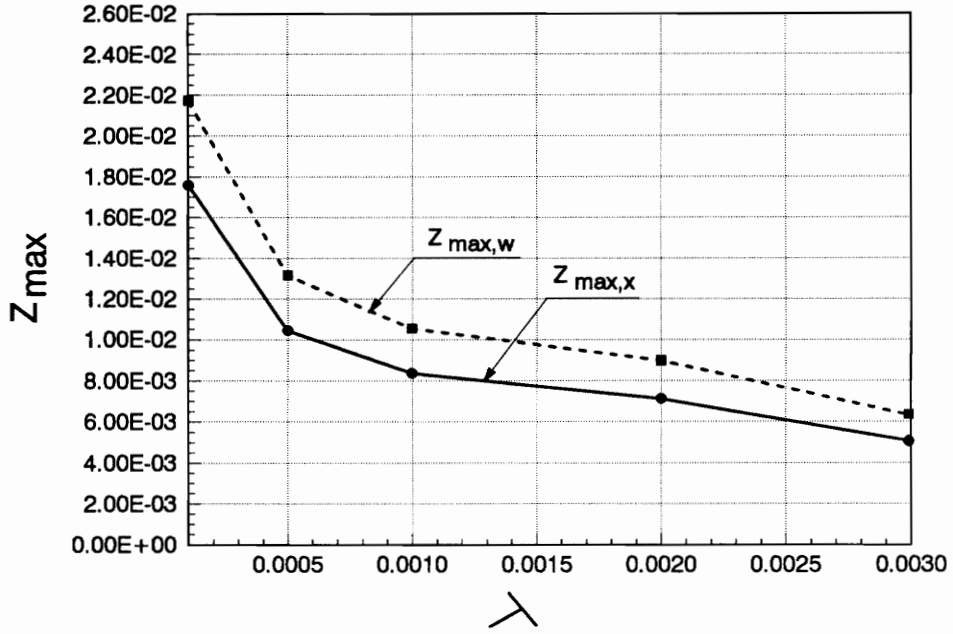

a. Linear Deceleration Rate vs. Z_{max}

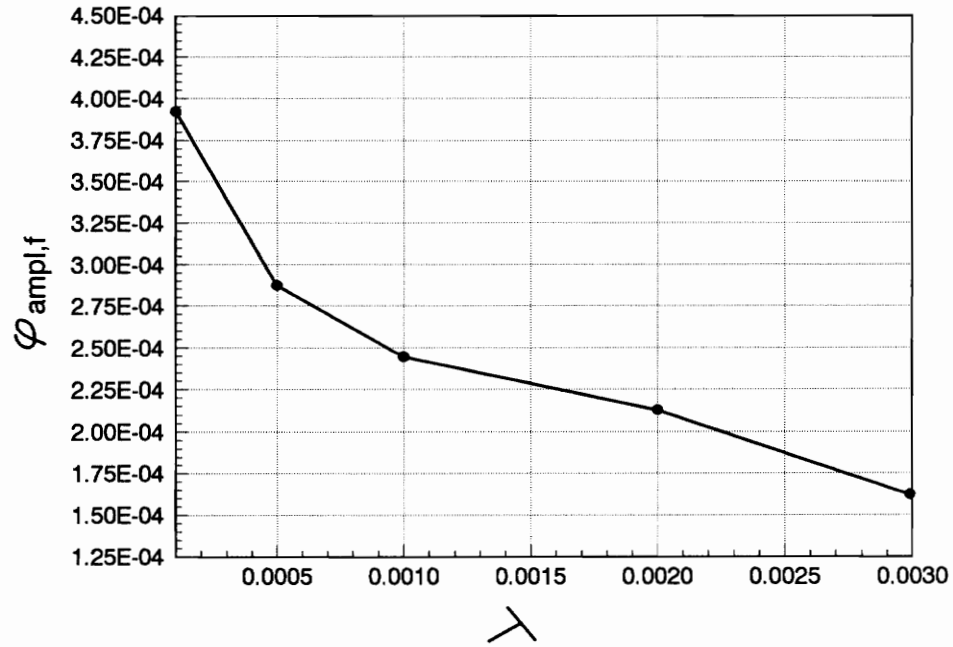

b. Linear Deceleration Rate vs. $\varphi_{ampl,f}$

Fig. 5.11 Influence of Linear Deceleration Rate

5.11.b.

Figures 5.12.a-f show the time histories of the z-displacement and ϕ-torsional deformation at location $\tilde{x}$=0.7 under the exponential deceleration. The torsional deformation in Fig. 5.12.b, d, and f decreases gradually from positive values, approaching zero. This is the opposite of the case of the exponential acceleration (Fig. 5.9.b, d, and f) where ϕ increases gradually, approaching zero from negative values.

5.5. Influence of External Damping

In this section, the influence of the external torsional damping d_T and external damping d_e for the standard case is investigated. Figures 5.4.f and 5.13.a-c show the influence of different torsional dampings $\tilde{d}_T$, i.e., $\tilde{d}_T$ = 0, 0.5, 1.0, and 1.5, on the ϕ-time histories at location $\tilde{x}$=0.7. The amplitudes of the ϕ-torsional deformation in those curves have similar characteristics except for differences in $\phi_{mean,f}$. For $\tilde{d}_T$=0, $\phi_{mean,f}$ is constant, and for $\tilde{d}_T > 0$, $\phi_{mean,f}$ decreases gradually. Larger $\tilde{d}_T$ causes more decrease in $\phi_{mean,f}$. If $\tilde{d}_T$ becomes twice as large, $\phi_{mean,f}$ decreases almost twice also. The time histories of the z-displacement for different values of the external torsional damping $\tilde{d}_T$ almost do not change anything in their characteristics and values. All of the cases give similar z-time histories to that in Fig. 5.4.e.

In Fig. 5.4.e and 5.14.a-d, the time histories of the z-displacement are displayed for the standard case at location $\tilde{x}$=0.7 with different values of external damping $\tilde{d}_e$, i.e., $\tilde{d}_e$ = 0.1, 0, 0.5, 1.0, and 1.5. Figures 5.4.f and 5.15.a-b show the time histories of the ϕ-torsional deformation with different external dampings $\tilde{d}_e$, i.e., $\tilde{d}_e$ = 0.1, 0, and 0.5. From those figures, it can be seen the external damping

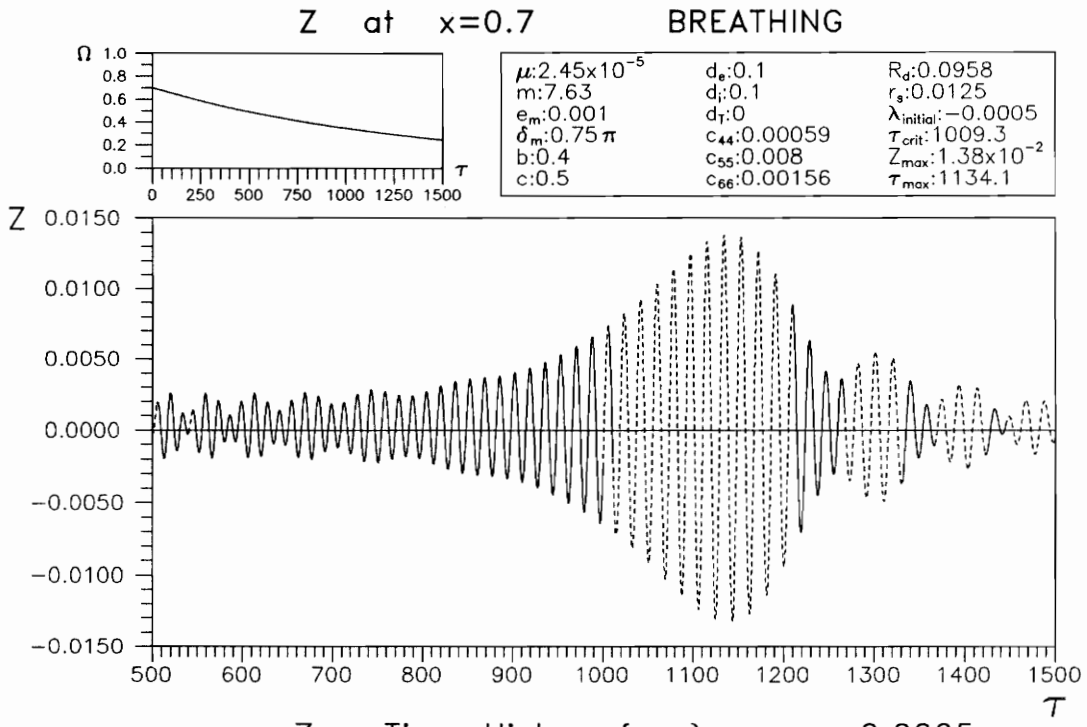

a. Z – Time History for $\lambda_{initial} = -0.0005$

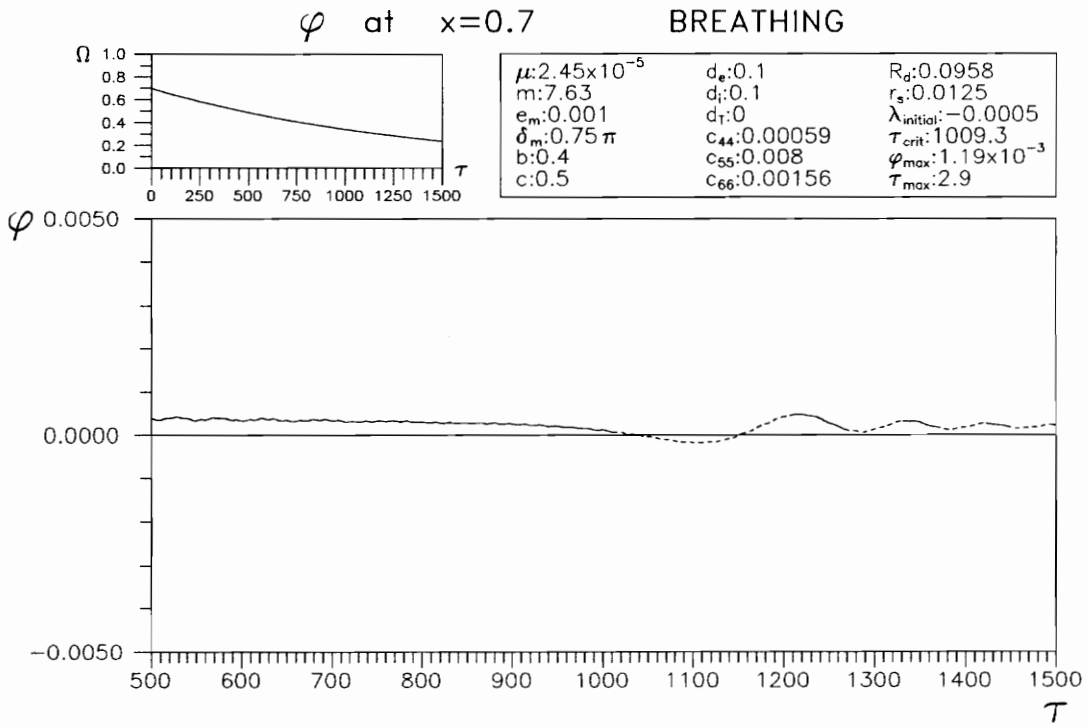

b. φ – Time History for $\lambda_{initial} = -0.0005$

Fig. 5.12 Time History for Exponential Deceleration

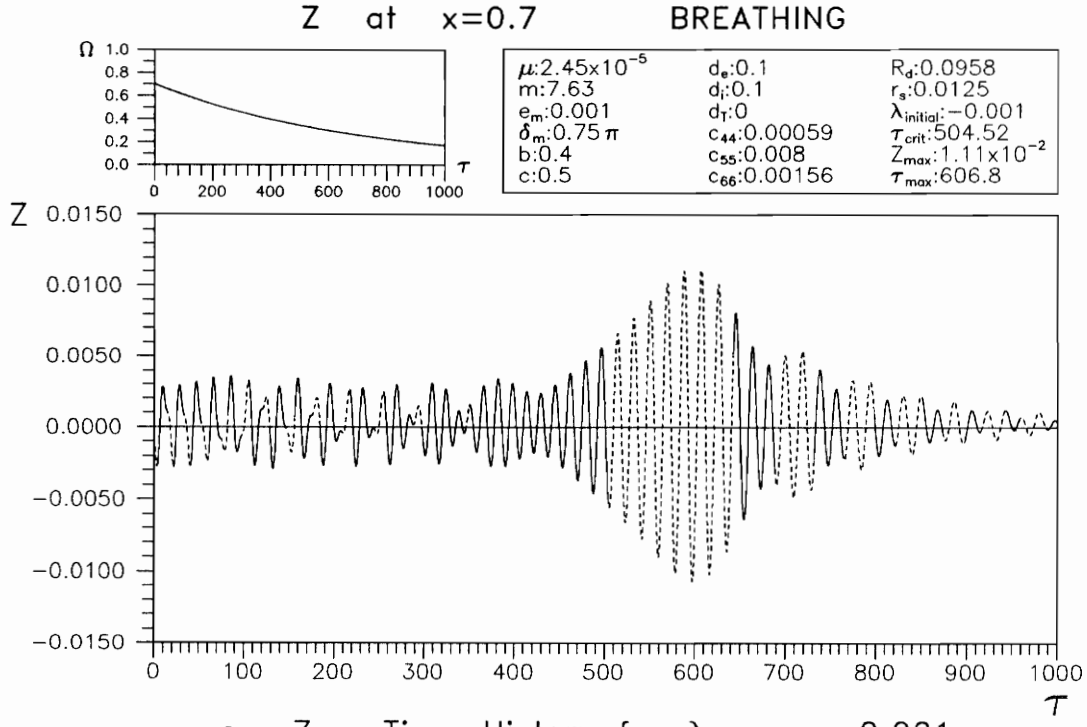

c. Z – Time History for $\lambda_{initial} = -0.001$

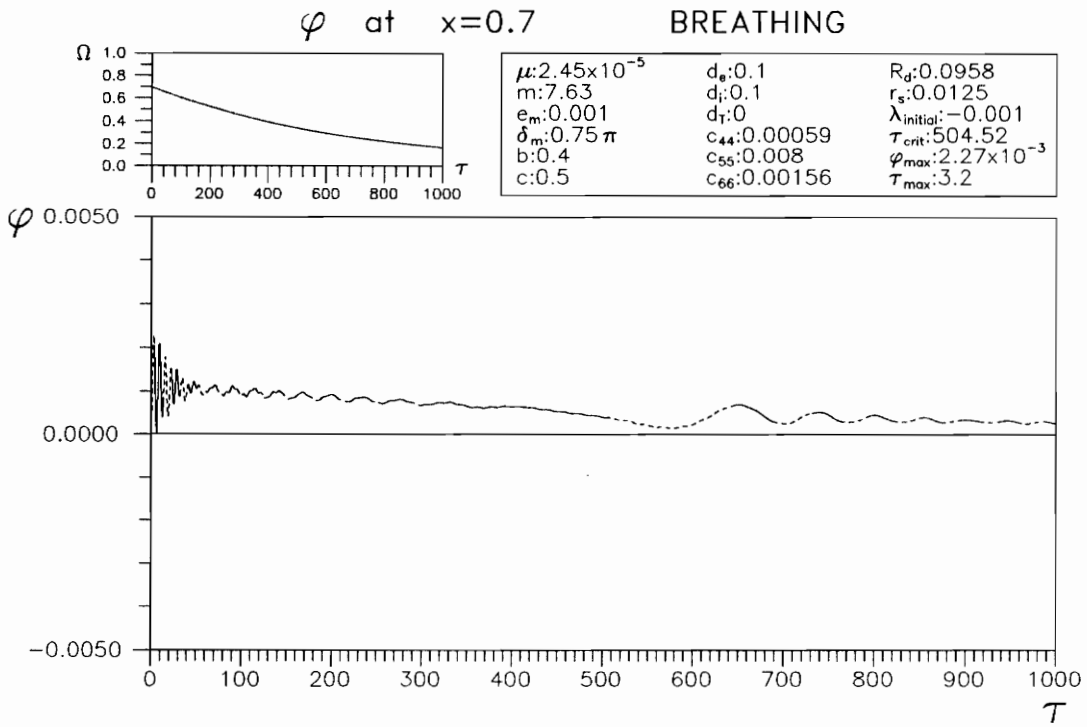

d. φ – Time History for $\lambda_{initial} = -0.001$

Fig. 5.12 Time History for Exponential Deceleration

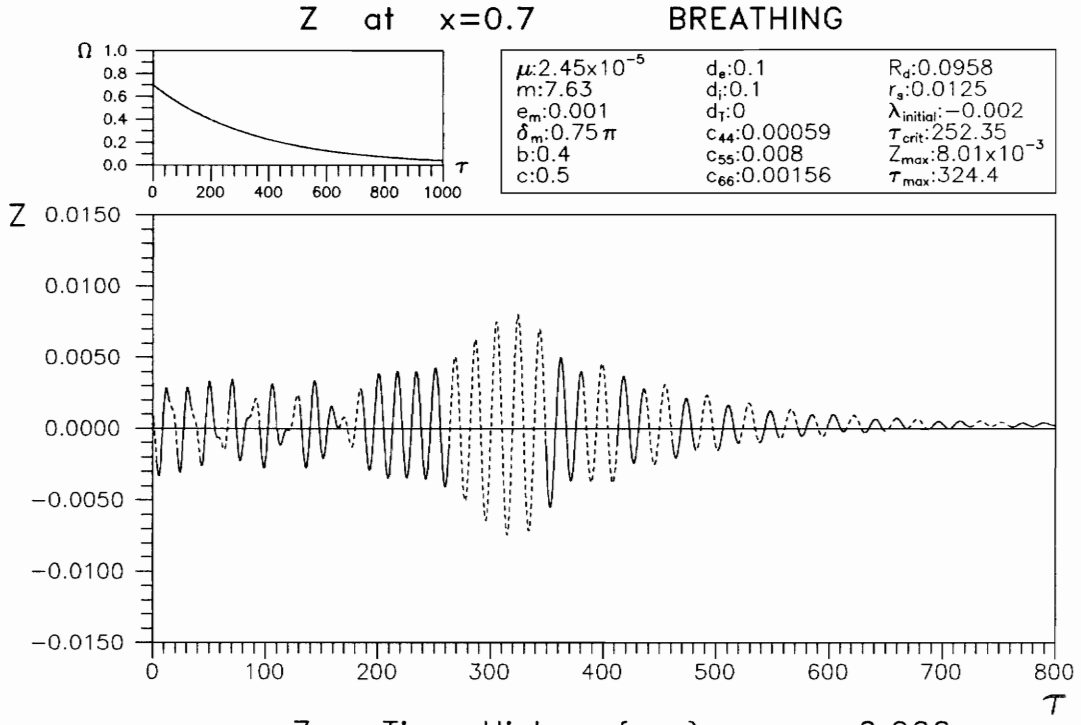

e. Z – Time History for $\lambda_{initial} = -0.002$

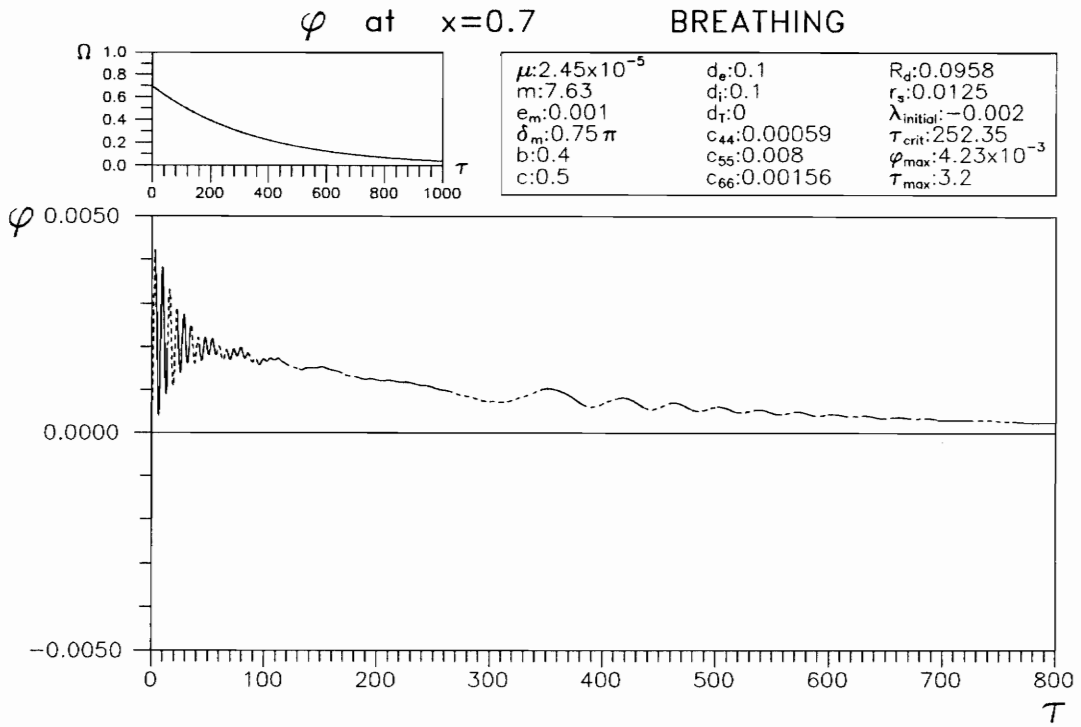

f. φ – Time History for $\lambda_{initial} = -0.002$

Fig. 5.12 Time History for Exponential Deceleration

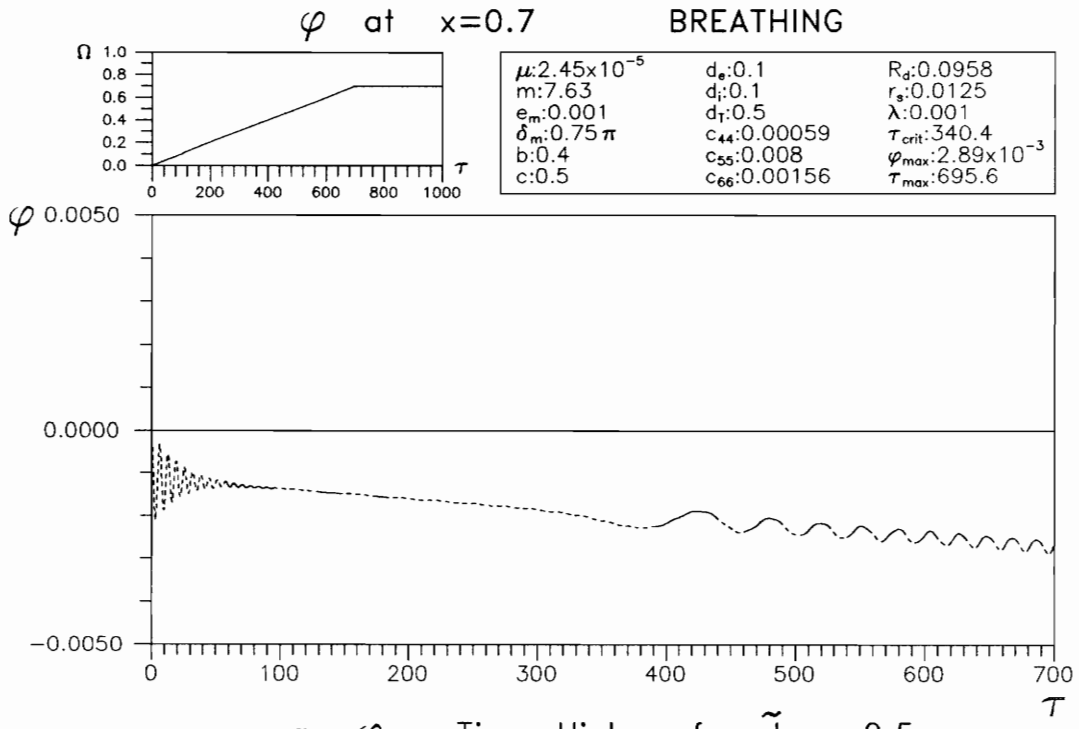

a. φ – Time History for $\tilde{d}_T = 0.5$

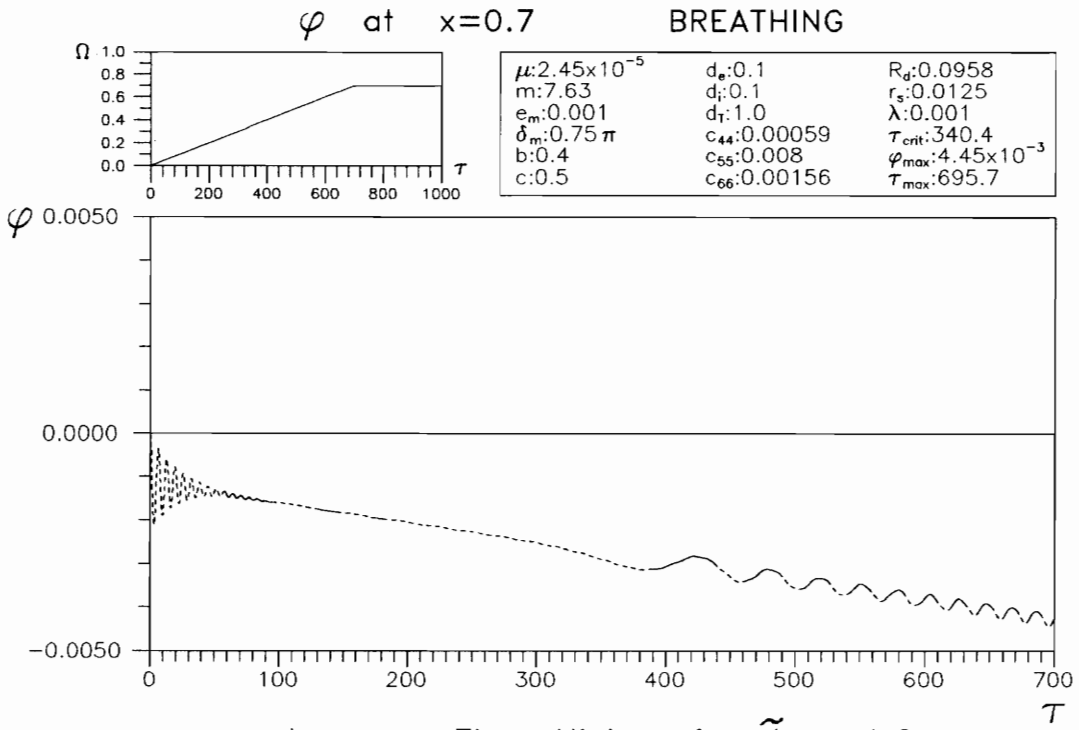

b. φ – Time History for $\tilde{d}_T = 1.0$

Fig. 5.13 φ – Time History with Torsional External Damping

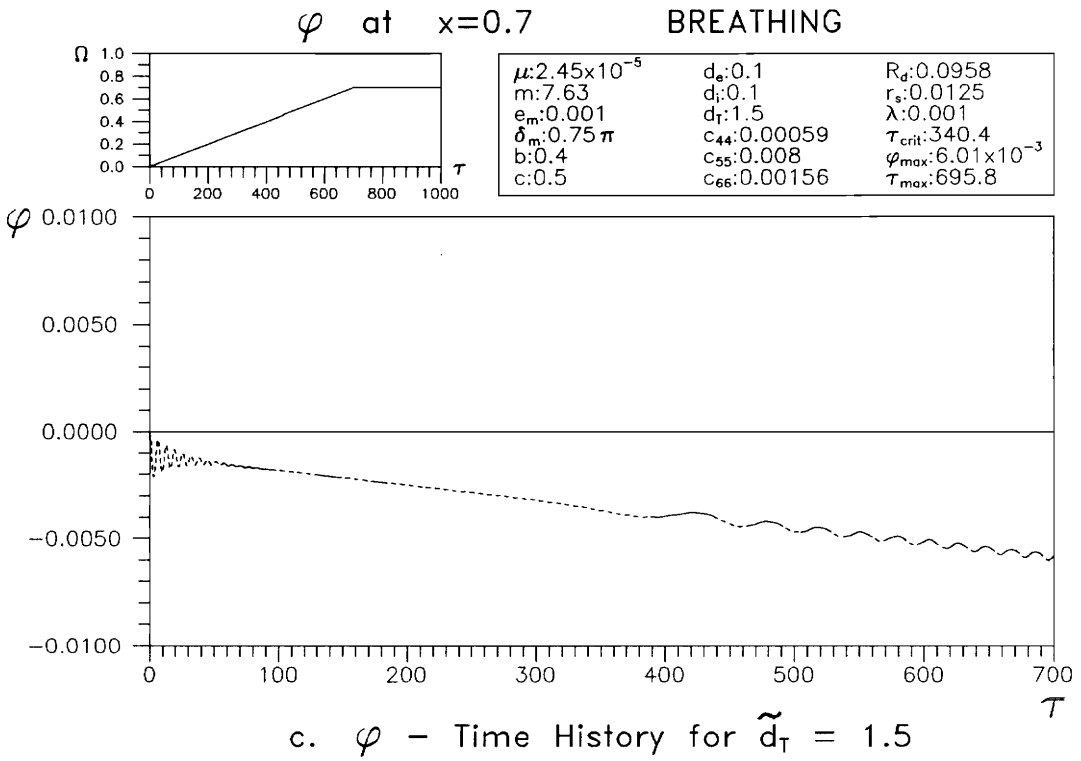

c. φ – Time History for $\tilde{d}_T = 1.5$

Fig. 5.13 φ – Time History with Torsional External Damping

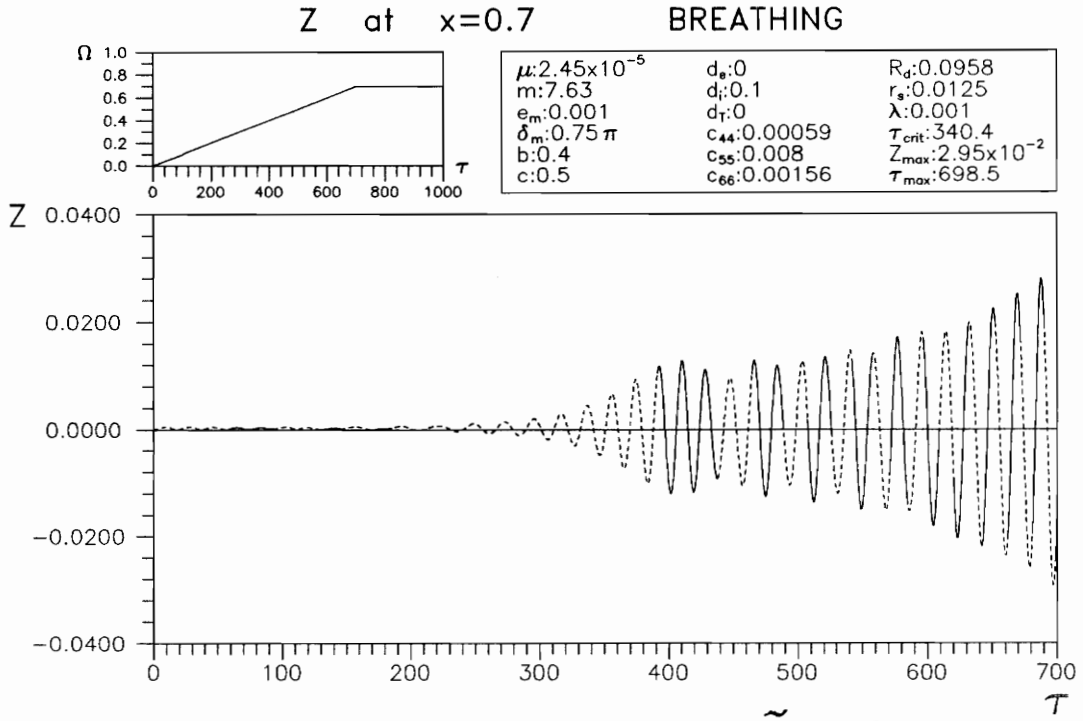

a. Z – Time History for $\tilde{d}_e = 0$

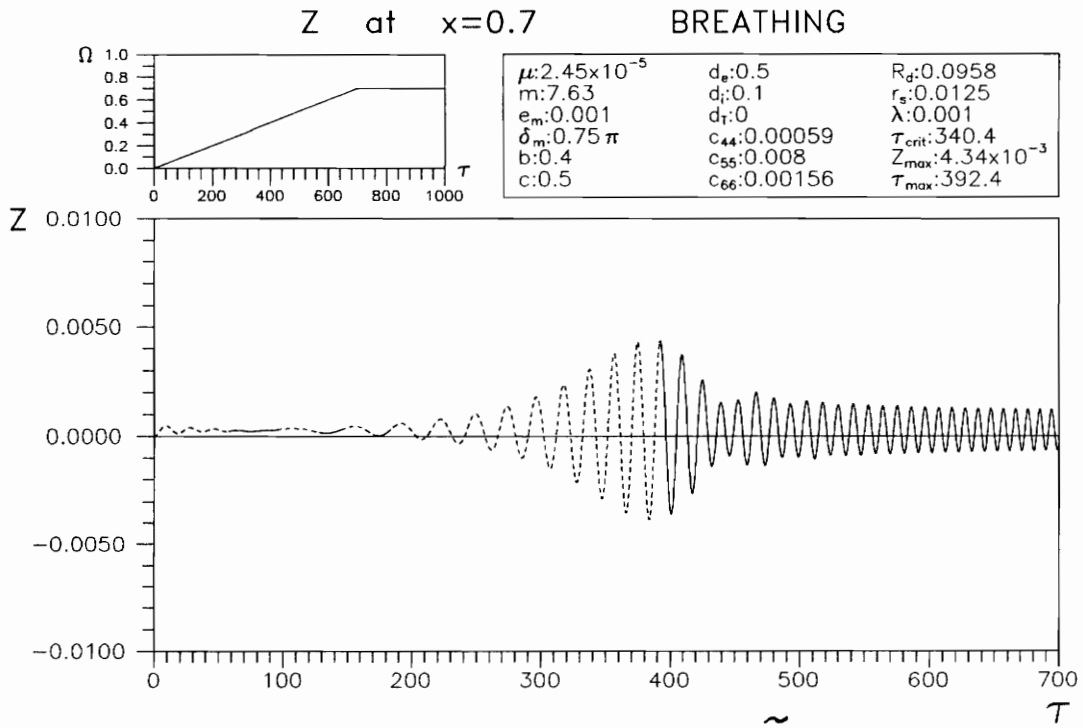

b. Z – Time History for $\tilde{d}_e = 0.5$

Fig. 5.14 Z – Time History with External Damping

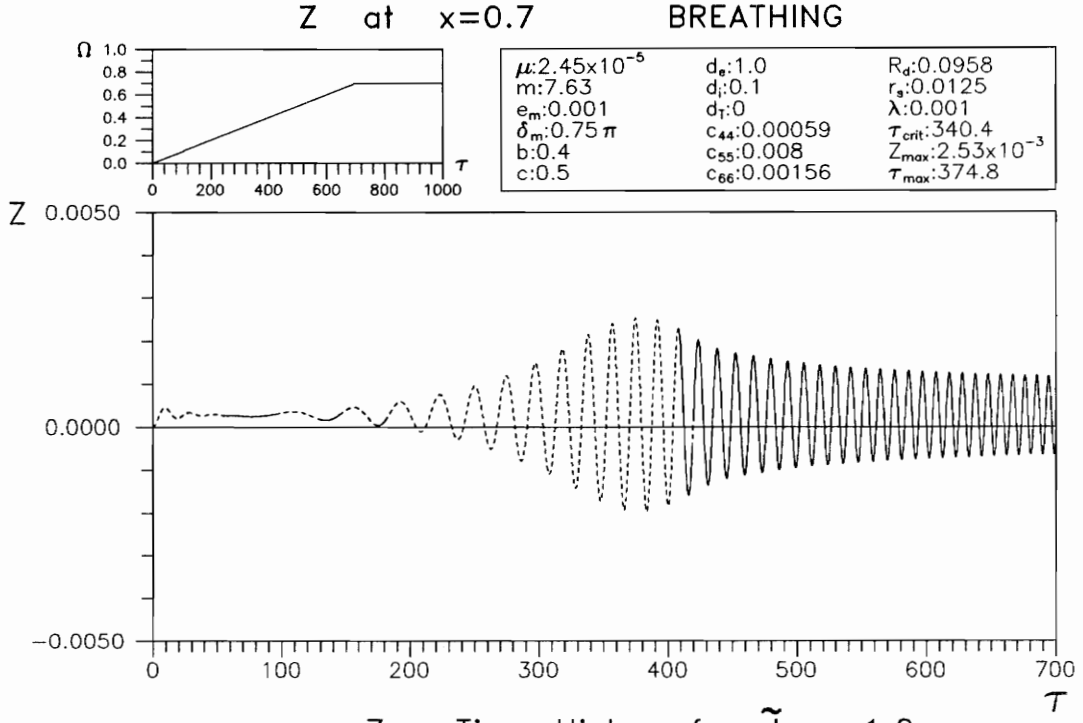

c. Z – Time History for $\tilde{d}_e = 1.0$

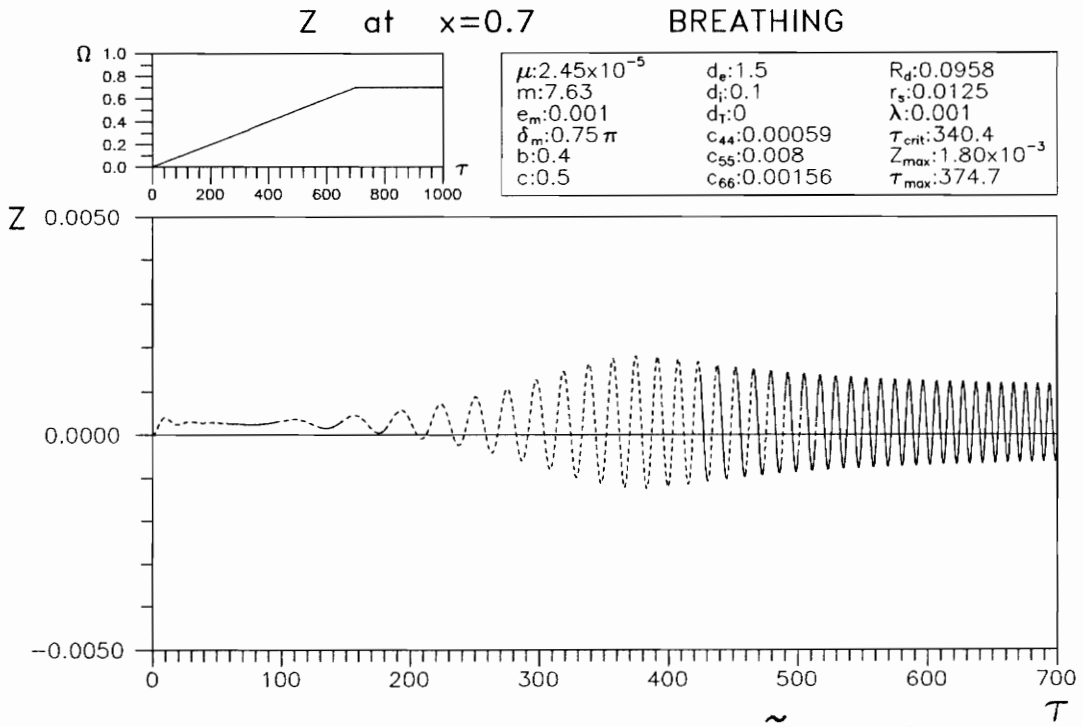

d. Z – Time History for $\tilde{d}_e = 1.5$

Fig. 5.14 Z – Time History with External Damping

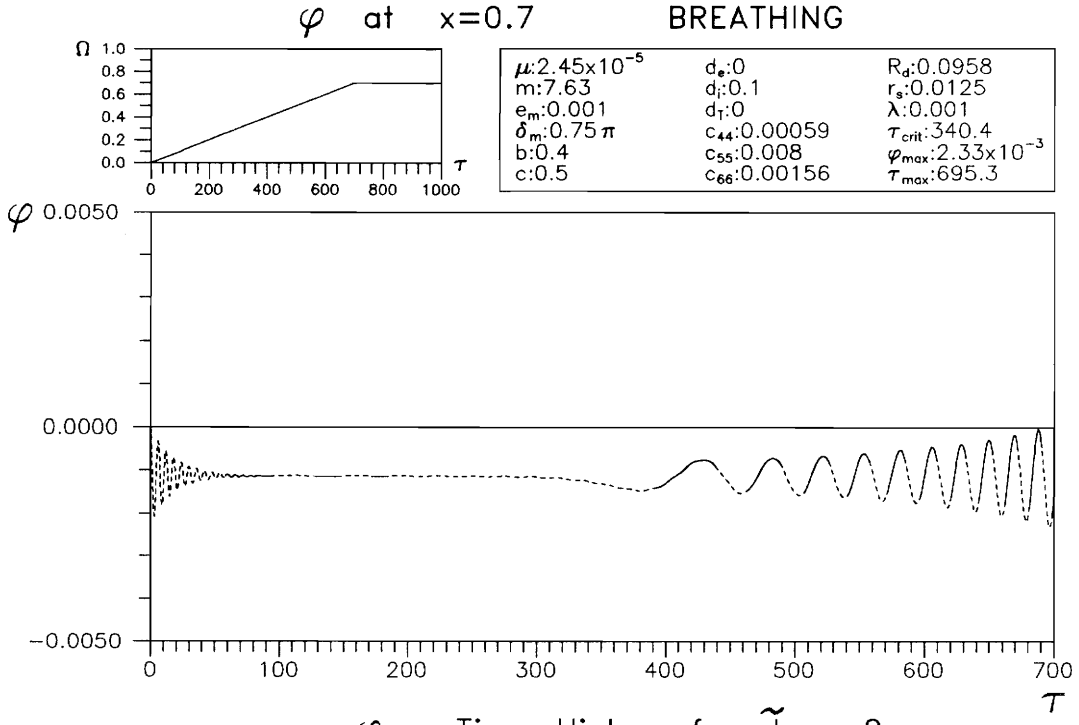

a. φ – Time History for $\tilde{d}_e = 0$

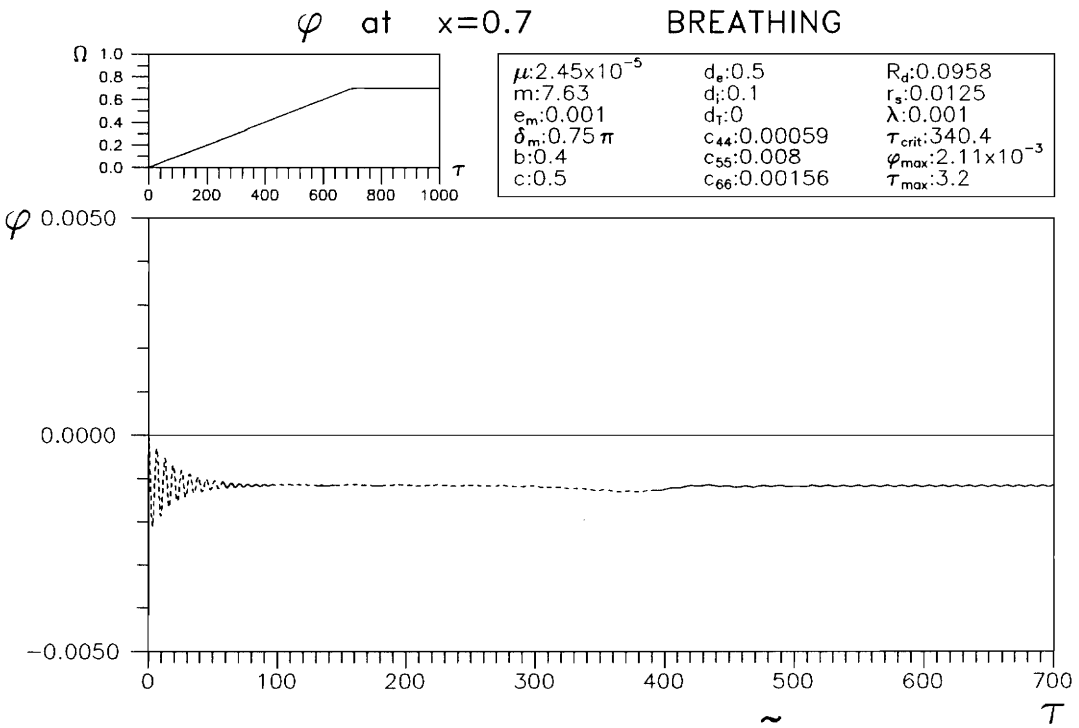

b. φ – Time History for $\tilde{d}_e = 0.5$

Fig. 5.15 φ – Time History with External Damping

$\tilde{d}_e$ has much influence on the z-displacement and the ϕ-torsional deformation. In the case of no external damping (Fig. 5.14.a and 5.15.a), the z-displacement and ϕ-torsional deformation for large τ do not decrease but increase. However, in the other cases, with $\tilde{d}_e > 0$ (Fig. 5.4.e and 5.14.b-d), the external damping $\tilde{d}_e$ makes the z-displacement decrease after reaching its maximum. The external damping $\tilde{d}_e$ also reduces the maximum z-displacement (see Table 5.7). For external damping $\tilde{d}_e > 0$, the crack on the rotating shaft is closed most of the time after the maximum z-displacement is reached. For the case of no external damping, the crack always exhibits a breathing condition.

Table 5.7 Influence of external damping

$\tilde{d}_e$	$z_{max,x}$	$z_{max,w}$
0.00	2.95×10^{-2}	3.69×10^{-2}
0.10	9.34×10^{-3}	1.17×10^{-2}
0.50	4.34×10^{-3}	5.45×10^{-3}
1.00	2.53×10^{-3}	3.17×10^{-3}
1.50	1.80×10^{-3}	2.25×10^{-3}

As shown in Fig. 5.4.f and 5.15.a-b, greater external damping causes smaller vibration of the ϕ-torsional deformation. The time histories of the ϕ-torsional deformation for $\tilde{d}_e = 1.0$ and $\tilde{d}_e = 1.5$ have similar characteristics to the case with $\tilde{d}_e = 0.5$, but with smaller vibration.

5.6. Infuence of Internal Damping

Based on the standard case of flexural-torsional deformation, the influence of internal damping $\tilde{d}_i$ is studied in this section. Table 5.8 shows the relation between the internal damping $\tilde{d}_i$ and the maximum z-displacement ($z_{max,x}$ at location $\tilde{x}$=0.7 and $z_{max,w}$ over the whole length). There are 6 different internal dampings, i.e., $\tilde{d}_i$ = 0, 0.025, 0.050, 0.075, 0.10, 0.125.

Table 5.8 Influence of internal damping

$\tilde{d}_i$	$z_{max,x}$	$z_{max,w}$
0	9.159×10^{-3}	1.150×10^{-2}
0.025	9.204×10^{-3}	1.155×10^{-2}
0.050	9.249×10^{-3}	1.160×10^{-2}
0.075	9.294×10^{-3}	1.166×10^{-2}
0.100	9.338×10^{-3}	1.172×10^{-2}
0.125	9.382×10^{-3}	1.177×10^{-2}

As mentioned in section 5.3, larger internal damping gives larger maximum z-displacement. If the internal damping is sufficiently large, the system becomes unstable after passing the critical speed, as shown in Fig. 5.16 for $\tilde{d}_i$=0.2. This was discussed for the constant angular velocity condition by Plaut[33]; internal damping increases the possibility of instability of the system. Huseyin[14] stated in his book that the unstable condition can be stabilized with the addition of

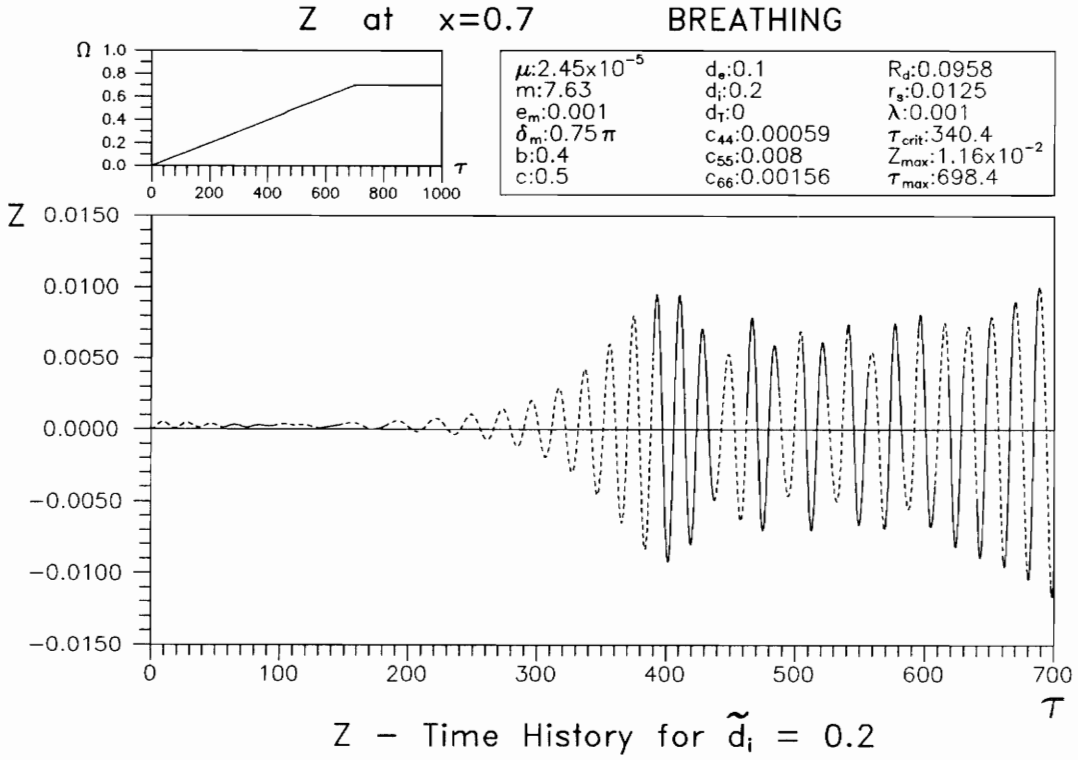

Z − Time History for $\tilde{d}_i = 0.2$

Fig. 5.16 Z − Time History with Internal Damping

external damping. It is interesting to know the relation between the internal damping and the external damping for stable conditions. Therefore, in the following paragraphs, this relation is derived using the procedure from Huseyin[14], page 162 (except the equations 5.149 and 5.150 in that reference contain errors).

Based on equations (4.22) and (4.23), the transition between stable and unstable conditions is determined for constant angular velocity Ω and no crack. It is also assumed that

- torsional external damping $\tilde{d}_T = 0$
- eccentricity of disk $\tilde{e}_m = 0$
- gravity $g = 0$
- circular cross section $\Gamma = 1$

In this case, the torsional deformation does not have an influence on the transverse motion.

Based on these assumptions, equations (4.22) and (4.23) for the first term only become

$$\ddot{\tilde{v}}_1 + \tilde{m} \sin^2 \alpha_1 \ddot{\tilde{v}}_1 = - \tilde{v}_1 + 2 \Omega \dot{\tilde{w}}_1 + \Omega^2 \tilde{v}_1 + \tilde{m} \sin \alpha_1 (2 \Omega \dot{\tilde{w}}_1 + \Omega^2 \tilde{v}_1) \sin \alpha_1 - \tilde{d}_e (\dot{\tilde{v}}_1 - \Omega \tilde{w}_1) - \tilde{d}_i \dot{\tilde{v}}_1 \quad (5.5)$$

$$\ddot{\tilde{w}}_1 + \tilde{m} \sin^2 \alpha_1 \ddot{\tilde{w}}_1 = - \tilde{w}_1 - 2 \Omega \dot{\tilde{v}}_1 + \Omega^2 \tilde{w}_1 - \tilde{m} \sin \alpha_1 (2 \Omega \dot{\tilde{v}}_1 - \Omega^2 \tilde{w}_1) \sin \alpha_1 - \tilde{d}_e (\dot{\tilde{w}}_1 + \Omega \tilde{v}_1) - \tilde{d}_i \dot{\tilde{w}}_1 \quad (5.6)$$

Let : $a = \tilde{d}_e + \tilde{d}_i$, $c = 1 + \tilde{m}^2 \sin^2 \alpha_1$

$b = 1 - \Omega^2 - \tilde{m} \Omega^2 \sin^2 \alpha_1$, $d = \tilde{d}_e$

Then, equations (5.5) and (5.6) can be written as follows:

$$c\,\ddot{\tilde{v}}_1 + a\,\dot{\tilde{v}}_1 - 2\,\Omega\,c\,\dot{\tilde{w}}_1 + b\,\tilde{v}_1 - d\,\Omega\,\tilde{w}_1 = 0 \tag{5.7}$$

$$c\,\ddot{\tilde{w}}_1 + a\,\dot{\tilde{w}}_1 + 2\,\Omega\,c\,\dot{\tilde{v}}_1 + b\,\tilde{w}_1 + d\,\Omega\,\tilde{v}_1 = 0 \tag{5.8}$$

With the complex displacement $y = \tilde{v}_1 + i\,\tilde{w}_1$, the equations (5.7) and (5.8) can be combined into one complex equation:

$$c\,\ddot{y} + a\,\dot{y} + 2\,\Omega\,c\,i\,\dot{y} + b\,y + d\,\Omega\,i\,y = 0 \tag{5.9}$$

Asumming $y = z\,e^{i\omega\tau}$, equation (5.9) becomes

$$-\omega^2\,c + a\,i\,\omega - 2\,\Omega\,c\,\omega + b + d\,\Omega\,i = 0 \tag{5.10}$$

At the onset of instability (ω real) there are two conditions that have to be satisfied, i.e.,

$$-\omega^2\,c - 2\,\Omega\,c\,\omega + b = 0 \tag{5.11}$$

$$a\,\omega + d\,\Omega = 0 \tag{5.12}$$

By eliminating ω using equation (5.12), equation (5.11) becomes a quadratic equation in $\frac{d}{a}$ as follows:

$$\frac{d}{a}^2 - 2\,\frac{d}{a} - \frac{b}{\Omega^2\,c} = 0 \tag{5.13}$$

Hence, the transition between stable and unstable regions can be defined by

$$\left(\frac{d}{a}\right)_{1,2} = 1 \pm \sqrt{1 + \frac{b}{\Omega^2\,c}}$$

From this result, the relation between the internal damping and external damping depends on the angular velocity Ω, the disk location $\tilde{c}$, and the mass of the disk $\tilde{m}$. By using the Routh-Hurwitz conditions (Huseyin[14], page 51), the system is stable if

$$\left(\frac{d}{a}\right)_1 < \frac{d}{a} < \left(\frac{d}{a}\right)_2 \tag{5.14}$$

For example, let $\tilde{m} = 7.63$, $\Omega = 0.7$, and $\tilde{c} = 0.5$. The transition points can be

determined to be

$$\left(\frac{d}{a}\right)_1 = 1.4863 \qquad \left(\frac{d}{a}\right)_2 = 0.5137$$

With the external damping $\tilde{d}_e = 0.1$, the system is stable if the internal damping $\tilde{d}_i$ is between 0 and 0.0947.

For the standard case, the angular velocity is a function of time. Also, there is a breathing crack, more than one mode is used, gravity is not neglected, and eccentricity is present. Therefore, this result can not be used directly. With $\tilde{d}_e$=0.1, the shaft becomes unstable for values of $\tilde{d}_i$ larger than approximately 0.15 (see Fig. 5.16).

The percentage of the damping ratio ($\tilde{d}_i$+$\tilde{d}_e$ relative to critical damping) for the transverse displacement of the first mode for the standard case with angular velocity Ω=0 is 3.40%, and the logarithmic decrement is 0.214. The percentage of the damping ratio (involving $\tilde{d}_i$ and $\tilde{d}_T$) for the torsional deformation for the same conditions is 5.26% and the logarithmic decrement is 0.331.

5.7. Influence of Crack Location

The influence of the crack location on flexural-torsional response is investigated. Figure 5.17.a presents the relation between the crack location and the maximum z-displacement ($z_{max,x}$ for $\tilde{x}$=0.7 and $z_{max,w}$ over the whole length). The crack location gives an almost symmetric condition about the middle of the shaft for $z_{max,x}$. Compared to the flexural response (Fig. 3.12), the results are almost the same, so the torsional motion does not have much influence in this case.

The relation between the crack location $\tilde{b}$ and the maximum amplitude of the ϕ-torsional deformation, $\phi_{ampl,f}$, is shown in Fig. 5.17.b. The largest computed

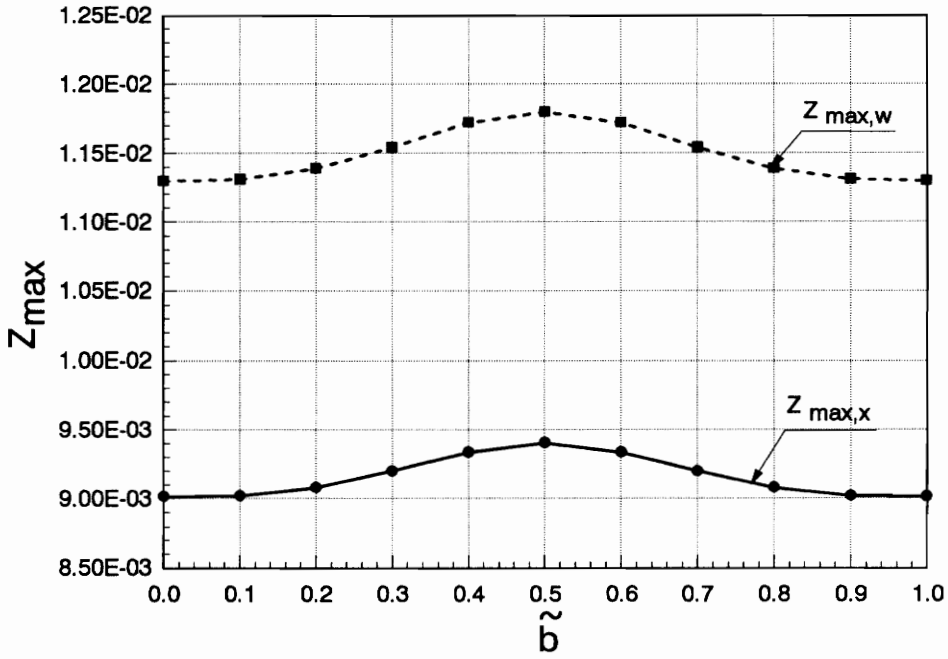

a. Crack Location vs. Z_{max}

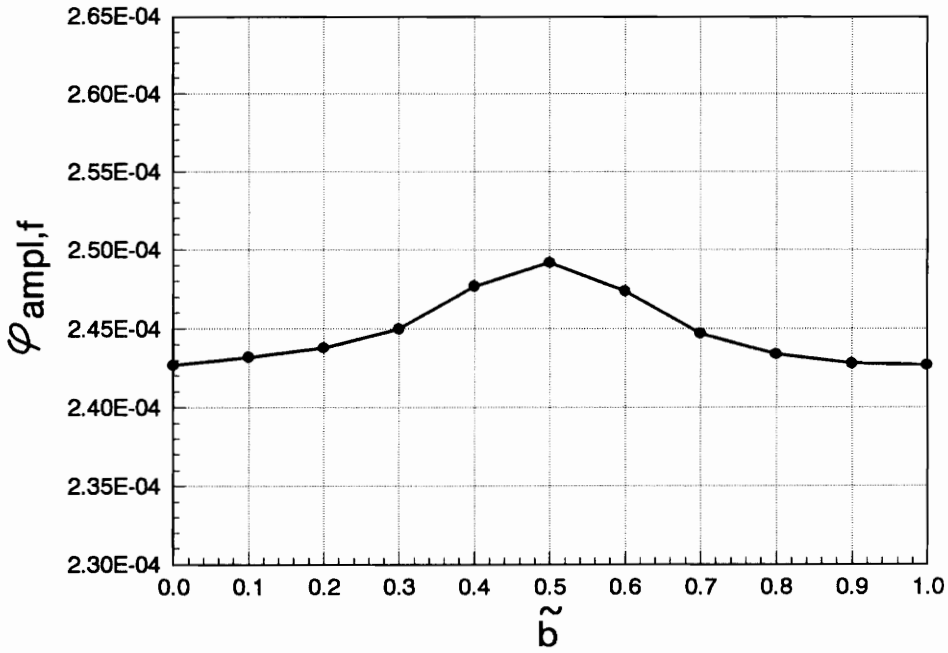

b. Crack Location vs. $\varphi_{ampl,f}$

Fig. 5.17 Influence of Crack Location

$\phi_{ampl,f}$ occurs if the crack is located at the middle of the shaft, like the z-displacement. The curve for $\phi_{ampl,f}$ does not give a symmetric condition about the middle of the shaft, because the boundary conditions for the ϕ-torsional deformation are not the same (fixed-free ends).

5.8. Influence of Disk Location

Based on the standard parameters and the linear acceleration λ=0.001, various locations of the disk ($\tilde{c}$) on the shaft are considered. Figure 5.18.a shows the relation between the disk location and the maximum z-displacement ($z_{max,x}$ at location $\tilde{x}$=0.7 and $z_{max,w}$ over the whole length of the shaft). This relationship does not give a symmetric condition for $z_{max,x}$. Compared to Fig. 3.14, the graphs are almost similar. The z-time histories for $\tilde{c}$=0.1 and $\tilde{c}$=0.9 are similar to Fig. 3.13 and the z-time histories for $\tilde{c}$ between 0.2 and 0.8 are similar to Fig. 5.4.e.

The ϕ-time history for $\tilde{c}$=0.1 is shown in Fig. 5.19. This curve is similar to that for $\tilde{c}$=0.9. Both curves are different from the curves for $\tilde{c}$ between 0.2 and 0.8, which are similar to Fig. 5.4.f. Because the curves are so different, the relation between $\phi_{ampl,f}$ and the disk location is only shown for $\tilde{c}$ between 0.2 and 0.8 in Fig. 5.18.b. From that figure, it can be seen that $\phi_{ampl,f}$ increases if the disk location moves closer to the right end where ϕ is "free".

5.9. Influence of Crack Depth

Five different relative crack depths (a/D) are studied, i.e., a/D=0, 0.1, 0.2, 0.25, and 0.30. The compliances $\tilde{c}_{44}$, $\tilde{c}_{55}$, and $\tilde{c}_{66}$, functions of the crack depth, are calculated based on the work of Papadopoulos and Dimarogonas[27]. They are

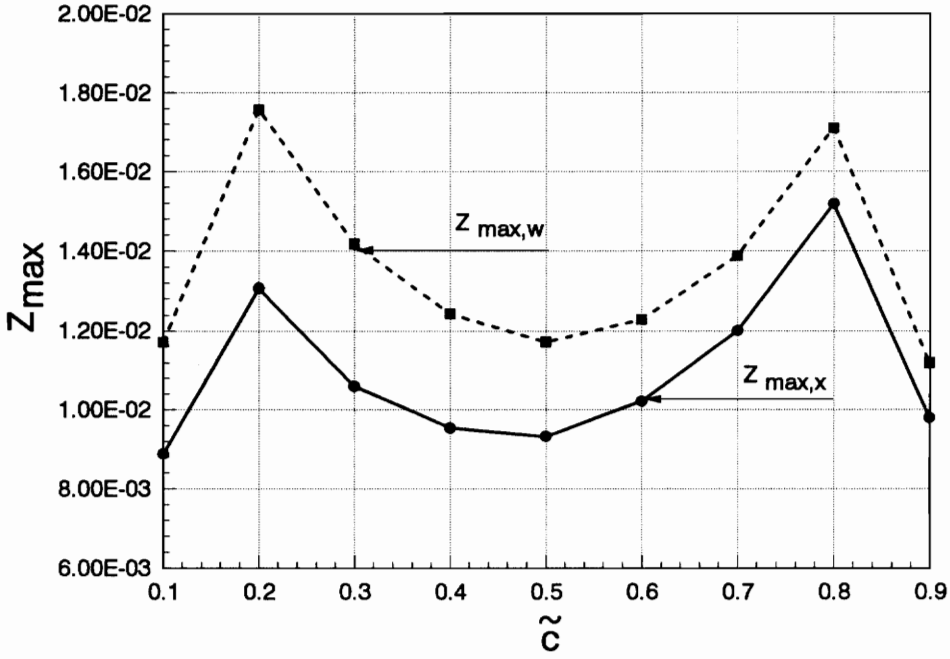

a. Disk Location vs. Z_{max}

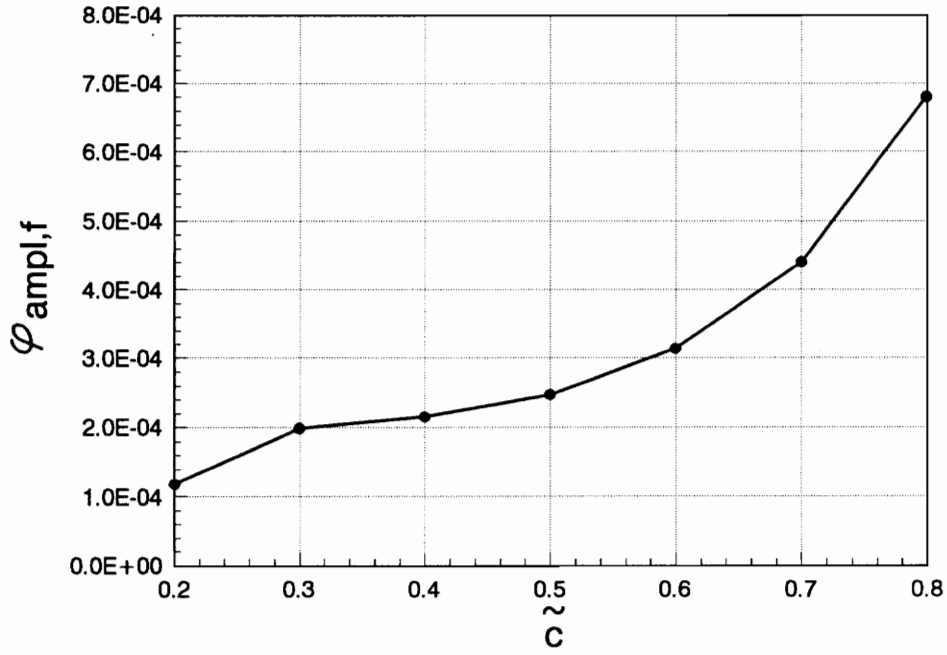

b. Disk Location vs. $\varphi_{ampl,f}$

Fig. 5.18 Influence of Disk Location

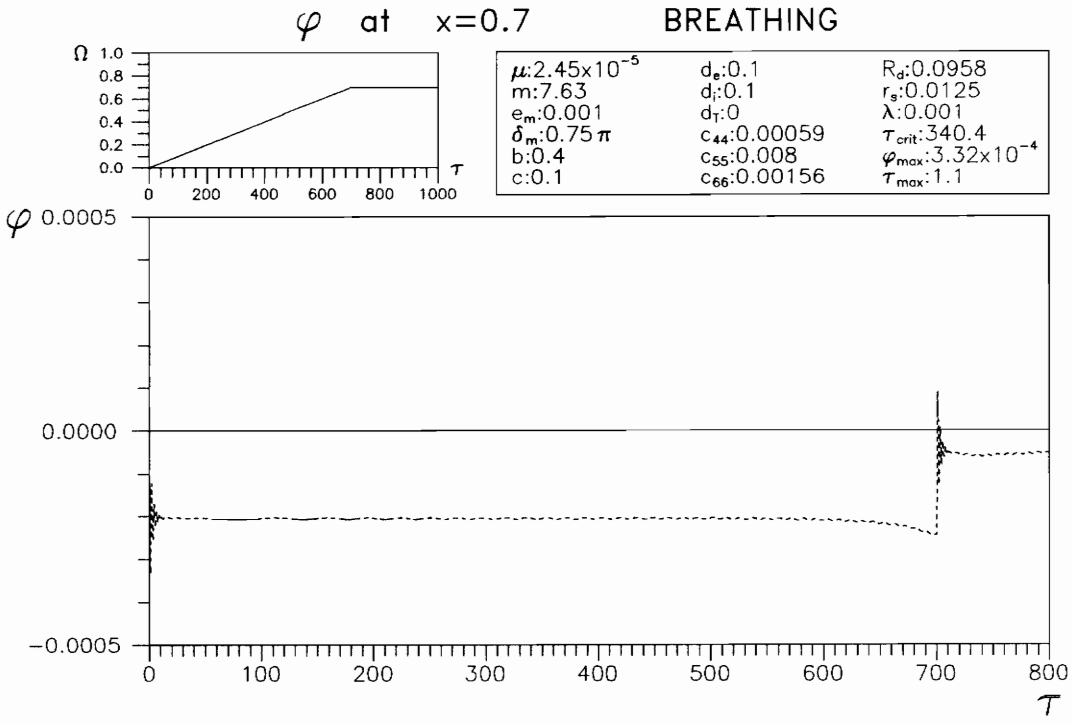

Fig. 5.19 φ – Time History for Disk Location $\tilde{c}$=0.1

shown in Table 5.9 (expanded Table 3.4)

The relation between the crack depth (a/D) and the maximum z-displacement at location $\tilde{x}$=0.7 is presented in Fig. 5.20.a. This relation is similar to the relation for the case without torsion (see Fig. 3.16). This means that the torsional motion does not have much influence on the transverse displacements. Figure 5.20.b shows the relation between the crack depth (a/D) and the maximum amplitude of the ϕ-torsional deformation after transient response ($\phi_{ampl,f}$). The difference of $\phi_{ampl,f}$ between a/D=0.2 and 0.3 is about three times as much as the difference of $\phi_{ampl,f}$ between a/D=0.1 and 0.2. However, the difference of $z_{max,x}$ between a/D=0.2 and 0.3 is about two times as much as the difference of $z_{max,x}$ between a/D=0.1 and 0.2. Table 5.10 gives the values of $z_{max,x}$ and $\phi_{ampl,f}$ related to the crack depth.

Table 5.9 Nondimensional compliances $\tilde{c}_{44}$, $\tilde{c}_{55}$, and $\tilde{c}_{66}$

a/D	$\tilde{c}_{44}$	$\tilde{c}_{55}$	$\tilde{c}_{66}$
0	0	0	0
0.10	0.00004	0.0012	0.00014
0.20	0.00059	0.0080	0.00156
0.25	0.00120	0.01292	0.0030
0.30	0.00215	0.02153	0.0054

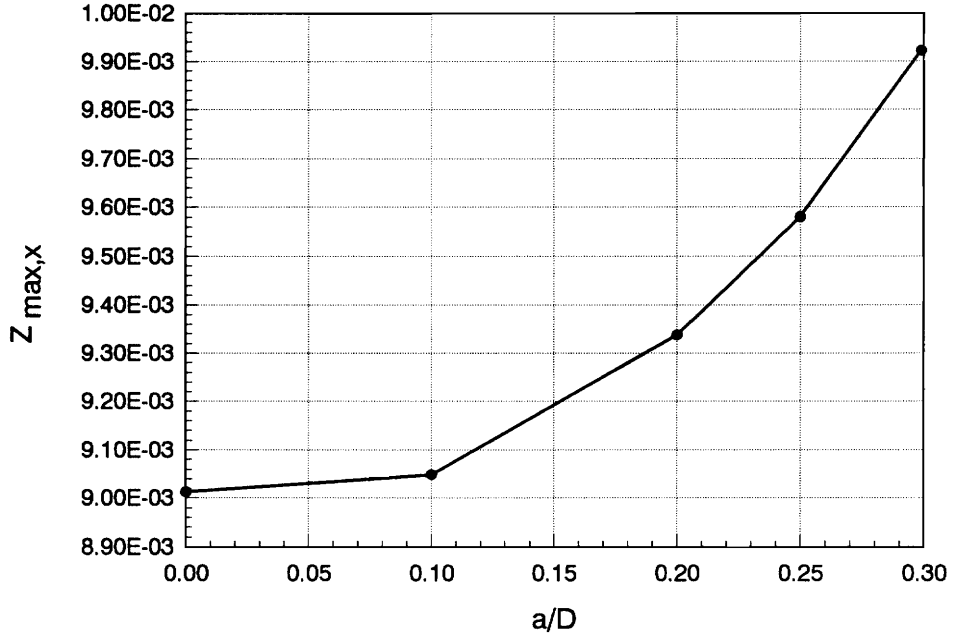

a. Crack Depth vs. $Z_{max,x}$

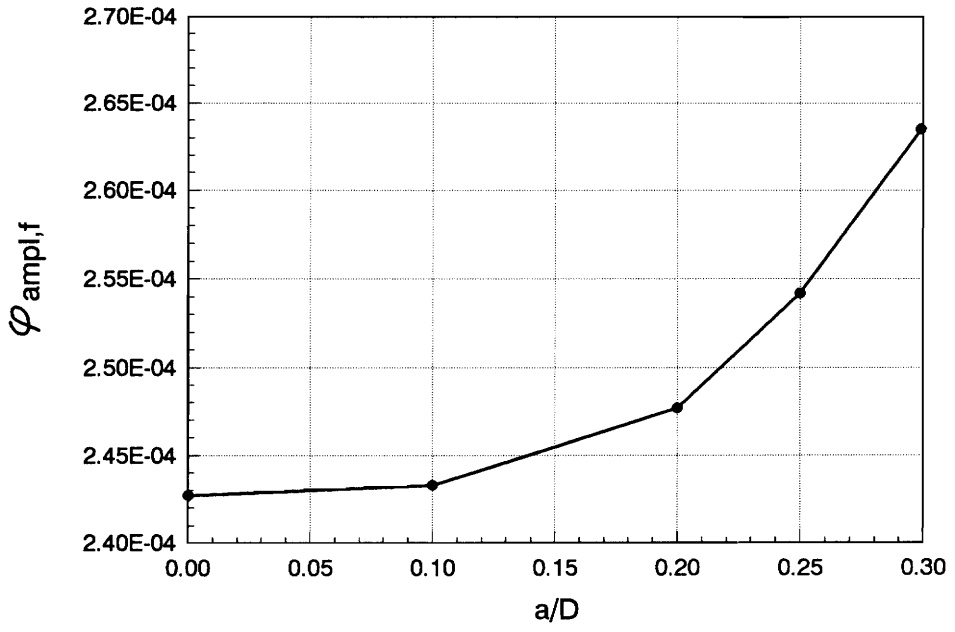

b. Crack Depth vs. $\varphi_{ampl,f}$

Fig. 5.20 Influence of Crack Depth

Table 5.10 Influence of crack depth

a/D	$z_{max,x}$	$\phi_{ampl,f}$
0.00	9.01×10^{-3}	2.43×10^{-4}
0.10	9.05×10^{-3}	2.43×10^{-4}
0.20	9.34×10^{-3}	2.48×10^{-4}
0.25	9.58×10^{-3}	2.54×10^{-4}
0.30	9.92×10^{-3}	2.64×10^{-4}

5.10. Influence of Disk Eccentricity Angle

Three cases of crack conditions, that is breathing crack, open crack, and no crack, are investigated in relation to the influence of the disk eccentricity angle δ_m. Figure 5.21.a shows the relation between δ_m and the maximum z-displacement at location $\tilde{x}$= 0.7 for the standard case. The result is similar to the result for the case of no torsion (see Fig. 3.17).

Figure 5.21.b gives the relation between the disk eccentricity angle and $\phi_{ampl,f}$ for the breathing crack, open crack and no crack. For the no-crack case, $\phi_{ampl,f}$ is almost constant for all conditions of the disk eccentricity angle; the difference is very small (less than 0.5%). For the other cases, $\phi_{ampl,f}$ has a greater variation for different values of the disk eccentricity angle. There are two basic ranges of δ_m for breathing crack and open crack conditions. First, the breathing crack gives a larger $\phi_{ampl,f}$ than the open crack if δ_m is between 0 and $1\frac{1}{4}\pi$ and between $1\frac{7}{8}\pi$ and

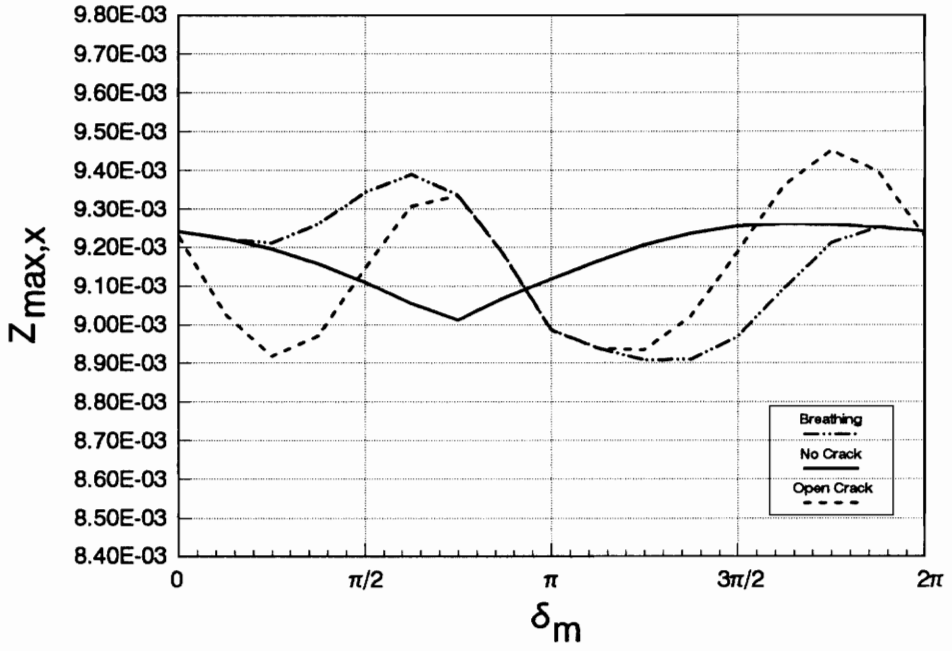

a. Disk Eccentricity Angle vs. $Z_{max,x}$

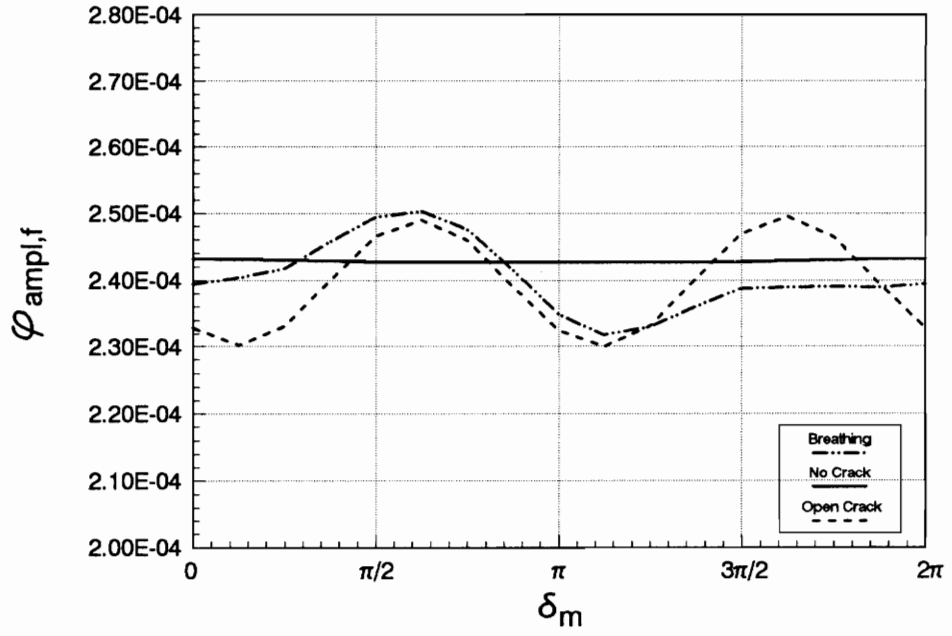

b. Disk Eccentricity Angle vs. $\varphi_{ampl,f}$

Fig. 5.21 Influence of Disk Eccentricity Angle

2π. Second, the open crack gives a larger $\phi_{ampl,f}$ if δ_m is between $1\frac{1}{4}\pi$ and $1\frac{7}{8}\pi$. The breathing crack condition gives a larger $\phi_{ampl,f}$, compared to the no-crack condition, if δ_m is located only between $\frac{1}{4}\pi$ and $\frac{7}{8}\pi$. If δ_m is located between $\frac{3}{8}\pi$ and $\frac{13}{16}\pi$, or between $1\frac{3}{8}\pi$ and $1\frac{13}{16}\pi$, the open crack condition gives a larger $\phi_{ampl,f}$ than the no-crack condition.

5.11. Influence of Disk Mass

The influence of the disk mass is presented in this section for $\tilde{m}$ between 1 and 10. If the disk is located at $\tilde{c}$=0.1, the z-time history and ϕ-time history have the same characteristics for all values of $\tilde{m}$ in this range as for $\tilde{m}$=1 (see Fig. 3.13 and 5.19). The disk in this case only has a small influence on the system. The other cases have the same characteristics as Fig. 5.4.e and 5.4.f.

Figures 5.22.a shows the relation between the disk mass and the maximum z-displacement at location $\tilde{x}$=0.7. The difference of $z_{max,x}$ between $\tilde{m}$=1 and $\tilde{m}$=2 is almost 20% and the difference of $z_{max,x}$ between $\tilde{m}$=2 and $\tilde{m}$=3 is about 12%. However, the difference of $z_{max,x}$ for the other consecutive disk mass cases is less than 5%. There is a tendency for $z_{max,x}$ to decrease as $\tilde{m}$ increases past $\tilde{m}$=6.

Figure 5.22.b presents the relation between the disk mass and $\phi_{ampl,f}$. In this relation, the variations of the disk mass are only between 2 and 10, because the ϕ-time history of m=1 is different from the other cases of the disk mass. With an increase of the disk mass, $\phi_{ampl,f}$ tends to increase also.

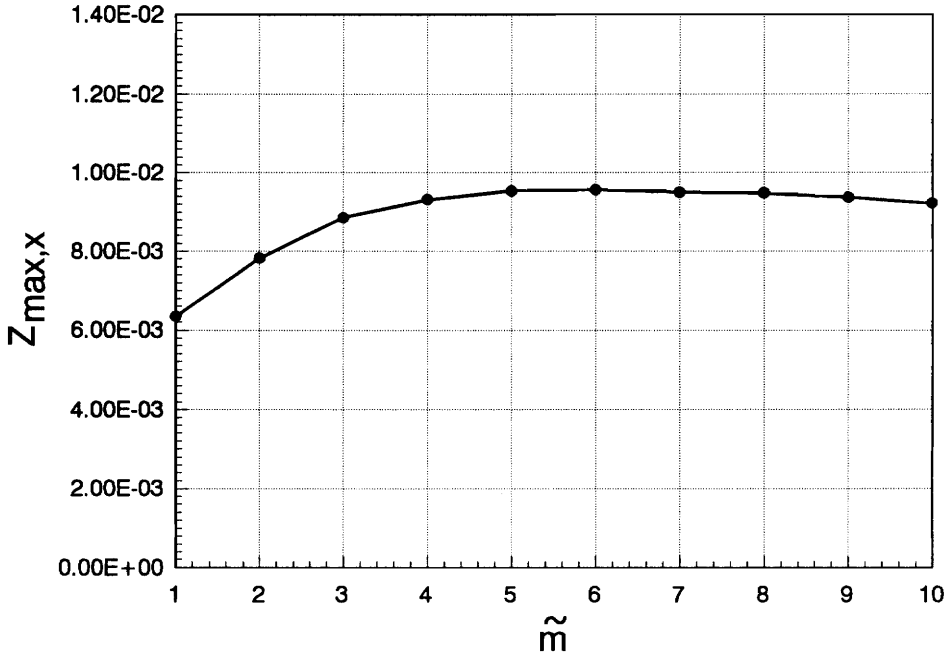

a. Disk Mass vs. $Z_{max,x}$

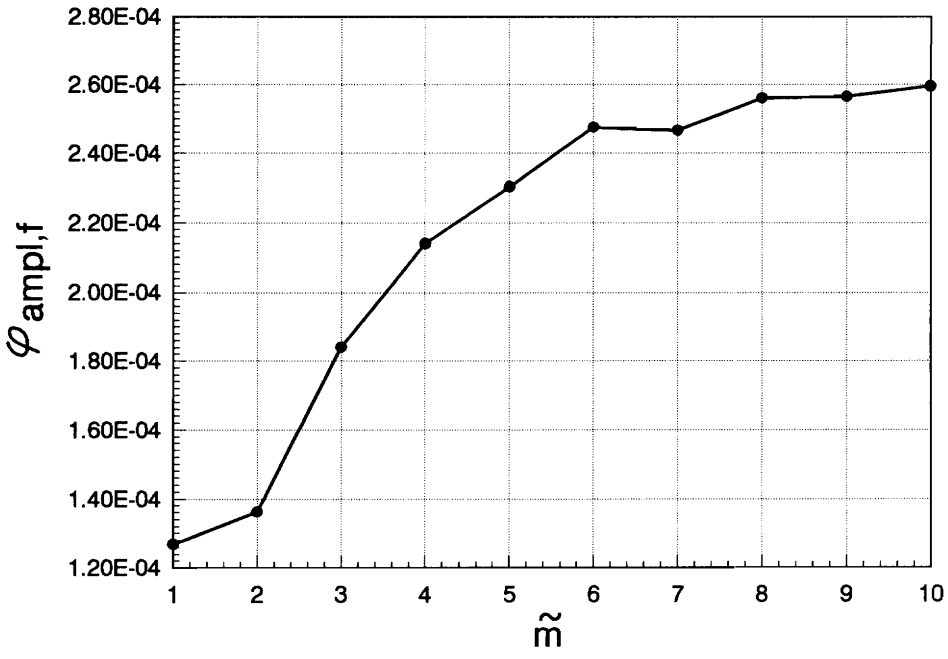

b. Disk Mass vs. $\varphi_{ampl,f}$

Fig. 5.22 Influence of Disk Mass

5.12. Transverse Displacements and Torsional Deformation at Certain Points

Based on the standard parameters, points along the shaft between 0.1 and 0.9 are studied in relation to the transverse displacements and torsional deformation. Figure 5.23.a shows the maximum z-displacement at points along the shaft. From this figure, the relation is almost symmetric about the middle of the shaft. The maximum z-displacement over the whole length occurs at the middle of the shaft.

Figure 5.23.b displays the maximum amplitude of the ϕ-torsional deformation after transient response ($\phi_{ampl,f}$) at points along the shaft. In this curve, there is no symmetric condition because the shaft is fixed at one end ($\tilde{x}$=0) and free at the other end ($\tilde{x}$=1) in relation to torsion. From this figure, $\phi_{ampl,f}$ increases until $\tilde{x}$=0.7 and then decreases. The decreasing condition is due to the simply supported boundary conditions on the transverse displacements and the interaction between the displacements.

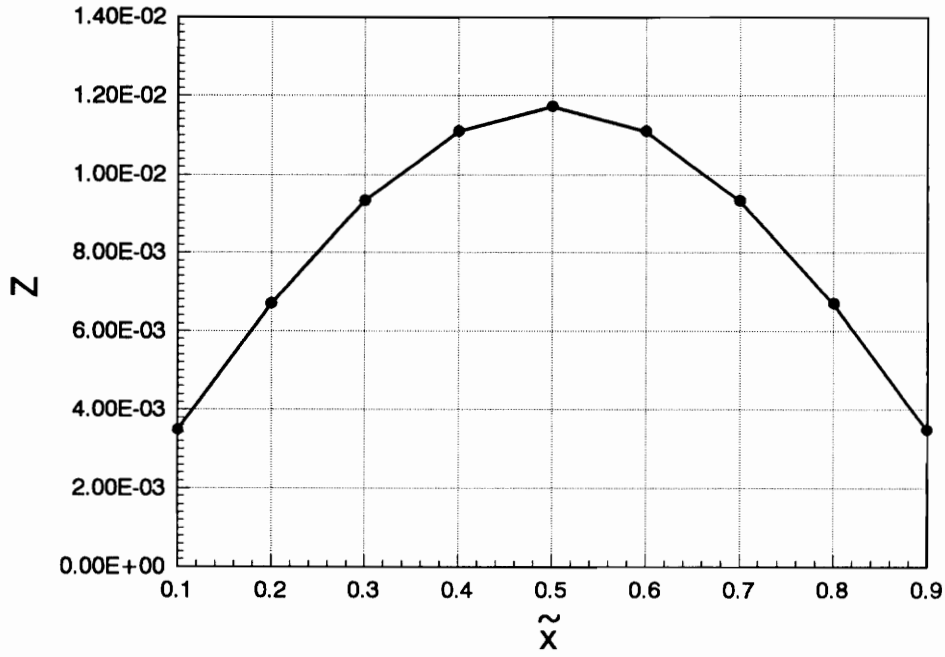

a. Location vs. Z

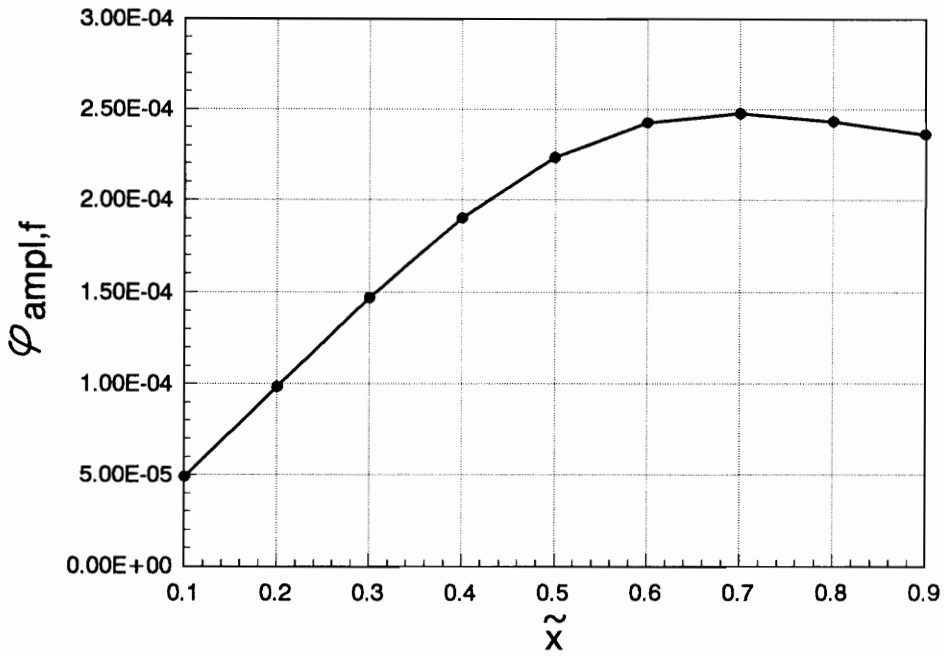

b. Location vs. $\varphi_{ampl,f}$

Fig. 5.23 Transverse Displacement and Torsional Deformation Along Shaft

Chapter 6
Conclusions and
Suggestions for Future Research

6.1. Conclusions

This study has investigated non-stationary motions of cracked rotating shafts with a disk under accelerating and decelerating angular velocity Ω passing through a critical speed. The first part of this study considered the flexural response of the cracked rotating shaft, and the second part considered the interaction between flexural and torsional responses. The effects of different parameters on the cracked rotating shaft was analyzed for the flexural response as well as the flexural-torsional response.

The general conclusions are as follows:

- The inclusion of torsional motion does not have much effect on the transverse displacements.
- Lower acceleration and lower deceleration give higher maximum z-displacement (transverse motion in the vertical direction) and higher maximum amplitude of ϕ-torsional deformation around the critical speed.
- The largest z-displacement and the largest maximum amplitude of the ϕ-torsional deformation occur if the crack is located at the middle of the shaft. However, if the disk is located at the middle of the shaft, the largest z-

displacement does not occur. The ϕ-torsional deformation increases if the disk is moved closer to the right end where ϕ is "free" until $\tilde{x}$=0.7 and then decreases.

- The variation of crack depth yields a non-linear result for the maximum z-displacement and the maximum amplitude of the ϕ-torsional deformation.
- A linear result for the maximum z-displacement is exhibited in the case of variation of the disk eccentricity.
- Different disk eccentricity angles give different maximum z-displacement and maximum amplitude of the ϕ-torsional deformation. Also, different disk eccentricity angles under different crack conditions give different effects on both responses: the largest response may occur for the shaft with a breathing crack, or an open crack, or no crack.
- Variations of the external torsional damping coefficient $\tilde{d}_T$ do not change the characteristics of the ϕ-time history and the z-time history, except for differences in the mean torsional deformation $\phi_{mean,f}$, which decreases gradually as $\tilde{d}_T$ increases.
- Large internal damping $\tilde{d}_i$ can cause instability of the system at angular velocities above the first critical speed. A relation between the external damping and the internal damping determines the stability of the system.

6.2. Suggestions for Future Research

Many aspects of the behavior of a cracked rotating shaft have not been studied.

- In this study, the cracked rotating shaft only has a single disk and a single crack. For future research, it is suggested that multiple disks and multiple cracks be considered.

- It would be interesting to know the behavior of a cracked rotating shaft under different boundary conditions, including flexible supports.
- A circular cross section has been used in this study. A non-circular cross section, compared to a circular cross section, might give significant changes in behavior.
- The frequency domain of the transverse displacement and torsional deformation should be analyzed. Also, cascade plots of a cracked shaft can be made to examine the effect of the change of the angular velocity (non-stationary motions).
- Using Euler-Bernoulli theory is different from using Timoshenko theory. Timoshenko theory includes shear deformation and rotatory inertia. It would be interesting to know how these would influence the behavior of a cracked rotating shaft.
- After appropiate experiments are conducted, the analytical results should be compared to the experimental results for verification.

References

1. **Aiba, S.,** ***On the Vibration of a Rotating Shaft Passing Through the Critical Speed,*** Bulletin of the JSME, 19, 1976, 95-102.
2. Andruet, R.H., ***Behavior of a Cracked Shaft During Passage Through a Critical Speed,*** M.S. Thesis, Virginia Polytechnic Institute and State University, Blacksburg, Virginia, 1991.
3. Bachschmid, N., Diana, G., and Pizzigoni, B., ***The Influence of Unbalance on Cracked Rotors***, in: Vibrations in Rotating Machinery, The Institution of Mechanical Engineers, London, 1984, 193-198.
4. Baker, J.G., ***Mathematical-Machine Determination of the Vibration of an Accelerated Unbalanced Rotor***, Transactions of the ASME, 61, 1939, A145-A150.
5. Bodger, W.K., ***Deceleration of an Unbalanced Rotor Through a Critical Speed***, Journal of Engineering for Industry, 89, 1967, 582-586.
6. Chang, H.Y., and Petroski, H.J., ***On Detecting a Crack by Tapping a Beam,*** International Journal of Pressure Vessels and Piping, 22, 1986, 41-55.
7. Christides, S., and Barr, A.D.S., ***Torsional Vibration of Cracked Beams of Non-Circular Cross-Section,*** International Journal of Mechanical Sciences, 28, 1986, 473-490.
8. Collins, K.R., Plaut, R.H., and Wauer, J., ***Detection of Cracks in Rotating Timoshenko Shafts Using Axial Impulses,*** Journal of Vibration and Acoustics,

113, 1991, 74-78.

9. Collins, K.R., Plaut, R.H., and Wauer, J., ***Free and Forced Longitudinal Vibrations of a Cantilevered Bar with a Crack***, Journal of Vibration and Acoustics, 114, 1992, 171-177.

10. Gasch, R., ***Dynamic Behaviour of a Simple Rotor with a Cross-Sectional Crack***, in: Vibrations in Rotating Machinery, The Institution of Mechanical Engineers, London, 1976, 123-128.

12. Gasch, R., Markert, R., and Pfützner, H., ***Acceleration of Unbalanced Flexible Rotors Through the Critical Speeds***, Journal of Sound and Vibration, 63, 1979, 393-409.

13. Gasch, R., Person, M., and Weitz, B., ***Dynamic Behaviour of the Laval Rotor with a Cracked Hollow Shaft - a Comparison of Crack Models***, in: Vibrations in Rotating Machinery, The Institution of Mechanical Engineers, London, 1988, 463-472.

13. Gudmundson, P., ***The Dynamic Behaviour of Slender Structures with Cross-Sectional Cracks***, Journal of the Mechanics and Physics of Solids, 31, 1983, 329-345.

14. Huseyin, K., ***Vibrations and Stability of Multiple Parameter Systems***, Sijthoff & Noordhoff International Publishers, The Netherlands, 1978.

15. Ishida, Y., Ikeda, T., Yamamoto, T., and Murakami, S., ***Nonstationary Vibration of a Rotating Shaft with Nonlinear Spring Characteristics During Acceleration Through a Critical Speed***, JSME International Journal, Series III, 32, 1989, 575-584.

16. Iwatsubo, T., Yamamoto, Y., and Kawai, R., ***Startup Torsional Vibration of Rotating Machine Driven by Synchronous Motor***, in: Dynamics of Multibody Systems, G. Bianchi and W. Schiehlen, eds., Springer-Verlag, Berlin, 1986,

91-102.

17. Jun, O.S., Eun, H.J., Earmme, Y.Y., and Lee, C.-W., ***Modelling and Vibration Analysis of a Simple Rotor with a Breathing Crack***, Journal of Sound and Vibration, 155, 1992, 273-290.

18. Jun, O.S., Lee, C.-W., Earmme, Y.Y., and Eun, H.J., ***New Approach for the Modelling and Simulation of Simple Cracked Rotor***, in: Proceedings, Fourth International Symposium on Transport Phenomena and Dynamics of Rotating Machinery, 1992, 351-359.

19. Kirmser, P.G., ***The Effect of Discontinuities on the Natural Frequency of Beams***, in: Proceeding, ASTM, 44, 1944, 879-904.

20. Lee, C.-W., Yun, J.-S., and Jun, O.S., **Modelling of a Simple Rotor with a Switching Crack and its Experimental Verification**, Journal of Vibration and Acoustics, 114, 1992, 217-225.

21. Lewis, F.M., ***Vibration During Acceleration Through a Critical Speed***, Transactions of the ASME, 54, 1932, 253-261.

22. Mayes, I.W., and Davies, W.G.R., ***A Method of Calculating the Vibrational Behaviour of Coupled Rotating Shafts Containing a Transverse Crack***, in: Vibrations in Rotating Machinery, The Institution of Mechanical Engineers, London, 1980, 17-27.

23. Muszynska, A., ***Shaft Crack Detection***, in: Proceedings, 7th Machinery Dynamics Seminar, Edmonton, Canada, 1982.

24. Naveh, B.M., and Brach, R.M., ***On the Transition of a Shaft Through Critical Speeds***, Journal of Dynamic Systems, Measurement, and Control, 99, 1977, 48-50.

25. Nelson, H.D., and Nataraj, C., ***The Dynamics of a Rotor System with a Cracked Shaft***, Journal of Vibration, Acoustics, Stress, and Reliability in

Design, 108, 1986, 189-196.

26. Ostachowicz, W.M., and Krawczuk, M., ***Coupled Torsional and Bending Vibrations of a Rotor with an Open Crack***, Archive of Applied Mechanics, 62, 1992, 191-201.

27. Papadopoulos, C.A., and Dimarogonas, A.D., ***Coupled Longitudinal and Bending Vibrations of a Rotating Shaft with an Open Crack***, Journal of Sound and Vibration, 117, 1987, 81-93.

28. Papadopoulos, C.A., and Dimarogonas, A.D., ***Coupling of Bending and Torsional Vibration of a Cracked Timoshenko Shaft***, Ingenieur-Archiv, 57, 1987, 257-266.

29. Papadopoulos, C.A., and Dimarogonas, A.D., ***Coupled Longitudinal and Bending Vibrations of a Cracked Shaft***, Journal of Vibration, Acoustics, Stress, and Reliability in Design, 110, 1988, 1-8.

30. Papadopoulos, C.A., and Dimarogonas, A.D., ***Stability of Cracked Rotors in the Coupled Vibration Mode***, Journal of Vibration, Acoustics, Stress, and Reliability in Design, 110, 1988, 356-359.

31. Petroski, H.J., ***Simple Static and Dynamic Models for the Cracked Elastic Beam***, International Journal of Fracture, 17, 1981, R71-R76.

32. Petroski, H.J., and Glazik, J.L., ***Effects of Cracks on the Response of Circular Cylindrical Shells***, Nuclear Technology, 51, 1980, 303-316.

33. Plaut, R.H., ***Stability of Rotating Shafts with Axial Load and Damping***, Mechanics in Engineering, R.N. Dubey and N.C. Lind, eds., SM Study No. 11, University of Waterloo, Waterloo, Ontario, 1977, 133-140.

34. Schmied, J., and Krämer, E., **Vibrational Behaviour of a Rotor with a Cross-Sectional Crack**, in: Vibrations in Rotating Machinery , The Institution of Mechanical Engineers, London, 1984, 183-192.

35. Thomson, W.J., ***Vibration of Slender Bars with Discontinuities in Stiffness***, Journal of Applied Mechanics, 17, 1949, 203-207.

36. Tsuchiya, K., ***Passage of a Rotor Through a Critical Speed***, Journal of Mechanical Design, 104, 1982, 370-374.

37. Wang, Y.B., Duan, Z.S., Huang, X.L., and Wen, B.C., ***The Responses of the Simple Rotor with Surface Transverse Crack***, in: Rotating Machinery Dynamics, Vol. 2, 11th Biennial Conference on Mechanical Vibration and Noise, Boston, ASME, 1987, DE-Vol. 2, 595-600.

38. Wauer, J., ***Secondary Effects in Transient Vibrations of Rotating Shafts Through Critical Speeds***, in: Proceedings, 1st International Conference on Vibration Problems in Engineering, X'ian, 1986, 763-768.

39. Wauer, J., ***On the Dynamics of Cracked Rotors: A Literature Survey***, Applied Mechanics Reviews, 43, 1990, 13-17.

40. Wauer, J., ***Modelling and Formulation of Equations of Motion for Cracked Rotating Shafts***, International Journal of Solids and Structures, 26, 1990, 901-914.

41. Ying, S.J., ***Transient Whirling of a Rotating Shaft with an Unbalanced Disk***, in: Rotating Machinery Dynamics, A. Muszynska and J.C. Simonis, eds., DE-Vol.2, ASME, New York, 1987, 537-543.

42. Zobnin, A.P., Kelzon, A.S., and Neigebauer, I.I., ***Influence of Gyroscopic Effect on Resonance Avoidance During Acceleration of Unbalanced Flexible Rotors***, Vibration Engineering, 1, 1987, 269-281.

VITA

Surjani Suherman was born on November 19, 1964 in Bandung, Indonesia. She graduated from Parahyangan Catholic University in March 1988 with a Bachelor of Civil Engineering degree. She worked for INACON Civil Engineering Consultant in Indonesia from 1988 until 1991. In August 1991, she began pursuing a Master of Science degree in Civil Engineering at Virginia Polytechnic Institute and State University.